Title

Wind-driven Sediment Transport Across the Solar System

Author

Bretzfelder, Jordan M

Publication Date

2023

Peer reviewed|Thesis/dissertation

UNIVERSITY OF CALIFORNIA

Los Angeles

Wind-driven Sediment Transport Across the Solar System

A dissertation submitted in partial satisfaction of the

requirements for the degree Doctor of Philosophy

in Geology

by

Jordan Melisande Zoe Bretzfelder

2024

ABSTRACT OF THE DISSERTATION

Wind-driven Sediment Transport Across the Solar System

by

Jordan Melisande Zoe Bretzfelder

Doctor of Philosophy in Geology

University of California, Los Angeles, 2024

Professor Mackenzie Denali Day, Chair

Evidence of wind-driven (aeolian) sediment transport has been observed on seven planetary bodies in our solar system to date. The movement of sediment across the surface of a planet can form depositional features, ranging from centimeter-scale ripples to vast and complex sand seas. Alternatively, this same transport process can cause erosion, carving complex structures out of bedrock over time. In some cases, aeolian features observed via remote sensing on other planets are not found on Earth, meaning our understanding of planetary processes is limited by the available analogs. The variety of atmospheric, sediment, and gravitational environments in which aeolian transport occurs indicates that though the conditions may vary, the fundamental physics involved is linked. Each of the research projects described here addresses an open question in a different area of planetary aeolian transport. The studies include two Mars-focused projects ((1) an analysis of dunes and ripples traversed by the Mars Science Laboratory Curiosity rover and (2) a survey of bedrock ridges in Gale crater), a field guide to the Ibex Dunes of Death Valley National Park, and a wind-tunnel experiment where analog sediments were used to simulate planetary aeolian transport.

The dissertation of Jordan Melisande Zoe Bretzfelder is approved.

David A. Paige

Seul Gi Moon

Craig E. Manning

Mackenzie Denali Day, Committee Chair

University of California, Los Angeles

2024

Table of Contents

List of Tables and Figures

Acknowledgements

Upon completion of a doctoratal program, a student may leave with a degree (or two), and a few extra letters tacked on to their title, and more grey hairs than when they started. These changes affect one person, but this does not capture the true nature of graduate school; where success is truly a group effort. So, I want to take this opportunity to thank everyone who made this possible.

Firstly, my advisor Mackenzie Day: Thank you for giving me this opportunity, and for all of the help and guidance along the way. Having a geology lab group full of three non-geologists must have been difficult. Your patience has been greatly appreciated, as well as your incredible support for all of my extracurricular endeavors. I have learned how to be a better scientist, writer, professional, and mentor by watching you, and I plan to carry all these lessons with me for the rest of my life. Thank you for trusting me to get things done, and for believing in me when I shared my plans for this degree and beyond. I hope I've been worth all the trouble!

Secondly, to my doctoral committee: Professors David Paige, Seulgi Moon, Craig Manning and An Yin. Thank you all for your help, feedback, and questions, which have helped me learn how to better assess my own work. Tragically we recently lost An, but I will always be grateful for his teaching, research guidance, and support. I am also extremely grateful to Professor Moon for joining the committee under these unfortunate circumstances, in addition to her and her student's contributions to chapter 4 of this work. And thank you to Dave for meeting with me at AGU all those years ago and suggesting I reach out to Mackenzie; you are the reason I ended up here today!

Next, to the EPSS department staff, who keep everything running smoothly, even with circumstances create seemingly impossibly complex situations. I am especially grateful to Eric Wessenauer, without whom chapter 5 of this dissertation would not exist. Truly the embodiment of 'above and beyond,' the department is so incredibly lucky to have you, and I am eternally grateful for all of your help. Until you have heard the sound a table tennis ball makes while going through a bandsaw, you cannot understand how much Eric dealt with to help me – nevermind all the work he does to help the rest of the department.

To my old lab mates: Taylor Dorn, Jonathan Sneed, Alana Archbold and Jacob Widmer – thank you all for being an absolute joy to work with. And thank you to all of you who helped with my experiments and field work over the years (especially Taylor and Alana – both of whom spent quite a bit of time hunched over in the wind tunnel with me). Thank you to Taylor and Jonathan for welcoming me to UCLA, you two were an absolute delight during the visit day, and made me feel confident in my choice to join the lab. To the new students: Sarah Preston, Imani Lawrence, and BreeAnn Getman – thank you for carrying on the spirit of the lab group! And to my classmates, thank you for the solidarity throughout the very complicated years we have spent together in this program. I am lucky to have found myself in such a positive environment.

For chapter 2, I would like to thank Jonathan Sneed for assistance with image processing. For chapter 3, I would like to thank my JPL internship mentors Drs. Abigail Fraeman and Kathryn Stack for the opportunity to work with them, and my co-athors William Dietrich and Alexander Bryk for their valuable insights, which greatly improved the final manuscript.

For chapters 4 and 5, I would like to acknowledge everyone else who helped with my research along the way: THANK YOU! The undergraduate and graduate students who helped me in the lab and the field were critical to the success of these projects, and I am extremely thankful to everyone who has taken time out of their day to help me do science. This includes (but is not limited to): Elisha Jhoti, Tyler Horvath, Morgan Carrington, and the several students who worked with me this fall in the wind tunnel. Additionally, I would like to refer the reader to the land acknowledgement in chapter 4, as the study site is on land that historically was occupied by the Timbisha Shoshone.

Now for my friends and family; thank you for putting up with me through this process. A PhD may not be easy, but having all of you in my life made it possible. I am not sure I can find the words (perhaps because I have used them all up writing the rest of this document) to articulate how valuable all of your support, encouragement, and love has been for me over the past several years. To my parents: thank you for letting me pursue my passions. Without you, absolutely none of this would have been possible. To my sister: thank you for giving me one more reason to come to UCLA. To my friends (Al-Baab, Lillie, Leander, Julian, Isaac, Julia, and everyone else): I hope I can be as good of a friend to all of you as you all have been to me throughout these past four years. Thank you for keeping me sane.

Curriculum Vita

Jordan M. Bretzfelder

EDUCATION

University of California Los Angeles – MS in Geology 2021

Department of Earth, Planetary, and Space Sciences - Advised by Professor Mackenzie Day

University of Southern California – BS in Physics 2019

HONORS AND AWARDS

Dissertation Year Fellowship – Awarded by UCLA 2023

Amelia Earhart Fellowship – Awarded by Zonta International 2022

Department Outreach Award 2022

NASA Space Grant Fellowship 2021

Eugene B. Waggoner Prize for Excellence in Original Research 2021

Honorable Mention in the NSF Graduate Research Fellowship Program Competition 2021

UCLA Graduate Council Diversity Fellowship 2020

Graduate Dean's Scholar Award 2019-2021

First Year Fellowship 2019-2020

Stephen E. Dwornik Award – Best Undergraduate Oral Presentation 2018

Dean's Merit Scholarship 2015-2019

PUBLICATIONS

1) **Bretzfelder, J. M.,** Stack, K. M., Fraeman, A. A., Day, M., Dietrich, W. E., & Bryk, A. B. (2024). Aeolian bedrock ridges in Gale crater, Mars. *Icarus*, *408*, 115855. https://doi.org/10.1016/j.icarus.2023.115855

2) Day, M., **Bretzfelder, J. M.**, Le, D., (2023) "Not Every Circle is a Crater: Kettle Hole Size Distributions and Their Implications in Planetary Surface Age Dating." *Geosciences 13*(1). doi: 10.3390/geosciences13010018

3) Kumari, N., **Bretzfelder, J. M.**, Ganesh, I., Lang, A., Kring, D., (2022) "Surface Conditions and Resource Accessibility at Potential Artemis Landing Sites 007 and 011." *Planetary Science Journal* 3(224). doi: 10.3847/PSJ/ac88c2

4) **Bretzfelder, J. M.** and M. Day (2021) "Alien Aeolian Bedforms: A Comparative Sedimentary Analysis of the Dingo Gap Bedform and Hidden Valley Ripple Traverses, Gale Crater, Mars." *Journal of Geophysical Research: Planets.* doi: 10.1029/2021JE006904

5) **Bretzfelder, J. M.,** et al. (2020) "Identification of Potential Mantle Rocks around the Lunar Imbrium Basin." *Geophysical Research Letters 47*(22). doi: 10.1029/2020GL090334

6) Klima, R. and **Bretzfelder, J. M.** (2020) "The Moon." Encyclopedia of Geology, 2nd Edition.

7) Kring, D., **Bretzfelder, J. M.**, Ganesh, I., Kumari, N., Lang, A., Siegler, M. (2020) "Artemis III EVA Opportunities on the Rim of de Gerlache Crater" [White Paper]. NASA-requested input to the Artemis III Science Definition Team.

8) Kring, D., **Bretzfelder, J. M.**, Ganesh, I., Kumari, N., Lang, A., Siegler, M. (2020) "Alternative Artemis III EVA Opportunities near de Gerlache Crater" [White Paper]. NASA-requested input to the Artemis III Science Definition Team.

9) Kring, D., **Bretzfelder, J. M.**, Ganesh, I., Kumari, N., Lang, A. (2020) "Artemis III EVA Opportunities on the Lunar Farside near Shackleton Crater" [White Paper]. NASA-requested input to the Artemis III Science Definition Team.

CHAPTER 1: Introduction

Aeolian (wind-driven) sediment transport occurs on the surface of at least seven planetary bodies in our solar system: Venus, Earth, Mars, Titan, Io, Pluto and Comet 67P/Churyumov–Gerasimenko (Greely, 1989; Lorenz, 2014; Jia et al., 2017; Diniega et al., 2017; Telfer et al., 2018; Macdondald et al., 2022). The dynamic relationship between a planet's atmosphere and surface can create both depositional and erosional features, and these features can be used to interpret formative wind directions, sediment fluxes, and climate histories (e.g., Sharp, 1963; Greely et al., 2001; Laity and Bridges, 2009; Bridges et al., 2010; Milliken et al., 2010; Chojnakci et al., 2011; Montgomery et al., 2012; Hugenholtz et al., 2015; Day and Kocurek, 2016; Day and Catling, 2018; Urso et al., 2018; Banham et al., 2022). These topics are areas of active research, with each new discovery adding to the list of known unknowns.

Depositional features, such as dunes and ripples, occur on all seven of the aforementioned planetary bodies (Greely, 1989; Lorenz, 2014; Jia et al., 2017; Diniega et al., 2017; Telfer et al., 2018; Mcdondald et al., 2022). These features form under a wide range of conditions, as each planetary body has a unique combination of atmospheric and sediment properties, as well as different gravitational accelerations. Even bodies with only transient or ephemeral atmospheres (such as Pluto, Io and Comet 67P; Jia et al., 2017; Telfer et al., 2018; Mcdondald et al., 2022) are shaped by aeolian transport, meaning it is an impactful and relevant process across the solar system (and beyond).

Aeolian transport has day-to-day impacts on life on Earth and on planetary exploration missions. Dune encroachment can disrupt and destroy urban developments, and dust storms pose a variety of dangers (e.g., Lam et al., 2011; Ahmady-Birgani et al., 2017; Gomez et al., 2018). As the climate changes, the negative impacts on man-made structures and daily life become more

frequent (e.g, Le Houérou, 1995; Huang et al., 2020; Burrell et al., 2020). Beyond Earth, aeolian sediment transport (and particularly dust storms) can pose a threat to planetary missions. For example, solar panels used to power rover missions to Mars have suffered power loss and eventual mission termination due to dust cover limiting power generation (e.g., the Mars Exploration Rover Opportunity and the InSight mission; Lorenz and Reiss, 2015; Kinch et al., 2015; Vicente-Retortillo et al., 2018; Witze, 2019). As human missions to Mars are planned, a well-developed understanding of the impacts of wind and dust storms will be critical to mission safety.

In our quest to better understand sediment transport beyond Earth, we have limited access to the systems we are investigating. We receive in-situ data from the Mars rovers, but at present these are the only planetary surface missions operating in a wind-dominated system. In order to supplement our remote observations of these planetary surfaces, we leverage analogs which are accessible to us on Earth. These analogs can include field sites that are relevant to certain aspects of other planetary systems (e.g., Barrett et al., 2008; Cary et al., 2010; de Silva et al., 2013; Bridges et al., 2015; Arvidson et al., 2016) , as well as laboratory techniques and materials that are able to simulate planetary systems (e.g., Burr et al., 2015a; Burr et al., 2015b; Swann et al., 2019).

The four research projects described here investigate various aspects of planetary aeolian transport: (1) the sedimentology and terra-mechanical properties of Martian dunes and ripples (Chapter 2; Bretzfelder and Day, 2021), (2) Martian paleo-winds and their impacts on the surface (Chapter 3; Bretzfelder et al., 2024), (3) a potential novel Mars analog site in Death Valley National Park (Chapter 4), and (4) an investigation into the fundamental processes of grain motion under planetary conditions (Chapter 5). These studies span a range of scales, from the short-term behavior of individual grains in a flow, to the impacts of 3 billion years of aeolian transport on the surface on Mars. These studies address open questions or knowledge gaps in a range of sub-topics

in the field of aeolian geology, and investigate the fundamental aspects of aeolian transport throughout our solar system.

1.1 References

Ahmady-Birgani, H., McQueen, K. G., Moeinaddini, M., & Naseri, H. (2017). Sand Dune Encroachment and Desertification Processes of the Rigboland Sand Sea, Central Iran. *Scientific Reports*, *7*(1), Article 1. https://doi.org/10.1038/s41598-017-01796-z

Banham, S. G., Gupta, S., Rubin, D. M., Bedford, C. C., Edgar, L. A., Bryk, A. B., Dietrich, W. E., Fedo, C. M., Williams, R. M., Caravaca, G., Barnes, R., Paar, G., Ortner, T., & Vasavada, A. R. (2022). Evidence for Fluctuating Wind in Shaping an Ancient Martian Dune Field: The Stimson Formation at the Greenheugh Pediment, Gale Crater. *Journal of Geophysical Research: Planets*, *127*(9), e2021JE007023. https://doi.org/10.1029/2021JE007023

Barrett, J. E., Virginia, R. A., Wall, D. H., Doran, P. T., Fountain, A. G., Welch, K. A., & Lyons, W. B. (2008). Persistent effects of a discrete warming event on a polar desert ecosystem. *Global Change Biology*, *14*(10), 2249–2261. https://doi.org/10.1111/j.1365-2486.2008.01641.x

Bretzfelder, J. M., & Day, M. (2021). Alien Aeolian Bedforms: A Comparative Sedimentary Analysis of the Dingo Gap Bedform and Hidden Valley Ripple Traverses, Gale Crater, Mars. *Journal of Geophysical Research: Planets*, *126*(8), e2021JE006904. https://doi.org/10.1029/2021JE006904

Bretzfelder, J. M., Stack, K. M., Fraeman, A. A., Day, M., Dietrich, W. E., & Bryk, A. B. (2024). Aeolian bedrock ridges in Gale crater, Mars. *Icarus*, *408*, 115855. https://doi.org/10.1016/j.icarus.2023.115855

Bridges, N. T., Banks, M. E., Beyer, R. A., Chuang, F. C., Noe Dobrea, E. Z., Herkenhoff, K. E., Keszthelyi, L. P., Fishbaugh, K. E., McEwen, A. S., Michaels, T. I., Thomson, B. J., & Wray, J. J. (2010). Aeolian bedforms, yardangs, and indurated surfaces in the Tharsis Montes as seen

by the HiRISE Camera: Evidence for dust aggregates. *Icarus*, *205*(1), 165–182. https://doi.org/10.1016/j.icarus.2009.05.017

Bridges, N. T., Spagnuolo, M. G., de Silva, S. L., Zimbelman, J. R., & Neely, E. M. (2015). Formation of gravel-mantled megaripples on Earth and Mars: Insights from the Argentinean Puna and wind tunnel experiments. *Aeolian Research*, *17*, 49–60. https://doi.org/10.1016/j.aeolia.2015.01.007

Burr, D. M., Bridges, N. T., Marshall, J. R., Smith, J. K., White, B. R., & Emery, J. P. (2015). Higher-than-predicted saltation threshold wind speeds on Titan. *Nature*, *517*(7532), Article 7532. https://doi.org/10.1038/nature14088

Burr, D. M., Bridges, N. T., Smith, J. K., Marshall, J. R., White, B. R., & Williams, D. A. (2015). The Titan Wind Tunnel: A new tool for investigating extraterrestrial aeolian environments. *Aeolian Research*, *18*, 205–214. https://doi.org/10.1016/j.aeolia.2015.07.008

Burrell, A. L., Evans, J. P., & De Kauwe, M. G. (2020). Anthropogenic climate change has driven over 5 million km2 of drylands towards desertification. *Nature Communications*, *11*(1), Article 1. https://doi.org/10.1038/s41467-020-17710-7

Cary, S. C., McDonald, I. R., Barrett, J. E., & Cowan, D. A. (2010). On the rocks: The microbiology of Antarctic Dry Valley soils. *Nature Reviews Microbiology*, *8*(2), Article 2. https://doi.org/10.1038/nrmicro2281

Chojnacki, M., Burr, D. M., Moersch, J. E., & Michaels, T. I. (2011). Orbital observations of contemporary dune activity in Endeavor crater, Meridiani Planum, Mars. *Journal of Geophysical Research: Planets*, *116*(E7). https://doi.org/10.1029/2010JE003675

Day, M. D., & Catling, D. C. (2018). Dune Casts Preserved by Partial Burial: The First Identification of Ghost Dune Pits on Mars. *Journal of Geophysical Research: Planets*, *123*(6), 1431–1448. https://doi.org/10.1029/2018JE005613

Day, M., & Kocurek, G. (2016). Observations of an aeolian landscape: From surface to orbit in Gale Crater. *Icarus*, *280*, 37–71. https://doi.org/10.1016/j.icarus.2015.09.042

de Silva, S. L., Spagnuolo, M. G., Bridges, N. T., & Zimbelman, J. R. (2013). Gravel-mantled megaripples of the Argentinean Puna: A model for their origin and growth with implications for Mars. *GSA Bulletin*, *125*, 1912–1929. http://dx.doi.org/10.1130/B30916.1

Diniega, S., Kreslavsky, M., Radebaugh, J., Silvestro, S., Telfer, M., & Tirsch, D. (2017). Our evolving understanding of aeolian bedforms, based on observation of dunes on different worlds. *Aeolian Research*, *26*, 5–27. https://doi.org/10.1016/j.aeolia.2016.10.001

Gómez, D., Salvador, P., Sanz, J., Casanova, C., & Casanova, J. (2018). Detecting Areas Vulnerable to Sand Encroachment Using Remote Sensing and GIS Techniques in Nouakchott, Mauritania. *Remote Sensing*, *10*(10), 1541. https://doi.org/10.3390/rs10101541

Greeley, R. (1989). *Aeolian Processes on Venus*. 21–22. http://adsabs.harvard.edu/full/1989LPICo.708...21G

Greeley, R., Kuzmin, R. O., & Haberle, R. M. (2001). Aeolian Processes and Their Effects on Understanding the Chronology of Mars. In R. Kallenbach, J. Geiss, & W. K. Hartmann (Eds.), *Chronology and Evolution of Mars* (Vol. 12, pp. 393–404). Springer Netherlands. https://doi.org/10.1007/978-94-017-1035-0_14

Huang, J., Zhang, G., Zhang, Y., Guan, X., Wei, Y., & Guo, R. (2020). Global desertification vulnerability to climate change and human activities. *Land Degradation & Development*, *31*(11), 1380–1391. https://doi.org/10.1002/ldr.3556

Hugenholtz, C. H., Barchyn, T. E., & Favaro, E. A. (2015). Formation of periodic bedrock ridges on Earth. *Aeolian Research*, *18*, 135–144. https://doi.org/10.1016/j.aeolia.2015.07.002

Jia, P., Andreotti, B., & Claudin, P. (2017). Giant ripples on comet 67P/Churyumov–Gerasimenko sculpted by sunset thermal wind. *Proceedings of the National Academy of Sciences*, *114*(10), 2509–2514. https://doi.org/10.1073/pnas.1612176114

Kinch, K. M., James F. Bell, I. I. I., Goetz, W., Johnson, J. R., Joseph, J., Madsen, M. B., & Sohl-Dickstein, J. (2015). Dust deposition on the decks of the Mars Exploration Rovers: 10 years of dust dynamics on the Panoramic Camera calibration targets. *Earth and Space Science (Hoboken, N.j.)*, *2*(5), 144. https://doi.org/10.1002/2014EA000073

Laity, J. E., & Bridges, N. T. (2009). Ventifacts on Earth and Mars: Analytical, field, and laboratory studies supporting sand abrasion and windward feature development. *Geomorphology*, *105*(3), 202–217. https://doi.org/10.1016/j.geomorph.2008.09.014

Lam, D. K., Remmel, T. K., & Drezner, T. D. (2011). Tracking Desertification in California Using Remote Sensing: A Sand Dune Encroachment Approach. *Remote Sensing*, *3*(1), Article 1. https://doi.org/10.3390/rs3010001

Le Houérou, H. N. (1996). Climate change, drought and desertification. *Journal of Arid Environments*, *34*(2), 133–185. https://doi.org/10.1006/jare.1996.0099

Lorenz, R. D. (2014). Physics of saltation and sand transport on Titan: A brief review. *Icarus*, *230*, 162–167. https://doi.org/10.1016/j.icarus.2013.06.023

Lorenz, R. D., Martínez, G. M., Spiga, A., Vicente-Retortillo, A., Newman, C. E., Murdoch, N., Forget, F., Millour, E., & Pierron, T. (2021). Lander and rover histories of dust accumulation on and removal from solar arrays on Mars. *Planetary and Space Science*, *207*, 105337. https://doi.org/10.1016/j.pss.2021.105337

Lorenz, R. D., & Reiss, D. (2015). Solar Panel Clearing Events, Dust Devil Tracks, and in-situ Vortex Detections on Mars. *Icarus*, *248*, 162–164. https://doi.org/10.1016/j.icarus.2014.10.034

McDonald, G. D., Méndez Harper, J., Ojha, L., Corlies, P., Dufek, J., Ewing, R. C., & Kerber, L. (2022). Aeolian sediment transport on Io from lava–frost interactions. *Nature Communications*, *13*(1), Article 1. https://doi.org/10.1038/s41467-022-29682-x

Milliken, R. E., Grotzinger, J. P., & Thomson, B. J. (2010). Paleoclimate of Mars as captured by the stratigraphic record in Gale Crater: STRATIGRAPHY OF GALE CRATER. *Geophysical Research Letters*, *37*(4). https://doi.org/10.1029/2009GL041870

Montgomery, D. R., Bandfield, J. L., & Becker, S. K. (2012). Periodic bedrock ridges on Mars. *Journal of Geophysical Research: Planets*, *117*(E3). https://doi.org/10.1029/2011JE003970

Sharp, R. P. (1963). Wind Ripples. *The Journal of Geology*. https://doi.org/10.1086/626936

Swann, C., Sherman, D. J., & Ewing, R. C. (2020). Experimentally Derived Thresholds for Windblown Sand on Mars. *Geophysical Research Letters*, *47*(3), e2019GL084484. https://doi.org/10.1029/2019GL084484

Telfer, M. W., Parteli, E. J. R., Radebaugh, J., Beyer, R. A., Bertrand, T., Forget, F., Nimmo, F., Grundy, W. M., Moore, J. M., Stern, S. A., Spencer, J., Lauer, T. R., Earle, A. M., Binzel, R. P., Weaver, H. A., Olkin, C. B., Young, L. A., Ennico, K., Runyon, K., & The New Horizons Geology, G. and I. S. T. T. (2018). Dunes on Pluto. *Science*, *360*(6392), 992–997. https://doi.org/10.1126/science.aao2975

Urso, A., Chojnacki, M., & Vaz, D. A. (2018). Dune-Yardang Interactions in Becquerel Crater, Mars. *Journal of Geophysical Research. Planets*, *123*(2), 353–368. https://doi.org/10.1002/2017JE005465

Vicente-Retortillo, Á., Martínez, G. M., Renno, N., Newman, C. E., Ordonez-Etxeberria, I., Lemmon, M. T., Richardson, M. I., Hueso, R., & Sánchez-Lavega, A. (2018). Seasonal Deposition and Lifting of Dust on Mars as Observed by the Curiosity Rover. *Scientific Reports*, *8*, 17576. https://doi.org/10.1038/s41598-018-35946-8

Witze, A. (2019). Opportunity lost: NASA says goodbye to pioneering Mars rover. *Nature*. https://doi.org/10.1038/d41586-019-00575-2

CHAPTER 2: Alien Aeolian Bedforms: a Comparative Sedimentary Analysis of the Dingo Gap Bedform and Hidden Valley Ripple Traverses, Gale Crater, Mars

Note: This chapter is modified from Bretzfelder and Day (2021) "Alien Aeolian Bedforms: a Comparative Sedimentary Analysis of the Dingo Gap Bedform and Hidden Valley Ripple Traverses, Gale Crater, Mars," *Journal of Geophysical Research: Planets.* doi: 10.1029/2021JE006904

2.1 Abstract

At the end of January 2014 (Sols 528-540), the Mars Science Laboratory rover Curiosity approached the a valley opening known as Dingo Gap. Spanning this gap was an unusual bedform with a maximum height of 1.34 m and a maximum width of ~8 m. Curiosity encountered, imaged, and successfully traversed this atypical bedform. In August of 2014, Curiosity began to traverse a field of ripples in Hidden Valley, but was forced to abort the attempt due to high wheel slip. The Hidden Valley ripples are ~1/6 of the height of the Dingo Gap bedform, and yet posed a serious hazard to the rover. Here, we present a sedimentological analysis of the Dingo Gap bedform and the Hidden Valley ripples and discuss how their differences may have impacted rover traversability. The Dingo Gap and Hidden Valley bedforms are morphologically similar to many commonly observed bedforms on Mars that have few clear analogs on Earth, and Curiosity's encounters provide a framework for studying these bedforms in detail. Furthermore, the rover tracks across the bedforms have persisted for >5 Earth years, even through a global dust storm. The longevity of the tracks demonstrates that on multi-year timescales 1) sediment transport on some Martian bedforms is inactive or slow enough that areas disturbed by the rover are not resurfaced, and 2) the rate of dust deposition on the Martian surface, even after a global dust storm, is too low to create an optically thick layer.

2.2 Introduction

Mars is presently dominated by aeolian activity, and hosts a variety of aeolian bedforms across its surface. Centimeter-tall wind ripples to kilometer-wide dunes (e.g., Cutts and Smith, 1973, Bourke et al., 2006, Balme et al., 2018, Lapotre et al., 2018), similar to those on Earth, are common on Mars. Other more enigmatic features, such as transverse aeolian ridges (TARs; Bourke et al., 2003, Balme et al., 2008, Zimbelman, 2010, Berman et al., 2011, Geissler and Wilgus, 2016; Silvestro et al., 2020) and large Martian ripples (Zimbelman et al., 2009; de Silva et al., 2013; Lapotre et al., 2016; Sullivan et al., 2020) are also abundant on the Martian surface. The variety of bedforms observed on Mars is at least as diverse as that of Earth, and their morphology, grain characteristics, and relationships with topography provide a tool for understanding wind-landscape interactions.

Nearly all landed missions to Mars have encountered aeolian bedforms. The Mars Pathfinder mission encountered various aeolian features including bedforms and ventifacts (Greeley et al., 1999).The Mars Exploration Rover Opportunity encountered wind ripples up to tens of centimeters tall, composed of a variety of grains, ranging from dust to 1-2 mm grains (Sullivan et al., 2005, Arvidson et al., 2011). Spirit encountered a field of wind ripples and coarse grain-armored megaripples (Sullivan et al., 2008). The Mars Science Laboratory (MSL) Curiosity rover has imaged a broad range of aeolian features, from centimeter-scale impact ripples formed by sand saltation (Bagnold, 1941; Anderson, 1987), to several meter high dunes in the Bagnold Dune Field (Bridges et al., 2017; Chojnacki and Fenton, 2017; Baker et al., 2018). Although the rovers have explored examples of many Martian bedforms, surface imaging has not captured the full suite of aeolian bedform morphologies (e.g., TAR fields, star dunes) and aeolian bedforms remain a target of interest for future exploration.

With limited analogs on Earth, bedforms like TARs and some Martian megaripples (de Silva et al., 2013, Zimbelman and Foroutan, 2020), remain poorly-understood. Little is known about their formation and evolution. As they cannot be easily studied on Earth, and given the limited interactions rovers have had with them thus far, the uncertainties about their interior structure and terramechanical properties mean they pose a significant risk to rover mobility.

In January, 2014, Curiosity encountered and traversed a meter-scale bedform at a location informally known as Dingo Gap (Fig. 2.1). Due to damage sustained by the rover wheels by this point in the mission, drives were planned through topographic low points which were expected to offer more "soft" sand cover to better protect the wheels (Arvidson et al., 2017). The Dingo Gap bedform was the first of this scale imaged and traversed by a rover, and was crossed because it blocked the entire valley (Sullivan et al., 2014). Later in the mission, at Hidden Valley, Curiosity attempted to traverse a field of ~20 cm high bedforms. Curiosity was forced to abort the attempt due to high wheel slip (Rothrock, et al., 2016, Arvidson et al., 2017). The traverses at Dingo Gap and Hidden Valley offer an opportunity to study contrasting bedforms and their sedimentological differences as observed at the surface. The Mars 2020 Perseverance rover will likely encounter bedforms in Jezero crater similar to those observed by Curiosity in Gale crater, and knowing more about the structure and properties of these bedforms will enable improved planning for Perseverance and future rovers over terrains such as the mapped Aeolian Bedforms surficial units (Stack et al., 2020).

2.3 Background Information and Geologic Context

The Dingo Gap study site is located in Gale crater, northwest of the Bagnold Dune Field (Fig. 2.1). Curiosity visited this region between Sols 528-540 of the MSL mission. Dingo Gap is the entrance to Moonlight Valley, and an aeolian bedform spans the width of the valley mouth. Curiosity traversed through the valley from east to west, meaning that the rover approached the eastern face of the bedform and crossed to the western face. The rover then traversed smaller ripples in Moonlight Valley. Dingo Gap and Moonlight Valley are located in the "Rugged Unit" as defined by orbital geologic mapping, which is characterized as unfractured, bright-toned and topographically variable terrain (Rice et al., 2013, Calef et al., 2013, Grotzinger et al., 2014). Based on in-situ imaging, this unit is now understood to be part of the Bradbury group (Siebach et al., 2017; Stack et al., 2017), and contains sandstones and conglomerates (Rice et al., 2017). Aeolian bedforms tend to concentrate in topographic low points, as is the case in Moonlight Valley.

The bedform at Dingo Gap is not readily characterized as a ripple, dune, or transverse aeolian ridge (TAR). Although the bedform satisfies the descriptive definition of a TAR, it is distinct from most described TARs, and unlike most aeolian bedforms, it stands alone. Based on its size and grain size distribution, the bedform has been labelled as either a megaripple (Sullivan et al., 2014, Arvidson et al. 2017), as a TAR (Weitz et al., 2018), or both (Zimbelman and Foroutan, 2020). Weitz et al. (2018) found a surface composed of coarse grains overlying an interior of fine grains and dust. Morphologically, the bedform is apparently symmetric across its width and has a sharp crest, differentiating this bedform from asymmetric small dunes and large ripples. Arvidson et al. (2017) used information from the MSL Engineering Team, including slip-corrected distances and elevation data, to measure bedform morphometry. We build on previous work with a comparative

analysis and focus on sedimentary processes to better understand the physical differences and practical implications of qualitatively similar bedforms on Mars.

The Hidden Valley study site, visited later in the mission, is located in what was initially defined as the Capping Unit of the Bradbury Group (Stack et al., 2017). The area is associated with well laminated, fine-grained rocks which are interpreted as having formed in a lacustrine environment (Edgar et al., 2020). The bedforms discussed here are part of the modern aeolian deposits overlying the unit (Stack et al., 2017). In August, 2014, (Sols 706-719) Curiosity entered the valley from the north and attempted a drive to the south (Arvidson et al., 2017). The rover encountered high wheel slip and was recalled to take another path.

2.4 Data and Methods

This study was completed using ground-based data from the Curiosity rover and orbital data from the High Resolution Imaging Science Experiment (HiRISE; McEwen et al., 2007) onboard the Mars Reconnaissance Orbiter. All data used in this study is available from the Planetary Data System archive. A list of images used to generate figures can be found in the supplemental materials and is archived online (Bretzfelder and Day, 2021 [Dataset]).

Images acquired by Curiosity were analyzed using the tools within the MSL Analyst's Notebook (Stein, 2014, Stein et al., 2016). Measurements of the dimensions of the bedforms, including heights, widths, slopes and wavelengths, were obtained using spatial information from the Navigation Cameras (Navcams; Maki et al., 2012), Hazard Cameras (Hazcams; Maki et al., 2012) and HiRISE. Surface properties of the bedforms and local wind-formed morphologies were studied using the Mast Camera (Mastcam; Malin et al., 2017). Grains were analyzed using images from

the Mars Hand Lens Imager (MAHLI; Edgett et al., 2012) and Chemistry & Camera (ChemCam) Remote Micro-Imager (RMI; Weins et al., 2012).

High-resolution (~25 cm/px) images from HiRISE were used to study the area surrounding the study sites. A series of images taken over ~6 Earth years were used to analyze the evolution of the tracks left by the rover. HiRISE image brightness and contrast often vary between images of the same area, depending on atmospheric dust, emission angle, and season. In order to optimally compare images of the same area, for each HiRISE image we used MATLAB to shift and stretch the distribution of pixel values in a subsample covering the study area to match a reference image taken after the rover made its tracks. The brightness of all pixels in the sub-region was adjusted linearly until average pixel values were identical to the reference, then the distribution was stretched to match the reference standard deviation in image brightness. This process highlights true surface changes over time rather than variations in atmospheric conditions, lighting, or mechanical differences in the photographic process such as acquisition angle. Digital Elevation Models (DEMs) developed by the HiRISE team from HiRISE stereo images were used to measure the local topography.

2.5 Sedimentology of the Dingo Gap and Hidden Valley Bedforms

2.5.1 Topography and Bedform Morphometry

2.5.1.1 Dingo Gap Bedform

An elevation transect across the study area shows that the Dingo Gap bedform and Moonlight Valley ripples sit atop underlying topography with ~2.5 m of relief (Fig. 2.2b). The terrain rises to a high point at the valley mouth, coincident with the location of the bedform. The Moonlight Valley ripples also sit on a slope, but unlike the Dingo Gap bedform they are not on local high points.

The bedform height was measured by comparing the elevation of the crest and the toe of the eastern and western faces. The western face of the bedform extends further downslope than the eastern face, leading to different bedform heights when calculated from the east or west (Fig. 2.2b, 3). When measured using Navcam and Hazcam stereo images (Fig. 2.3), the bedform has a maximum height of 1.34 meters near its center. The bedform height decreases to the north and south, away from the center along the crest. The elevation of the bedform crest appears constant, and the laterally decreasing height results from the valley topography that rises at the margins.

As measured using the HiRISE DEM, the east and west faces of the bedform are approximately 0.3 m and 0.5 m high at the bedform midpoint, respectively, however, the 1 m/px resolution of the DEM is of order the size of the bedform and, therefore, an imprecise measure. The more precise Navcam stereo image measurements suggest the DEM-based measurement underestimates the bedform height. Arvidson et al. (2015) estimated the Moonlight Valley ripples to be ~0.1-0.15 m high with wavelengths of ~2-3 m. The DEM post-spacing is comparable to the wavelength of the Moonlight Valley ripples and, therefore, does not resolve elevation values for many of the ripples in the valley.

The Dingo Gap bedform is approximately symmetrical along its length (~8 m N-S), which is constrained by the valley walls. The relative sharpness of the crest is visible in Figure 2.3. Five width measurements (E-W, across the crest) of the bedform were taken from HiRISE images. In plan-view, the bedform has a “lemon” morphology: widest in the middle (8.2 m) and tapering to a point at the termini. Arvidson et al. (2015) calculated a width of ~7 m based on engineering data

from Curiosity, and given the angle of the traverse this width is consistent with the measurements from the HiRISE image. Height-to-width aspect ratios were calculated for each measured height (Fig. 2.3). The result was an average ratio of 0.24 ±0.09 (for details see Table 2.S1).

The apparent slope on the eastern face of the bedform was estimated by using the heights (measured from Navcam and Hazcam stereo data) and widths (from HiRISE) along its length. At the edges of the bedform the slope is ~29º ± 1.9º and near the center it is ~17º ± 1.4 º. The apparent difference in slope along the length of the bedform is likely due to the use of HiRISE for width measurements. At the base of the bedform there is an area of light-toned material which extends beyond the break in slope which would typically define the edge of the bedform (Fig. 2.2a). It is not possible to distinguish between the base of the bedform and this material in the HiRISE images, which may lead to an overestimate of the width at the center of the bedform, and thus an underestimate of the slope.

2.5.1.2 Hidden Valley Ripples

The primary Hidden Valley bedforms are straight, sharp crested large ripples which show evidence of interactions such as bifurcations (e.g., Ewing and Kocurek, 2010). Stereo data from is limited in the area, but two ripples were successfully measured and have heights of 0.35 and 0.43 m. The bedforms measured were adjacent to the rover's path, as they were the most visible with Navcam. Using engineering data, Arvidson et al. (2017) measured the portions of the ripples traversed by the rover as ~0.15-0.20 m high. HiRISE images show that the ripples have wavelengths of ~3-4 m. The valley opening in the area of the attempted traverse (Fig. 2.1e) slopes downward (see Fig. 2.S1). Ripples fill the majority of the valley interior and no bedrock is exposed between the ripples. The topography of the valley indicates the floor may be filled with up to ~1 m of sediment, of

which the top ~20-40 cm are expressed as the observed ripple field (see supplemental materials for details).

2.5.2 Analysis of Local Wind Patterns

The modern local wind patterns at both sites were interpreted based on surface indications of aeolian sediment transport and deposition. Sand shadows form when sediment is deposited in the lee of obstacles as they obstruct the path of the wind. Similarly, wake patterns form due to the disruption of fluid flow by an obstacle. The orientation of sand shadows and wake patterns indicate the direction of formative wind. Centimeter-scale wind ripples provide additional indications of wind direction. Ripples form normal to the local winds (Sharp, 1963) and ripple asymmetry indicates a singular wind direction. However, ripple asymmetry is not always distinguishable in rover images. Finally, the bedforms in both Dingo Gap and Hidden Valley are considered transverse, oriented normal to the prevailing formative winds.

2.5.2.1 Dingo Gap

The features interpreted on and around Dingo Gap (Figs. 2.4, 2.5) indicate winds from both the east and west which converge in Dingo Gap. Sand shadows on and near both faces of the bedform indicate sediment transport toward the crest of the bedform. The observed wind ripples support the interpreted transport of material to both the east and west. There is also evidence of lateral sediment transport near the base of the bedform in the complex or secondary ripple crests.

In addition to sand shadows and ripples around the bedform, crest-parallel lineations exposed near the brink of the northern part of the eastern face of the bedform (Fig. 2.6) provide potential evidence of recent wind direction. The pattern of lineations, their orientation, and their exposure

on only one side of the bedform suggests the observed pattern represents bedform cross strata, capturing the migration of the lee face of the bedform. In this case, the most recent period of migration was toward the west, caused by easterly winds. The interpreted cross strata are only exposed in a small area near the crest, therefore, the dominant transport direction for only the most recent era of migration can be determined. No bounding surfaces were observed within the exposed strata that could indicate the reversal of the bedform migration direction or combination of multiple bedforms.

2.5.2.2 Hidden Valley

The large meter-scale ripples are oriented at 320.1º ± 5.5 º. The ripples exhibit asymmetry across northeast- and southwest-facing slopes, with longer, more shallowly dipping southwestern faces and shorter, more steeply dipping northeastern faces. The asymmetry suggests these be interpreted as stoss and lee slopes of the wind formed ripples (Fig. 2.7b). Thus, the primary wind direction is interpreted as towards the northeast, out of the valley. The large ripples are the strongest indicator of wind direction, however, wake patterns and impact ripples are also present. The wake features present as sediment accumulated in a v-shape originating at two rocks and opening towards the southwest (Fig. 2.7a). These indicate a secondary wind direction, towards the southwest, opposite to the direction suggested by the large ripples. The impact ripples superimposed on the large ripples are oriented approximately north-south, ~30º oblique to the large ripple crests (Fig. 2.7b). Any asymmetry in the impact ripples is not discernible and the ripples could, therefore, have been formed by winds from the west or east. In the first case, the ripples could have formed from northeasterly winds that encountered the large ripple crests obliquely and were deflected to the north. In the second case, winds from the west may have formed the impact ripples as they were deflected by the existing large ripples.

2.5.3 Surface Properties

2.5.3.1 Dingo Gap

The bedform surface is covered with ~1-2 mm diameter, well-rounded grains (Weitz et al., 2018; Sullivan et al., 2014; Figs. 2.8b, 2.8e-f). At the scale of the ChemCam RMI and Mastcam images, the large (coarse to very coarse sand) grains are evenly distributed on the bedform surface, but exhibit closer packing at the base of the bedform (Fig. 2.8e) than the top of the bedform (Fig. 2.8f). There is an elevation difference of 0.33 m between the locations of Figures 2.8e and 2.8f (positions shown in Fig. 2.2). The apparent difference in grain packing is interpreted as being related to the elevation difference. The difference in lateral positioning may also contribute to the difference in packing.

In most images, individual grains cannot be resolved, but based on some Mastcam images it appears that lighter toned material at the bedform margins is associated with relatively finer grains while darker material (i.e., the bedform surface) is dominated by coarse grains (i.e., Figs. 2.8a, 2.8c). Fine grained (light toned) ripples were observed overlying a surface of coarser grains (darker toned) at the base of the Dingo Gap bedform (Fig. 2.8a) and at its margin to the northeast (Fig. 2.4i). There is an overall change in tone of the sediment at the base of the feature (Fig. 2.2a). This change appears to be associated with grain size, with the larger grains comprising the darker material on the bedform face and finer grained materials seen as lighter beyond the bedform toe (Figs. 2.8c, 2.2a, 2.2e). The dominant grain size changes at a break in slope at the toe of the bedform (Fig. 2.2d) and to the east of the bedform larger grains can be seen protruding through the cover of finer grains (Figs. 2.8c, 2.2e). Light toned sand shadows to the east of the bedform

formed in the wake of the boulders near the base of the bedform, and are interpreted to be composed of finer sands (Fig. 2.8c).

Weitz et al. (2018) measured a median grain size of 1.595 mm for the larger grains (Fig. 2.8e). These grains appear 'fuzzy' as they are coated in dust. The smallest grains resolved in the MAHLI images (200-300 μm; Fig. 2.8e) may represent individual grains but alternatively may be dust aggregates (Sullivan et al., 2014, Weitz et al., 2018). The placement of the Alpha Particle X-Ray Spectrometer (APXS) on the bedform surface disturbed the dust layer on some of the grains, revealing the dark color of the coarse grains. The disruption also exposed one grain which is lighter than the others, which is unusual as most sediment studied in the region is dark with basaltic mineralogies (Weitz et al. 2018; Fig. 2.8e).

The rover wheel scuffed the bedform, exposing dust and dust aggregates beneath the surface armor of coarse grains. The wheel track exposed the fine grained interior of the bedform as a matrix of dust with a few millimeter-sized grains (Fig. 2.8d). The cohesion of the compressed sediment within the track, resulting in the clear definition of the disruptions caused by the wheel treads is interpreted as being a result of the high dust content of the interior of the bedform. The walls of the track are stable and steeper than the angle of repose (>33°), another indication that the material is cohesive (Sullivan et al., 2014).

2.5.3.2 Hidden Valley

Coarse grains are observed on the exterior of the Hidden Valley ripples while the interiors are composed of relatively finer sands and dust, similar to the Dingo Gap bedform (Fig. 2.9 b-d). As

measured using a ChemCam RMI image of Target Mule Springs (Fig. 2.9b), the coarse grains are approximately 1 mm in diameter on average (coarse sand grains, smaller than the average for the coarse surface grains at Dingo Gap). The grains are dust coated and slightly more angular than was seen at Dingo Gap. A wheel track across the ripple somewhat maintained the wheel shape (Fig. 2.9a-b), but portions of the walls of the track failed and created slopes, suggesting less cohesion to the sediment than was observed at Dingo Gap. Sand-sized grains are resolvable in the track wall and slumped sediment. In the center of the track, the sediment partially retained the shape of the wheel tread, indicating that some cohesion is occurring in the sediment. Along the tread impressions the sediment forms clods that demonstrate some cohesion but not enough to clearly preserve the wheel shape. Based on the overall appearance of the wheel tracks, the Hidden Valley ripples are interpreted to have a lower dust content than the Dingo Gap bedform.

2.5.4 Evolution of Rover Tracks

As seen in images from the rover, wheel tracks created by Curiosity across the bedforms disrupted the surface layer of sediment (Fig. 2.8d, 2.9b). We studied the evolution of these wheel tracks over time in order to bound the timescale of resurfacing. Provided enough time and sufficient wind, the disturbed portions of the bedforms should be resurfaced and the tracks should be destroyed. Using six Earth years of HiRISE images we studied changes in the tracks over time.

2.5.4.1 Dingo Gap

Curiosity entered the Dingo Gap area from the southeast in January 2014 (Sol 528) and completed the crossing of the Moonlight Valley ripples by early February 2014 (Sol 540). Arvidson et al.

(2015) estimated the depth of the tracks across the Dingo Gap bedform and Moonlight Valley ripples to be between ~5 and ~7 cm, and ~4 to ~7 cm deep, respectively. This disruption of the surface is resolved in a HiRISE image taken ~70 days after the traverse. We used HiRISE images spanning slightly over three Mars years (approximately five Earth years) after the traverse to search for remnants of the tracks.

In the first image taken after the traverse (April 2014; Fig. 2.10a), the rover tracks can be seen on the Dingo Gap bedform, the Moonlight Valley ripples and on the terrain to the east, west and in between the bedforms. The wheels did not sink as deeply into the terrain in between the bedforms because the layer of sediment over the bedrock in those areas is thin, and in some places is nearly nonexistent. In these areas, the wheels only disturbed the layer of dust coating the bedrock, and the tracks are barely visible by December 2014 (approx. 315 days after the traverse, slightly less than half of a Mars year; Fig. 2.10c). The tracks over the bedrock are completely erased by April 2015 (approx. 430 days; Fig. 2.10d), although the tracks over the bedforms remain clearly distinguishable. Figures 10f and 10g show the tracks over the bedforms fading, but they are clearly visible on the bedforms in December 2016 (985 days after the traverse; Fig. 2.10h).

The MY34/2018 Global Dust Storm (GDS), occurred between the HiRISE observations in Figures 2.10h and 2.10i (Bertrand et al., 2020). The tracks on the bedforms persist beyond this GDS, meaning that the deposition of dust and other sediment on the bedform surface associated with the event was insufficient to cover the tracks, and any sediment transport was insufficient to resurface the tracks. Nearly five Earth years elapsed between Curiosity's traverse through the area and the HiRISE observation in Figure 10h, and as the tracks persist over this timespan the bedforms are,

therefore, inactive in that they neither migrate nor respond to the disequilibrium of the wheel tracks.

2.5.4.2 Hidden Valley

The tracks Curiosity left in the mouth of Hidden Valley are visible from December 2014 (three months after the traverse; Fig. 2.11a) until the most recent image in May 2020 (nearly six Earth years later; Fig. 2.11f). As with the rover tracks at Dingo Gap, the tracks at Hidden Valley survived the GDS. Some fading of the tracks is evident over the duration of the images, but the tracks are still discernible. The pattern of ripple crests has not changed over the duration of imaging. This indicates that these bedforms are inactive on the time scale of these images, and that sediment transport over that time has been insufficient to erase the tracks or obscure them with surficial dust.

2.6 Discussion

Sedimentological differences between the bedforms at Dingo Gap and Hidden Valley provide some basis for understanding how these qualitatively similar bedforms differ in their mechanical properties, and how they might have formed or will evolve. The result that these unconsolidated bedforms, when disturbed, maintained visible tracks for multiple years suggests that sediment transport on modern Mars may be much less active than previously thought.

2.6.1 Past and Present Sediment Transport

At Dingo Gap, sediment deposition patterns indicate that recent convergent winds, forming small ripples and sand shadows, transported sediment toward the bedform crest from the east and west. The sand shadows and ripples represent the most recent local aeolian activity.

As the bedform is inactive on the timescale of HiRISE observations (Fig. 2.10), it remains unclear whether the bedform migrated to its current location or formed in place. If the bedform did not form in place then the exposed cross strata indicate that at least in the most recent period of migration, which may have been prior to the formation of the smaller features, the bedform was migrating to the west (Fig. 2.6). However, if the bedform formed in place, the cross strata may not be indicative of true bedform migration, but rather vertical aggradation and spillover of sediment down the western face. The shadowing effect observed in the megaripples of the Argentinian Puna permits deposition of fine grained sediment in the lee of the bedforms (de Silva et al., 2013). This mechanism may have permitted sediment to accumulate further down the western face of the bedform compared to the eastern, explaining both the cross strata and observed longer runout on the western face. The high dust content of the bedform interior can be explained by dust trapping related to surface charge of the dust and/or kinetic sieving of fines beneath the armoring surface grains (de Silva et al., 2013, Zimbelman and Foroutan, 2020). In either a migrational or vertical growth scenario, given the apparent dominance of sediment transport to the west during the latest period of bedform activity, the rover ascended the equivalent of the stoss slope. Sediment is more tightly packed on the stoss face of a bedform compared to the lee (Atkins and McBride, 1992), meaning that the eastern (stoss) face would have been better suited to enable the ascent versus a lee slope of similar scale. Such an interpretation would imply that bedforms like Dingo Gap, despite being symmetrical across the crest, exhibit stoss and lee grain differentiation mechanics similar to dunes.

At Hidden Valley, the large ripples (~20 cm high; Fig. 2.7), appear to have formed under southwesterly winds. However, the wake patterns indicate northeasterly winds. The impact ripples superimposed on the large ripples could either be the result of westerly winds (~30° oblique to the winds which formed the large ripples) or northeasterly winds, deflected to the north by the crests of the large ripples. The interpreted opposing wind directions suggest a convergent or reversing wind, but the feature superposition suggests that the wind regimes were not active at the same time, meaning that the large ripples formed first and then at some later time the wake features developed. In either case, large ripple formation by southwesterly winds implies that the northeast facing slopes of the bedforms, those first contacted by the rover, represent lee faces of the bedforms. We speculate that traversability issues may be related to poor grain consolidation on lee faces of the ripples. Sediment is deposited on the lee face of bedforms via grain fall and grain flow (Sutton et al., 2013), and sediment deposited via these mechanisms is more loosely packed than materials in on the stoss (Atkins and McBride, 1992), which may explain the high wheel slip.

2.6.2 Modern Inactivity Implied by Track Persistence

Although there is evidence of bimodal modern wind activity at both sites, the longevity of the wheel tracks indicates that sediment transport is presently inactive at both study areas, at least on the ~3 Mars year (~6 Earth year) timescale of observation. This inactivity is in contrast to the ~0.5 m/Earth yr migration rates measured from orbit for (surface) dust-free dunes and meter-scale ripples in the Bagnold Dune Field (Silvestro et al., 2013), and activity of dust-free impact ripples captured by Curiosity (Bridges & Ehlmann, 2018). Elsewhere on Mars, tracks from the Spirit and Opportunity rovers were typically erased within one Martian year, persisting an additional Martian year in areas sheltered from the wind (Geissler et al., 2010). In areas where large grains were

pressed into cohesive substrates, the tracks persisted beyond a Martian year (Geissler et al., 2010). The dust coated grains at both study areas in this work validate the common interpretation that bright-toned bedforms observed in satellite images are dust-covered, and further emphasizes the association between dust and inactivity.

It is commonly interpreted that aeolian transport has dominated surface processes on Mars since the cessation of liquid water on the surface. Unconsolidated, aeolian sands develop bedforms that migrate in a wide range of Martian settings. Although some high albedo bedforms are interpreted as covered in, or composed of dust and immobile (e.g., Geissler et al., 2010), the activity observed in low albedo bedforms (e.g., in the Bagnold Dune Field) supports the assumption that sand and dust in medium-toned bedforms is actively transported on multi-year timescales, even if that activity is not significant enough to cause observable bedform migration. However, our observations defy this assumption and demonstrate that, not only are these bedforms not migrating, but there is so little sediment transport on the bedforms that the areas disturbed by the rover have not been resurfaced or re-equilibrated to the rest of the bedform in >5 Earth years. Further, the tracks are still visible as dark trails, meaning that they have also not been covered by an optically thick layer of surface dust. Considering that the observed time frame includes a major global dust storm, we suggest that it would take decades or longer, and perhaps many global dust storms, to accumulate a non-trivial layer of surface dust.

Morphologically, there are many similarities between the large Martian ripples in the Bagnold Dune Field and the Hidden Valley bedforms, and between some dunes and the Dingo Gap bedform. The most notable differences are the amount of surface and interior dust, and the presence

of coarse-sized grains. Based on the results of this work, this small difference in grain size distribution may be responsible for the difference between activity and inactivity on otherwise similar bedforms, suggesting that the role of dust and coarse grains in inhibiting transport may currently be under appreciated.

2.6.3 Sand Depth and Impacts on Traversability

Although the Dingo Gap bedform is >1 m in height, it may not actually represent 1 m of sand. Based on the topographic profile, the bedform sits on a rise at the valley mouth (Fig. 2.2). It is possible that some, perhaps a significant portion, of the apparent bedform height is a result of the underlying topography and that the Dingo Gap bedform drapes over this high point. In this case, the depth-to-bedrock of the sediment may be significantly less than the measured bedform height. At Hidden Valley, the underlying topography of the valley is difficult to determine (Fig. 2.S1). Unlike Moonlight Valley, where bedrock is exposed between bedforms, the inter-bedform space in the Hidden Valley ripples provides no indication of the sand depth. Given the valley geometry, we estimate that there may be ~1 m of sand filling the valley floor; meaning that although the Hidden Valley ripples appear to be ~1/6 the height of Dingo Gap, the accumulated sand may extend some depth beyond the ripples troughs, possibly beyond the apparent height of the Dingo Gap bedform (see Fig. 2.S1). Increased traction between the wheels and underlying bedrock may explain why the rover was able to successfully navigate the Moonlight Valley and Dingo Gap bedforms, which are comparable in scale to those at Hidden Valley. Looking forward, sediment in inter-bedform troughs could be partially excavated to expose underlying strata, providing information about previous activity and migration that may not be otherwise observable.

2.6.4 Looking Ahead

The inactivity of the modern aeolian bedforms studied in this work juxtaposed with active bedforms just a few kilometers away, highlights that much is still unknown about Martian aeolian sediment transport. Orbital images provide an important baseline, but detailed, grain-scale measurements will be needed to understand more about the processes driving bedform formation and evolution. The Mars 2020 Perseverance rover landed in Jezero crater on 18 February, 2021 (Fig. 2.12a). There are many aeolian bedforms in the region with similar morphologies to the Dingo Gap bedform and the Hidden Valley ripples (Chojnacki et al., 2018, Day and Dorn, 2019; Fig. 2.12), and these provide a key opportunity to better understand sediment transport and bedform formation on Mars as a whole. Investigation of these bedforms is balanced by mobility risks to the rover, however, the insights gained by Curiosity and observations described here provide some guidance for safe robotic exploration. Given the diversity of Martian bedforms and the limited number studied in-situ thus far, additional observations have the potential to enhance our understanding of aeolian features significantly by quantifying the relationship between activity and grain properties.

2.7 Conclusions

The limited number of Martian meter-scale aeolian bedforms investigated by rovers, and their limited analogs on Earth, has led to significant uncertainty in our understanding of these bedforms and their terramechanical properties. Though apparently similar at the scale of HIRISE images, in-situ observations of the interior and exterior of these bedforms suggest that small differences in bedform geometry, grain size distribution, dust content, and sand depth, can have significant effects on the how bedforms behave and evolve.

Although the bedforms at Hidden Valley and Dingo Gap are similar in that they consist of fine grained interiors armored by coarse to very coarse sand, differences in their interior dust content appear to have a significant effect on their terramechanical properties. The rover wheel tracks and bedform surfaces at Hidden Valley and Dingo Gap showed clear differences in the level of sediment cohesion. The Dingo Gap bedform sediment, with higher dust content than the Hidden Valley bedforms, retained the wheel shape, showing cohesive strength along track walls (Fig. 2.8d) that was not present in the Hidden Valley tracks (Fig. 2.9b). The tracks through Dingo Gap maintained walls steeper than the angle of repose (Fig. 2.8d), showing more cohesion than the track walls at Hidden Valley, which had failed into slopes closer to the angle of repose (Fig. 2.9b). The comparison suggests that dust content in bedforms enhances the stability of the sediment when disturbed. The interpretation that dust stabilizes sediment is further supported by the longevity of the tracks. Over 6 Earth years, sediment transport in the study areas was insufficient to resurface the wheel tracks. Even with the occurrence of a global dust storm, the tracks remain visible across the bedforms. Slightly more fading of the tracks in Hidden Valley with respect to Dingo Gap is consistent with the slightly lower dust content in the Hidden Valley bedforms. Our results show that in dust-covered regions of Gale crater, sediment transport is inhibited by surface dust, and optically thick dust deposition does not occur on the timescales observed.

Bedforms in Dingo Gap and Hidden Valley demonstrate that grain-scale observations of bedforms are necessary to further our understanding of aeolian bedform formation on Mars. Although bedforms pose some risk to rover mobility (as demonstrated by Spirit, Opportunity, and Curiosity rovers), in-situ observations are needed to close current gaps in our understanding of one of the most common features on the Martian surface. Lessons learned from Curiosity suggest several strategies for leveraging observable characteristics of bedforms to decrease the risk of traversing

bedforms, including consideration of the sand depth and approaches from the stoss side. In-situ observation of aeolian bedforms, including those along the Perseverance traverse, are a necessary next step in Mars surface exploration.

2.8 Figures

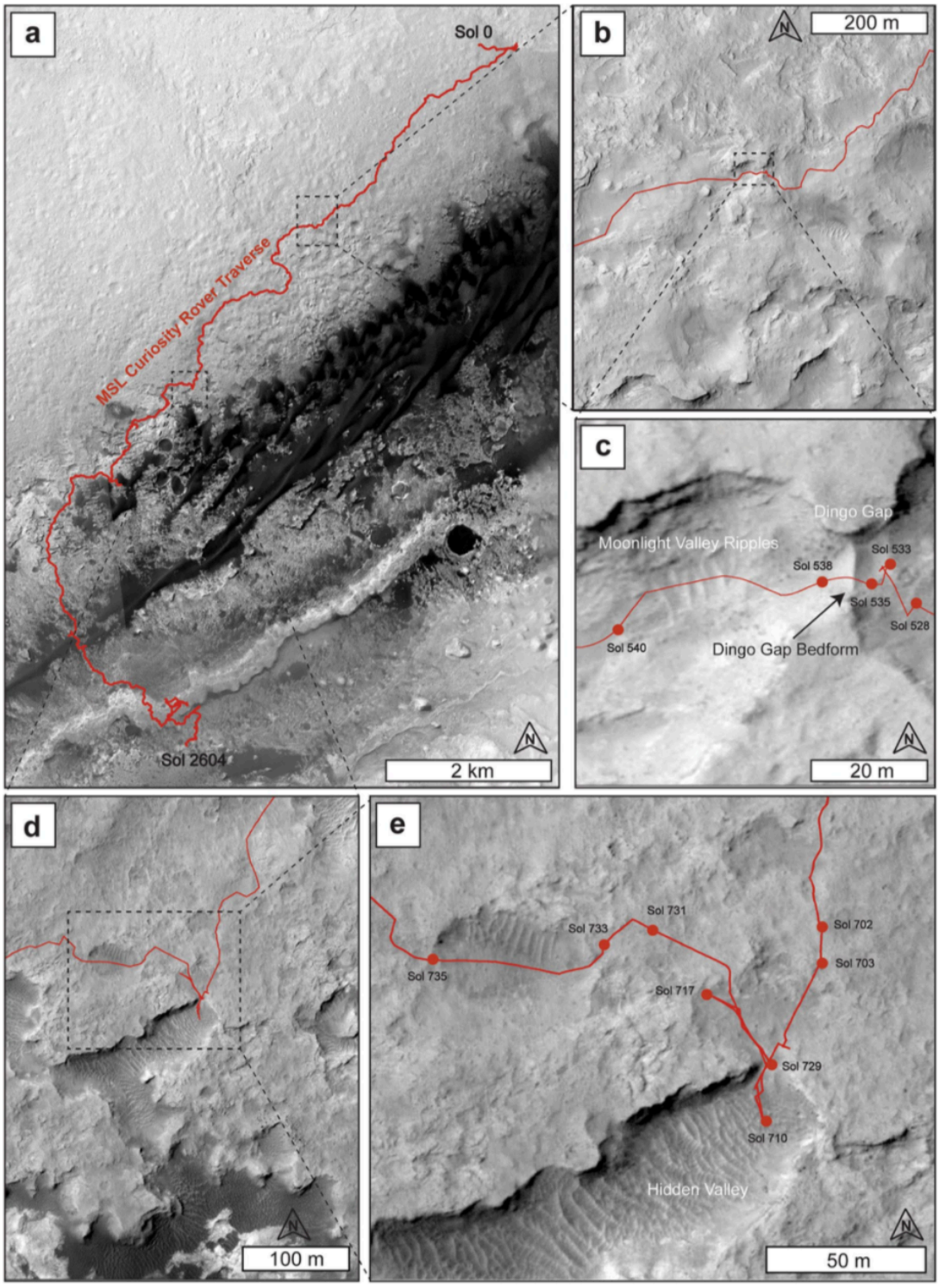

Figure 2.1 MSL Curiosity traverse through Dingo Gap and Hidden Valley. (A) Rover traverse through mission sol 2604. (B) View of the Rugged Unit, a part of the Bradbury Group (Rice et al., 2013, Calef et al., 2013, Grotzinger et al., 2014). (C) Dingo Gap and Moonlight Valley study site.

(D) View of the Capping Unit of the Bradbury Group (Stack et al., 2017). (E) Hidden Valley study site showing large (~20-30 cm high) ripples. For all figures, north is up in satellite images.

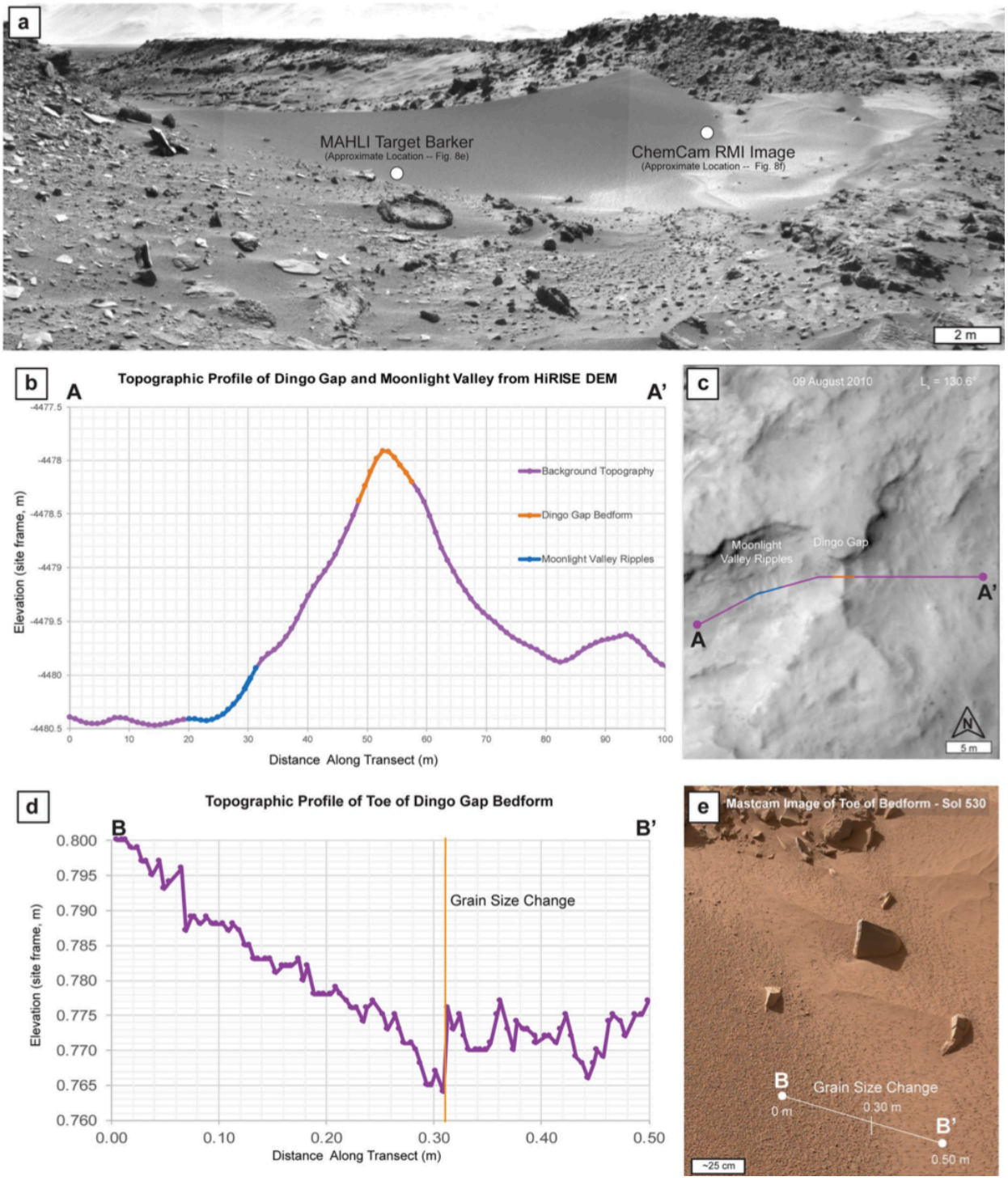

Figure 2.2 Topographic profiles of Dingo Gap and Moonlight Valley.
(a) Navcam mosaic of the eastern face of the bedform taken from the south as Curiosity approached Dingo Gap (Sol 527). The approximate locations of MAHLI Target "Barker" and a ChemCam RMI image are shown, indicating locations of images used to study grains. (b) Topographic profile

generated from a 100 m transect from a HiRISE DEM. The transect crosses the ripples in Moonlight Valley (blue) and the bedform in Dingo Gap (orange). The background topography of the valley is shown in purple. (c) Transect A-A' overlain on HiRISE image ESP_018920_1755. (d) Topographic profile across the eastern toe of the Dingo Gap bedform showing the relationship between slope and grain size. Profile generated from Navcam stereo data. (e) Image showing the observed "Grain Size Change" which corresponds to the boundary between where individual grains can (east, left) and cannot (right, west) be resolved.

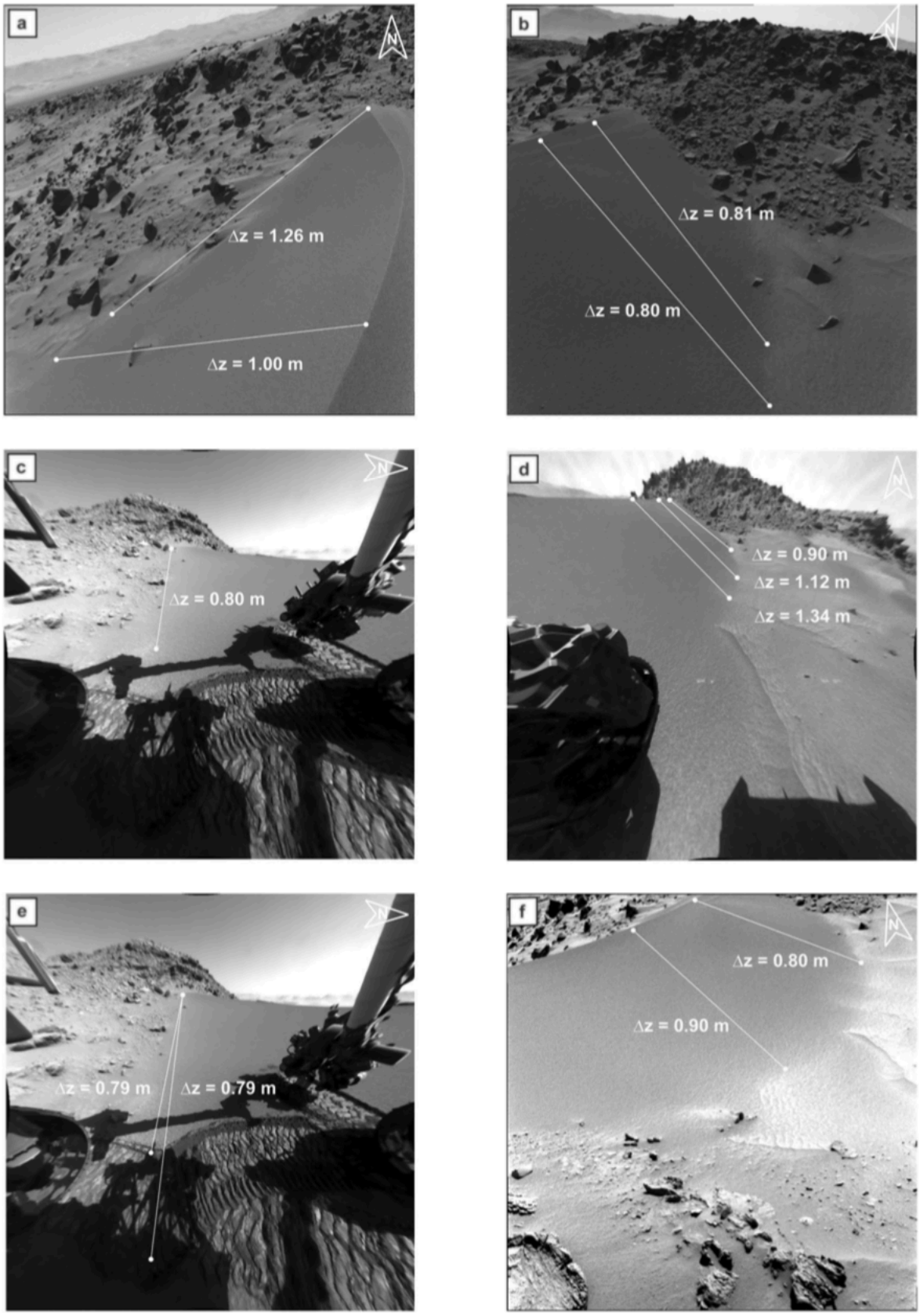
a
Δz = 1.26 m
Δz = 1.00 m
b
Δz = 0.81 m
Δz = 0.80 m
c
Δz = 0.80 m
d
Δz = 0.90 m
Δz = 1.12 m
Δz = 1.34 m
e
Δz = 0.79 m
Δz = 0.79 m
f
Δz = 0.80 m
Δz = 0.90 m

Figure 2.3 Height measurements from Navcam and Hazcam images. Images a-f show transects from which the height of the bedform was measured by differencing the elevation coordinate of the endpoints using spatial information from stereo imaging. (a) Western face of the bedform. (b-f) Eastern face.

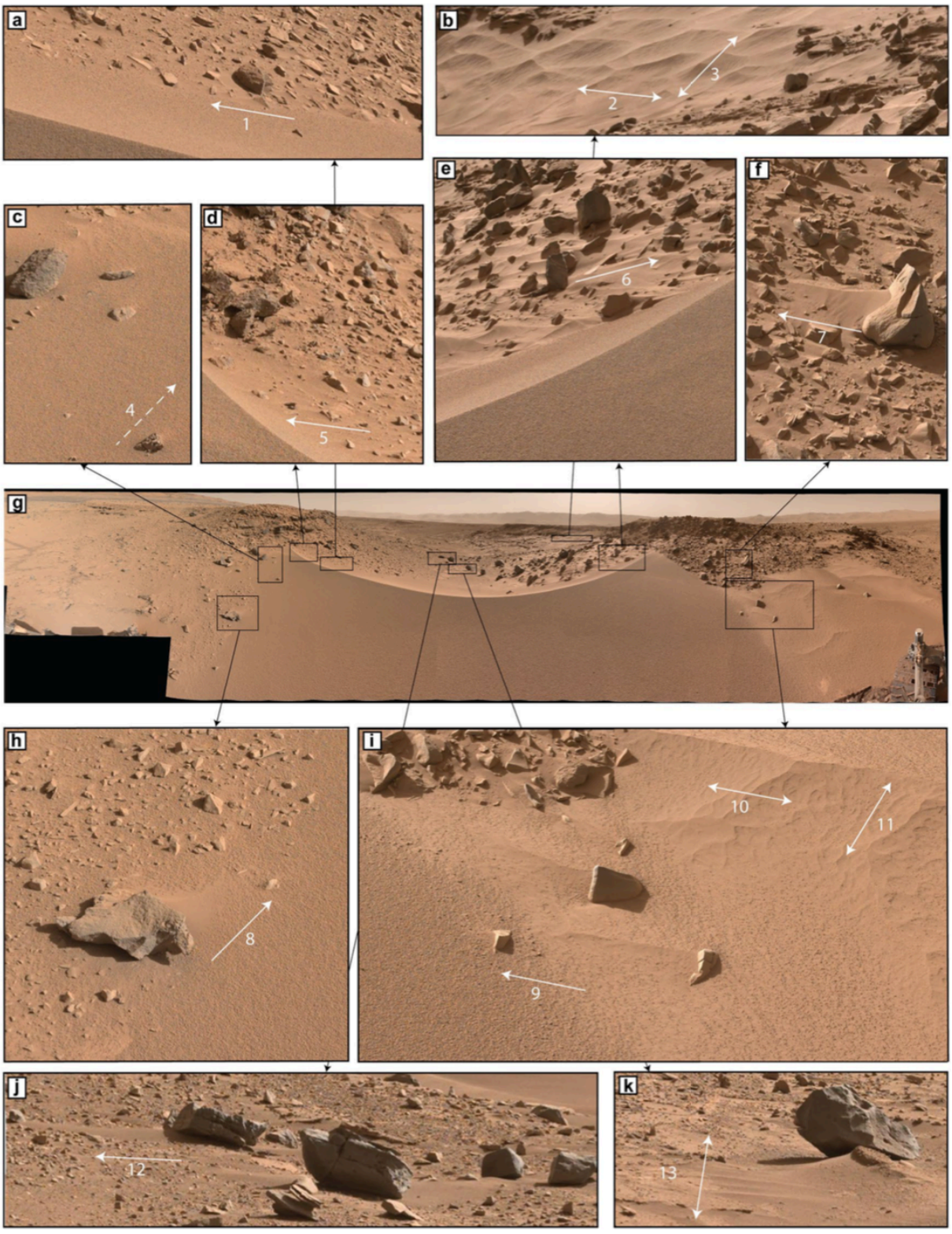

Figure 2.4 Dingo Gap with annotated wind directions.
Surface features that record a formative wind direction were interpreted to understand the recent wind regime. Wind ripples (b, i, k) and sand shadows (a, c-f, h-j) all reflect aeolian transport.

Arrows show the interpreted wind directions based on these features. Double-tipped arrows reflect ambiguity in interpretation. Numbers correspond to the arrows in Figure 2.5.

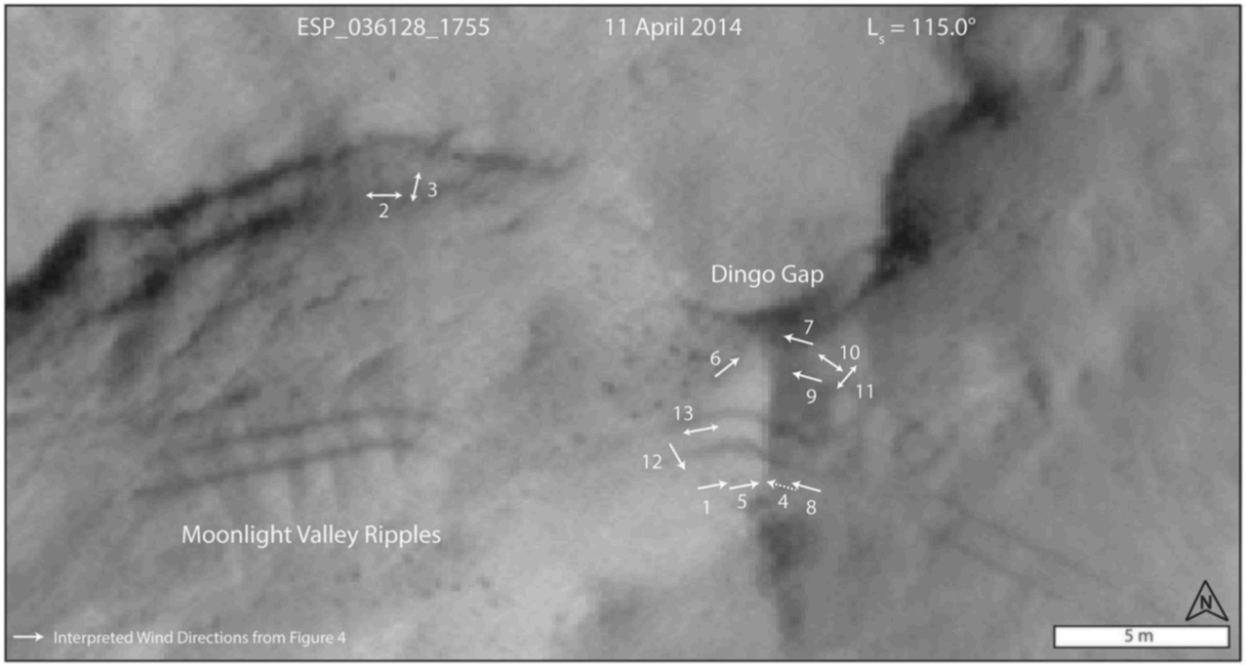

Figure 2.5 Interpreted wind directions around Dingo Gap.
Interpreted wind directions shown in plan-view overlain on a HiRISE image. Numbered arrows correspond to those in Figure 2.4. All arrows are the same length, and this length does not correspond to magnitude or wind velocity. Double-tipped arrows reflect ambiguity in interpretation.

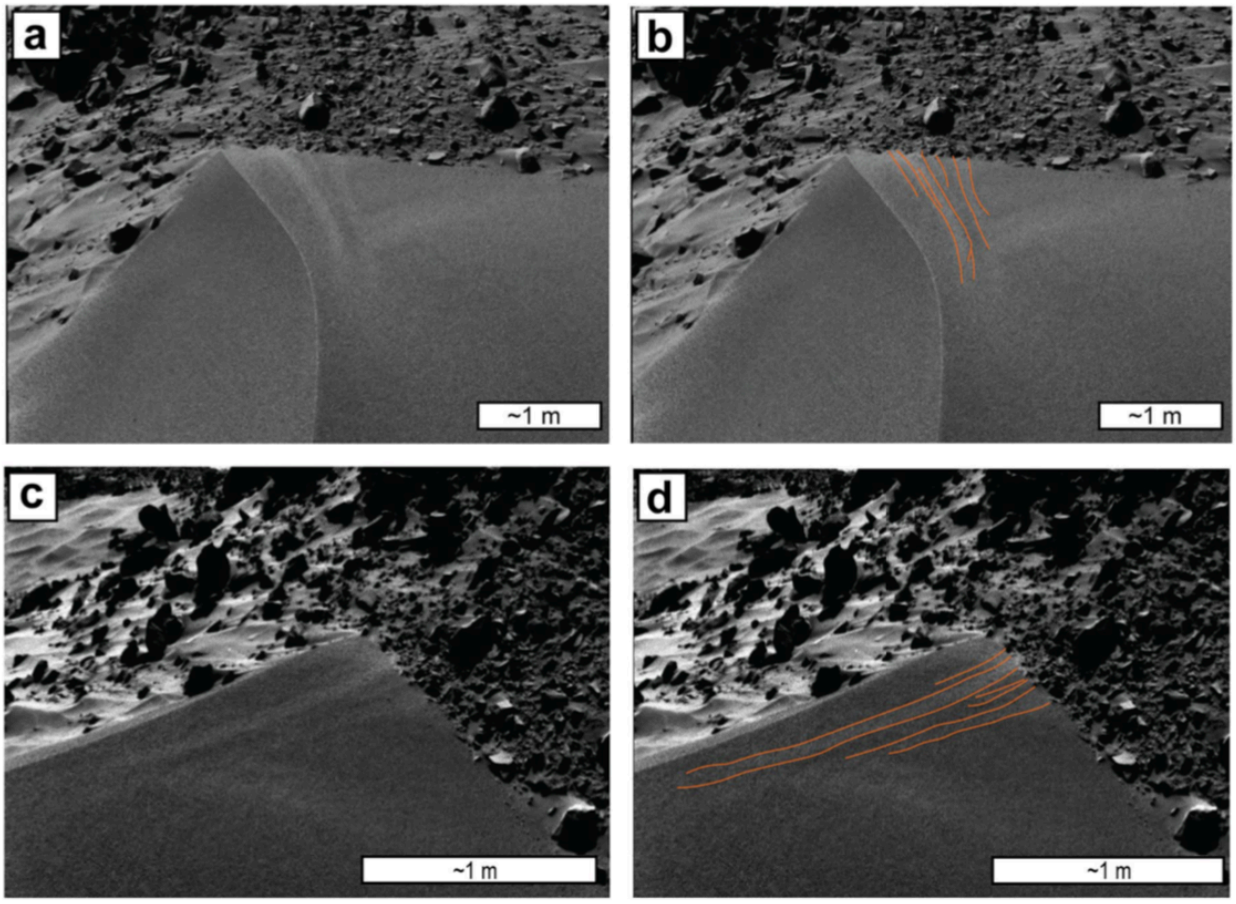

Figure 2.6 Cross strata exposed on eastern face of the Dingo Gap bedform. (a) Exposed cross strata visible on the eastern (right) face. (b) Panel a in enhanced contrast with cross strata outlined in orange. (c) Another view of the eastern face of the bedform. (d) Panel c in enhanced contrast with cross strata outlined in orange.

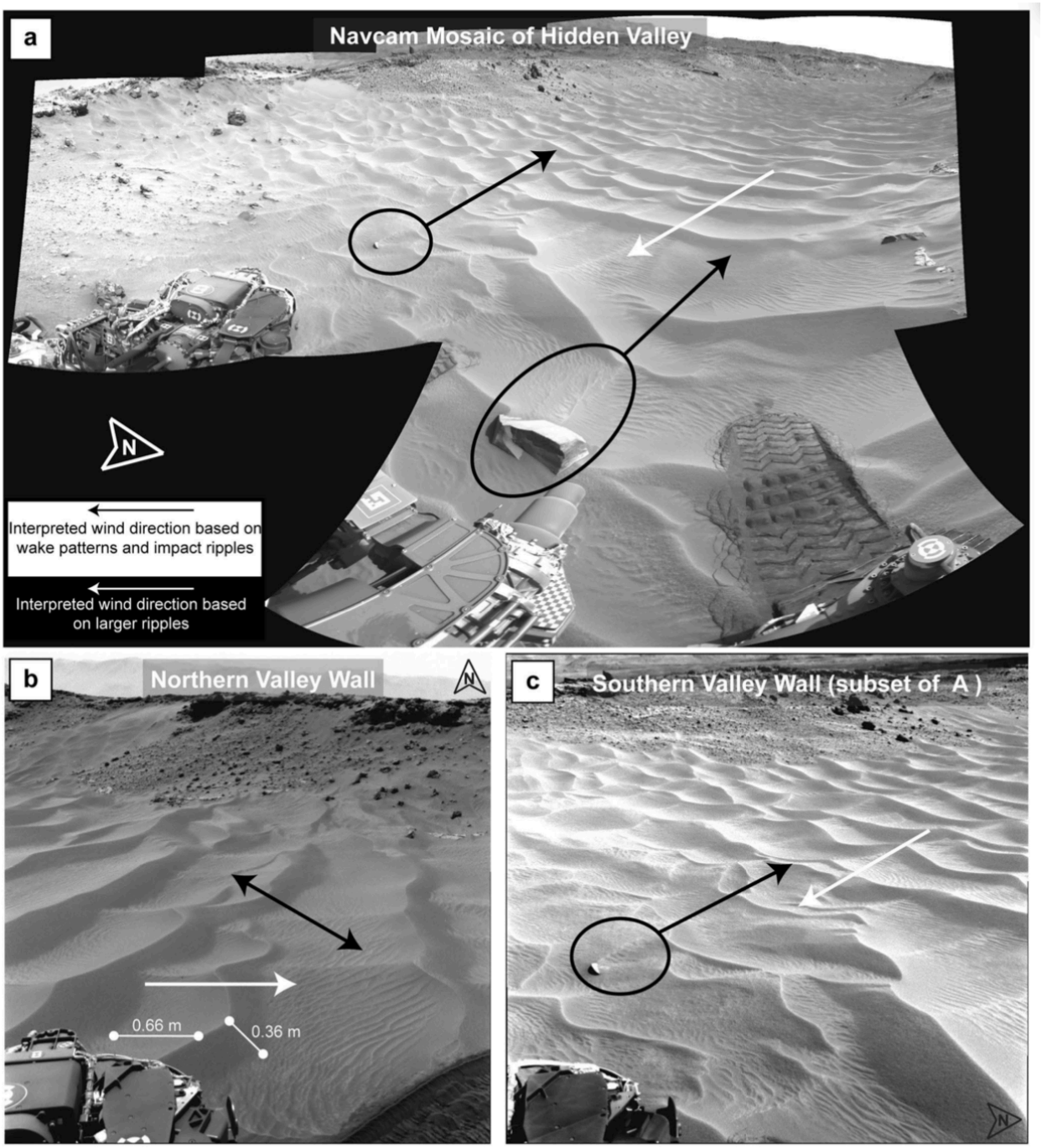

Figure 2.7 Hidden Valley with interpreted wind directions. Wind directions were interpreted based on large ripples (white arrows), wake patterns (single-tipped black arrows), and impact ripples (double-tipped black arrow). Wake features are highlighted in black ellipses. (a) Navcam mosaic from Sol 706 looking down the valley, showing large ripples, impact ripples and wake features. (b) View towards the north. Length measurements of the stoss (southwest) and lee (northeast) of a large ripple shown. (c) Subset of a highlighting opposing wind indicators.

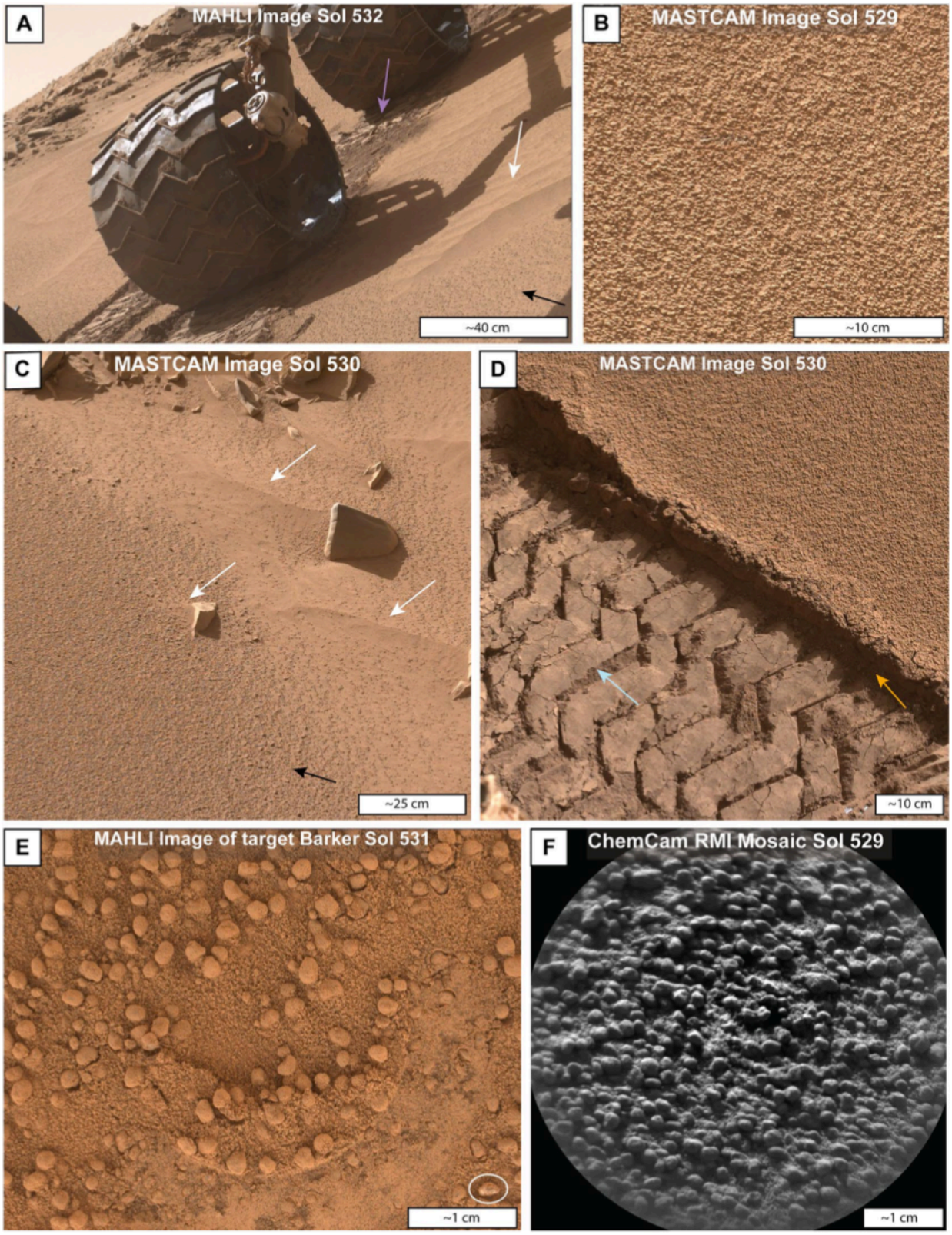

Figure 2.8 Diverse grain sizes of Dingo Gap. (a) The base of Dingo Gap is covered with resolvable coarse grains (black arrows) superimposed by fine grained ripples (white arrows).

Tracks beneath the rover wheel expose darker material where the surface is disturbed (purple arrow). (b) Eastern face of the bedform, with evenly distributed, uniformly sized coarse (1-2 mm) dust-coated grains. (c) Eastern toe of the bedform, with resolvable coarse grains (black arrow) on the bedform and finer material forming ripples and sand shadows (white arrows; see Fig. 2.2b-c). (d) Wheel track across the eastern face of the bedform exposing subsurface grains. Interior of the bedform is composed of finer sands and dust. Cohesive behavior of the interior material shown in the "cracks" in between the wheel treads (blue arrow) and in the steep and stable walls of the track (orange arrow). (e) MAHLI image of well-rounded, "fuzzy" dust-coated grains at Barker, on the eastern face of the bedform. Dust has been removed from the surface of some grains by the placement of the APXS (circular depression). The grain circled in white is significantly lighter in color than the other grains in the image. (f) ChemCam RMI image from the eastern face of the bedform showing denser packing of the coarse grains than at Barker nearby. Location of e and f labelled in Figure 2.2a.

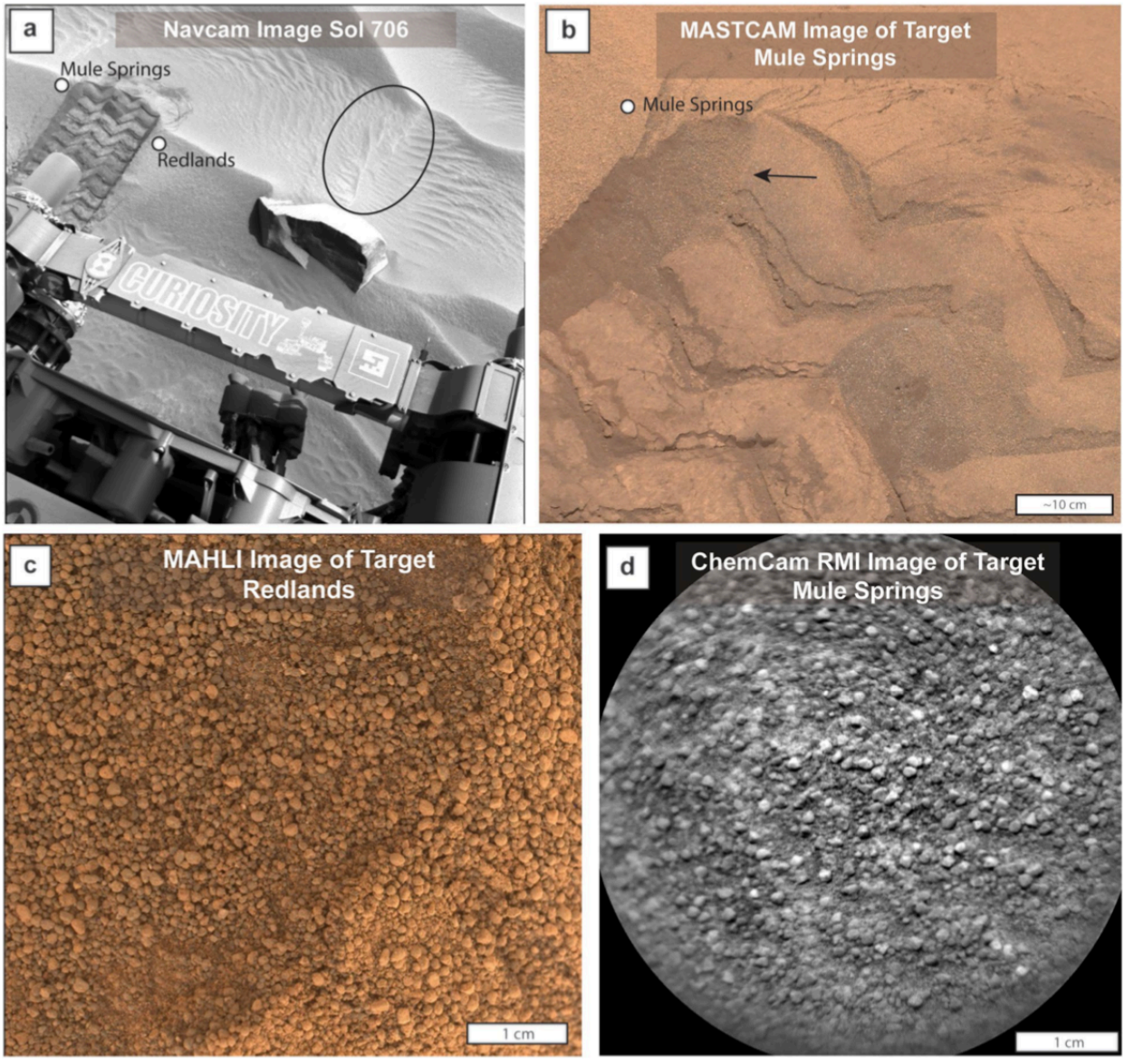

Figure 2.9 Grains and cohesion at Hidden Valley. (a) Locations of panels b-d. View of wake feature shown in Figure 2.7 (black circle). (b) View of the wheel tracks near the crest of a ripple. Finer grained particles are shown underneath the larger surface grains. The failed walls of the track (black arrow) and loose material exposed by the tread marks show less cohesion of the interior materials than the tracks made across the Dingo Gap Bedform. (c) MAHLI image of the surface grains on the crest of a bedform showing evenly distributed dust-coated coarse grains. (d) ChemCam view of the coarse surface grains.

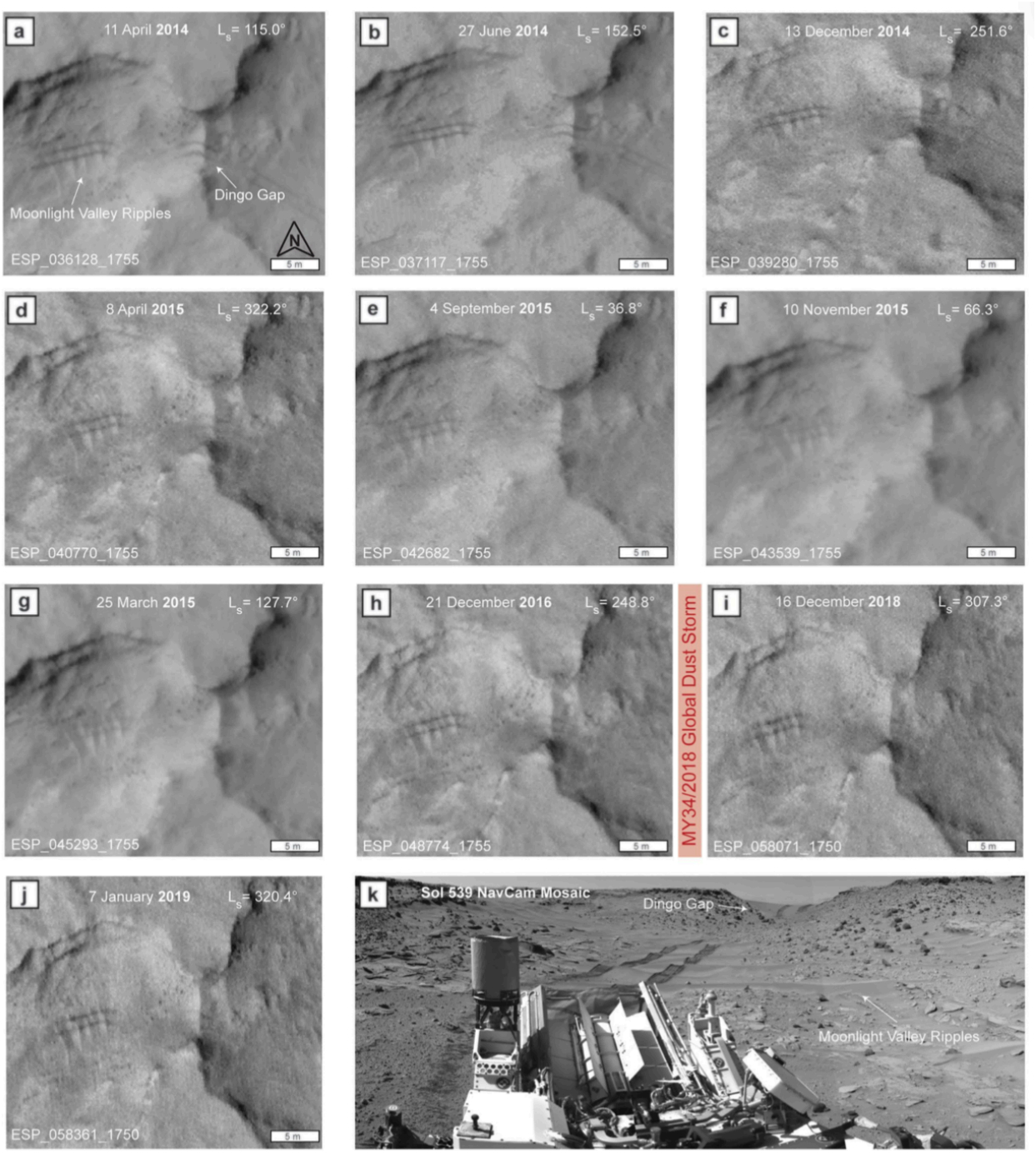

Figure 2.10 Timeline of MSL traverse tracks through Dingo Gap. HiRISE images of wheel tracks beginning in April 2014 (a) through January 2019 (j). North is up. The MY34/2018 Global Dust Storm (GDS) occurred between (h) and (i). Tracks are still visible over the bedforms in (j), though they are lost in the areas in between. (k) Mosaic showing fresh tracks as the rover departed the study area.

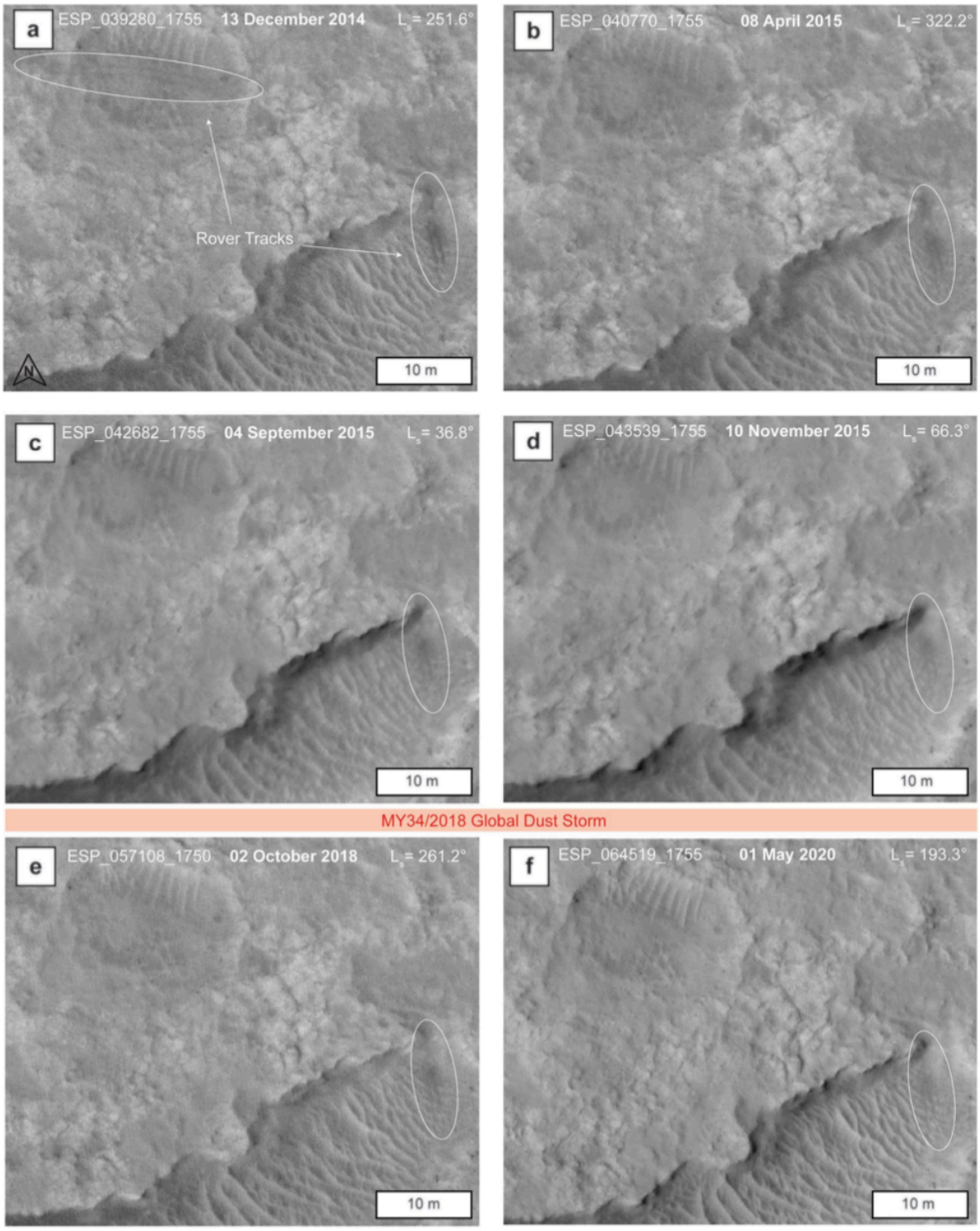

Figure 2.11 MSL tracks at Hidden Valley through time. HiRISE images of wheel tracks through hidden valley beginning in December 2014 (a) through May 2020 (f). North is up. The

MY34/2018 GDS occurred between images (d) and (e). Tracks are still visible across the bedforms in Hidden Valley in (f).

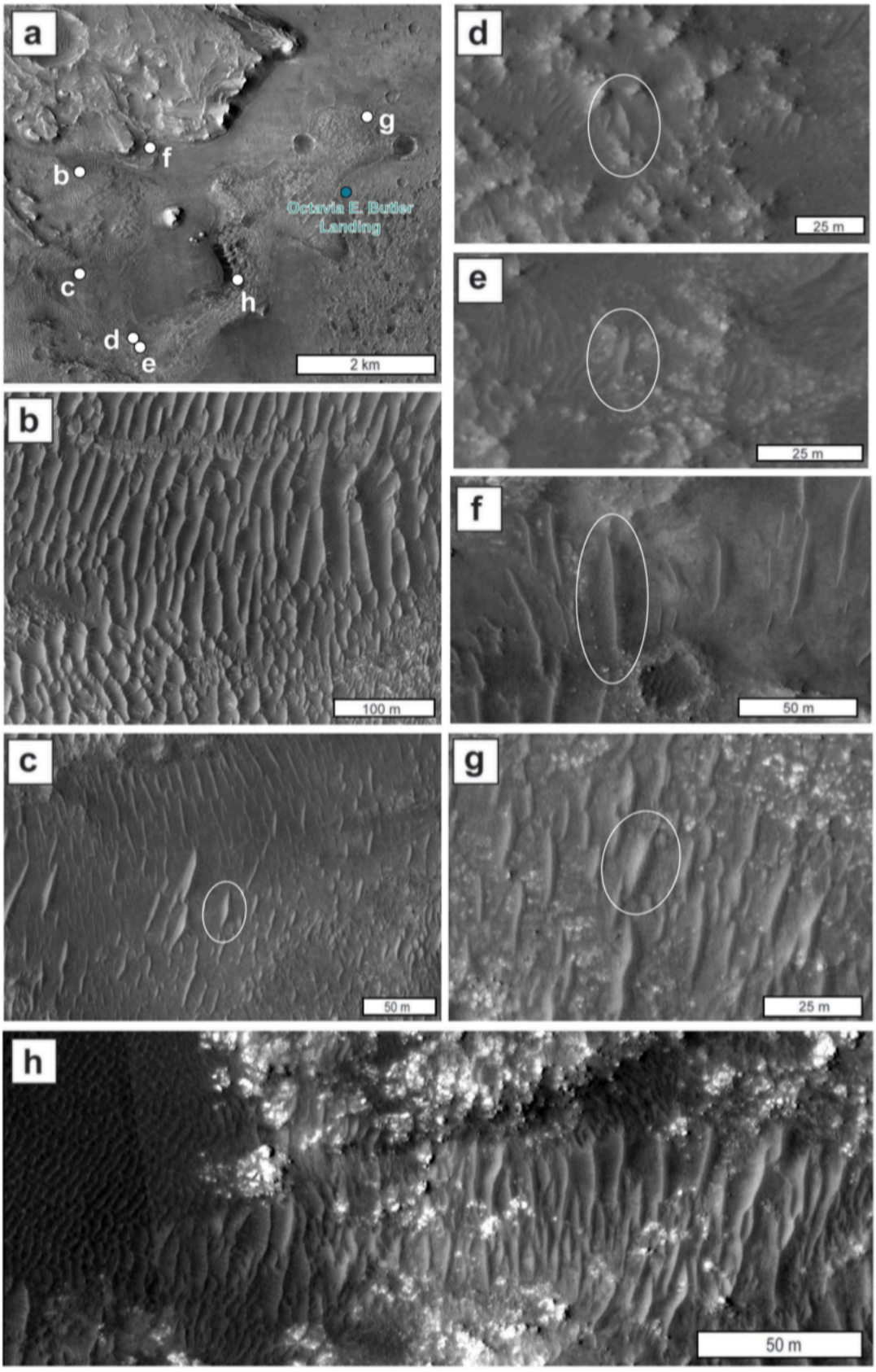
a
g
f
b
Octavia E. Butler
Landing
c
h
d
e
2 km
d
25 m
e
25 m
b
100 m
f
50 m
c
50 m
g
25 m
h
50 m

Figure 2.12 Bedforms in Jezero Crater. North is up in all panels. (a) Jezero crater delta with the Octavia E. Butler landing site of the Perseverance Rover. (b) A field of large, apparently symmetric bedforms with superimposed ripples. The symmetry of the large features is similar to that of Dingo Gap, but the complex interactions and scale are different. (c) A bedform similar in scale to the one at Dingo Gap, with smaller bedforms to the north. (d-g) Bedforms similar to Dingo Gap in both scale and morphology in various topographic settings. (h) Bedforms similar to the Hidden Valley ripples.

2.9 Appendix

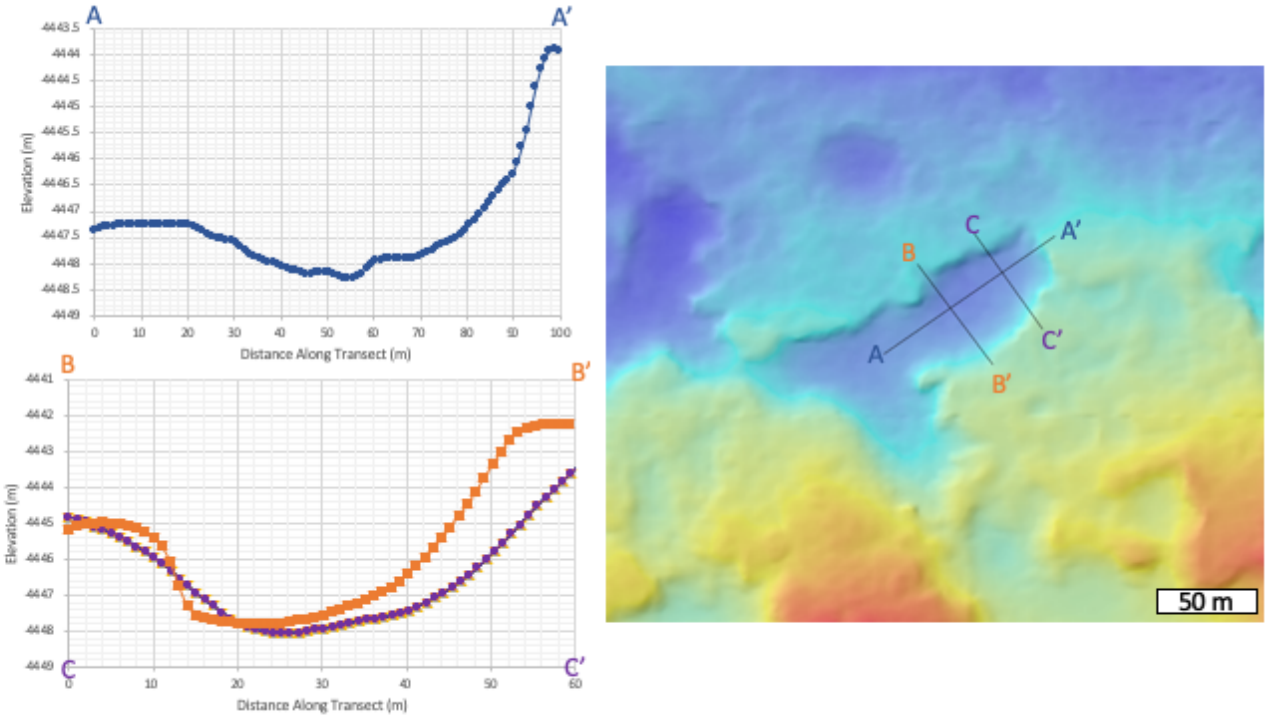

Figure 2.S1. Topographic profiles of Hidden Valley. Transect A-A' shows that upon entering the valley (near A') Curiosity was travelling downslope. Transect B-B' and C-C' show the topography across the width of the valley. Based on these profiles, there appears to potentially be ~1 m of sand filling the base of the valley, shown in the profiles as the 'flattening' in the center of the valley. Extrapolating the curve of the valley walls (B-B' and C-C') to infer the shape of the underlying bedrock, it appears that the bedrock floor may currently lie under ~1 m of sediment. The ripples encountered by the rover represent the top ~20 cm of the total accumulated sediment. HiRISE DEM resolution is 1 m/px and north is up.

2.10 References

Anderson, Robert S. "A theoretical model for aeolian impact ripples." *Sedimentology* 34.5 (1987): 943-956.

Arvidson, R. E., Ashley, J. W., Bell, J. F., Chojnacki, M., Cohen, J., Economou, T. E., Farrand, W. H., Fergason, R., Fleischer, I., Geissler, P., Gellert, R., Golombek, M. P., Grotzinger, J. P., Guinness, E. A., Haberle, R. M., Herkenhoff, K. E., Herman, J. A., Iagnemma, K. D., Jolliff, B. L., Wolff, M. J. (2011). Opportunity Mars Rover mission: Overview and selected results from Purgatory ripple to traverses to Endeavour crater. *Journal of Geophysical Research: Planets*, *116*(E7). https://doi.org/10.1029/2010JE003746

Arvidson, Raymond E., Iagnemma, K. D., Maimone, M., Fraeman, A. A., Zhou, F., Heverly, M. C., Bellutta, P., Rubin, D., Stein, N. T., Grotzinger, J. P., & Vasavada, A. R. (2017). Mars Science Laboratory Curiosity Rover Megaripple Crossings up to Sol 710 in Gale Crater. *Journal of Field Robotics*, *34*(3), 495–518. https://doi.org/10.1002/rob.21647

Atkins, J., & Mcbride, E. (1992). Porosity and packing of Holocene river, dune, and beach sands. *Aapg Bulletin, 75(3),* 339-335.

Bagnold, R.A., 1941. The physics of blown sand and desert dunes. Methuen, New York.

Baker, M. M., Lapotre, M. G., Minitti, M. E., Newman, C. E., Sullivan, R., Weitz, C. M., ... & Lewis, K. W. (2018). The Bagnold Dunes in southern summer: Active sediment transport on Mars observed by the Curiosity rover. *Geophysical Research Letters*, *45*(17), 8853-8863.

Balme, M., Berman, D. C., Bourke, M. C., & Zimbelman, J. R. (2008). Transverse Aeolian Ridges (TARs) on Mars. *Geomorphology*, *101*(4), 703–720. https://doi.org/10.1016/j.geomorph.2008.03.011

Balme, M., Robson, E., Barnes, R., Butcher, F., Fawdon, P., Huber, B., Ortner, T., Paar, G., Traxler, C., Bridges, J., Gupta, S., & Vago, J. L. (2018). Surface-based 3D measurements of small aeolian bedforms on Mars and implications for estimating ExoMars rover traversability hazards. *Planetary and Space Science*, *153*, 39–53. https://doi.org/10.1016/j.pss.2017.12.008

Berman, D. C., Balme, M. R., Rafkin, S. C. R., & Zimbelman, J. R. (2011a). Transverse Aeolian Ridges (TARs) on Mars II: Distributions, orientations, and ages. *Icarus*, *213*(1), 116–130. https://doi.org/10.1016/j.icarus.2011.02.014

Bertrand, T., Wilson, R. J., Kahre, M. A., Urata, R., & Kling, A. (2020). Simulation of the 2018 Global Dust Storm on Mars Using the NASA Ames Mars GCM: A Multitracer Approach. *Journal of Geophysical Research: Planets*, *125*(7), e2019JE006122. https://doi.org/10.1029/2019JE006122

Bourke, M. C., Wilson, S. A., Zimbelman, J. R. (2003). The Variability of Transverse Aeolian Ridges in Troughs on Mars. Paper Presented at the 34th Lunar and Planetary Science Conference, Clear Lake, TX. Abstract #2090.

Bourke, M. C., Balme, M., Beyer, R. A., Williams, K. K., & Zimbelman, J. (2006). A comparison of methods used to estimate the height of sand dunes on Mars. *Geomorphology*, *81*(3), 440–452. https://doi.org/10.1016/j.geomorph.2006.04.023

Bretzfelder, J. M., & Day, M. (2021). *Dingo Gap Bedform Dimensions and Images Used for Comparison to the Hidden Valley Ripples* [Data set]. Zenodo. https://doi.org/10.5281/zenodo.4929238

Bridges, N. T., Spagnuolo, M. G., de Silva, S. L., Zimbelman, J. R., & Neely, E. M. (2015). Formation of gravel-mantled megaripples on Earth and Mars: Insights from the Argentinean

Puna and wind tunnel experiments. *Aeolian Research*, *17*, 49–60. https://doi.org/10.1016/j.aeolia.2015.01.007

Bridges, N. T., Sullivan, R., Newman, C. E., Navarro, S., Van Beek, J., Ewing, R. C., ... & Rapin, W. (2017). Martian aeolian activity at the Bagnold Dunes, Gale Crater: The view from the surface and orbit. *Journal of Geophysical Research: Planets*, *122*(10), 2077-2110.

Bridges, N. T., & Ehlmann, B. L. (2018). The Mars Science Laboratory (MSL) Bagnold Dunes Campaign, Phase I: Overview and introduction to the special issue. *Journal of Geophysical Research: Planets*, *123*(1), 3–19. https://doi.org/10.1002/2017JE005401

Calef III, F. J., Dietrich, W. E., Edgar, L., Farmer, J., Fraeman, A., Grotzinger, J., Palucis, M. C., Parker, T., Rice, M., Rowland, S., Stack, K. M., Summer, D., Williams, J., and the MSL Science Team (2013). Geologic Mapping of the Mars Science Laboratory Landing Ellipse. Paper Presented at the 44th Lunar and Planetary Science Conference, The Woodlands, TX. Abstract #2511. https://www.lpi.usra.edu/meetings/lpsc2013/pdf/2511.pdf

Chojnacki, M., & Fenton, L. K. (2017). The Geologic Exploration of the Bagnold Dune Field at Gale Crater by the Curiosity Rover. *Journal of Geophysical Research: Planets*, *122*(11), 2216–2222. https://doi.org/10.1002/2017JE005455

Chojnacki, M., Banks, M., & Urso, A. (2018). Wind-Driven Erosion and Exposure Potential at Mars 2020 Rover Candidate-Landing Sites. *Journal of Geophysical Research: Planets*, *123*(2), 468–488. https://doi.org/10.1002/2017JE005460

Cutts, J. A., & Smith, R. S. U. (1973). Eolian deposits and dunes on Mars. *Journal of Geophysical Research (1896-1977)*, *78*(20), 4139–4154. https://doi.org/10.1029/JB078i020p04139

Day, M., & Dorn, T. (2019). Wind in Jezero Crater, Mars. *Geophysical Research Letters*, *46*(6), 3099–3107. https://doi.org/10.1029/2019GL082218

de Silva, S. L., Spagnuolo, M. G., Bridges, N. T., & Zimbelman, J. R. (2013). Gravel-mantled megaripples of the Argentinean Puna: A model for their origin and growth with implications for Mars. *GSA Bulletin*, *125*, 1912–1929. http://dx.doi.org/10.1130/B30916.1

Edgar, L., Fedo, C. M., Gupta, S., Banham, S. G., Fraeman, A. A., Grotzinger, J. P., Stack, K. M., Stein, N. T., Bennett, K. A., Rivera-Hernandez, F., Sun, V. Z., Edgett, K. S., Rubin, D. M., House, C., & Van Beek, J. (2020). A Lacustrine Paleoenvironment Recorded at Vera RubinRidge, Gale Crater: Overview of the Sedimentology and Stratigraphy Observed by the Mars ScienceLaboratory Curiosity Rover. *Journal of Geophysical Research: Planets.* doi:10.1029/2019JE006307

Edgett, K. S., Yingst, R. A., Ravine, M. A., Caplinger, M. A., Maki, J. N., Ghaemi, F. T., Schaffner, J. A., Bell, J. F., Edwards, L. J., Herkenhoff, K. E., Heydari, E., Kah, L. C., Lemmon, M. T., Minitti, M. E., Olson, T. S., Parker, T. J., Rowland, S. K., Schieber, J., Sullivan, R. J., … Goetz, W. (2012). Curiosity's Mars Hand Lens Imager (MAHLI) Investigation. *Space Science Reviews*, *170*(1), 259–317. https://doi.org/10.1007/s11214-012-9910-4

Ewing, R. C., & Kocurek, G. A. (2010). Aeolian dune interactions and dune-field pattern formation: White Sands Dune Field, New Mexico. *Sedimentology*, *57*(5), 1199–1219. https://doi.org/10.1111/j.1365-3091.2009.01143.x

Geissler, P. E., Sullivan, R., Golombek, M., Johnson, J. R., Herkenhoff, K., Bridges, N., Vaughan, A., Maki, J., Parker, T., & Bell, J. (2010). Gone with the wind: Eolian erasure of the

Mars Rover tracks. *Journal of Geophysical Research: Planets*, *115*(E7). https://doi.org/10.1029/2010JE003674

Geissler, P. E., & Wilgus, J. T. (2017). The morphology of transverse aeolian ridges on Mars. *Aeolian Research*, *26*, 63–71. https://doi.org/10.1016/j.aeolia.2016.08.008

Greeley, R., Kraft, M., Sullivan, R., Wilson, G., Bridges, N., Herkenhoff, K., Kuzmin, R. O., Malin, M., & Ward, W. (1999). Aeolian features and processes at the Mars Pathfinder landing site. *Journal of Geophysical Research: Planets*, *104*(E4), 8573–8584. https://doi.org/10.1029/98JE02553

Grotzinger, J. P., Crisp, J., Vasavada, A. R., Anderson, R. C., Baker, C. J., Barry, R., Blake, D. F., Conrad, P., Edgett, K. S., Ferdowski, B., Gellert, R., Gilbert, J. B., Golombek, M., Gómez-Elvira, J., Hassler, D. M., Jandura, L., Litvak, M., Mahaffy, P., Maki, J., … Wiens, R. C. (2012). Mars Science Laboratory Mission and Science Investigation. *Space Science Reviews*, *170*(1), 5–56. https://doi.org/10.1007/s11214-012-9892-2Grotzinger, J. P., Summer, D. Y., Kah, L. C., Stack, K. M., Gupta, S., Edgar, L., Rubin, D., Lewis, K. W., Schieber, J., Mangold, N., Milliken, R., Conrad, P. G., DesMarais, D., Farmer, J., Siebach, K., Calef III, F., Hurowitz, J., McLennan, S. M., Ming, D. W., … MSL Science Team. (2014). A Habitable Fluvio-Lacustrine Environment at Yellowknife Bay, Gale Crater, Mars. *Science, 343*. doi: 10.1126/science.1242777

Lapotre, M. G. A., Ewing, R. C., Lamb, M. P., Fischer, W. W., Grotzinger, J. P., Rubin, D. M., Lewis, K. W., Ballard, M. J., Day, M., Gupta, S., Banham, S. G., Bridges, N. T., Marais, D. J. D., Fraeman, A. A., Grant, J. A., Herkenhoff, K. E., Ming, D. W., Mischna, M. A., Rice, M. S., Yingst, R. A. (2016). Large wind ripples on Mars: A record of atmospheric evolution. *Science*, *353*(6294), 55–58. https://doi.org/10.1126/science.aaf3206

Lapotre, M. G. A., Ewing, R. C., Weitz, C. M., Lewis, K. W., Lamb, M. P., Ehlmann, B. L., & Rubin, D. M. (2018). Morphologic Diversity of Martian Ripples: Implications for Large-Ripple Formation. *Geophysical Research Letters*, *45*(19), 10,229-10,239. https://doi.org/10.1029/2018GL079029

Maki, J., Thiessen, D., Pourangi, A., Kobzeff, P., Litwin, T., Scherr, L., Elliott, S., Dingizian, A., & Maimone, M. (2012). The Mars Science Laboratory Engineering Cameras. *Space Science Reviews*, *170*(1–4), 77–93. https://doi.org/10.1007/s11214-012-9882-4

Malin, M. C., Ravine, M. A., Caplinger, M. A., Tony Ghaemi, F., Schaffner, J. A., Maki, J. N., Bell, J. F., Cameron, J. F., Dietrich, W. E., Edgett, K. S., Edwards, L. J., Garvin, J. B., Hallet, B., Herkenhoff, K. E., Heydari, E., Kah, L. C., Lemmon, M. T., Minitti, M. E., Olson, T. S., Jensen, E. H. (2017). The Mars Science Laboratory (MSL) Mast cameras and Descent imager: Investigation and instrument descriptions. *Earth and Space Science*, *4*(8), 506–539. https://doi.org/10.1002/2016EA000252

McEwen, A. S., Eliason, E. M., Bergstrom, J. W., Bridges, N. T., Hansen, C. J., Delamere, W. A., Grant, J. A., Gulick, V. C., Herkenhoff, K. E., Keszthelyi, L., Kirk, R. L., Mellon, M. T., Squyres, S. W., Thomas, N., & Weitz, C. M. (2007). Mars Reconnaissance Orbiter's High Resolution Imaging Science Experiment (HiRISE). *Journal of Geophysical Research: Planets*, *112*(E5). https://doi.org/10.1029/2005JE002605

Rice, M. S., Williams, J. M., Calef III, F., Anderson, R. B., Edgar, L., Stack, K., Summer, D. Y., Newsom, H. E., Grotzinger, J. P., King, P. (2013). Detailed Geologic Mapping Along the Mars Science Laboratory (MSL) Curiosity Traverse Path from Glenelg to Mount Sharp. Paper Presented at the 44th Lunar and Planetary Science Conference, The Woodlands, TX. Abstract #2892. https://www.lpi.usra.edu/meetings/lpsc2013/pdf/2892.pdf

Rice, M. S., Gupta, S., Treiman, A. H., Stack, K. M., Calef, F., Edgar, L. A., Grotzinger, J., Lanza, N., Deit, L. L., Lasue, J., Siebach, K. L., Vasavada, A., Wiens, R. C., & Williams, J. (2017). Geologic overview of the Mars Science Laboratory rover mission at the Kimberley, Gale crater, Mars. *Journal of Geophysical Research: Planets*, *122*(1), 2–20. https://doi.org/10.1002/2016JE005200

Rothrock, B., Kennedy, R., Cunningham, C., Papon, J., Heverly, M., & Ono, M. (2016). Spoc: Deep learning-based terrain classification for mars rover missions. In *AIAA SPACE 2016* (p. 5539).

Sharp, R. P. (1963). Wind Ripples. *The Journal of Geology*. https://doi.org/10.1086/626936

Siebach, K. L., Baker, M. B., Grotzinger, J. P., McLennan, S. M., Gellert, R., Thompson, L. M., & Hurowitz, J. A. (2017). Sorting out compositional trends in sedimentary rocks of the Bradbury group (Aeolis Palus), Gale crater, Mars. *Journal of Geophysical Research: Planets*, *122*(2), 295-328.

Silvestro, S., Chojnacki, M., Vaz, D. A., Cardinale, M., Yizhaq, H., & Esposito, F. (2020). Megaripple Migration on Mars. *Journal of Geophysical Research: Planets*, *125*(8), e2020JE006446. https://doi.org/10.1029/2020JE006446

Silvestro, S., Vaz, D. A., Ewing, R. C., Rossi, A. P., Fenton, L. K., Michaels, T. I., Flahaut, J., & Geissler, P. E. (2013). Pervasive aeolian activity along rover Curiosity's traverse in Gale Crater, Mars. *Geology*, *41*(4), 483–486. https://doi.org/10.1130/G34162.1

Stack, K. M., Cofield, S. M., & Fraeman, A. A. (2017). Geologic Map of the MSL Curiosity Rover Extended Mission Traverse of Aeolis Mons, Gale Crater, Mars. *48th Lunar and Planetary Science Conference (2017), Abstract #1899.* https://www.hou.usra.edu/meetings/lpsc2017/pdf/1889.pdf

Stack, K. M., Williams, N. R., Calef, F., Sun, V. Z., Williford, K. H., Farley, K. A., Eide, S., Flannery, D., Hughes, C., Jacob, S. R., Kah, L. C., Meyen, F., Molina, A., Nataf, C. Q., Rice, M., Russell, P., Scheller, E., Seeger, C. H., Abbey, W. J., … Yingst, R. A. (2020). Photogeologic Map of the Perseverance Rover Field Site in Jezero Crater Constructed by the Mars 2020 Science Team. *Space Science Reviews*, *216*(8). https://doi.org/10.1007/s11214-020-00739-x

Stein, T, Arvidson, R., & Zhou, F. (2016). PDS Analyst's Notebook for MSL and MER: Addition of Image Measurement Tools. *47th Lunar and Planetary Science Conference (2016)*, *Abstract #1192*. https://www.hou.usra.edu/meetings/lpsc2016/pdf/1192.pdf

Stein, Thomas. (2014). PDS MSL Analyst's Notebook: Supporting Active Rover Missions and Adding Value to Planetary Data Archives. *40th COSPAR Scientific Assembly, Abstract # B0.8-10-14.*

Sullivan, R., Banfield, D., Bell, J. F., Calvin, W., Fike, D., Golombek, M., Greeley, R., Grotzinger, J., Herkenhoff, K., Jerolmack, D., Malin, M., Ming, D., Soderblom, L. A., Squyres, S. W., Thompson, S., Watters, W. A., Weitz, C. M., & Yen, A. (2005). Aeolian processes at the Mars Exploration Rover Meridiani Planum landing site. *Nature*, *436*(7047), 58–61. https://doi.org/10.1038/nature03641

Sullivan, R., Arvidson, R., Bell, J. F., Gellert, R., Golombek, M., Greeley, R., Herkenhoff, K., Johnson, J., Thompson, S., Whelley, P., & Wray, J. (2008). Wind-driven particle mobility on Mars: Insights from Mars Exploration Rover observations at "El Dorado" and surroundings at Gusev Crater. *Journal of Geophysical Research: Planets*, *113*(E6). https://doi.org/10.1029/2008JE003101

Sullivan, R., Bridges, N., Herkenhoff, K., Hamilton, V., Rubin, D. (2014). Transverse Aeolian Ridges (TARs) as Megaripples: Rover Encounters at Meridiani Planum, Gusev, and Gale. *Eighth International Conference on Mars, Abstract #1424.*

Sullivan, R., Kok, J. F., Katra, I., & Yizhaq, H. (2020). A Broad Continuum of Aeolian Impact Ripple Morphologies on Mars is Enabled by Low Wind Dynamic Pressures. *Journal of Geophysical Research: Planets*, *125*(10), e2020JE006485. https://doi.org/10.1029/2020JE006485

Sutton, S. L. F., C. McKenna Neuman, and W. Nickling (2013), Lee slope sediment processes leading to avalanche initiation on an aeolian dune, *J. Geophys. Res. Earth Surf., 118*, 1754–1766, doi:10.1002/jgrf.20131.

Viúdez-Moreiras, D., Gómez-Elvira, J., Newman, C. E., Navarro, S., Marin, M., Torres, J., & de la Torre-Juárez, M. (2019). Gale surface wind characterization based on the Mars Science Laboratory REMS dataset. Part I: Wind retrieval and Gale's wind speeds and directions. *Icarus*, *319*, 909–925. https://doi.org/10.1016/j.icarus.2018.10.011

Weitz, C. M., Sullivan, R. J., Lapotre, M. G. A., Rowland, S. K., Grant, J. A., Baker, M., & Yingst, R. A. (2018). Sand Grain Sizes and Shapes in Eolian Bedforms at Gale Crater, Mars. *Geophysical Research Letters*, *45*(18), 9471–9479. https://doi.org/10.1029/2018GL078972

Wiens, R. C., Maurice, S., Barraclough, B., Saccoccio, M., Barkley, W. C., Bell, J. F., Bender, S., Bernardin, J., Blaney, D., Blank, J., Bouyé, M., Bridges, N., Bultman, N., Caïs, P., Clanton, R. C., Clark, B., Clegg, S., Cousin, A., Cremers, D., … Wong-Swanson, B. (2012). The ChemCam Instrument Suite on the Mars Science Laboratory (MSL) Rover: Body Unit and Combined System Tests. *Space Science Reviews*, *170*(1), 167–227. https://doi.org/10.1007/s11214-012-9902-4

Zimbelman, J. R. (2010). Transverse Aeolian Ridges on Mars: First results from HiRISE images. *Geomorphology*, *121*(1), 22–29. https://doi.org/10.1016/j.geomorph.2009.05.012

Zimbelman, J. R., Irwin, R. P., Williams, S. H., Bunch, F., Valdez, A., & Stevens, S. (2009). The rate of granule ripple movement on Earth and Mars. *Icarus*, *203*(1), 71–76. https://doi.org/10.1016/j.icarus.2009.03.033

Zimbelman, J. R., Williams, S. H., & Johnston, A. K. (2012). Cross-sectional profiles of sand ripples, megaripples, and dunes: A method for discriminating between formational mechanisms. *Earth Surface Processes and Landforms*, *37*(10), 1120–1125. https://doi.org/10.1002/esp.3243

Zimbelman, J. R., & Foroutan, M. (2020). Dingo Gap: Curiosity went up a small transverse aeolian ridge and came down a megaripple. *Journal of Geophysical Research: Planets*, *125*, e2020JE006489. https://doi.org/10.10292020JE006489

CHAPTER 3: Aeolian bedrock ridges in Gale crater, Mars.

Note: This chapter is modified from Bretzfelder et al. (2024) "Aeolian bedrock ridges in Gale crater, Mars." *Icarus*, *408*, 115855. https://doi.org/10.1016/j.icarus.2023.115855

3.1 Abstract

Fields of parallel, regularly-spaced, bedrock ridges observed on Mars and rarely on Earth have been interpreted as aeolian surface features oriented perpendicular to a formative wind. The exact formation process for these ridges, however, including the role of aeolian erosion versus deposition, continues to be debated. We identified forty fields of bedrock ridges on and within the sedimentary strata of Gale crater's central mound, Aeolis Mons. To better constrain the development of these landforms and the winds responsible for their formation, we characterized ridge morphology, orientation, geographic distribution, stratigraphic relationships, and interactions with other aeolian landforms. The study area of Aeolis Mons was chosen to leverage the extensive high-resolution image coverage from orbit, as well as to build upon the detailed stratigraphy compiled from in situ exploration with the Mars Science Laboratory Curiosity rover. Using the orientation of the ridges, we present a wind vector map of Aeolis Mons. The orientation of bedrock ridges in the Mound Skirting Unit, which unconformably drapes Aeolis Mons, suggests the average wind direction in Gale crater may have remained consistent since that unit was emplaced (~3.8-3.1 Ga). This study explores the implications of these ridges for the history of wind, deposition, and erosion in Gale crater.

3.2 Introduction

Aeolian (wind-formed) features such as dunes (Hayward et al., 2014; Fenton, 2020), ripples (Silvestro et al., 2013; Lapotre et al., 2016), transverse aeolian ridges (TARs; Balme et al., 2008; Berman et al., 2011; Geissler, 2014), and yardangs (Ward, 1979; Liu et al., 2020) are common across the surface of Mars and form via erosional or depositional processes as wind transports sand across the landscape. These features can be modern or ancient, formed over short or long timescales, but all have the potential to record the formative wind direction, which can be interpreted based on their morphologies.

Active, unconsolidated, depositional bedforms , can be used to study modern wind patterns, as sand is transported on short time scales (i.e., Silvestro et al., 2010; Chojnacki et al., 2011; Ewing et al., 2017; Baker et al., 2018; Silvestro et al., 2020). Lithified or indurated bedforms record past eras of wind activity. (i.e., Hunt et al., 2022), and instances of these fossil- or paleo-dunes have been identified in several locations on the surface of Mars (Edgett and Malin, 2000; Malin and Edgett, 2001; Kerber and Head, 2012; Milliken et al., 2014; William and Weitz, 2014; Day and Catling, 2018; Chojnaki et al., 2020; Runyon et al., 2021; Hunt et al., 2022). The bedform lithification process can occur via burial, either by pyroclastic deposition (i.e., de Silva et al., 2010; Runyon et al., 2021) or via cementation of the grains through a variety of mechanisms (i.e., Bridges et al., 2010; Milliken et al., 2014; Day and Catling, 2018; Runyon et al., 2021). The paleo-bedforms can then be re-exposed via erosion. Regardless of the mechanism, the lithification process preserves a record of the wind regime at the time of induration.

Sediment moving across a bedrock surface can carve, as well as build. For example, yardangs (Blackwelder, 1934) and ventifacts (Higgins, 1956; Laity, 1994) are surface features carved by wind that record the formative wind directions in their characteristic shape. Just over a decade ago, an additional class of aeolian landform was identified: periodic bedrock ridges (PBRs;

Montgomery et al., 2012). PBRs are periodic, straight-crested to sinuous bedrock bedforms, with a few meters of topographic relief, and wavelengths in the tens of meters. These ridges are similar in scale and pattern to TARs, but whereas TARs are unconsolidated (Balme et al., 2008; Berman et al., 2011; Geissler, 2014), PBRs are indurated, and can often be identified by the presence of polygonally fractured bedrock comprising their surfaces (Montgomery et al., 2012; Hugenholtz et al., 2015; Favaro et al., 2021; Silvestro et al., 2021; Stack et al., 2022). PBRs have been proposed to form via two main mechanisms: (1) flow separation patterns in the wind moving across the bedrock (Montgomery et al., 2012), or (2) shielding of the bedrock by unconsolidated bedforms (Hugenholtz et al., 2015). Few Earth analogs exist for comparison (de Silva et al., 2013; Hugenholtz et al., 2015), and open questions regarding their formation persist, though they are consistently interpreted as erosional features carved into bedrock that form transverse to the dominant sand-transporting winds (Montgomery et al., 2012; Hugenholtz et al., 2015, Favaro et al., 2021; Silvestro et al., 2021; Stack et al., 2022).

Fields of bedrock ridges have been observed within Gale crater (Anderson and Bell, 2010; Milliken et al., 2014; Kronyak et al., 2019; Stack et al., 2022), the landing site and exploration area for the Mars Science Laboratory (MSL) mission's Curiosity rover (Grotzinger et al., 2012). Though the term PBR is generally associated with erosional aeolian bedforms, the more general term 'bedrock ridge' can be used to describe erosional aeolian bedforms, in addition to features of a variety of origins including as lithified depositional aeolian bedforms (i.e. paleo-dunes); 'bedrock ridge' can also be applied to tectonic or impact-related structures (e.g. lineaments), volcanic constructs, inverted fluvial channel bodies, preferentially cemented bedrock, or mineralized fractures or fracture fill,. Some bedrock ridges investigated by Curiosity in Gale crater have been interpreted as ridges carved into the bedrock by aeolian erosion (Anderson and Bell, 2010; Stack et al., 2022).

Others have been interpreted as fields of lithified TARs or dunes (Anderson and Bell, 2010; Milliken et al., 2014). Still other ridge fields throughout Gale have been interpreted as pre-existing fractures in the bedrock filled with erosionally-resistant materials, which were eventually exposed as positive relief features (Anderson and Bell, 2010; Kronyak et al.2019; Edgett et al., 2021).

This work explores fields of bedrock ridges identified on and around the central mound of Gale crater (Aeolis Mons, also known informally as Mount Sharp; Fig. 3.1) to search for insights into the evolution of the mound. Our observations, reported here, indicate all the features we identified are of aeolian origin and thus can be used to document long-acting wind patterns. The analysis presented here highlights the large number of bedrock ridge fields present in Gale crater and uses them as a tool to interpret paleo-winds.

3.3 Background

3.3.1 Gale crater and Aeolis Mons

Gale crater is ~154 km in diameter, with an estimated age of ~3.61 Ga, located along the Martian hemispheric dichotomy (Fig. 3.1; Thomson et al., 2011). Currently home to the Curiosity rover, the crater is a target of particular scientific interest due to interpretations of past aqueous environments, with relevance to habitability (i.e., Anderson and Bell, 2010; Le Deit et al., 2013; Vasavada, 2022 and references therein), and the ~5 km high mound of sedimentary deposits in the center of the crater, which appears to record a global shift in climate conditions from a wetter to drier environment (i.e., Milliken et al., 2010; Horvath and Andrews-Hanna, 2017; Liu et al., 2021; Horvath and Andrews-Hanna, 2021). After deposition, strata of this central mound (Aeolis Mons)

were eroded by wind, carving the topography and mound morphology observed today (Malin and Edgett, 2000; Day et al., 2016).

Aeolis Mons is comprised of several stratigraphic units defined from orbital data (e.g., Thomson et al., 2011; Anderson and Bell, 2010; Le Deit et al., 2013), which in situ observations have shown include different lithologies that range from mudstones formed in a paleo-lake to sandstones deposited during more arid periods (see review in Vasavada, 2022 and references therein). The bedrock ridges mapped here occur in most of the stratigraphic units, which have ages estimated to span the late Noachian to Hesperian epochs (Thomson et al., 2011).

The study area was bounded by the extent of Aeolis Mons and the unconformably overlying Mound Skirting unit (MSU; originally defined from orbital data; Anderson and Bell, 2010). Anderson and Bell (2010) noted that bedrock ridges are particularly abundant in the MSU. Anderson and Bell (2010) also noted the generally higher thermal inertia of the MSU material, which was later used by Fraeman et al., (2016) to re-classify the MSU material as the High Thermal Inertia unit 1 in their map of lower Aeolis Mons. Following in situ observations of the unit, strata of the MSU seen along the rover traverse were later renamed the Siccar Point group (i.e., Fraeman et al., 2016; Kronyak et al., 2019; Stack et al., 2019; Banham et al., 2018; 2021; 2022; Fedo et al., 2022; Watkins et al., 2022) and includes aeolian strata of the Stimson formation (Banham et al., 2018). Based on continued in situ exploration with Curiosity, the traversed portion of the MSU (Siccar Point group, Stimson formation) has been interpreted as aeolian, paleo-dune strata, deposited unconformably over the mudstones of the Murray formation (Grotzinger et al., 2015; Banham et al. 2021; Liu et al., 2021; Watkins et al., 2022). For simplicity, we refer to this unit as the MSU throughout this paper to emphasize its mapping from orbiter rather than in situ data. The

MSU is superposed in Gale crater by deposits interpreted to reflect late-stage hydrogeomorphic activity that occurred after the lithification of the MSU (Milliken et al., 2014; Palucis et al., 2016).

3.3.2 Bedrock Ridges in Gale crater

As noted above, bedrock ridges are particularly abundant in the MSU (Anderson and Bell, 2010), and were interpreted as either exhumed lithified depositional bedforms, or the result of preferential erosion along parallel joints or fractures (i.e. Kroynak et al., 2019). Later, Milliken et al. (2014) identified fields of bedrock ridges both within the MSU and elsewhere on Aeolis Mons. Their interpretation was also that these fields represent lithified bedforms.

In situ exploration of periodic bedrock ridge fields with the instruments on Curiosity provides additional context for ridge fields identified in orbiter images (Fig. 3.2). Three different ridge fields, each with a unique morphology, have been explored, at 1) the Emerson and Naukluft plateaus (Fig. 3.2A-B), 2) Glen Torridon (Fig. 3.2A, 3.2C, 3.2F), and 3) the Greenheugh pediment (Fig. 3.2A, 3.2C, 3.2D). The Emerson and Naukluft plateaus are the lowest elevation exposures of the aeolian Stimson formation (Banham et al., 2018; 2021; 2022), and exhibit bedrock ridge fields with pitted, rough-textured crests, similar to the ridges characterizing the MSU (Fig. 3.2B). By contrast, ridges in the Glen Torridon region exhibit sharp, well-defined crestlines and tuning-fork junctions (Fig. 3.2C). Found in the Glasgow and Knockfarril Hill members of the Carolyn Shoemaker formation (Fedo et al., 2022), the Glen Torridon ridges sit in a different stratigraphic group than the Emerson and Naukluft ridges. However, using both orbital and in situ data, the Glen Torridon ridges were interpreted as erosional features post-dating the exhumation of Aeolis Mons (Stack et al., 2022). Finally, bedrock ridges also cap the surface of the Greenheugh Pediment (Fig. 3.2D-E). Strata at the Greenheugh Pediment were also interpreted as lateral deposits of the same

Stimson formation (Banham et al., 2018; 2022), here unconformably overlying the Carolyn Shoemaker formation. The pattern of ridges on the surface of the pediment differs from the other visited ridge fields, as both primary and secondary crestlines are present. The networked morphology of ridges has been compared to networked aeolian bedform patterns (Fig. 3.2D-E; Bryk et al., 2020). The Greenheugh pediment exhibits a unique surface texture which has been described as 'gatorback' terrain, with blocks of heavily ventifacted material forming the crestlines of the ridges (Fig. 3.2E). In contrast, the erosional surface of the Glen Torridon ridges is overall smoother, with a cover of smaller clasts (Fig. 2F; Stack et al., 2022; Khan et al., 2023). These fine-scale observations are possible due to the in situ perspective of Curiosity, and help illuminate the variability within bedrock ridge morphologies.

3.4 Methods

This study examined bedrock ridges in the center of Gale crater, specifically on Aeolis Mons and the MSU (including the area traversed by Curiosity) using the available High Resolution Imaging Science Experiment (HiRISE; McEwen et al., 2007) image coverage (see Supplemental Material Fig. 3.S1 for extent of image coverage). Ridge morphology, orientation, and geographic distribution, stratigraphic relationships, and interactions with other aeolian landforms are characterized in order to determine the origin of the bedrock ridges, and what they mean for the history of wind, deposition, and erosion in Gale crater. The MSU/Siccar Point group was remapped for this study at a scale of 1:20,000, exclusively where the material was visible in HiRISE images (Fig. 3.3 and Supplemental Fig. 3.S1). The MSU material was identified based on the unit

description and original mapping work from Anderson and Bell (2010), namely by identifying areas with the characteristic ridged, pitted, and fractured textures described in their work.

The analysis presented here was conducted using HiRISE images at ~25 cm/px within the global mosaic available from ArcGIS online (Plesea et al., 2019; see Fig. 3.1 in supplemental materials). Available images covering Aeolis Mons were surveyed for fields of bedrock ridges. The bedrock ridge fields were identified by searching for areas with multiple (>3) raised linear bedrock features aligned parallel to one another. We required that the ridges were of similar scales and morphologies, and that the pattern of ridges exhibited some periodicity. Ridges also have apparent topography, identified based on shadows in the HiRISE images. Lone features were not considered for this work, as the periodicity of the ridges is a defining feature of PBRs.

Once ridge fields were identified in HiRISE images, we measured ridge wavelengths and orientations. Orientations were measured along the crests of each ridge, manually approximating the straight-line trace of the ridge. Ridge wavelengths in a given field were measured perpendicular to the ridge orientation and between adjacent crests. We report the wavelength of a given field as the mean of these measurements (at least 50 measurements were made in each field, except where <50 bedrock ridges were present in a field) plus or minus one standard deviation. After we identified all fields of bedrock ridges in the study area in available HiRISE images, we grouped the bedrock ridges based on morphology. HiRISE images were also used to identify nearby aeolian surface features such as yardangs and dunes, which were used to interpret local sand-transporting wind directions (e.g., Greeley et al., 2008; Day and Kocurek, 2016; Schieber et al., 2020). Digital terrain models (DTMs) generated from HiRISE stereo-pairs were used to measure the vertical

relief of the ridge fields (see supplemental materials Table 3.2 for a list of DTMs). For additional information on ridge field locations, see supplemental materials Figure and Table 3.1.

3.5 Results

3.5.1 Ridge Distribution Across Aeolis Mons

Forty bedrock ridge fields were identified in the Aeolis Mons study area (Figs. 3.1, 3.3). This included eleven fields previously identified by Milliken et al. (2014), and three fields visited by Curiosity (Fig. 3.2) at the Emerson and Naukluft plateaus (Fig. 2B; Banham et al., 2018), Greenheugh pediment (Fig. 3.2D-E; Bryk et al., 2020), and Glen Torridon (Fig. 3.2C, 3.2F; Stack et al., 2022).

Bedrock ridges are widespread across Aeolis Mons, and are observed over an elevation range spanning from -4,500 m (base of the mound) to ~800 m at the top of Aeolis Mons. Bedrock ridges occur in a variety of different geomorphic (Figs. 3.1 and 3.2, Anderson and Bell, 2010; Le Deit et al., 2013; Fraeman et al., 2016) and mineralogically-defined units (e.g., clay- and sulfate-bearing units; Milliken et al., 2010; Fraeman et al., 2016). Ridge field populations vary, with the smallest field containing only six ridges, to the largest fields consisting of over 4000 ridges. The largest field on Aeolis Mons (excluding those in the MSU) covers ~11 km^2, though most fields are much smaller. A total of ten ridge fields cover a total ~148 km^2 of the MSU, meaning they make up approximately half of the total surface of that unit as seen with HiRISE (~371 km^2; Fig. 3.2).

3.5.2 Ridge Morphologies and Classification

In all of the identified fields, ridge wavelengths measure in the tens of meters, falling between ~10-90 m. Many of the bedrock ridges are morphologically similar to sandy TARs. For example,

some bedrock ridges branch in plan-view, forming Y-junctions (also known as 'tuning-fork junctions'), which are common elements of aeolian bedform patterns (i.e., Bullard et al., 1994; see Figs. 3.4 and 3.5). Y-junctions were identified in approximately half of the ridge fields. However, there are several important differences between the bedrock ridges studied in this work and unconsolidated aeolian bedforms, specifically: (a) sharp-rimmed small craters (10s of meters in diameter) without discernable ejecta superpose the bedrock ridges (Fig. 3.4A), (b) rugged surface textures, including those where the bedrock texture is visible within the ridge forms (c) stratigraphic superposition across multiple units, or in the case of the ridges in the MSU, stratigraphic confinement within certain units and (d) where the bedrock ridges are present near scarps, there is no unconsolidated sediment at the base of the scarp. If present, this loose material would indicate that the ridges were composed of unconsolidated material that was transported down slope during migration of the ridges, but the absence of sediment indicates that the bedrock ridges are composed of indurated materials.

Four main morphological groups were identified across the forty fields, and the defining characteristics of each are outlined below. The distribution of ridge field locations by morphologic type can be seen in Figure 3.3.

(1) **Type 1:** (N= 25) Bedrock ridges are sharp-crested, continuous, and appear overall smooth between ridges, except where interrupted by small craters. Any roughness on the surface of these ridges, aside from the visible craters, is below the resolution limit of the images (~25 cm/px; Fig. 3.4A). Ridges are approximately symmetric across their crests. A small subset of these ridges have crest-perpendicular lineations on the ridge faces and in the inter-ridge troughs (see supplemental Fig. 3.2). Some ridges

were observed to crosscut bedding planes. Average wavelength (μ±σ): 35.0m ± 28.3m.

Type 1 ridges are the most similar in appearance to TARs. The Glen Torridon ridges explored by Curiosity (Fig. 3.2C; Stack et al., 2022) are an example of this type.

(2) **Type 2:** (N = 4) These bedrock ridges vary in apparent height and width along their length as sections of the ridge crest appear to be partially missing. Some ridges are discontinuous, presenting as parallel, linear rows of knobs (Fig. 3.4B). Average wavelength (μ±σ): 28.1m ± 15.2m.

(3) **Type 3:** (N = 3) This group consists of sharp crested bedrock ridges, with generally bright crests. Unlike Type 1 ridges, these appear rough at the scale of the HiRISE images; they are pitted, especially along the inter-ridge areas, and are overall weathered in appearance. Circular depressions, likely craters, interrupt the ridge crests, but otherwise they are continuous (Fig. 3.4D). Average wavelength (μ±σ): 42.1m ± 6.9m.

Type 3 ridges have previously been referred to as 'washboard terrain,' and are abundant and exclusively observed in the MSU (Anderson and Bell, 2010).

(4) **Type 4:** (N = 6) As with Type 3, these bedrock ridges are heavily pitted and weathered. These ridges also have a similar average wavelength to Type 3. However,

these ridges have diffuse crests, which give the ridges a flatter or wider appearance than Type 3 (Fig. 3.4E). Average wavelength (μ±σ): 45.1m ± 12.0m.

The Emerson and Naukluft Plateau ridges visited by Curiosity (Fig. 3.2B; Banham et al., 2018) are an example of Type 4 ridges. This ridge type was only identified in the MSU.

Other: (N = 2) Two bedrock ridge fields exhibit morphologies not well aligned with the types described above. The first is on the Greenheugh pediment, in which both primary and secondary crests are observed (resembling networked TARs, Figs. 3.2D, 3.4F; i.e., Milliken et al., 2014; Nagle-McNaughton and Scuderi, 2021), a feature which was not seen in any other ridge field. The other field occurs along the wall of a valley south of Aeolis Mons, and is unique in both its placement along an apparently steep slope and in having a ribbed texture to the ridges where it appears preferential erosion is forming fins across the ridge crestlines as different layers crosscut by the ridges erode at different rates (For location information, see field 27 in supplementary materials).

Fractured: In some bedrock ridge fields, the bedrock in which the ridges occur appears to be fractured. These fractures manifest as either filled fractures with a boxwork texture near the ridges (Fig. 3.4B; i.e., Anderson and Bell. 2010; Siebach and Grotzinger, 2014; de Silva and Bailey, 2017), or a cracked appearance manifesting as dark networks of polygonal lines in otherwise brighter bedrock (Fig. 3.4C). The fractures in the bedrock do not appear to impact the morphology of the ridges.

Across the upper portion of Aeolis Mons, we identified thirteen fields where bedrock ridges crosscut bedding planes (Fig. 3.5A-B). Some other ridge fields on the upper mound form on slopes,

and contain bedrock ridges that are oriented obliquely to *inferred* horizontal bedding, but no bedding was resolved in the particular HiRISE image. In contrast, at least four fields in the MSU contain ridges that appear confined to a particular layer within the unit's stratigraphy. The relationship between these MSU bedrock ridges and remnants of overlying non-ridged bedrock, suggests that the MSU bedrock ridges are in the process of being exhumed as superimposed bedrock layers are eroded. Where the superimposed bedrock remains, the ridge crests can be projected across the buried portion (Fig. 3.5C-F). These bedrock ridges can be constrained stratigraphically given the superposition of younger bedrock. However, the ridges that are only visible on the modern upper surface and do not have a relationship to superposed bedrock, and thus do not have a lower-limit on their age. The only relative age constraint for these ridges is that they must be younger than the bedrock in or on which they are occur. Those bedrock ridges that crosscut bedding planes must also be post-depositional features.

Topographic profiles of the bedrock ridges were collected everywhere available HiRISE DTM coverage coincided with ridge fields (Fig. 3.6). These profiles show that the bedrock ridges appear to be mostly below the resolution of the DTM, meaning they can only have a few meters of vertical relief. Stack et al. (2022) used images from Curiosity to confirm that the Glen Torridon ridges were ~1-3 m in height, consistent with them being just at or below the 1 m/px post-spacing of the DTMs. A field of bedrock ridges in a canyon on the southern portion of Aeolis Mons occur on an apparently steep slope, and possesed a unique morphology, so were placed into the "other" morphologic category (Fig. 3.6D).

3.5.3 Ridge Orientations and Relationships to other Surface Features

Across the entire study area, ridge orientations vary widely, with some bedrock ridges oriented north-south, and others oriented east-west, with most somewhere in between (Figs. 3.7 and 3.8). A one-sample Kolmogorov-Smirnov test was conducted to test whether the mean orientations of the studied fields were normally distributed. Three tests were conducted (on the means of all fields, on those in the MSU, and on all fields excluding those in the MSU), and in all cases, the null hypothesis that the samples are drawn from a normal distribution (centered on ~90°) was not rejected. Within a given field, ridge orientations are generally consistent, with the mean of the standard deviations across all fields being ± 14°. The variability in the MSU ridges is lower than the overall dataset, with an average standard deviation of ± 8°.

With the exception of the bedrock ridges in the MSU, which are exposed in ten locations around the base of Aeolis Mons (Anderson and Bell, 2010; Milliken et al., 2014) and are all consistently oriented east-west (average orientation 87°± 8°; Figs. 3.7 and 3.8A-J), ridge orientation does not appear to correlate systematically with the geologic or mineralogic units identified by Anderson and Bell, 2010, Le Deit et al., 2013 and Fraeman et al., 2016.

For particularly large regions of bedrock ridges, where some topography such as mounds or valleys existed within the otherwise continuous field of ridges, ridges on either side of the topographic feature were measured separately. This separation was done in order to determine if modern topography, which should influence modern wind regimes, has any impact on resulting ridge orientation. The primary example of this is in an extensive field of Type 1 ridges located near the top of Aeolis Mons (Figs. 3.7 and 3.8L-N). Though the bedrock ridges in this region appear to represent a continuous field, based on consistent morphology and scale across the area, they extend

across multiple mounds and valleys (~100 m of topographic relief). The ridge orientations vary widely (average orientations of the fields range across ~100°; between 10.95°±15.12° and 112.89°±18.90°, Figs. 7, 8L-N) over the relatively small area (~11 km^2; Fig. 3.7), in stark contrast to the MSU ridges which are consistent (average orientations within ~17°; between 80°±8° to 97°±17°; Figs. 3.7, 8A-K) across much greater distances (~148 km^2), and on either side of much more substantial topography (namely Aeolis Mons). This indicates that modern local topography influenced the orientation of some of the ridges, namely those outside of the MSU.

The measured ridge orientations can be used to interpret formative wind directions. These interpretations contain 180° of ambiguity; as the bedrock ridges are expected to form transverse to the sand-transporting winds, there are two possible wind directions that could produce the same ridge orientation. However, previous work has interpreted the regional scale wind pattern across Gale crater to be dominated by northerly winds (Hobbs et al., 2010; Day and Kocurek, 2016; Baker et al., 2018), therefore, we assume the more northerly of the two interpretable options. In addition, at each of the ridge fields we searched for other features which could provide additional context for local wind directions (Fig. 3.9). The primary examples were yardangs, as they are abundant on Aeolis Mons and at the scale of HiRISE images their morphology can be used to infer a formative wind direction (i.e. Fig. 3.9A). The blunted end is upwind, with the narrower, tapered end extending downwind (Blackwelder, 1934; Ward, 1979). Three ridge fields are coincident with groups of yardangs (for example, Fig. 9A). Where they are seen together, the bedrock ridges are oriented transverse to the yardangs, implying the same winds that carved the flow-parallel yardangs likely created the flow-normal ridge fields, further supporting the interpretation that the bedrock ridges developed in response to aeolian processes.

The orientation of unconsolidated bedforms such as dunes and TARs can be used to infer more recent formative wind patterns and compare against the inferred formative winds for the bedrock ridges. However, we found only a few examples of bedrock ridges near unconsolidated bedforms (Fig. 3.9). A few instances of bright-toned TARs were seen in the vicinity of ridge fields, but the TARs were often located in topographic depressions, such as valleys and craters, meaning that their orientation was likely controlled by the local topography and not necessarily reflective of the same winds forming the nearby bedrock ridges (Fig. 3.9A). One field of dark (active) dunes was seen migrating over ridges in the MSU (Fig. 3.9B). The dune migration direction in this area, a part of the Bagnold Dune field (Bridges et al., 2018), has been interpreted as toward the southwest, around the topography of Aeolis Mons (Hobbs et al., 2010; Day & Kocurek, 2016). The dunes have multiple slip faces, indicating a complex wind regime, though previous work has determined that winds from the north contribute to the S-SW migration of these dunes (Hobbs et al., 2010; Silvestro et al., 2013). The bedrock ridges in the area are oriented east-west (80 ± 7°; 3.8b), suggestive of winds from the north and potential migration to the south. South of Aeolis Mons, at another field of MSU ridges that is bordered by dark dunes, the dune orientation does not match that of the ridges. In some areas, bright toned ripples between and underneath the dunes could also be seen. The networked morphology of these partially-buried TARs implies a multidirectional and

complex wind regime, likely associated with their position in topographic lows between dunes (i.e., Nagle-McNaughton and Scuderi, 2021).

3.6 Discussion

3.6.1 Ridge Field Formation and Morphology

The bedrock ridges observed in this study show evidence of induration, demonstrating that they are not currently unconsolidated bedforms. Nevertheless, many of the bedrock ridges are morphologically similar in pattern and scale to aeolian bedforms on Mars, raising the question: how did these bedrock ridge fields form? Did their periodicity arise from fundamentally depositional or erosional processes? One way to explain the observed patterns is through the lithification of aeolian bedforms. Preserved bedforms have been identified on Mars in a variety of settings (Edgett and Malin., 2000; Kerber and Head, 2012; Williams and Weitz, 2014; Milliken et al., 2014; Day & Catling, 2018; Chojnacki et al., 2020; Runyon et al., 2021). The scale of the bedrock ridges studied in this work, including their heights and spacings, is most analogous to TARs (Balme et al., 2008; Berman et al., 2011). Both fields exhibit patterns of straight-crested bedrock ridges with occasional tuning-fork bifurcations (Y-junctions). Preserved TARs have been interpreted in the Apollinaris Sulci region of Mars (Edgett and Malin, 2000), exhumed from beneath less resistant deposits (Hunt et al., 2022), providing some precedent that aeolian bedforms of this scale can be preserved and exhumed.

However, bedrock ridge fields of a similar scale and pattern as fields of aeolian bedforms have also been interpreted to form predominantly by erosion, with the ridge pattern and periodicity carved directly into bedrock (Montgomery et al., 2012; Hugenholtz et al., 2015). Precisely how these erosional ridge fields develop remains a subject of debate. Montgomery et al. (2012)

suggested that periodicity develops as a consequence of turbulent length scales set by Mars' atmosphere and gravity, whereas Hugenholtz et al. (2015) suggested that the periodicity results from erosion in the inter-bedform space between armoring dunes or TARs. Regardless of the specific formation mechanism, erosional ridge fields can be distinguished from lithified bedforms when the bedrock ridges contain through-going bedding or stratigraphy.

In Gale crater, previous work has suggested that the NNE-SSW trending bedrock ridges in Glen Torridon were formed by aeolian erosion -- via the mechanism proposed by Montgomery et al. (2012) for PBRs -- cutting directly into lacustrine and fluvial bedrock (Stack et al., 2022). Conversely, a nearby ridge field on the upper surface of the Greenheugh Pediment exhibits ridge crests with an average WNW-ESE orientation. The pediment is composed of aeolian Stimson formation strata (Banham et al., 2018; 2021) and vertical exposures of the Stimson at the north edge of the pediment revealed three depositional intervals, which (from bottom to top of the section) varied from northward net transport, to southward transport and then to the west in the shallowest preserved sediments. The best-preserved bedrock ridges, which are interpreted as paleo-bedforms, are found at the southern end of the pediment surface, with crest lines oriented NW-SE (about 107°; Bryk et al., 2020).

Given that rover-based observations suggest both erosional and depositional periodic ridge fields are present in Gale crater, it is reasonable to expect that both may be represented amongst the ridge fields studied in this work. In 13 of 40 of the Gale ridge fields, bedding planes or resolvable layers were cross-cut by bedrock ridges, suggesting that these, at least, were formed by erosion. In the remaining fields, these crosscutting relationships were not observed. In these latter examples it is possible that (1) layers were present, but not resolved in the HiRISE images, (2) layers were not

present, but the bedrock ridges still eroded into locally massive strata, (3) the ridge patterns preserve lithified bedforms, or (4) some combination of (1)-(3).

Although all the bedrock ridges studied here are regularly-spaced ridges of indurated bedrock, a variety of ridge morphologies were observed between the fields (Types 1-4, Fig. 4). The fields are relatively consistent in their wavelength and overall pattern (with patterns similar to modern TAR fields), but the most variation is observed in ridge surface texture and definition, which range from smooth surfaces with sharp, well-defined crestlines (Type 1), to rugged surfaces marked by degraded craters and jagged, ill-defined crestlines (Type 4). One explanation for the differences in observed morphologies (assuming a common formation mechanism for type 1-4 bedrock ridges) is that they may represent a spectrum of degradation, influenced by bedrock lithology and cementation, where the bedrock ridges generally begin with a smoother, sharp-crested appearance (Type 1), and via weathering and erosion, become more textured or pitted, with diffuse crests. Depending on the lithology and rock hardness, the ridges transition from Type 1 to either Type 2 or Type 3 ridges. Type 2 ridges are knobby and discontinuous, indicating that the material is susceptible to erosion, and the original ridge form has degraded. By contrast, Type 3 ridges maintain their continuous and sharp crests, but have an overall more pitted appearance than Type 1, and are more heavily cratered than Type 1 or 2, indicating they are less prone to erosion than Type 2 ridges, and also likely older. This difference between Type 2 and 3 ridges could be explained by differences in lithology, with a softer material eroding more quickly to form Type 2 ridges and material with higher strength eroding more slowly to form the Type 3 ridges. Type 3 ridges which undergo additional erosion eventually lose the sharp crests, and these diffuse crests

give the ridges an overall wider and flatter appearance, while remaining continuous linear ridge features, resulting in Type 4 ridges.

Weathering and degradation have been invoked to explain morphological variations in a variety of landscape features on Mars (e.g., craters; Greely et al., 2000; Pain et al., 2007; Robbins and Hynek, 2012; Roberts et al., 2021). Calling on a similar mechanism to explain the observed morphologies is, therefore, not without precedent. However, during the past several billion years, aeolian erosion and impact gardening have been the two dominant drivers of landscape change and degradation at the latitude of Gale crater (i.e., Bibring et al., 2006; Newsom et al., 2015; Day and Kocurek, 2016). Impacts alone cannot explain the rough surface texture and muted crestlines in the Type 2-4 ridge fields, and given the age of the bedrock in which they are found, the ridges have been exposed to ~3 Ga of aeolian erosion. Given that many of these features formed by aeolian erosion (recall that those cross-cutting bedding planes must be geologically modern and erosional), how can aeolian erosion transition from creating a ridge field, to degrading and weathering it? Aeolian erosion could have initially created the periodic ridge patterns, but the patterns might be unstable over geologic time. For example: in the Hugenholtz et al. (2015) model, the bedrock ridges might be susceptible to erosion after the (unconsolidated) TARs migrate away from the ridged surface, as the loose sediment would no longer be present to shield the ridge forms. Differing diagenesis could also have changed the way that the bedrock ridge fields, if they were once buried, respond to aeolian erosion after exhumation (i.e. Milliken et al., 2014). Exhumed paleo-bedforms would be subject to erosion in the same way any exposed bedrock surface is eroded, and would be expected to degrade over time. Alternatively, Milliken et al., (2014) proposed that what we identify here as Type 3 ridges may be preserved bedforms, while Type 4 ridges may be preserved interdune material. This difference is invoked to explain the wider, flatter

appearance of the Type 4 ridges (Milliken et al., 2014). Morphology may provide a way to distinguish between erosional ridge fields and depositional ones, with the pristine-looking Type 1 fields forming via erosion (Montgomery et al., 2012; Hugenholtz et al., 2015) and the rougher-looking Types 2-4 fields reflecting preserved bedform fields (Anderson and Bell, 2010; Milliken et al., 2014; Hunt et al., 2022). Additional information is needed to differentiate between these possibilities, but the morphological range observed in this work suggests that these ridge fields may record more information and complexity than previously appreciated.

3.6.2 Ridge Orientations and Formative Wind Regime

Both erosional ridge fields (Montgomery et al., 2012; Hugenholtz et al., 2015), and preserved TARs (Balme et al., 2008; Hunt et al., 2022), have been interpreted to develop ridge crests aligned normal to the formative wind direction. Even where depositional versus erosional formation mechanisms for the ridge fields cannot be distinguished, we can reasonably interpret the winds that formed each field to be perpendicular to ridge orientation (Figs. 3.7, 3.9). The bedrock ridges on Aeolis Mons have large variations in orientation across different fields, with no correlation between orientation and either geologic unit or morphology, aside from the bedrock ridges in the MSU. Orientations vary within local areas where bedrock ridges exist on either side of a topographic feature, such as a mound or valley (i.e., Figs. 3.7 and 3.8). Present-day topography is expected to influence the direction of modern wind flow, as the wind is deflected around an obstacle or along the path of a valley. Indeed, Aeolis Mons itself represents a topographic obstacle over and around which the wind must flow. Previous work based on orbital geomorphology (Day and Kocurek, 2016), surface observations (Cornwall et al., 2018; Baker et al., 2018), and numerical modeling (Rafkin et al., 2016; Steele et al., 2017; Viúdez-Moreiras et al., 2019) have shown that the regional-scale winds across Gale crater enter from the north, and are deflected around the

Aeolis Mons topography. Yardangs reflect the dominant north-south orientation (Fig. 3.9A; Day and Kocurek, 2016), but rover-scale measurements show variability at the surface and significant, topography-driven deviations from strictly northerly winds (Cornwall et al., 2018; Baker et al., 2018). The variability of ridge orientations across Aeolis Mons observed in this work could be explained entirely by local-scale topography funneling and deflecting northerly winds as they cross Aeolis Mons. With the net north-to-south wind pattern of previous work in mind, the 180° ambiguity in wind direction interpreted from the bedrock ridges can be resolved and the ridge fields used to create a vector map of wind flow across Gale crater's central mound (Fig. 3.10). This map shows the wind direction at the time of formation of each ridge field, and thus spans ~3 billion years, from the formation of the MSU to relatively recent erosion.

Although the bedrock ridge fields found in the upper stratigraphy of Aeolis Mons exhibit highly variable orientations, the fields specifically within the MSU are, by contrast, very consistent in their orientation, varying by only a few degrees across the entirety of the mapped unit. The MSU is exposed around the base of the mound, placing the ridge fields on this unit upwind and downwind of the mound topography (Figs. 3.3, 3.10). All ridge fields in the MSU are oriented east-west (Figs. 3.7, 3.8), irrespective of where around the base of the mound they are found. This is consistent with the northerly winds interpreted in previous work (Day and Kocurek, 2016; Rafkin et al., 2016; Steele et al., 2017; Cornwall et al., 2018; Baker et al., 2018; Viúdez-Moreiras et al., 2019). The position of the ridge fields in the MSU at the edges of the mound topography means they occur where the fetch of the wind is greater and the influence of deflection around Aeolis Mons would be less. One could make the argument that the position of the MSU ridges and their consistent orientation bounds the length scale over which winds are deflected by Aeolis

Mons, assuming the MSU ridges formed after Aeolis Mons reached its current size. However, the stratigraphic position of the MSU introduces additional complexity, which we discuss below.

3.6.3 Mound Skirting Unit Ridges

The MSU is exposed around the circumference of Aeolis Mons, unconformably overlying the lowermost strata of the mound (Fig. 3.3; Anderson and Bell, 2010; Watkins et al., 2022). Ridge fields were identified in the MSU north and south of the mound (Figs. 3.3, 3.7), all with a strikingly consistent east-west orientation (interpreted to reflect northerly formative winds). Except atop the Greenheugh pediment, the MSU ridges have a consistent morphology (Type 3 and 4) and overall pitted appearance across the entire unit. This pitting and overall rougher texture compared to Type 1 and 2 ridges is interpreted as evidence of age and weathering.

Stratigraphically, the MSU represents late-stage deposition after the formation and erosion of Aeolis Mons (Watkins et al., 2022), creating a morphologically distinct unit unconformably draped along the base of the mound ("skirting" the mound topography). Observations by the Curiosity team have suggested that, at least where visited by the rover, the MSU is dominated by the Stimson formation (Banham et al., 2018; 2021), an aeolian sandstone recording the migration of sinuous and straight-crested paleo-dunes (Banham et al., 2022). If the entirety of the MSU is aeolian sandstone, as seems to be the case along the rover traverse (Banham et al., 2018; 2021; Watkins et al., 2022), the possibility that the ridge fields observed in the MSU are preserved bedforms cannot be ruled out (conversely, if it could be demonstrated that the MSU was mostly not aeolian in origin, it would be unlikely that the ridge fields preserve paleo-bedforms). The bedrock ridges may reflect

crests of paleo-bedforms, or erosionally resistant bounding surfaces. Additionally, none of the bedrock ridges in the MSU were observed to cross-cut resolvable bedding planes.

Although the formation mechanism of these specific ridge fields cannot be confidently determined, their stratigraphic position bounds the timing of northerly winds. In several locations, the MSU and associated ridge fields are overlain by deposits interpreted to have formed during late-stage hydrogeomorphic activity after the formation of Aeolis Mons (Fig. 3.5; Milliken et al., 2014; Palucis et al., 2016). As these deposits erode, the MSU ridges are exhumed from beneath. The superposition of deposits over the MSU ridges demonstrates that these ridge fields are not geologically modern. Furthermore, the east-west orientation of the ridge fields in the MSU suggests that winds across Gale crater at the time were also dominated by northerly sediment transport (southerly transport is also possible, but requires a serendipitous 180° reversal of the wind), rather than very local influences as appears to be the case for more recent ridge formation. Previous work estimated this activity to have occurred at ~3.4 Ga. (Palucis et al., 2016), bounding the dominance of northerly, sand-transporting winds to at least 3.4 Ga.

3.7 Conclusions

The umbrella term “bedrock ridge” includes aeolian features that are both depositional (i.e., paleo-dunes; Day and Catling, 2018; Chojnaki et al., 2020; Runyon et al., 2021; Hunt et al., 2022) and erosional bedforms (Montgomery et al., 2012; Hugenholtz et al., 2015, Silvestro et al., 2021; Favaro et al., 2021; Stack et al., 2022). In this work, 13 of 40 ridge fields in the study area were seen to contain cross-cutting bedding planes. This necessitates that these are post-depositional features created by erosion. Additionally, three ridge fields were observed within fields of yardangs, with ridge orientations transverse to the wind direction interpreted based on the

yardangs. These yardangs have previously been interpreted as geologically young erosional features (Day and Kocurek, 2016). Based on their consistently overall smooth appearance, and relatively low number of retained craters, all Type 1 ridges are also interpreted to be geologically young (Fig. 3.4A). The few craters that superpose Type 1 ridges are crisp in their morphology and ridge crestlines are sharp and well-defined. Combining these observations with evidence for the pervasiveness of aeolian abrasion within Gale crater (Bridges et al., 2013; Day and Kocurek 2016; Dromart et al., 2021), we suggest that Type 1 ridges (Fig. 3.4A) are erosional, and likely relatively modern, features.

The ridges found in the MSU (Types 3 and 4; Fig. 3.4D-E), are interpreted as older than the Type 1 ridges, as several sets of these ridges are in the process of being exhumed from beneath superimposed (younger) bedrock (Fig. 3.5C-F). Additionally, they show evidence of additional weathering and cratering, further implying that they may be relatively old. Given the consistency in morphology, orientation, and wavelength across the ridge fields in the MSU, we propose that the bedrock ridges across the laterally extensive area of the MSU formed under similar wind conditions, during approximately the same time period. Previous work has suggested that the MSU ridges are paleo-bedforms (Anderson and Bell, 2010; Milliken et al., 2014), and our analysis did not find any evidence to the contrary.

Recent work suggests that the MSU sediments were deposited after significant sculpting of Aeolis Mons, above an unconformity (Liu et al., 2021; Watkins et al., 2022), but prior to late-stage hydrogeomorphic activity which eventually (at least partially) buried the MSU ridges (Milliken et al., 2014; Palucis et al., 2016). The unconformity has been dated to between 3.8-3.5 to 3.3-3.1 Ga, though the absolute age of the MSU is presently unknown (Grant et al., 2014; Grotzinger et al., 2015; Watkins et al., 2022). Our proposed timeline for the formation of the bedrock ridges in this

study is as follows: (1) The MSU is deposited, and ridges are formed in the sandstone (via either the lithification of migrating bedforms as suggested by Anderson and Bell (2010) and Milliken et al., (2014), or potentially via erosion of bedrock). This creates what will become the Type 3-4 ridges. (2) Later hydrogeomorphic activity buried these ridges (Milliken et al., 2014; Palucis et al., 2016). (3) Aeolis Mons undergoes additional erosion, forming both yardangs and the Type 1 (erosional) ridges, such as those in Glen Torridon (Stack et al., 2022). This erosion also exhumes the MSU ridges from beneath the younger material.

The development of the Type 2 ridges is less clear, though a few potential explanations for their appearance have emerged as a result of this study. One option is that these bedrock ridges are erosional features, and are older than the Type 1 ridges – meaning they reflect an advanced stage of erosion, a point beyond which the ridge form was stable, and thus has begun to degrade. Another option is that these ridges occur in bedrock with different properties, perhaps softer, more easily eroded, or poorly cemented rock, that has been eroded more quickly than other bedrock. In this scenario, the ridges could be either depositional or erosional, but have been weathered more than their Type 1, 3, or 4 counterparts.

Bedrock ridge orientation is dependent on wind patterns, and local topography influences the orientation of ridges over relatively small areas (Figs. 3.7 and 3.8L-N). The majority of ridge orientations observed in this work can be explained by the effects of local topography still present today. The consistency in orientation of the MSU ridges indicates that though they cover an expansive area and surround a large topographic barrier (Aeolis Mons), the extent of the MSU was exposed to consistent sediment-transporting winds during ridge formation. Their orientation is consistent with current interpretations of a net northerly wind regime in Gale, indicating that this same wind regime has likely been active since the deposition of the MSU. These results expand

our understanding of both the diversity within the class of features known as ‘bedrock ridges,’ as well as the history of wind in Gale crater.

3.8 Figures

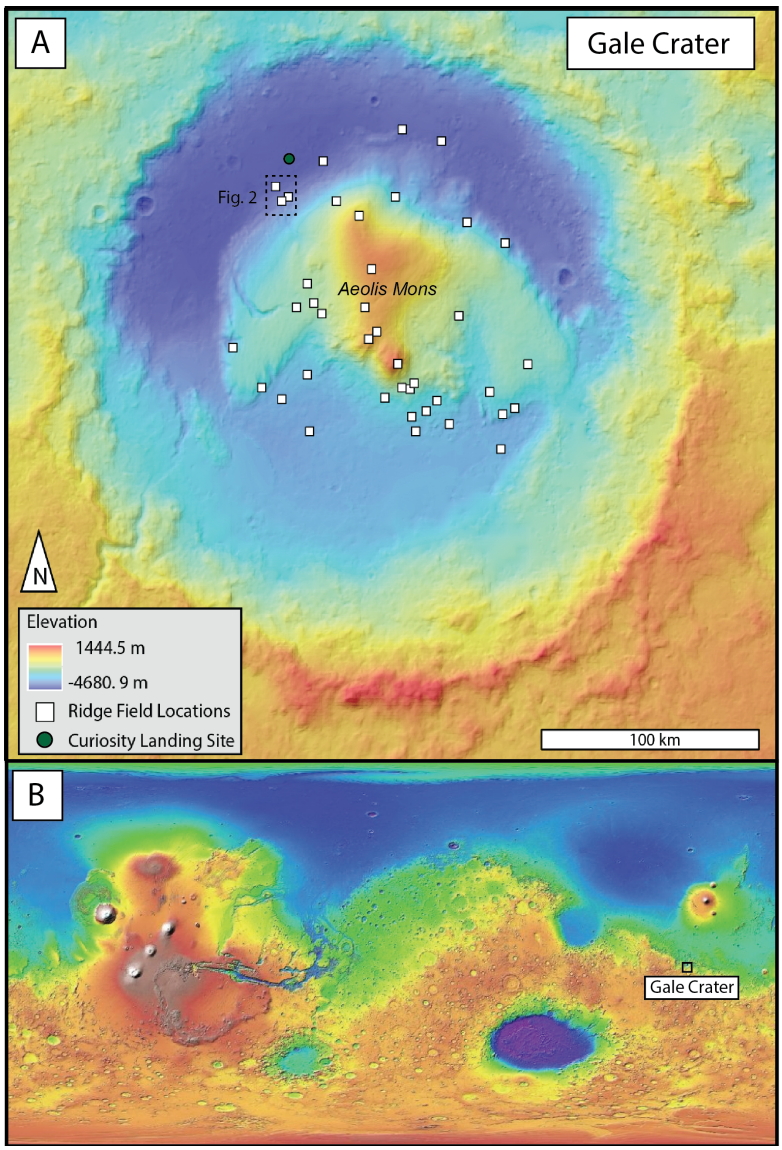

Figure 3.1. Gale Crater and Bedrock Ridge Locations. (A) Bedrock ridge field locations identified in this work (white boxes) overlain on High Resolution Stereo Camera (HRSC; Neukum et al., 2004, Persuad et al., 2021) colorized elevation mosaic. Green point indicates landing site of the Curiosity rover. **(B)** Global topography of Mars from the Mars Orbiter Laser Altimeter (MOLA; Zuber et al., 1992).

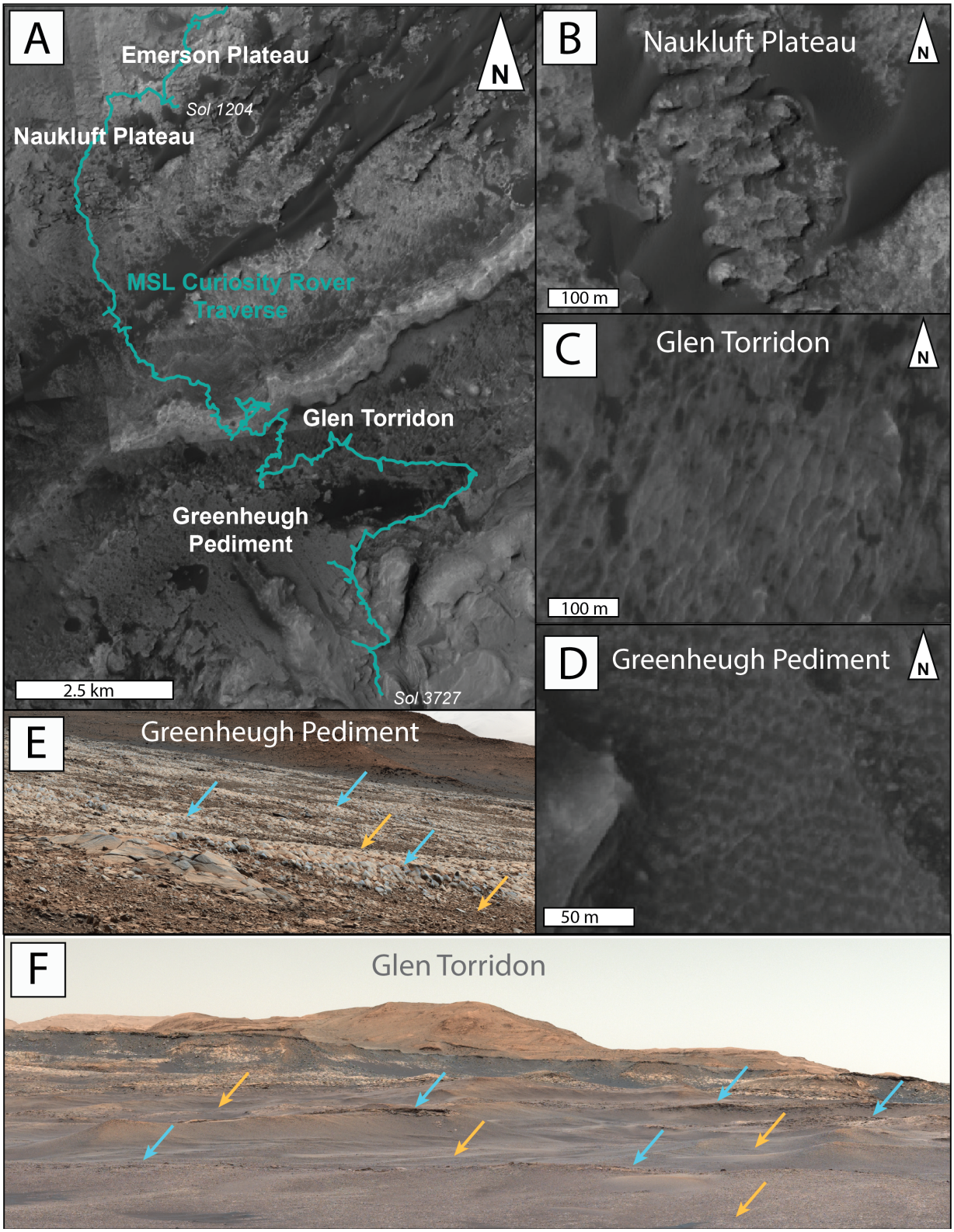

Figure 3.2. Curiosity's traverse and ridge field encounters. (A) Later portion of Curiosity's traverse (path shown in teal), with locations of ridge fields labelled. **(B)** HiRISE view of Naukluft plateau ridges, occurring in the MSU/Siccar point group. Previously interpreted as lithified bedforms (Anderson and Bell, 2010, Milliken et al., 2014). For location information, refer to field

35 in supplemental materials. **(C)** Glen Torridon ridges as seen by HiRISE, identified as erosional features, found eroded into the Murray and Carolyn Shoemaker Formations (Stack et al., 2022). For location information, refer to field 34 in supplemental materials. **(D)** Greenheugh pediment ridges, interpreted as possible preserved bedforms (Banham et al., 2018, 2022; Bryk et al., 2020), as seen by HiRISE. For location information, refer to field 33 in supplemental materials. **(E)** Mastcam mosaic of the 'gatorback' terrain of the Greenheugh Pediment. Blocky material forms the ridge crestlines. Crests indicated with cyan arrows, troughs indicated with orange arrows. Mastcam 100 mosaic is from sol 3415, SeqID mcam01644.4000a. **(F)** Mastcam view of the Glen Torridon ridges. Ridges and interridge spaces are coated with a layer of clasts (Stack et al., 2022). Crests indicated with cyan arrows, troughs indicated with orange arrows Mastcam 34 mosaic is from sol 2365, SeqID mcam12542.0000a. Mastcam mosaics in (E) and (F) were processed by the Mastcam team at Malin Space Science Systems, individual frames available on the PDS are listed in supplementary table 3. Image credit NASA/JPL-Caltech/MSSS.

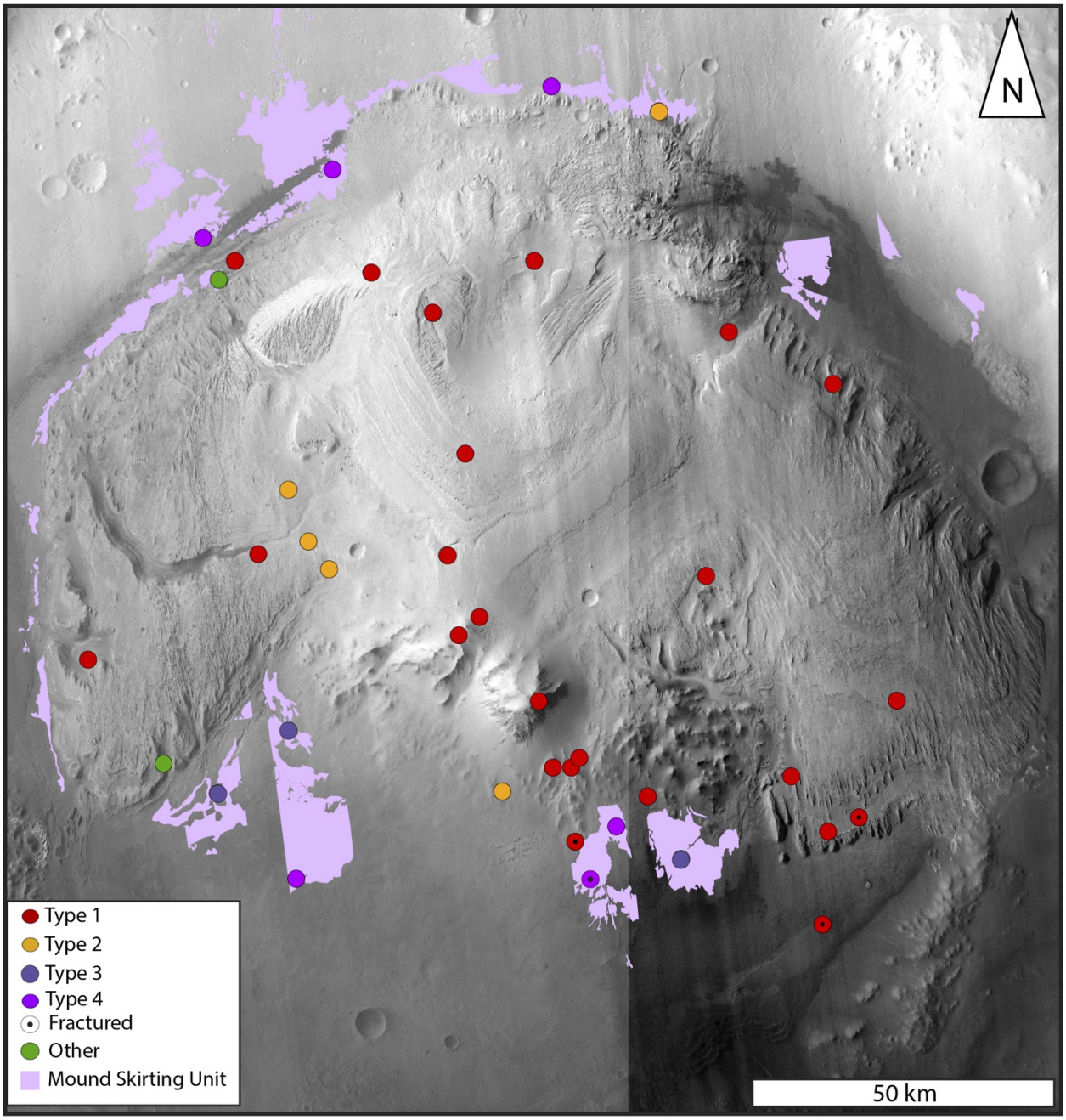

Figure 3.3. Ridge Fields and the Mound Skirting Unit. Context Camera (CTX; Malin et al., 2007) mosaic of the central portion of Gale crater. Ridge field locations are color-coded by morphology; descriptions of each type can be found in section 4.2. Fractured ridge fields are identified by a black point within a location circle. The extent of the MSU as mapped on available HiRISE images is shown in lilac. For HiRISE image coverage, see supplemental materials Fig. 3.1.

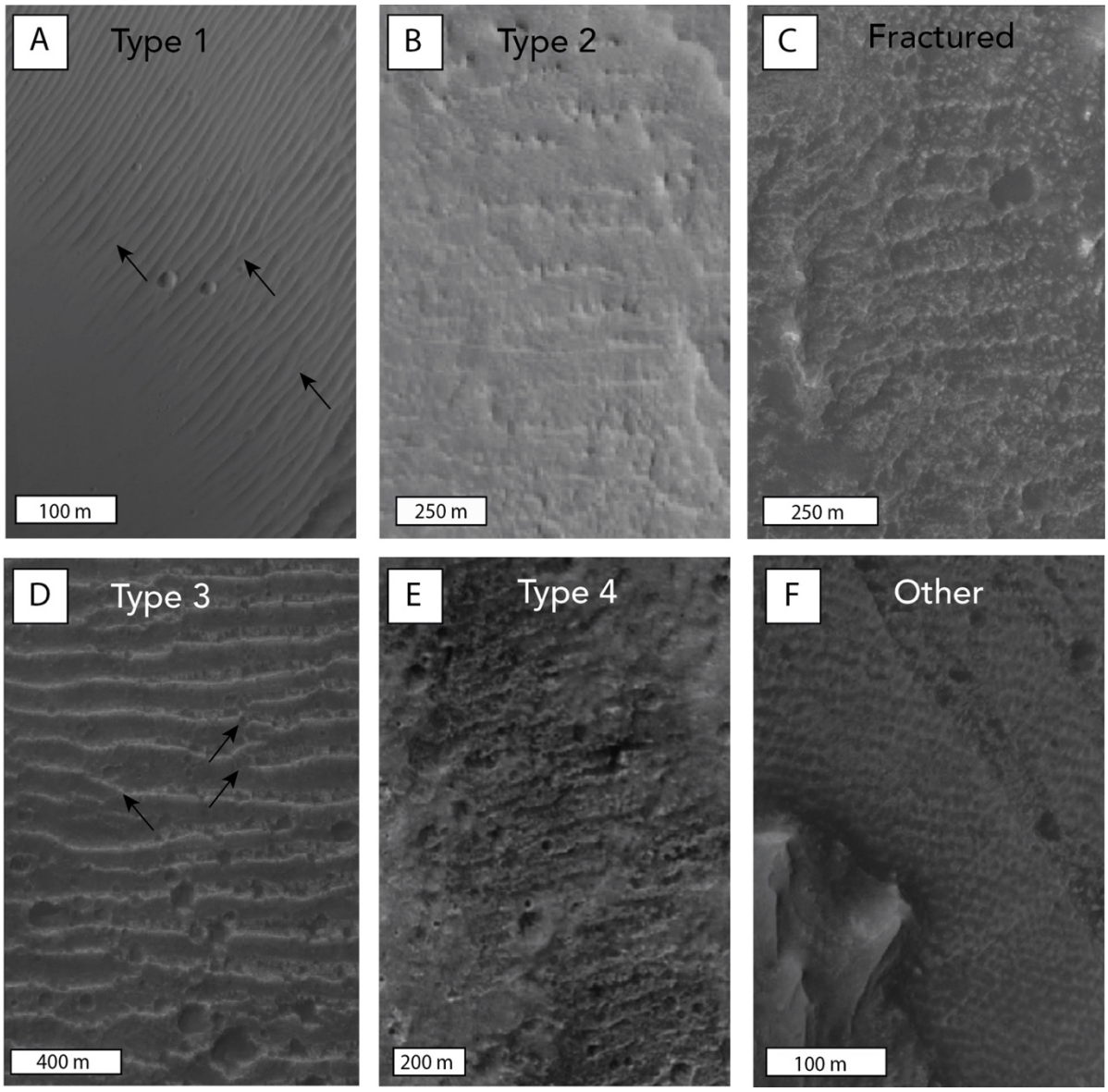

Figure 3.4. Bedrock ridge morphologies. For descriptions of each bedrock ridge type, see section 4.2. North is up in all images. Examples of Y-junctions are indicated by black arrows. The locations of each panel can be found in the supplemental materials (Supplemental Fig. 3.S1 and Table 3.S1). **(A)** Type 1 ridges seen near the highest point on Aeolis Mons. For location information, refer to field 17 in supplemental material. **(B)** Type 2 ridges identified on the western flank of Aeolis Mons. For location information, refer to field 19 in supplemental materials. **(C)** Ridges in fractured bedrock seen to the south of Aeolis Mons. For location information, refer to field 10 in supplemental materials. **(D)** Type 3 ridges found in the MSU, south of Aeolis Mons. For location information, refer to field 23 in supplemental materials. **(E)** Type 4 ridges identified in the MSU, south of Aeolis Mons. For location information, refer to field 22 in supplemental materials. **(F)** Ridges at the Greenheugh pediment, an example of a unique morphology not grouped into one of the four types used in this study. Both primary and secondary ridge crests are seen, with a similar overall appearance to networked TARs. For location information, refer to field 33 in supplemental materials.

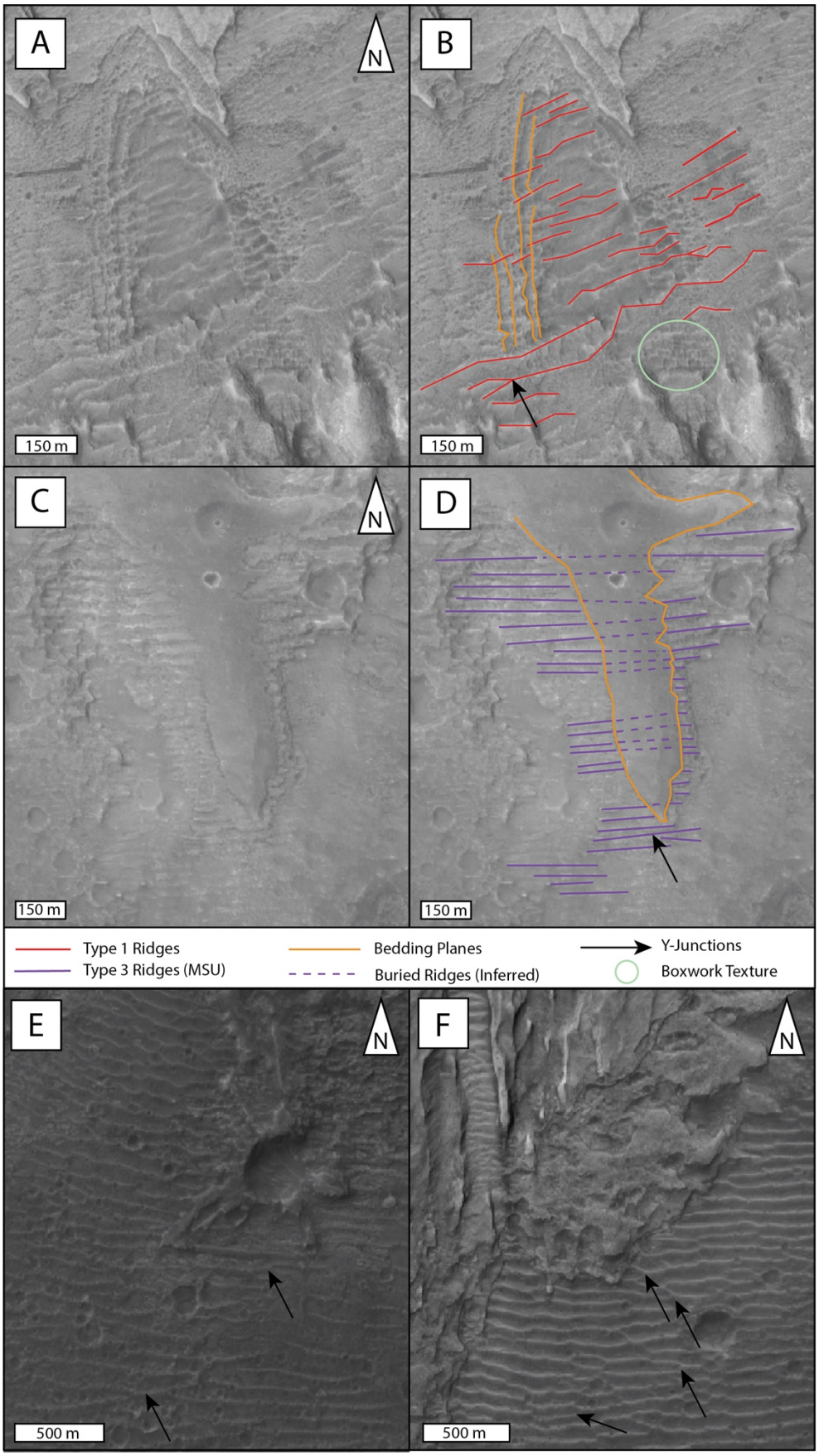
A
N
150 m
B
150 m
C
N
150 m
D
150 m
Type 1 Ridges
Type 3 Ridges (MSU)
Bedding Planes
Buried Ridges (Inferred)
Y-Junctions
Boxwork Texture
E
N
500 m
F
N
500 m

Figure 3.5. Bedrock ridges and bedding planes. Two examples of bedrock ridges interacting with the stratigraphy of Aeolis Mons. Y-junctions are indicated with black arrows. **(A-B)** Type 1 ridges (red), crosscutting bedding planes (orange), in the southern portion of the study area. A fracture pattern, previously referred to as a boxwork texture, is circled in green. For location information, refer to field 2 in supplemental materials. **(C-D)** Type 3 ridges (purple) in the MSU being exhumed from beneath superposed bedrock (outlined in orange). Ridges are outlined in solid purple, with the buried sections marked with dashed lines (inferred positions). Where exposed, the layer beneath the ridged material does not contain ridges. For location information, refer to field 8 in supplemental materials. **(E)** Ridges in the MSU, south of Aeolis Mons, with overprinted crater. For location information, refer to field 23 in supplemental materials. **(F)** MSU ridges exposed beneath later fluvial deposits south of Aeolis Mons. For location information, refer to field 23 in supplemental materials. Images in (E) and (F) show portions of a ridge field previously identified by Milliken et al., (2014).

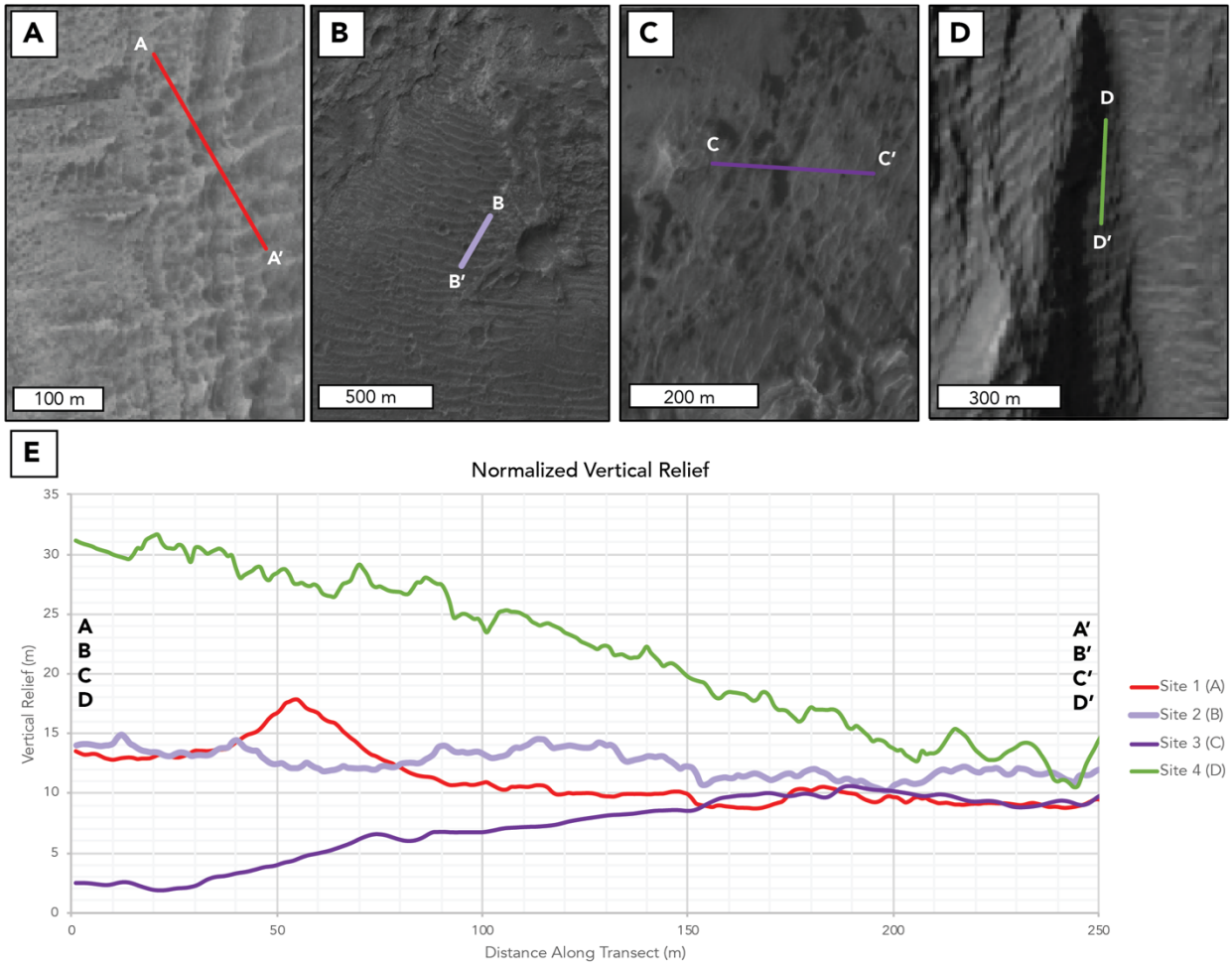

Figure 3.6. Ridge Field Topography. North is up in all images. **(A)** Site 1 – Type 1 ridges on the southern portion of Aeolis Mons. Transect taken from an area where the bedrock ridges are seen crosscutting bedding planes (this is a portion of Fig. 4A-B). For location information, refer to field

2 in supplemental materials. **(B)** Site 2 – Type 3 ridges in the MSU (this is a portion of the field shown in Fig. 5E.) For location information, refer to field 23 in supplemental materials. **(C)** Site 3 – Type 1 ridges at Glen Torridon. For location information, refer to field 34 in supplemental materials. **(D)** Site 4 – Bedrock ridges on a slope in a valley or canyon on the southern flank of Aeolis Mons. For location information, refer to field 27 in supplemental materials. **(E)** Normalized vertical relief of the transects in (A-D), with no vertical exaggeration. The individual bedrock ridges have a few meters of relief and are largely below the resolution limits of the DTMs. Actual elevation values of each transect ranged from approximately -4150 m to -2900 m when extracted from HiRISE DTMs (at 1 m/px). These values are shown without vertical exaggeration but were translated to lie within a similar elevation range (>0 m) to simplify display and comparison.

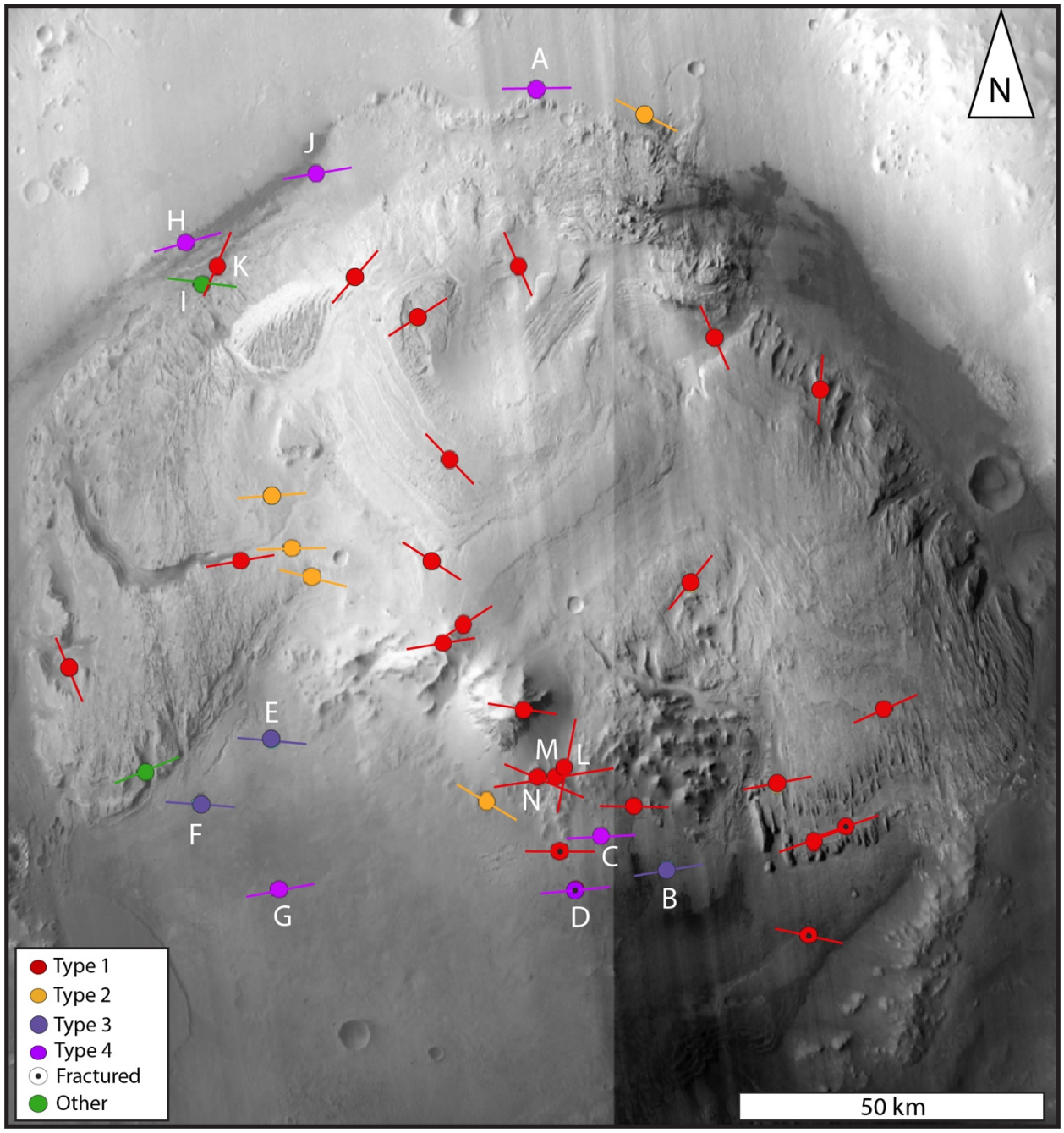

Figure 3.7. Average Ridge Orientations. Lines represent the average orientation measured for each field. Orientations were measured along the crests of each ridge in a given field. See Figure 8 for additional detail on ridge orientation variation for fields at points A-N.

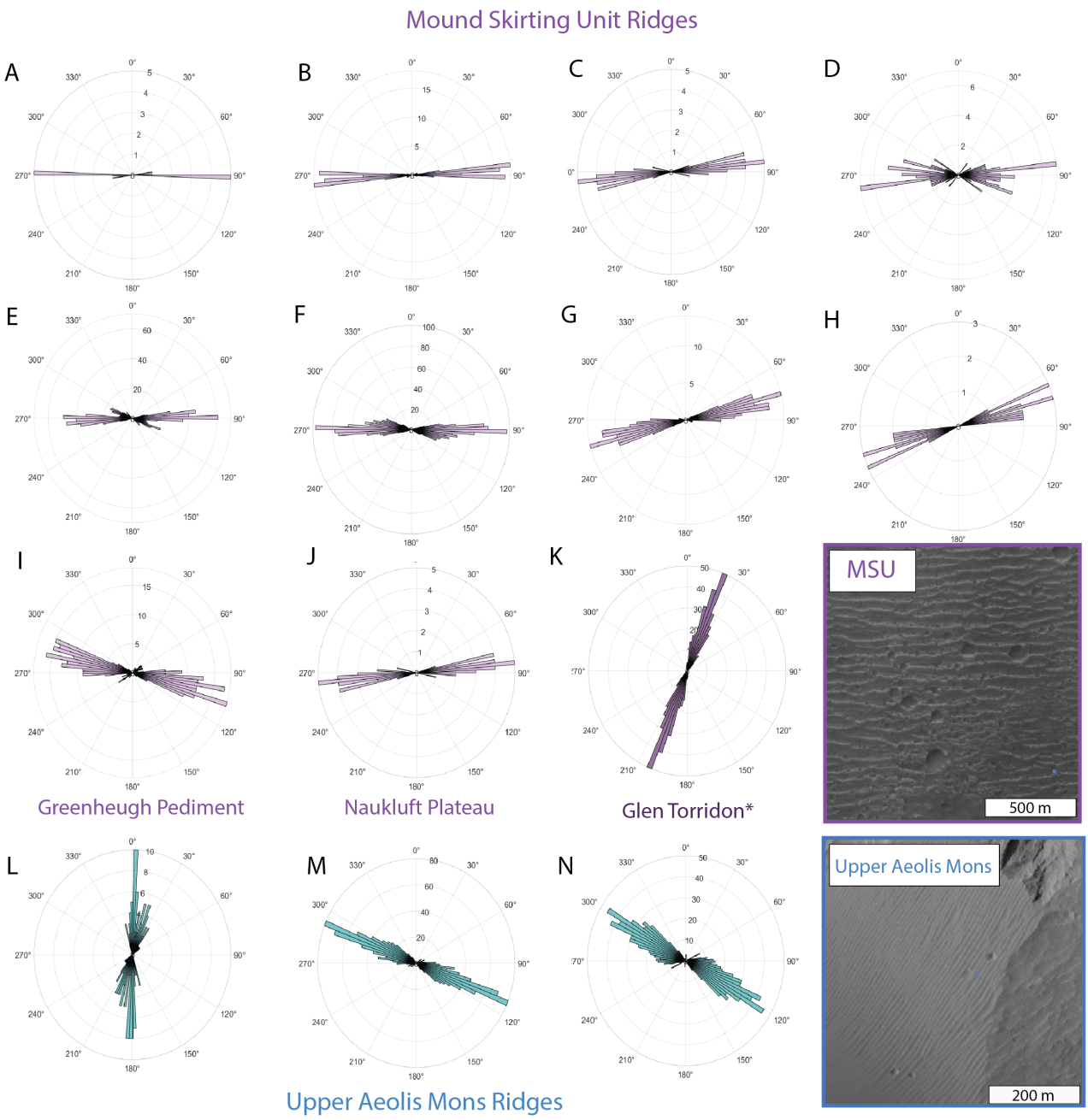

Figure 3.8. Polar Histograms of Bedrock Ridge Orientations. (A-N) correspond to fields labelled in Figure 7. The distribution of ridge orientations in each field is shown in these polar histograms, which have a bin size of 3°. **(A-J)** Light purple: MSU ridge fields, ridge Types 3 and 4. Ten MSU ridge fields were identified, with an overall consistent east-west orientation (average 87°± 8°). A type example of these bedrock ridges is shown in the panel labelled MSU. North is up in this image. For location information, refer to field 23 in supplemental materials. **(I)** Ridge orientations of the primary (larger) crestslines at the Greenheugh pediment, one site explored by Curiosity. **(J)** Bedrock ridge orientation at the Naukluft Plateau, another location traversed by Curiosity. **(K)** Dark purple: Glen Torridon ridge field explored by Curiosity. *These bedrock ridges are not part of the MSU. **(L-M)** Blue: Type 1 ridges near the highest point of the central

mound (Upper Aeolis Mons). A type example of these bedrock ridges is shown in the 'Upper Aeolis Mons' panel. The orientation of these ridge fields varies widely over a relatively small area (~11 km^2) because of local topography separating the fields. North is up in this image. For location information, refer to field 17 in supplemental materials.

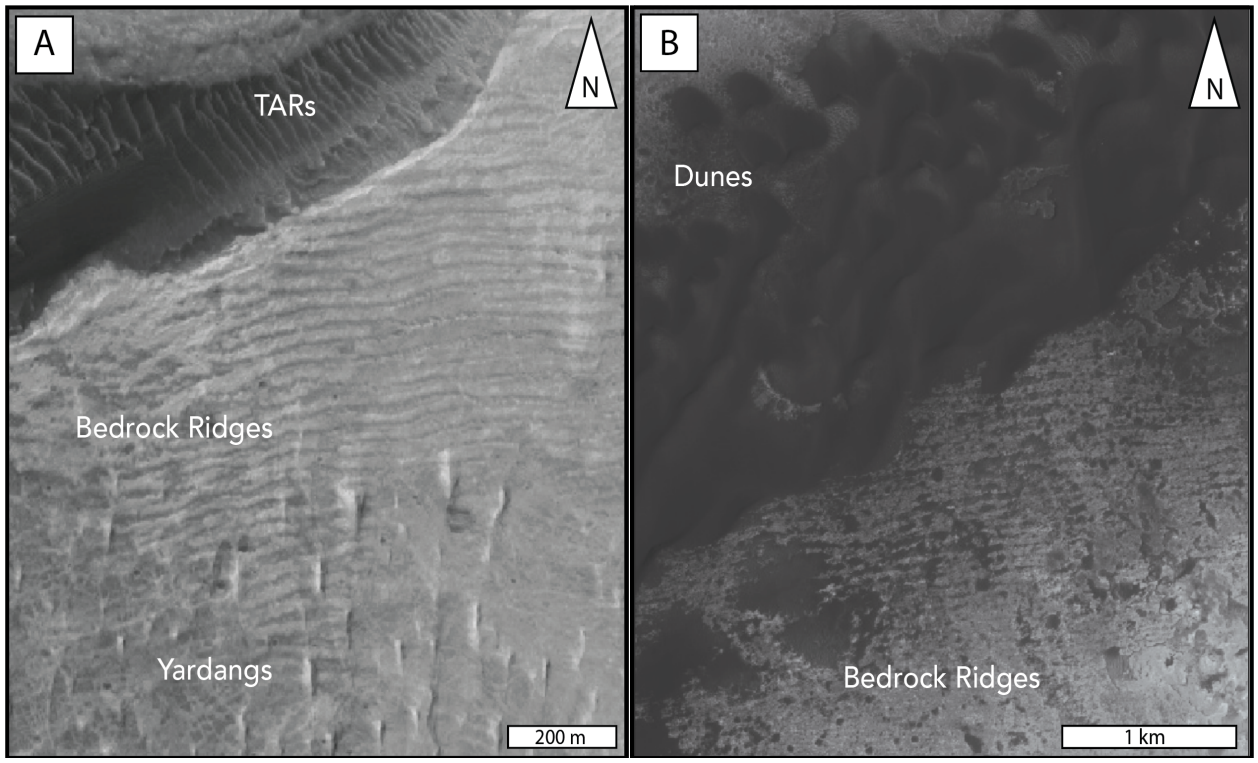

Figure 3.9. Bedrock ridges and other aeolian surface features. (A) Type 1 ridges on Aeolis Mons, with yardangs and TARs nearby. The TARs occur in a topographic depression, while the bedrock ridges and yardangs are on a topographically higher area. The blunted ends of the yardangs indicate that the formative winds originated from the north. The bedrock ridges are oriented transverse to the yardangs. For location information, refer to field 20 in supplementary materials. **(B)** Dark dunes migrating across Type 4 ridges in the MSU. The net dune migration direction is toward the southwest, suggesting formative winds from the north-northeast (Hobbs et al., 2010; Silvestro et al., 2013). The bedrock ridges are oriented oblique to the dune crests. For location information, refer to field 37 in supplemental materials.

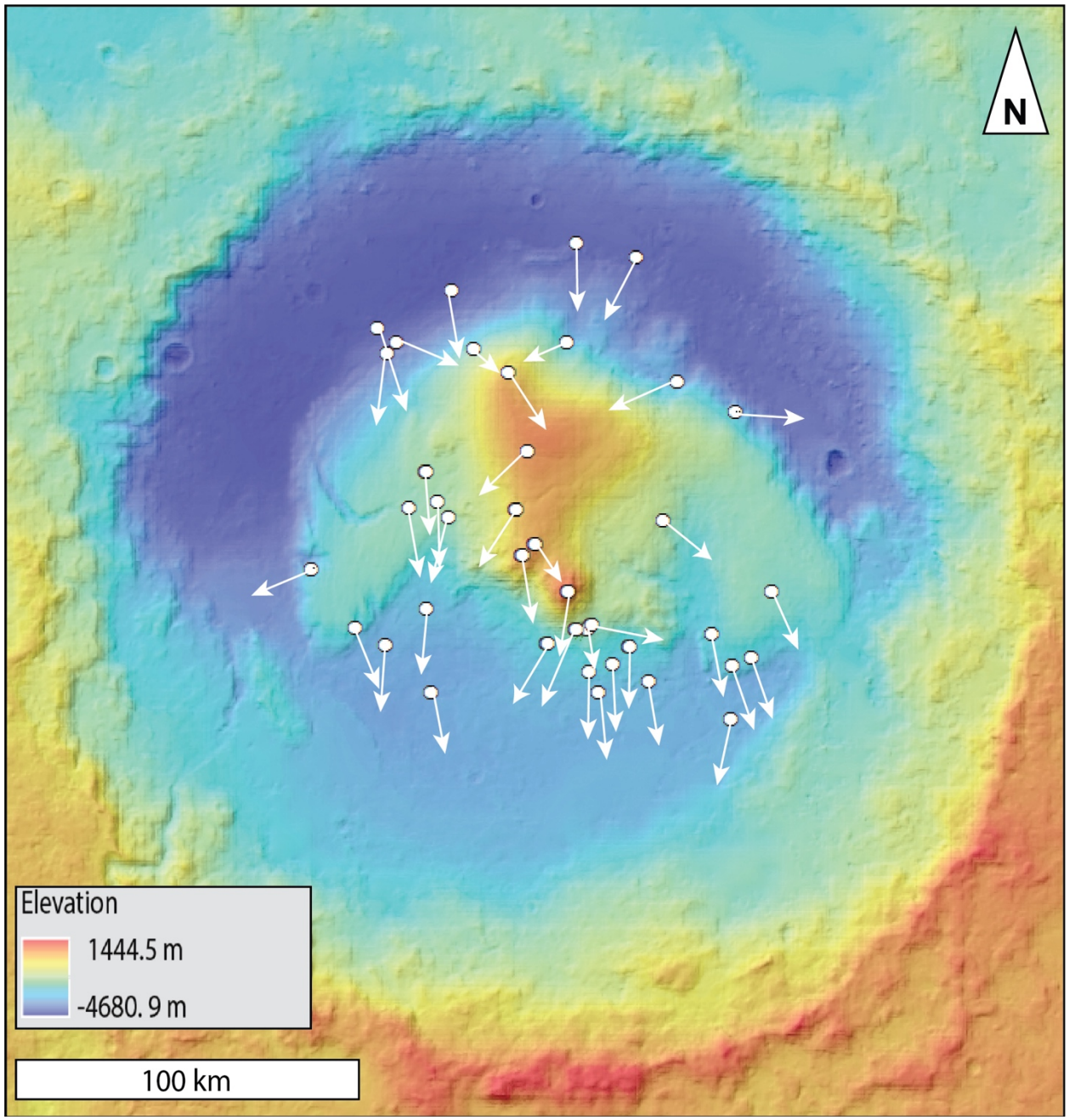

Figure 3.10. Wind vector map of Aeolis Mons. Interpreted formative wind direction at each ridge field is indicated with a white arrow. Arrow length does not correspond to an interpreted strength. Wind direction is expected to be transverse to the average orientation of the bedrock ridges in each field, and the 180° ambiguity in the interpreted direction has been resolved by assuming winds originate in the north (after Day and Kocureck, 2016; Rafkin et al., 2016; Steele et al., 2017; Cornwall et al., 2018; Baker et al., 2018; Viúdez-Moreiras et al., 2019). HRSC mosaic used for background topography.

3.10 Appendix (Supplemental Materials)

The figures and tables below provide additional information and details on the results and interpretations presented in the main text. Figure and Table 1 identify the ridge field locations in order to aid in future investigations of these sites. Figure 2 provides an additional example of ridge morphologic variability. Tables 2 and 3 provide image IDs used in measurements (DTMs) and figure creation (Mastcam mosaics).

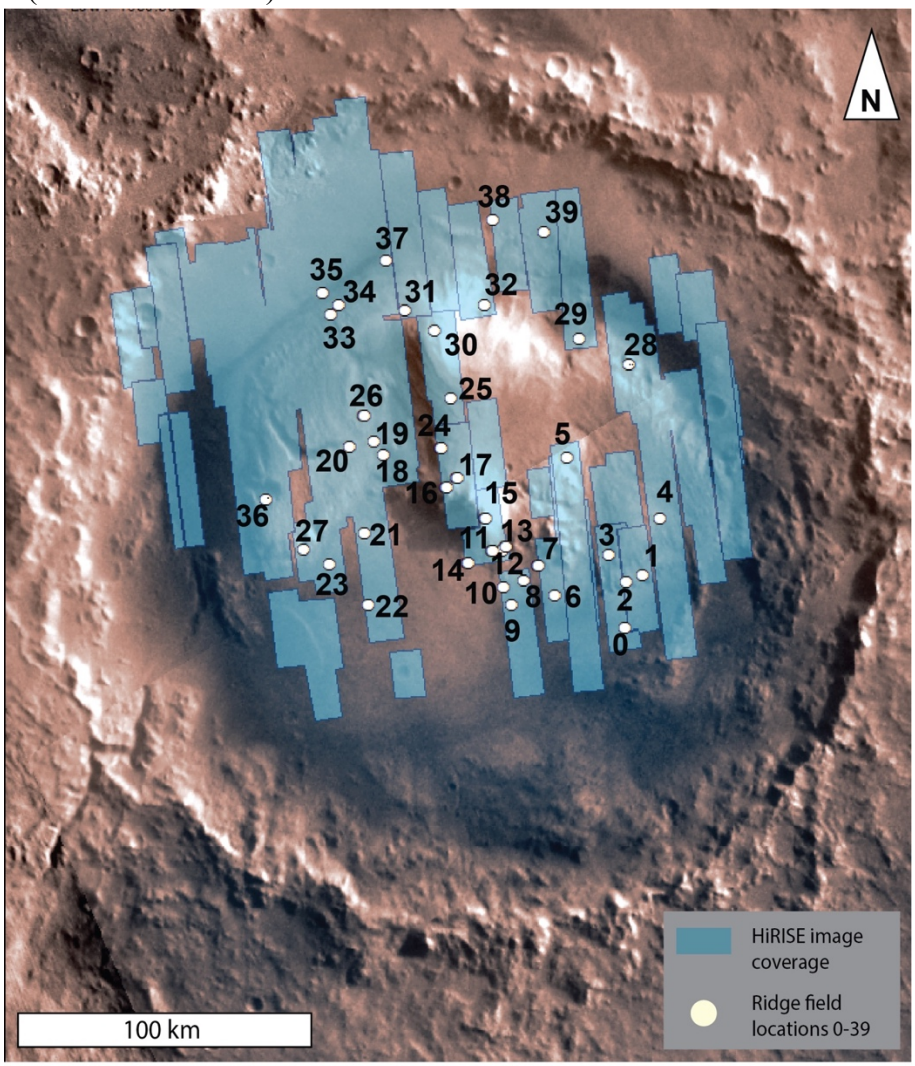

Supplementary Figure 3.S1. HiRISE footprints and ridge field locations. Surface area covered by the HiRISE images used for this study is shown in blue. Ridge field locations are shown as white circles. Background image is a Viking mosaic. Field numbers correspond to supplemental materials Table 1.

Supplementary Table 3.S1. Bedrock ridge field locations. Latitude and longitude values (in meters) from the Mars Equirectangular projection in ArcGIS. Field positions identified based on the HiRISE global mosaic available from ArcGIS online. Field numbers correspond to supplemental materials Figure 1.

Ridge Field	Latitude	Longitude
0	-338879.3741	8197210.345
1	-329359.0505	8200454.307
2	-330628.427	8197668.731
3	-325691.9629	8194389.508
4	-318957.2154	8203804.05
5	-307850.1712	8186808.51
6	-333061.3986	8184587.101
7	-327666.5485	8181554.702
8	-330170.041	8178839.646
9	-334824.4215	8176547.717
10	-331509.9384	8175172.559
11	-324951.4933	8174819.954
12	-324069.9818	8175525.163
13	-324916.2328	8173197.973
14	-327067.1207	8168684.634
15	-319027.7364	8171928.597
16	-313174.5004	8164735.463
17	-311517.2588	8166639.528
18	-307289.5299	8153229.976
19	-304821.2979	8151396.432
20	-305914.3721	8146883.093
21	-321640.5363	8149633.409
22	-334827.9475	8150303.358
23	-327246.9491	8143321.787
24	-305998.9972	8163709.384
25	-296972.32	8165401.886
26	-300188.0737	8149605.201
27	-324560.1022	8138491.104
28	-290879.3129	8198180.007
29	-286140.3073	8188814.83
30	-284504.2221	8162468.216
31	-280921.7596	8156973.226
32	-279906.2584	8171528.743
33	-281514.1353	8143433.21
34	-279821.6333	8144871.837
35	-277790.6309	8141994.584
36	-315364.1748	8131585.696
37	-271697.6238	8153531.805
38	-264250.6151	8173051.995
39	-266620.1179	8182530.006

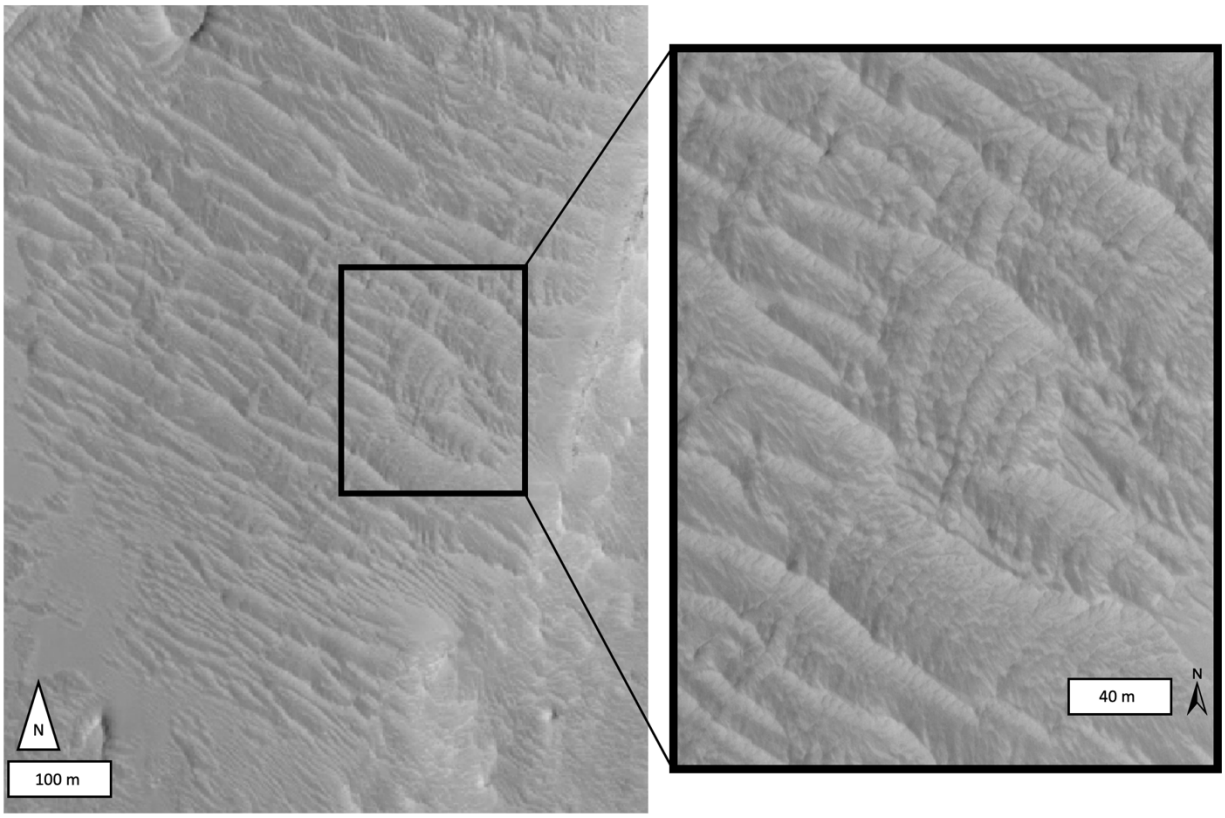

Supplementary Figure 3.S2. Type 1 ridges with crest-normal lineations. HiRISE image of ridges on Aeolis Mons with inter-ridge spaces exhibiting a scalloped texture due to crest-perpendicular lineations. These lineations are interpreted as bedding planes. Four fields were identified with this morphology, which were classified as Type 1 ridges given the sharp crests of the ridges. Ridges shown here from field 30 (see supplementary Fig. 3.S1 and Table 3.S1).

Supplementary Table 3.S2. HiRISE Digital Terrain Models. DTMs generated by the University of Arizona using HiRISE stereo pairs, which are available online. Transect labels correspond to Figure 6. DTM post-spacing is ~1 m/px.

Transect	DTM
A-A’	DTEEC_014186_1745_020410_1745_A01
B-B’	DTEEC_063319_1745_052242_1745_A01
C-C’	DTEEC_040770_1755_039280_1755_U01
D-D’	DTEEC_063319_1745_052242_1745_A01

Supplementary Table 3.S3. Mastcam frames included in figures 2E and 2F. Mosaics processed by the Mastcam team at Malin Space Science Systems, individual frames are available on the PDS.

Mosaic sol	Frames
Sol 3514 (Fig. 2E)	3415MR1016440001600167C00, 3415MR1016440011600168C00, 3415MR1016440021600169C00, 3415MR1016440031600170C00, 3415MR1016440041600171C00, 3415MR1016440051600172C00, 3415MR1016440061600173C00, 3415MR1016440071600174C00, 3415MR1016440081600175C00, 3415MR1016440091600176C00, 3415MR1016440101600177C00, 3415MR1016440111600178C00, 3415MR1016440121600179C00, 3415MR1016440131600180C00, 3415MR1016440141600181C00,
Sol 2365 (Fig. 2F)	2365ML012542000900453C00, 2365ML012542010900454C00, 2365ML012542020900455C00, 2365ML012542030900456C00, 2365ML012542040900457C00, 2365ML012542050900458C00, 2365ML012542060900459C00, 2365ML012542070900460C00, 2365ML012542080900461C00

3.10 References

Anderson, R., & Bell III, J. (2010). Geologic mapping and characterization of Gale Crater and implications for its potential as a Mars Science Laboratory landing site. *Mars the International Journal of Mars Science and Exploration*, *5*, 76–128. https://doi.org/10.1555/mars.2010.0004

Baker, M. M., Lapotre, M. G. A., Minitti, M. E., Newman, C. E., Sullivan, R., Weitz, C. M., Rubin, D. M., Vasavada, A. R., Bridges, N. T., & Lewis, K. W. (2018). The Bagnold Dunes in Southern Summer: Active Sediment Transport on Mars Observed by the Curiosity Rover. *Geophysical Research Letters*, *45*(17), 8853–8863. https://doi.org/10.1029/2018GL079040

Balme, M., Berman, D. C., Bourke, M. C., & Zimbelman, J. R. (2008). Transverse Aeolian Ridges (TARs) on Mars. *Geomorphology*, *101*(4), 703–720. https://doi.org/10.1016/j.geomorph.2008.03.011

Banham, S.G., Gupta, S., Rubin, D.M., Watkins, J.A., Sumner, S.Y., et al., "Ancient Martian aeolian processes and palaeomorphology reconstructed from the Stimson formation on the lower slope of Aeolis Mons, Gale crater, Mars," Sedimentology, 65(4), 2018.

Banham, S. G., Gupta, S., Rubin, D. M., Edgett, K. S., Barnes, R., Van Beek, J., Watkins, J. A., Edgar, L. A., Fedo, C. M., Williams, R. M., Stack, K. M., Grotzinger, J. P., Lewis, K., Ewing, R. C., Day, M., & Vasavada, A. R. (2021). A Rock Record of Complex Aeolian Bedforms in a Hesperian Desert Landscape: The Stimson Formation as Exposed in the Murray Buttes, Gale Crater, Mars. *Journal of Geophysical Research: Planets*, *126*(4), e2020JE006554. https://doi.org/10.1029/2020JE006554

Banham, S. G., Gupta, S., Rubin, D. M., Bedford, C. C., Edgar, L. A., Bryk, A. B., Dietrich, W. E., Fedo, C. M., Williams, R. M., Caravaca, G., Barnes, R., Paar, G., Ortner, T., &

Vasavada, A. R. (2022). Evidence for Fluctuating Wind in Shaping an Ancient Martian Dune Field: The Stimson Formation at the Greenheugh Pediment, Gale Crater. *Journal of Geophysical Research: Planets*, *127*(9), e2021JE007023. https://doi.org/10.1029/2021JE007023

Berman, D. C., Balme, M. R., Rafkin, S. C. R., & Zimbelman, J. R. (2011). Transverse Aeolian Ridges (TARs) on Mars II: Distributions, orientations, and ages. *Icarus*, *213*(1), 116–130. https://doi.org/10.1016/j.icarus.2011.02.014

Bibring, J.-P., Langevin, Y., Mustard, J. F., Poulet, F., Arvidson, R., Gendrin, A., Gondet, B., Mangold, N., Pinet, P., Forget, F., Berthé, M., Bibring, J.-P., Gendrin, A., Gomez, C., Gondet, B., Jouglet, D., Poulet, F., Soufflot, A., Vincendon, M., … Neukum, G. (2006). Global Mineralogical and Aqueous Mars History Derived from OMEGA/Mars Express Data. *Science*, *312*(5772), 400–404. https://doi.org/10.1126/science.1122659

Blackwelder, E., 1934, Yardangs: Bulletin of the Geological Society of America, v. 45, p. 159–166.

Bridges, N. T., Banks, M. E., Beyer, R. A., Chuang, F. C., Noe Dobrea, E. Z., Herkenhoff, K. E., Keszthelyi, L. P., Fishbaugh, K. E., McEwen, A. S., Michaels, T. I., Thomson, B. J., & Wray, J. J. (2010). Aeolian bedforms, yardangs, and indurated surfaces in the Tharsis Montes as seen by the HiRISE Camera: Evidence for dust aggregates. *Icarus*, *205*(1), 165–182. https://doi.org/10.1016/j.icarus.2009.05.017

Bridges, N. T., Calef, F. J., Hallet, B., Herkenhoff, K. E., Lanza, N. L., Le Mouélic, S., ... & Yingst, R. A. (2014). The rock abrasion record at Gale crater: Mars Science Laboratory results from Bradbury landing to Rocknest. *Journal of Geophysical Research: Planets*, *119*(6), 1374-1389.

Bridges, N. T., & Ehlmann, B. L. (2018). The Mars Science Laboratory (MSL) Bagnold Dunes campaign, phase I: overview and introduction to the special issue. *Journal of Geophysical Research: Planets*, *123*(1), 3-19.

Bryk, A. B., Dietrich, W. E., Fox, V. K., Bennett, K. A., Banham, S. G., Lamb, M. P., Grotzinger, J. P., Vasavada, A. R., Stack, K. M., Arvidson, R., Fedo, C. M., Gupta, S., Wiens, R. C., Williams, R. M. E., Turner, M. L., Lewis, K. W., Rubin, D. M., Rapin, W. N., Deit, L. L., … Bedford, C. C. (2020). *THE STRATIGRAPHY OF CENTRAL AND WESTERN BUTTE AND THE GREENHEUGH PEDIMENT*.

Chojnacki, M., Burr, D. M., Moersch, J. E., & Michaels, T. I. (2011). Orbital observations of contemporary dune activity in Endeavor crater, Meridiani Planum, Mars. *Journal of Geophysical Research: Planets*, *116*(E7). https://doi.org/10.1029/2010JE003675

Chojnacki, M., Fenton, L. K., Weintraub, A. R., Edgar, L. A., Jodhpurkar, M. J., & Edwards, C. S. (2020). Ancient Martian Aeolian Sand Dune Deposits Recorded in the Stratigraphy of Valles Marineris and Implications for Past Climates. *Journal of Geophysical Research: Planets*, *125*(9), e2020JE006510. https://doi.org/10.1029/2020JE006510

Cornwall, C., Jackson, D. W. T., Bourke, M. C., Beyers, M., & Cooper, J. A. G. (2018). Seasonal Variations in Airflow Over the Namib Dune, Gale Crater, Mars: Implications for Dune Dynamics. *Geophysical Research Letters*, *45*(18), 9498–9507. https://doi.org/10.1029/2018GL079598

Day, M. D., & Catling, D. C. (2018). Dune Casts Preserved by Partial Burial: The First Identification of Ghost Dune Pits on Mars. *Journal of Geophysical Research: Planets*, *123*(6), 1431–1448. https://doi.org/10.1029/2018JE005613

Day, M., & Kocurek, G. (2016). Observations of an aeolian landscape: From surface to orbit in Gale Crater. *Icarus*, *280*, 37–71. https://doi.org/10.1016/j.icarus.2015.09.042

Day, M., Anderson, W., Kocurek, G., & Mohrig, D. (2016). Carving intracrater layered deposits with wind on Mars. *Geophysical Research Letters*, *43*(6), 2473-2479.

Day, M., & Kocurek, G. (2018). Pattern similarity across planetary dune fields. *Geology*, *46*(11), 999–1002. https://doi.org/10.1130/G45547.1

de Silva, S. L., & Bailey, J. E. (2017). Some unique surface patterns on ignimbrites on Earth: A "bird's eye" view as a guide for planetary mappers. *Journal of Volcanology and Geothermal Research*, *342*, 47–60. https://doi.org/10.1016/j.jvolgeores.2017.06.009

de Silva, S. L., Bailey, J. E., Mandt, K. E., & Viramonte, J. M. (2010). Yardangs in terrestrial ignimbrites: Synergistic remote and field observations on Earth with applications to Mars. *Planetary and Space Science*, *58*(4), 459–471. https://doi.org/10.1016/j.pss.2009.10.002

de Silva, S.L., Spagnuolo, M.G., Bridges, N.T., and Zimbelman, J.R., 2013, Gravel-mantled megaripples of the Argentinean Puna: A model for their origin and growth with implications for Mars: GEOLOGICAL SOCIETY OF AMERICA BULLETIN, v. 125, p. 1912–1929, doi:10.1130/b30916.1.

Dromart, G., Le Deit, L., Rapin, W., Gasnault, O., Le Mouélic, S., Quantin-Nataf, C., ... & Wiens, R. C. (2021). Deposition and erosion of a Light-Toned Yardang-forming unit of Mt Sharp, Gale crater, Mars. *Earth and Planetary Science Letters*, *554*, 116681.

Edgett, K. S., and Malin, M. C. (2000), New views of Mars eolian activity, materials, and surface properties: Three vignettes from the Mars Global Surveyor Mars Orbiter Camera, *J. Geophys. Res.*, 105(E1), 1623– 1650, doi:10.1029/1999JE001152.

Edgett, K. S., & Sarkar, R. (2021). Recognition of Sedimentary Rock Occurrences in Satellite and Aerial Images of Other Worlds—Insights from Mars. *Remote Sensing*, *13*(21), Article 21. https://doi.org/10.3390/rs13214296

Ewing, R. C., Hayes, A. G., & Lucas, A. (2015). Sand dune patterns on Titan controlled by long-term climate cycles. *Nature Geoscience*, *8*(1), Article 1. https://doi.org/10.1038/ngeo2323

Ewing, R. C., Lapotre, M. G. A., Lewis, K. W., Day, M., Stein, N., Rubin, D. M., Sullivan, R., Banham, S., Lamb, M. P., Bridges, N. T., Gupta, S., & Fischer, W. W. (2017). Sedimentary processes of the Bagnold Dunes: Implications for the eolian rock record of Mars. *Journal of Geophysical Research: Planets*, *122*(12), 2544–2573. https://doi.org/10.1002/2017JE005324

Favaro, E. A., Balme, M. R., Davis, J. M., Grindrod, P. M., Fawdon, P., Barrett, A. M., & Lewis, S. R. (2021). The aeolian environment of the landing site for the ExoMars Rosalind Franklin Rover in Oxia Planum, Mars. *Journal of Geophysical Research: Planets*, 126, e2020JE006723. https://doi.org/10.1029/2020JE006723

Fenton, L.K., 2020, Updating the global inventory of dune fields on mars and identification of many small dune fields: Icarus, p. 114018.

Fraeman, A. A., Ehlmann, B. L., Arvidson, R. E., Edwards, C. S., Grotzinger, J. P., Milliken, R. E., Quinn, D. P., & Rice, M. S. (2016). The stratigraphy and evolution of lower Mount Sharp from spectral, morphological, and thermophysical orbital data sets. *Journal of Geophysical Research: Planets*, *121*(9), 1713–1736. https://doi.org/10.1002/2016JE005095

Geissler, P. E. (2014). The birth and death of transverse aeolian ridges on Mars. *Journal of Geophysical Research: Planets*, *119*(12), 2583–2599. https://doi.org/10.1002/2014JE004633

Grant, J. A., Wilson, S. A., Mangold, N., Calef III, F., & Grotzinger, J. P. (2014). The timing of alluvial activity in Gale crater, Mars. *Geophysical Research Letters*, *41*(4), 1142–1149. https://doi.org/10.1002/2013GL058909

Greeley, R., Kuzmin, R. O., & Haberle, R. M. (2001). Aeolian Processes and Their Effects on Understanding the Chronology of Mars. In R. Kallenbach, J. Geiss, & W. K. Hartmann (Eds.), *Chronology and Evolution of Mars* (Vol. 12, pp. 393–404). Springer Netherlands. https://doi.org/10.1007/978-94-017-1035-0_14

Grotzinger, J. P., Gupta, S., Malin, M. C., Rubin, D. M., Schieber, J., Siebach, K., Sumner, D. Y., Stack, K. M., Vasavada, A. R., Arvidson, R. E., Calef, F., Edgar, L., Fischer, W. F., Grant, J. A., Griffes, J., Kah, L. C., Lamb, M. P., Lewis, K. W., Mangold, N., … Wilson, S. A. (2015). Deposition, exhumation, and paleoclimate of an ancient lake deposit, Gale crater, Mars. *Science*, *350*(6257), aac7575. https://doi.org/10.1126/science.aac7575

Greeley, R. et al., 2008, Columbia Hills, Mars: Aeolian features seen from the ground and orbit: Journal of Geophysical Research - Planets, v. 113.

Hayward, R.K., Fenton, L.K., and Titus, T.N., 2014, Mars Global Digital Dune Database (MGD(3)): Global dune distribution and wind pattern observations: ICARUS, v. 230, p. 38–46, doi:10.1016/j.icarus.2013.04.011.

Higgins, C.G., 1956, Formation of small ventifacts: The Journal of Geology, v. 64, p. 506–516.

Hobbs, S.W., Paull, D.J., and Bourke, M.C., 2010, Aeolian processes and dune morphology in Gale Crater: Icarus, v. 210, p. 102–115.

Horvath, D. G., & Andrews-Hanna, J. C. (2017). Reconstructing the past climate at Gale crater, Mars, from hydrological modeling of late-stage lakes. *Geophysical Research Letters*, *44*(16), 8196–8204. https://doi.org/10.1002/2017GL074654

Horvath, D. G., & Andrews-Hanna, J. C. (2021). The hydrology and climate of Mars during the sedimentary infilling of Gale crater. *Earth and Planetary Science Letters*, *568*, 117032. https://doi.org/10.1016/j.epsl.2021.117032

Hugenholtz, C. H., Barchyn, T. E., & Favaro, E. A. (2015). Formation of periodic bedrock ridges on Earth. *Aeolian Research*, *18*, 135–144. https://doi.org/10.1016/j.aeolia.2015.07.002

Hunt, A. R. G., Day, M., Edgett, K. S., & Chojnacki, M. (2022). The lithified aeolian dune field adjacent to the Apollinaris Sulci, Mars: Geological history and paleo-wind record. *Icarus*, *373*, 114788. https://doi.org/10.1016/j.icarus.2021.114788

Laity, J.E., 1994, Landforms of Aeolian Erosion, *in* Abrahams, A.D. and Parsons, A.J. eds., Geomorphology of Desert Environments, Dordrecht, Springer Netherlands, p. 506–535, doi:10.1007/978-94-015-8254-4_19.

Kerber, L. and Head, J.W. (2012), A progression of induration in Medusae Fossae Formation transverse aeolian ridges: evidence for ancient aeolian bedforms and extensive reworking. Earth Surf. Process. Landforms, 37: 422-433. https://doi.org/10.1002/esp.2259

Khan, S. Y., Stack, K. M., Yingst, R. A., & Bergmann, K. (2022). Characterization of clasts in the Glen Torridon region of Gale crater observed by the Mars Science Laboratory Curiosity Rover. *Journal of Geophysical Research: Planets*, 127, e2021JE007095. https://doi.org/10.1029/2021JE007095

Kronyak, R. E., Kah, L. C., Miklusicak, N. B., Edgett, K. S., Sun, V. Z., Bryk, A. B., & Williams, R. M. E. (2019). Extensive Polygonal Fracture Network in Siccar Point group Strata:

Fracture Mechanisms and Implications for Fluid Circulation in Gale Crater, Mars. *Journal of Geophysical Research: Planets*, *124*(10), 2613–2634. https://doi.org/10.1029/2019JE006125

Lapotre, M.G.A. et al., 2016, Large wind ripples on Mars: A record of atmospheric evolution: Science, v. 353, p. 55–58, doi:10.1126/science.aaf3206.

Le Deit, L., Hauber, E., Fueten, F., Pondrelli, M., Rossi, A. P., & Jaumann, R. (2013). Sequence of infilling events in Gale Crater, Mars: Results from morphology, stratigraphy, and mineralogy. *Journal of Geophysical Research: Planets*, *118*(12), 2439–2473. https://doi.org/10.1002/2012JE004322

Liu, J., Di, K., Gou, S., Yue, Z., Liu, B., Xiao, J., and Liu, Z., 2020, Mapping and spatial statistical analysis of Mars Yardangs: Planetary and Space Science, v. 192, p. 105035.

Liu, J., Michalski, J. R., & Zhou, M.-F. (2021). Intense subaerial weathering of eolian sediments in Gale crater, Mars. *Science Advances*, *7*(32), eabh2687. https://doi.org/10.1126/sciadv.abh2687

Malin, M. C., Bell III, J. F., Cantor, B. A., Caplinger, M. A., Calvin, W. M., Clancy, R. T., Edgett, K. S., Edwards, L., Haberle, R. M., James, P. B., Lee, S. W., Ravine, M. A., Thomas, P. C., & Wolff, M. J. (2007). Context Camera Investigation on board the Mars Reconnaissance Orbiter. *Journal of Geophysical Research: Planets*, *112*(E5). https://doi.org/10.1029/2006JE002808

Malin, M. C., & Edgett, K. S. (2000). Sedimentary rocks of early Mars. *Science*, *290*(5498), 1927-1937.

Mars HiRISE Image Mosaic—Overview. (n.d.). Retrieved February 13, 2023, from https://www.arcgis.com/home/item.html?id=c1c4c750a2154842ae523c984cc14fa5

McEwen, A. S., Eliason, E. M., Bergstrom, J. W., Bridges, N. T., Hansen, C. J., Delamere, W. A., Grant, J. A., Gulick, V. C., Herkenhoff, K. E., Keszthelyi, L., Kirk, R. L., Mellon, M. T., Squyres, S. W., Thomas, N., & Weitz, C. M. (2007). Mars Reconnaissance Orbiter's High Resolution Imaging Science Experiment (HiRISE). *Journal of Geophysical Research: Planets*, *112*(E5). https://doi.org/10.1029/2005JE002605

Milliken, R. E., Grotzinger, J. P., & Thomson, B. J. (2010). Paleoclimate of Mars as captured by the stratigraphic record in Gale Crater: STRATIGRAPHY OF GALE CRATER. *Geophysical Research Letters*, *37*(4). https://doi.org/10.1029/2009GL041870

Milliken, R. E., Ewing, R. C., Fischer, W. W., & Hurowitz, J. (2014a). Wind-blown sandstones cemented by sulfate and clay minerals in Gale Crater, Mars. *Geophysical Research Letters*, *41*(4), 1149–1154. https://doi.org/10.1002/2013GL059097

Milliken, R. E., Ewing, R. C., Fischer, W. W., & Hurowitz, J. (2014b). Wind-blown sandstones cemented by sulfate and clay minerals in Gale Crater, Mars. *Geophysical Research Letters*, *41*(4), 1149–1154. https://doi.org/10.1002/2013GL059097

Montgomery, D. R., Bandfield, J. L., & Becker, S. K. (2012). Periodic bedrock ridges on Mars. *Journal of Geophysical Research: Planets*, *117*(E3). https://doi.org/10.1029/2011JE003970

Nagle-McNaughton, T. P., & Scuderi, L. A. (2021). Networked configurations as an emergent property of transverse aeolian ridges on Mars. *Communications Earth & Environment*, *2*(1), Article 1. https://doi.org/10.1038/s43247-021-00286-5

Neukum, G., & Jaumann, R. (2004). *HRSC: the High Resolution Stereo Camera of Mars Express*.

Newsom, H. E., Mangold, N., Kah, L. C., Williams, J. M., Arvidson, R. E., Stein, N., Ollila, A. M., Bridges, J. C., Schwenzer, S. P., King, P. L., Grant, J. A., Pinet, P., Bridges, N. T., Calef, F., Wiens, R. C., Spray, J. G., Vaniman, D. T., Elston, W. E., Berger, J. A., … Palucis, M. C. (2015). Gale crater and impact processes – Curiosity's first 364 Sols on Mars. *Icarus*, *249*, 108–128. https://doi.org/10.1016/j.icarus.2014.10.013

Pain, C. F., Clarke, J. D. A., & Thomas, M. (2007). Inversion of relief on Mars. *Icarus*, *190*(2), 478–491. https://doi.org/10.1016/j.icarus.2007.03.017

Palucis, M. C., Dietrich, W. E., Williams, R. M. E., Hayes, A. G., Parker, T., Sumner, D. Y., Mangold, N., Lewis, K., & Newsom, H. (2016). Sequence and relative timing of large lakes in Gale crater (Mars) after the formation of Mount Sharp. *Journal of Geophysical Research: Planets*, *121*(3), 472–496. https://doi.org/10.1002/2015JE004905

Persaud, D. M., Putri, A. D. R., & Muller, J.-P. (2021). *30-m HRSC DTM Mosaic of Gale Crater, Mars* [Data set]. Zenodo. https://doi.org/10.5281/zenodo.5808354

Plesea, L., Hare, T. M., (2019). Uncontrolled Global HiRISE Mosaic (Abstract #1986) 50th *Lunar and Planetary Science Conference.* *https://www.hou.usra.edu/meetings/lpsc2019/pdf/1986.pdf*

Rafkin, S. C. R., Pla-Garcia, J., Kahre, M., Gomez-Elvira, J., Hamilton, V. E., Marín, M., Navarro, S., Torres, J., & Vasavada, A. (2016). The meteorology of Gale Crater as determined from Rover Environmental Monitoring Station observations and numerical modeling. Part II: Interpretation. *Icarus*, *280*, 114–138. https://doi.org/10.1016/j.icarus.2016.01.031

Robbins, S. J., & Hynek, B. M. (2012). A new global database of Mars impact craters ≥1 km: 2. Global crater properties and regional variations of the simple-to-complex transition

diameter. *Journal of Geophysical Research: Planets*, *117*(E6). https://doi.org/10.1029/2011JE003967

Roberts, A. L., Fawdon, P., & Mirino, M. (2021). Impact crater degradation, Oxia Planum, Mars. *Journal of Maps*, *17*(2), 581–590. https://doi.org/10.1080/17445647.2021.1976685

Runyon, K. D., Viviano, C. E., & Day, M. (2021). Abraded pyroclastic linear paleodunes in Syria and Daedalia Plana, Mars. *Earth and Planetary Science Letters*, *557*, 116719. https://doi.org/10.1016/j.epsl.2020.116719

Schieber, J., Minitti, M.E., Sullivan, R., Edgett, K.S., Malin, M.C., Parker, T., and Calef, F., 2020, Engraved on the rocks—Aeolian abrasion of Martian mudstone exposures and their relationship to modern wind patterns in Gale Crater, Mars: The Depositional Record, v. 6, p. 625–647.

Siebach, K. L., & Grotzinger, J. P. (2014). Volumetric estimates of ancient water on Mount Sharp based on boxwork deposits, Gale Crater, Mars. *Journal of Geophysical Research: Planets*, *119*(1), 189–198. https://doi.org/10.1002/2013JE004508

Silvestro, S., Fenton, L. K., Vaz, D. A., Bridges, N. T., & Ori, G. G. (2010). Ripple migration and dune activity on Mars: Evidence for dynamic wind processes. *Geophysical Research Letters*, *37*(20). https://doi.org/10.1029/2010GL044743

Silvestro, S., Vaz, D.A., Ewing, R.C., Rossi, A.P., Fenton, L.K., Michaels, T.I., Flahaut, J., and Geissler, P.E., 2013, Pervasive aeolian activity along rover Curiosity's traverse in Gale Crater, Mars: GEOLOGY, v. 41, p. 483–486, doi:10.1130/g34162.1.

Silvestro, S., Chojnacki, M., Vaz, D. A., Cardinale, M., Yizhaq, H., & Esposito, F. (2020). Megaripple Migration on Mars. *Journal of Geophysical Research. Planets*, *125*(8), e2020JE006446. https://doi.org/10.1029/2020JE006446

Silvestro, S., Pacifici, A., Salese, F., Vaz, D. A., Neesemann, A., Tirsch, D., Popa, C. I., Pajola, M., Franzese, G., Mongelluzzo, G., Ruggeri, A. C., Cozzolino, F., Porto, C., & Esposito, F. (2021). Periodic Bedrock Ridges at the ExoMars 2022 Landing Site: Evidence for a Changing Wind Regime. *Geophysical Research Letters*, *48*(4), e2020GL091651. https://doi.org/10.1029/2020GL091651

Stack, K. M., Grotzinger, J. P., Lamb, M. P., Gupta, S., Rubin, D. M., Kah, L. C., Edgar, L. A., Fey, D. M., Hurowitz, J. A., McBride, M., Rivera-Hernández, F., Sumner, D. Y., Van Beek, J. K., Williams, R. M. E., & Aileen Yingst, R. (2019). Evidence for plunging river plume deposits in the Pahrump Hills member of the Murray formation, Gale crater, Mars. *Sedimentology*, *66*(5), 1768–1802. https://doi.org/10.1111/sed.12558

Stack, K. M., Dietrich, W. E., Lamb, M. P., Sullivan, R. J., Christian, J. R., Newman, C. E., O'Connell-Cooper, C. D., Sneed, J. W., Day, M., Baker, M., Arvidson, R. E., Fedo, C. M., Khan, S., Williams, R. M. E., Bennett, K. A., Bryk, A. B., Cofield, S., Edgar, L. A., Fox, V. K., … Van Beek, J. K. (2022). Orbital and In-Situ Investigation of Periodic Bedrock Ridges in Glen Torridon, Gale Crater, Mars. *Journal of Geophysical Research: Planets*, *127*(6), e2021JE007096. https://doi.org/10.1029/2021JE007096

Steele, L. J., Kite, E. S., & Michaels, T. I. (2018). Crater Mound Formation by Wind Erosion on Mars. *Journal of Geophysical Research: Planets*, *123*(1), 113–130. https://doi.org/10.1002/2017JE005459

Thomson, B.J., Bridges, N.T., Milliken, R., Baldridge, A., et al., "Constrains on the origin and evolution of the layered mount in Gale Crater, Mars using Mars Reconnaissance Orbiter Data," Icarus, 214(2). 2011.

Vasavada, A.R., “Mission Overview and Scientific Contributions from the Mars Science Laboratory Curiosity Rover After Eight Years of Surface Operations,” Space Science Reviews, 218. 2022.

Viúdez-Moreiras, D., Richardson, M. I., & Newman, C. E. (2021). Constraints on Emission Source Locations of Methane Detected by Mars Science Laboratory. *Journal of Geophysical Research: Planets*, *126*(12), e2021JE006958. https://doi.org/10.1029/2021JE006958

Watkins, J. A., Grotzinger, J. P., Stein, N. T., Banham, S. G., Gupta, S., Rubin, D. M., Morgan, K. S., Edgett, K. S., Frydenvang, J., Siebach, K. L., Lamb, M. P., Sumner, D. Y., & Lewis, K. W. (2022). Burial and Exhumation of Sedimentary Rocks Revealed by the Base Stimson Erosional Unconformity, Gale Crater, Mars. *Journal of Geophysical Research: Planets*, *127*(7), e2022JE007293. https://doi.org/10.1029/2022JE007293

Ward, A.W., 1979, Yardangs on Mars - Evidence of recent wind erosion: Journal of Geophysical Research, v. 84, p. 8147–8166, doi:10.1029/JB084iB14p08147.

Williams, R. M. E., & Weitz, C. M. (2014). Reconstructing the aqueous history within the southwestern Melas basin, Mars: Clues from stratigraphic and morphometric analyses of fans. *Icarus*, *242*, 19–37. https://doi.org/10.1016/j.icarus.2014.06.030

Zuber, M. T., Smith, D. E., Solomon, S.C., Muhleman, D. O., Head, J. W., Garvin, J. B., Abshire, J. B., Bufton, J. L. (1992). *The Mars Observer Laser Altimeter Investigation,* Journal of Geophysical Research (97), 7781-7798.

CHAPTER 4: A Field Guide to The Ibex Dunes of Death Valley National Park, California: Characterization and Assessment for use as a Martian Analog

4.1 Introduction

Death Valley is the driest place in North America, receiving an average of <5 cm of rain per year, with several years during which the area receives no rain at all (National Park Service, 2020). In the southeast corner of Death Valley National Park, between the Ibex- and Saddle Peak Hills, lies the under-studied Ibex Dune Field (Fig. 4.1). Covering an area of ~3 km^2, these dunes are within the Ibex Wilderness and are not frequented by park visitors or researchers. While only ~4 hours from Los Angeles, CA, the dunes are only accessible via an unpaved road, requiring a 4-wheel drive vehicle with high clearance to access. This remote, backcountry setting minimizes recreational activity at the site. The area is also protected by the California Desert Protection Act of 1994, so vehicles and sandboarding are prohibited, which further preserves this natural laboratory. Previous research on the dunes is limited, but includes two studies related to the Mojave Fringe-toed lizard (Murphy et al., 2006; Gottscho et al., 2014), a recent field study of aeolian abrasion (Dorn and Day, 2023), and a review of aeolian processes in the western United States (Zimbelman and Williams, 2007). The latter work briefly discusses the Ibex dunes, describing a field of star dunes with a maximum height of ~50 m, and notes that some of the smaller (meter-scale) ripple features in the area may be analogous to bedforms on Mars (transverse aeolian ridges, large Martian ripples, and/or megaripples; i.e. Balme et al., 2008; Berman et al., 2011; de Silva et al., 2013; Geissler, 2014; Zimbelman, 2019; Lapotre et al., 2021; Day and Zimbelman, 2021). Older studies of the region refer to the dunes as the "Saratoga dunes," a reference to the nearby Saratoga Springs (Fig. 1; i.e., Pavlik, 1989).

Extremely arid environments (such as Death Valley National Park) are useful as Mars analogs, though most of these sites are in extremely remote and difficult to access locations, such as the Argentinian Puna (i.e., de Silva et al., 2013; Bridges et al., 2015) and the Antarctic Dry Valleys (i.e., Cary et al., 2010). Though remote, the Ibex dunes are easier to access than these other sites, and may be a new and valuable analog site for studying aeolian activity on Mars. Given the lack of previous work focused on the dunes themselves, several key aspects of this dune field remain undefined. Using a combination of orbital images and data collected during visits to the field site, we characterize the variety of bedform morphologies at the site and their evolution through time, as well as the sand mineralogy and grain morphology, and the local wind patterns, in order to assess how the dunes have evolved through time and provide a baseline study to support future work in the area.

4.2 Land Acknowledgement

The Timbisha Shoshone Tribe are the original residents of *Tüppipüh,* land that was taken, at first slowly, by ranchers and miners, and more completely in 1933 via executive order during the creation of Death Valley National Monument (Stringfellow, 2016), and which eventually became a National Park. The national monument was created under the incorrect assumption that there were few to no permanent residents of the area, but evidence suggests that the Timbisha have lived in the region for over 1,000 years (Stringfellow, 2016). Though the Timbisha have been able to recover some of their ancestral lands, the research presented here was conducted on land that is presently part of the National Park, but was historically part of their lands.

4.3 Study Area and Environs

4.3.1 The Ibex Dune Field

The dunes which are the focus of this study are within Death Valley National Park, near the Nevada-California border, and are centered at 35º41'39.25'' N, 116º22'08.21'' W (Figs. 4.1, 4.2). The area is accessed via Death Valley road (State Route 127) and Saratoga Springs Road. The dunes are in a valley, which varies in width between ~2-4 km, and is bounded by the Ibex hills to the west and the Saddle Peak Hills to the east, with the dunes along the base of the Saddle Peak Hills (Fig. 4.1, 4.2). The dunes formed on a shallow alluvial fan (Dorn and Day, 2023). On the northern valley floor are features which appear to be dunes in satellite images, but in the field were determined to be ridges of the same alluvial fan material with <1 m high accumulations of sand on the ridge peaks. Approximately 5 km to the west, on the opposite side of the Ibex hills, lies Saratoga Spring, which is the only source of persistent surface water in the area. The Amargosa river lies to the south, but this portion of the river is typically dry, with water only present during storms (Fig. 4.1; Day and Dorn, 2023).

4.3.2 The Dumont Dunes, Little Dumont, and others

The Dumont dunes lie ~13.5 km to the east of the Ibex study area and consist of two areas, the main dune field (Dumont Dune Field) and Little Dumont (Figs. 41, 4.2; i.e., Nielsen and Kocurek, 1987; Zimbelman and Williams, 2007; Vriend et al., 2012; Arvidson et al., 2016). Both fields are located outside the national park boundaries, and are a popular destination for off-highway vehicles (OHVs), meaning that the dunes are regularly disturbed by human activity. The main Dumont dunes have been used for engineering tests for the Mars Science Laboratory Curiosity

rover (Curiosity; Arvidson et al., 2016). Sand samples were collected from bedforms at Little Dumont, for comparison to the Ibex Dunes.

Other nearby dune fields inside the national park include the Mesquite Flats dunes (122 km from the Ibex dunes), the Panamint dunes (125 km away), Saline Valley dunes (170 km away), and Eureka dunes (194 km away; NPS, 2021).

4.4 Data and Methods

4.4.1 Remote Sensing - Dune Crestline Mapping and Vegetation Coverage

To assess changes in the dune field over time, dune crestline positions in the Ibex Dune Field were mapped using available historical images within Google Earth Pro. The images span 35 years, between 1985-2020, and include images provided by Landsat/Copernicus (for the years 1985, 1994, 2005, 2014), the U.S. Geological Survey (for a portion of the coverage in 1994), Maxar Technologies (for the year 2003), the USDA/FPAC/GEO (for the year 2009), and CNES/Airbus (for the year 2020). Resolvable crestlines were mapped in each image, but as image resolution increased over time, additional details were visible in later images, meaning more crestlines, especially those of smaller bedforms were resolvable. Field mapping of the crest positions of some of the larger dunes was conducted in 2010 and 2022, using a Real Time Kinematic (RTK) Differential GPS. The field measurements were compared to the those collected from the orbital images in Google Earth Pro.

Remote sensing was also used to quantify the degree of vegetation coverage at the field site. Maps of vegetation indices covering southern California are available from the National Oceanic and Atmospheric Administration (NOAA) JSTAR Mapper site. We used the Normalized Difference

Vegetation Index (NDVI) Top of Canopy (TOC) map, as well as the Green Vegetation Fraction (GVF) map (NOAA, 2018). Using the TOC reflectance acquired by the Visible Infrared Imaging Radiometer Suite (VIIRS; NOAA, 2011), the NDVI can be calculated using the difference between the measured red and near-infrared reflectance, which is associated with (green) vegetation (Weier and Herring, 2000; NOAA, 2018, Carter et al., 2020). The GVF is the fractional vegetation coverage over a specific area, and is also calculated from visible and near-infrared spectral data from VIIRS (Jiang et al., 2021; Yu, 2022). The NDVI TOC is provided at 0.009-degree resolution, and the GVF is given in 4-km/pixel, both of which are processed by and publicly available from NOAA.

4.4.2 Age Dating via Optically Stimulated Luminesce

Two samples were collected for age dating using optically stimulate luminescence (OSL; Fig. 4.1). One was collected from alluvial fan material in the north of the study area at the depth of ~0.40 m (sample ID: OSL-N), and one sample was collected from the base of a large star dune at the depth of ~0.43 m (sample ID: OSL-S). These samples were prepared and measured at the UCLA Luminescence Laboratory, using a TL-DA-20 Risø automated reader (Bøtter-Jensen et al., 2003) equipped with a 90Sr/90Y beta source with a dose rate of 5.995 Gy/min. Small single-aliquots were prepared by mounting multiple grains (e.g., ~80–100 grains per disc, respectively) on aluminum discs using silicon oil and subsequently coated with acrylic spray. The samples were then stimulated using IR and blue diodes and emissions were detected using an EMI QA9235 photomultiplier tube equipped with a 7.5 mm Hoya U-340 filter (Bøtter-Jensen et al., 2000).

We applied a modified quartz single-aliquot regenerative dose (SAR) protocol to measure the equivalent doses (D_e; Murray and Wintle, 2000, 2003). The acceptable small aliquots for OSL-N and OSL-S have an overdispersion (OD), ~40% and ~10%, respectively (see supplemental materials). Such a high OD (e.g., > 15%) is often interpreted as the result of partial bleaching (Arnold and Roberts, 2009). We therefore assume that the youngest subpopulation of the distribution is the representative D_e value for OSL-N. A minimum age model (MAM; Galbraith et al., 1999) with three parameters was used to estimate the burial doses. For OSL-S, we used the central age model to estimate luminescence ages (CAM; Galbraith et al., 1999). OSL ages (Table 4.1) were calculated in the DRAC v. 1.2 online calculator (Durcan et al., 2015). Age ± 1σ uncertainty is used to report all the luminescence ages (Table 4.1). We determined that the samples did not have signals from feldspars or other contaminants based on the relatively low signal-to-background ratios for IRSL and high signal-to-background ratios for blue light stimulated luminescence.

4.4.3 Grain Analysis

Sand grains were collected from six locations around the field site (Fig. 4.3). One sample was collected from the crest of one of the large star dunes, to represent the composition of the largest bedforms in the study area (thin section D; Figs. 4.1, 4.2, 4.3D). In addition to the large dunes, granule- or coarse-grained ripples (up to ~10 cm in height) are also common at site, and were found both in the margins of the dune field and superimposed on toes of some of the dunes. Two grain samples were collected from these ripples, one from granule ripples to the west of the dunes (thin section A; Figs. 4.1, 4.2, 4.3A), and one from granule ripples found on the face of a dune (thin section C; Figs. 4.1, 4.2, 4.3C). Thin section C was also collected from an example of

compound ripples (consisting of superposed primary and secondary ripples of different scales), which are found throughout the site. An additional grain sample was collected from a set of compound ripples in an interdune space (thin section B; Figs. 4.1, 4.2, 4.3B). In order to better understand the relationship between the Ibex and Dumont dune fields, two samples from the Little Dumont dunes were collected for comparison, one from the surface of a dune (thin section E, Figs. 4.1, 4.2, 4.3E), and one from a granule ripple (thin section F; Figs. 4.1, 4.2, 4.3F). Grains from each location were mounted on slides and cut to thin section thickness for optical microscopy. A point count was conducted on each thin section to quantify the distribution of grain size and mineralogy characteristics. Specifically, we measured grain size, identified the mineralogy, and assessed grain morphology. Between 160 and 174 grains were characterized for each of the six thin sections.

4.4 Weather Monitoring

Two NovaLynx 110 WS-25 modular weather stations were deployed at the field site (Fig. 4.1). The stations monitored wind activity 2.5 m above the ground, and collected data for approximately 18 months, between March 23, 2021 and October 15, 2022. Wind speed measurements were stored as an average of the speeds measured in the sampling intervals (1 minute), and wind gusts are reported as the highest speed measured in that same interval (Dorn and Day, 2023). Wind measurements were processed into figures using Windrose for Matlab (Pereira, 2021).

4.5 Results

4.5.1 Bedform Morphologies

Aeolian bedform morphologies are dependent on local wind patterns and sediment supply (i.e. Wilson, 1972; Pye and Tsoar, 2009, Lü et al., 2018). As noted by a previous survey, the largest dunes in the Ibex study area are star dunes (Figs. 4.1, 4.2, 4.4A-B; Zimbelman and Williams, 2007), which form under multidirectional winds (Nielsen and Kocurek, 1987; Narteau et al., 2014). The multiple wind directions create multiple crests as sand is transported in various directions. The largest of the star dunes is ~50 m high, and ~0.80 km long (as measured along the longest crestline, which is oriented approximately north-south, parallel to the Saddle Peak Hills; see location for thin section E in Figs. 4.1, 4.2). Slightly to the north of the larger star dunes are smaller bedforms, including smaller transverse dunes (Fig. 4.2). The entire dune field is located on a slope, as the dunes are on an alluvial fan at the base of the Saddle Peak Hills (Dorn and Day, 2023). The topography of the hills limits dune migration to the east (towards the Saddle Peak hills). However, there is one longitudinal climbing dune, which stretches 1.72 km along its crest, which is ascending a portion of the slope over the Saddle Peak Hills.

Large ripples (up to ~10 cm high), known as granule/coarse grained/megaripples (Figs. 4.3A-C, 4.3F, 4.4C-E; i.e., Zimbelman and Williams, 2007; Zimbelman, 2019; Day and Zimbelman, 2021), occur on the surface of larger dunes and in interdune spaces (Figs. 4.4C-E). In several cases, these large (primary) ripples are superimposed by an additional scale of smaller (secondary) impact ripples (~a few cm high), forming complex/compound bedforms (Figs. 4.3A-C, 4.4C-E). Often, the primary ripples are armored by coarser grains, which are generally darker, while their interiors are composed of finer sand which is lighter in color (Fig. 4.4F). The coarser grains were generally concentrated on the crests of the granule ripples (see Fig. 4.4C), and are frequently composed of quartz, though some are lithic fragments. The impact ripples are also composed of the lighter, finer

sand (e.g., Sample C; Figs. 4.3C, 4.4F). We found areas where compound ripples on the surface of a dune transitioned into simple impact ripples at the toe of the dunes, over a very short distance (Fig. 4.4C). At the edges of both the Ibex and Little Dumont dune fields, granule ripples were found migrating across mud cracks, which were exposed in the inter-ripple spaces (see example in Fig. 4.3E). These granule ripples were also often found alongside larger clasts (pebbles and larger), which were not seen on the dune surfaces.

The Little Dumont dune field also consists of transverse dunes (Figs. 4.1, 4.2), but these dunes are smaller than the largest dunes in the Ibex region. The Little Dumont dunes are on the order of meters high, and ~0.2 - 0.8 km long. Granule ripples and mud cracks were also seen at the margin of this field (Fig. 4.3E), though as this area is used for OHV activity, a significant portion of the surface has been disturbed by tire tracks.

4.5.2 Ibex Dune Field Evolution through Time

4.5.2.1 Crestline Mapping

Dunes are typically mobile features; they will migrate given sufficient wind is available to mobilize the sand grains. Studies of other dune fields using a variety of methods have measured movements rates between 0 – 60 m/yr for dune fields around the world (i.e. Yang et al., 2021 and references therein; Schueth and Laycock, 2022). Crestline positions of the Ibex dunes were tracked between 1985 and 2022 using a combination of orbital data and RTK differential GPS measurements. Based on the orbital images, the dune field has maintained a consistent position and extent for the past 37 years (Fig. 4.5). In this time, the crests of the largest dunes have net-migrated between 0 m and 50 m, from their first measurement (using images acquired in 1985) to

the latest field measurements in 2022 (Figs. 4.5A, 4.5C, 4.6). However, the crests shift back and forth over time, rather than consistently advancing in a particular direction, meaning that total movement over this period is >50 m. Field GPS measurements from 2010 and 2022 show a maximum change in position of ~30 m in that 12 year time span, though there are many locations in which there was little to no change over that period (Fig. 4.6). Overall, the largest dunes, regardless of their morphology, have not experienced much net motion over the observation period (which is consistent with the expected behavior of star dunes; Figs. 4.5A, 4.5C, 4.6A; i.e. Nielsen and Kocurek, 1987; Narteau, 2014).

Smaller (meter-scale) dunes, especially in the northern part of the field, changed significantly between orbital images (Fig. 4.5B), though they are only resolvable in the most recent 17 years of coverage (2003-2020 images). The primary and secondary crests of these dunes shift substantially (up to 90º rotation of primary crests; see Fig. 4.5B) between images, to the point where it becomes challenging to track individual features. In images from 2014 these small dune crestlines are nearly parallel to the Saddle Peak Hills (oriented approximately north-south), but in images from 2020 the crestlines are oriented perpendicular to the hills (approximately east-west). Due to their relatively small size, the migration of these features changes their appearance, position, and orientation more drastically than that of the larger dunes.

4.5.2.2 OSL Exposure Ages

To bound the age of the dune field, we collected two samples for analysis with OSL: one from the largest dune, and one from the sediment in the underlying alluvial fan. OSL exposure dating measures the length of time a sample has been buried, and each time grains are brought to the

surface and exposed to the sun the burial age resets (Huntley et al., 1985; Rhodes, 2011; Nelson et al., 2017). Previous work to date actively migrating aeolian sands with OSL has faced challenges, as the constant shifting of the dunes resets the burial age of the grains (Edwards, 1993; Wintle, 1993; Madsen and Murray, 2009), meaning that burial ages are much younger than the actual age of the dune. However, these measurements do provide a minimum age for the dune.

OSL ages for the two samples were obtained by dividing the D_e by the annual geologic dose-rates (Table 4.1). This yields a burial age of 2.68 ± 0.48 ka for the alluvial fan sample, (OSL-N; Table 4.1; see appendix) and a burial age of 0.16 ± 0.03 ka for large star dune sample; OSL-S; Table 4.1; see appendix). The age of the underlying fan (OSL-N) provides a maximum age for the dune field to have been present in it's current position, as it superposes the fan. The dune sample (OSL-S) was collected near the base of a large star dune. Star dunes tend to grow vertically rather than migrating (Narteau et al., 2014), and the core of the dune remains relatively stationary while the crests or arms of the dune shift. The sample was taken from the base of the dune in order to access the less mobile sand in the dune core, which accounts for the ~0.16 ka burial age estimate from the OSL analysis (see appendix for additional information on sample OSL-S).

4.5.3 Sand Mineralogy and Grain Descriptions

The large Ibex dunes and surrounding smaller bedforms are composed of sands of various mineralogies and sizes. Using the six thin sections prepared from grain samples collected at the site, we assessed grain size, morphology and mineralogy. The dunes are composed of a light tan or beige sand (Figs. 4.2, 4.3, 4.4). However, in several places, especially in local topographic low points and interdune spaces, dark coarse grains armor the much finer, lighter toned sand (see

examples in Figs. 4.4A, 4.4B, 4.4F, 4.4G). Grains ranged from well-rounded to very angular in each sample, and the D_{50} values for the grains ranged from very fine to medium sand (Table 4.2; Fig. 4.7). Overall, nearly all measured grains were at or below coarse sand size (1 mm; Table 4.2, Fig. 4.7), as expected for aeolian sand dunes. The largest measured grain was 6 mm in diameter, found in the granule ripples on the margin of the Little Dumont dunes. However, the two samples from Little Dumont (thin sections E and F) contained overall smaller grains than those collected from the Ibex dunes (Table 4.2, Fig. 4.7).

Analysis of thin sections A-E (Fig. 4.8) shows that they all have compositions comparable to a sublitharenite sandstone (Fig. 4.8a). The compositions of the samples were very consistent, with most consisting of between 40-50% quartz, 40-50% lithic fragments, and up to 10% feldspars. Thin sections D (collected from a large star dune in the Ibex field) and E (collected from a dune at Little Dumont) contained the most quartz (~64%), and the remainder of these two samples consisted of 27% lithic fragments and 8% feldspar. In addition to mono- and poly-crystalline quartz, other minerals identified include: plagioclase, hornblende, biotite, carbonates (including dolomite), epidote, talc, chlorite, calcite, and oxides (examples shown in Figs. 4.8B-C).

4.5.4 Wind Patterns

As reported by Dorn and Day (2023), the majority of the winds at the study site originate from the northeast (Fig. 4.9A). However, winds originating from the west and the southeast were also observed (Fig. 4.9). The maximum wind speeds measured were 20.8 m/s (station 1) and 26.2 m/s (station 2), with averages of 3.00 ± 2.27 m/s from 13.0° ± 104.4°, and 3.15 ± 2.21 m/s from 17.6° ± 99.6°, respectively (Dorn and Day, 2023). While there were diurnal fluctuations in wind speed

and direction, there were no clear seasonal trends in wind direction, though speeds were generally higher in spring (Dorn and Day, 2023). The data presented here was collected from station 1 for simplicity (Fig. 4.9).

During visits to the site, sand was observed actively saltating across the crests of the dunes, up to ~1 m above the surface. Sand shadows (wake features) were also seen in the lee of small topographic features such as small boulders and vegetation (Fig. 4.4G). These features form as wind slows in the wake of an obstacle and grains being transported fall out of suspension, eventually building up in the lee of the obstacle and forming a 'shadow.' These shadows can be used to interpret the direction of sand transporting winds. The example shown in Figure 4.4G was from an area between two large dunes, which likely heavily influenced the flow in that interdune space. The topography can create localized, small-scale wind patterns, which may differ from the overall wind flow in the region, meaning shadows in these areas are simply a representation of the flow in that small area. During different field visits across the study period, the shadows seen on the dune field margins (further away from the topographic influence of the dunes) changed direction, sometimes indicative of winds from the north, and other times winds from the west.

There is a minimum wind speed required to mobilize sand grains of a given size and composition, which can be calculated using the analytical approximation for the threshold friction velocity (u_{*t}) from Shao and Lu (2000):

$$u_{*t} = \sqrt{A_N(\sigma_p g d + \frac{\gamma}{\rho d})}$$

Where A_N is 0.0123, γ is 3 x 10^{-4} kg/s^2, g is the acceleration due to gravity (9.8 m/s^2 on Earth), σ_p is the ratio of particle density to air density (using quartz grains – 2650 kg/m^3, and atmospheric density of 1.2 kg/m^3), d is the grain diameter, and ρ is the air density. This shear velocity (u_{*t}) can be converted to a critical wind velocity, which can be compared to our measurements from the field, using the 'law of the wall' (Spalding, 1961):

$$U_{cr} = (u_{*t}/\kappa)(\ln(\frac{Z}{Z_0}))$$

Where κ is the von Kármán constant (0.4), Z is the measurement height (2.5 m above the ground), and Z_0 is the roughness length scale (here 0.0003 m).

Assuming grains of 0.50 mm, based on our analysis of the collected samples, we used this expression to calculate a critical wind velocity (U_{cr}) of 8.43 m/s. The majority of measured winds were below 5.6 m/s, meaning that these winds, though frequent, would be insufficient to transport 0.50 mm grains. During the entire study period, only 1.96% of measured winds were above the fluid threshold velocity (minimum velocity to initiate saltation). However, once saltation is initiated, for example by a brief gust of wind above the fluid threshold, it can be maintained at slower wind speeds, until the wind speed drops below the impact threshold (wind speed at which saltation ceases). Previous studies have shown that the impact threshold is about 80% of the fluid threshold (Bagnold, 1937), meaning that winds of ~6.74 m/s may be sufficient to maintain saltation once initiated. The winds capable of initiating transport (>8.43 m/s) originated primarily from the west (Fig. 4.9B). This explains why the dunes are located on the eastern side of the valley, as net transport via winds from the west would cause any available sand in the valley to be transported to the east, until the topography of the Saddle Peak Hills acts as a barrier to further motion. Repeating this calculation for smaller grains (0.15 mm), which were also seen in our thin sections,

we find that the critical wind velocity is 5.6 m/s, which occurred 8.7% of the time. The strongest of these transporting winds originate from the west, as before, though some southeasterly winds, though insufficient to move the larger grains, would contribute to saltation of these finer grains.

4.5.5 Vegetation

Vegetation can stabilize bedforms, which can lead to dune formation (i.e. nebkha or coppice dunes; i.e. Durán and Herrmann, 2006). In the field, sparse vegetation was seen throughout the valley (Figs. 4.4A, 4.4B, 4.10B), though none was seen on the Ibex dunes themselves (Fig. 4.10A). Plants were also seen in some interdune spaces where the underlying alluvial fan was exposed (Fig. 4.4B). Aside from sand shadows seen in the lee of plants on the valley floor, there did not appear to be any nebkha dunes or other plant-stabilized bedforms within the main Ibex dune field.

Viewed from orbit, there are several parameters that describe the vegetation coverage of a given area. One example, the Normalized Difference Vegetation Index Top of Canopy (NDVI TOC) index, ranges from -1 to 1, where an area covered by vegetation would be considered a 1, an area with no green vegetation is a 0, and open water is -1 (Carter et al., 2020). The entire study area falls <0.04, meaning the vegetation is very sparse (Fig. 4.10C). On the Green Vegetation Fraction (GVF; Jiang et al., 2021), another index derived from orbital observations, which ranges from 0 (no vegetation coverage) – 100 (complete coverage), the site falls in the 0-5 range, again indicating how extremely sparse the vegetation is at the site (Fig. 4.10D). This is perhaps unsurprising, given the extremely arid environment.

4.6 Discussion

4.6.1 The Ibex Dunes: Activity, Evolution and Wind Patterns

The morphology of the large star dunes within the Ibex study area indicates they formed under a complex and multidirectional wind regime (Nielsen and Kocurek, 1987; Narteau et al., 2014). Additionally, the dune position at the base of the hills on the eastern side of the valley suggests that net transport may be towards the east (Figs. 4.1, 4.2). Our measurements of the wind activity at the site confirm that the majority of the sand transporting winds originate from the west (Fig. 4.9B), pushing the dunes to the eastern side of the valley. The measurements also show that winds from the northeast and southeast are very active at the site (Fig. 4.9A), though these winds would only be able to transport the finer grains. Overall, much of the measured wind would not be sufficient to initiate grain saltation, meaning that a small percentage of the total winds (<10%) are actually contributing to dune migration. This, combined with the multiple wind directions transporting sand back-and-forth, results in minimal net-migration over the 37 years for which we have images of the star dunes (Figs. 4.5, 4.6), which is consistent with expected behaviors. The smaller dunes change position and orientation between images, but are only resolvable in the more recent, higher resolution images (Figs. 4.5A-B).

Though the star dunes have not migrated very far during this period (Figs. 4.5, 4.6), during field visits we experienced high winds and made observations of actively saltating sands on the dunes. A recent study by Dorn and Day (2023) highlighted the abundance of ventifacts in the valley, and the effect of aeolian abrasion on test materials deployed in the study area, both of which show that sand is being transported, even if sporadically. The geometry of the valley, namely the slope on which the dunes sit (Dorn and Day, 2023), likely limits their ability to migrate further east, trapping

much of the sand in the valley. However, one longitudinal dune does climb up the Saddle Peak Hills (Fig. 4.5A), and it appeared that some sand does leave the valley to the east via this dune.

All sand samples collected from the Ibex study area were found to be compositionally similar to a sublitharenite sandstone (Fig. 4.8A). This composition is typical of continental sediments, specifically those from a recycled orogen (Dickinson et al., 1983).

4.6.2 Dunes in the Death Valley Region

Compositionally, the Ibex dune samples are very similar to the samples collected at the nearby Little Dumont dunes, which lie ~7 km to the east (Fig. 4.8A). In fact, the compositions of the dunes at both sites (thin section D, taken from a star dune at the Ibex field, and thin section E, taken from a dune at Little Dumont; Figs. 4.3, 4.8A), were almost identical. All of the samples collected from both sites are compositionally similar, falling into the range of compositions typical of sublitharenite sandstones (Fig. 4.8A). The primary difference between the two locations is in the grain sizes, with the Little Dumont grains being on average smaller than those from Ibex (Table 4.2; Fig. 4.7). The other main distinction between the two areas is that the Little Dumont dunes are smaller, only a few meters high, while the Ibex dunes reach heights of ~50 m (Figs. 4.1, 4.2, 4.3).

Information on the dune fields within the national park is limited, however previous studies of the region have identified quartz and feldspar sands at the Mesquite Flats dunes (Hanko and Foster, 2015), and in the Dumont dunes (Vriend et al., 2012), while other nearby dunes are reportedly composed of travertine (Kiver and Harris, 1999). Macdonald (1966) reports that the Dumont dunes

are formed from sediments originating from the Amargosa river (to the southeast of the Ibex dunes; Fig. 4.1) and alluvial fans in the region, and that the dunes likely post-date the last high-stand of paleo-lake Manly, approximately 18,000 years ago (i.e. Blackwelder, 1933; Hooke, 1999; Matsubara and Howard, 2009; NPS, 2022). Based on a survey of endemic species in the dune fields of the Mojave Desert, Pavlik (1989) determined that the Ibex dunes were among the youngest in their study area, with the Dumont dunes being slightly older. The minimum age of the dune fields was given as 2000 years, based on radiocarbon dating (Pavlik, 1989), and their results suggested that both the Ibex and Dumont dune fields likely developed at some point in the late Holocene.

Dunes are seen across arid and coastal regions of Earth. Though Death Valley is presently an extremely dry environment, ancient lakes once covered much of the area (NPS, 2022). These lakes dried up at the end of the last ice age, approximately 10,000 years ago (Blackwelder, 1933; Hooke, 1999; Matsubara and Howard, 2009; NPS, 2022). The dunes we see today may have started forming during this period, as the climate warmed and dried (i.e. Barrett et al., 2008). Perhaps sediments exposed in the newly dried lakebeds contributed to the dune growth. Our analysis of the dune age using OSL was limited by the migratory nature of dunes, as burial ages are reset each time sand is exposed to the sun, the migration of dunes constantly resets the burial age. However, our results do provide a minimum age for the dunes (0.16 ± 0.03 ka) and indicated that the upper layers of the underlying alluvial fan are at least 2200 years old. Previous OSL studies in the region report values between 4,000-17,000 for samples from the Kelso dunes (Clarke et al., 1995), and Mahan et al. (2007) report ages between 2900-4600 years for alluvial fan deposits south of the Dumont dunes. Though these studies did not sample the Ibex dunes or Saddle Peak Hills, their

measurements from nearby alluvial fan deposits are consistent with our value (which was collected from a relatively shallow depth) for the alluvial fan beneath the Ibex dunes.

4.6.3 The Ibex Dunes as a Mars Analog

The surface of Mars is covered in wind-formed features, including ripples, dunes, ventifacts, and yardangs (i.e., Hayward et al., 2014; Fenton, 2020; Silvestro et al., 2013; Lapotre et al., 2016; Ward, 1979; Liu et al., 2020, Bretzfelder and Day, 2021; Laity and Bridges, 2009), many of which we also see in arid regions of Earth (though some are unique to Mars; Lapotre et al., 2017). The Mars rovers are able to give us an in-situ view of these features, but dunes and large ripples pose a driving hazard to the rovers and are thus often avoided (i.e., Arvidson et al., 2016; Bretzfelder and Day, 2021). Different sites on Earth may act as suitable analogs for the Martian surface, depending on the area of investigation (i.e. geothermal vents, ice caps, impact craters, etc.). In this case, we are interested in whether the Ibex dunes may be a reasonable analog location for studying aeolian activity on Mars, and are thus most interested in the similarities and differences in the bedforms and climate at Ibex compared to Mars.

The observed compound ripples on and around the Ibex dunes are similar to bedforms seen on Mars by Curiosity (Fig. 4.11; i.e., Bretzfelder and Day, 2021, Zimbelman and Williams, 2007). The granule ripples at Ibex were armored by coarse grains with finer-grained interiors, similar to features traversed by Curiosity (Figs. 4.3C, 4.4F, 4.11; i.e., Bretzfelder and Day, 2021, and references therein). For example, the ripples encountered by Curiosity in Hidden Valley were slightly larger (in both height and wavelength) than those at the Ibex dunes: both have heights < 1 m and wavelengths of ~ 1 m, and show both larger primary ripples superimposed by smaller (cm-

scale impact ripples; Fig. 4.11). These similarities suggest this area could provide a new opportunity to study these features.

Though similar in scale and morphology, the mineralogy of the features at Ibex are not directly comparable to that of bedforms on Mars. Aeolian sands on Mars, and more specifically in the area explored by Curiosity, are generally dominated by basalts including plagioclase, olivine and pyroxenes (i.e. Achilles et al., 2017; Lapotre et al., 2017; Rampe et al., 2018). Curiosity also identified magnetite, hematite, quartz, and anhydrite in the dunes along its traverse (Achilles et al, 2017). Though we also identified plagioclase in our samples, our analysis of the sand collected from Ibex (and Little Dumont) indicates that the majority of the grains are quartz and lithic fragments, with a small feldspar component (Fig. 4.8A). The grains of the Bagnold dune field, explored by Curiosity, were mostly comprised of 0.05-0.15 mm grains, with larger (0.2-0.5 mm) also seen in abundance (Weitz et al., 2018). Grains of the same size range were also identified in the samples from Ibex, as between 65-98% of the grains in each sample were ≤0.5 mm (Fig. 4.7 and Table 4.2). While mineralogically distinct, grain sorting in the armored bedforms on Mars and the granule ripples at the Ibex site were similar (coarse grains armoring finer materials), indicating their morphology and formation may be a suitable analog for these Martian features.

In addition to mineralogy, another key difference between modern Mars and Earth is that fluvial activity is a significant driver of landscape formation on Earth, while on Mars aeolian activity and impact cratering have been the driving forces for the past ~3.5 Ga (Di Achille and Hynek, 2010). Given the lack of water on Mars, extremely arid environments are often the best analogs for the modern Martian surface. The yearly average precipitation in Death Valley is extremely low (<5

cm/yr), making it the driest place in North America (National Park Service, 2020). The historic weather activity of 2023, including a storm that resulted in 5.6 cm of rain within Death Valley (National Park Service, 2023), occurred after the conclusion of this study and thus these events are not recorded in our field data. The conditions are typically comparable to that of the Argentinian Puna, an area which has been used as an analog for Mars, to study similar ripple features (de Silva et al., 2013; Bridges et al., 2015). Taylor Valley, Antarctica, which is considered one of the best Earth analogs for Mars, receives <10 cm of precipitation per year (Barrett et al., 2008; Cary et al., 2010). The Ibex dunes are located in an even drier area, away from substantial sources of surface water; with the exception of Saratoga Spring (located ~5 km away on the opposite side of the Ibex hills), there are no glaciers or lakes, unlike in Taylor Valley. Additionally, observations of widespread ventifacts throughout the study area indicate that the region has dominated by aeolian processes for at least the past few hundred years, rather than fluvial action (Dorn and Day, 2023), as is the case on modern Mars, further highlighting the similarities with this field site.

The lack of precipitation and surface water at the site results in very sparse vegetation. As modern Mars has no vegetation, and given that plants can stabilize bedforms and act as a control on dune formation, heavily vegetated areas are less analogous to Mars's surface. Though there is some vegetation in the interdune areas and at the dune margins (Figs. 4.4A, 4.4B, 4.10B), the lack of vegetation on the dunes themselves (Fig. 4.10A), and overall extremely sparse vegetation locally (Figs. 4.10C-D), indicates that recent evolution of these dunes is unlikely to have been strongly influenced by biological activity, improving their value as a Mars analog.

4.7 Conclusion

The Ibex dune field in Death Valley National Park consists of several large star and subordinate transverse dunes accumulated on a shallow alluvial fan at the base of the Saddle Peak Hills (Figs. 1, 2). Over 37 years of observations, the dunes have exhibited relatively little net-migration (10s of meters; Figs. 4.5, 4.6), as multi-directional winds (Fig. 4.9), combined with the valley geometry, limit the dune motion in any particular direction. The sand composition of the dunes is comparable to a sublitharenite sandstone (Fig. 4.8), and is similar to the composition of the nearby Little Dumont dunes. The remote setting of the Ibex dunes makes them ideal for field studies, as recreational activity is low and thus unlikely to be a large factor in dune formation and evolution. The extremely arid environment, lack of vegetation (Fig. 4.10), and morphology of ripple features at the site (Figs. 4.3, 4.4), indicate that the area could be used as a reasonable analog for surface processes on Mars. The results reported here provide a baseline characterization of the dune field to enable future studies at the site.

4.8 Figures and Tables

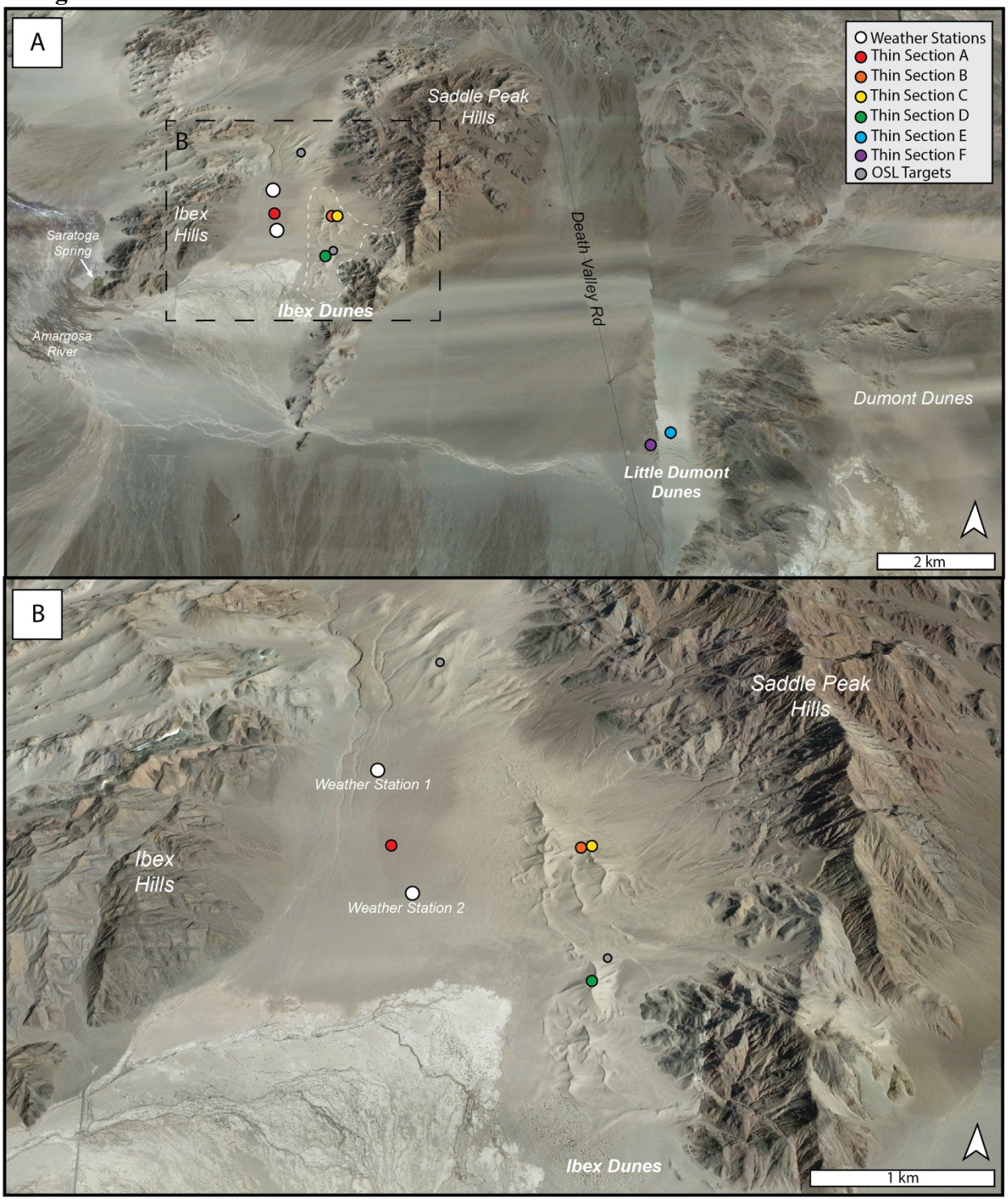

Fig. 4.1. The Ibex dunes and surrounding environs. (A) View of the Ibex dune field study area and geologic features in the area. Dune field extent is marked by a white dashed line. Sample collected at the marked points were analyzed in thin section (red, orange, yellow, green, blue, purple circles) or via optically stimulated luminescence (OSL; grey circles). Two weather stations

(white circles) recorded wind direction and magnitude for approximately 18 months. (B) A closer view of the Ibex dunes and the valley in which they are located. The Ibex hills are to the west, and the Saddle Peak Hills are to the east. Background image acquired in 2014.

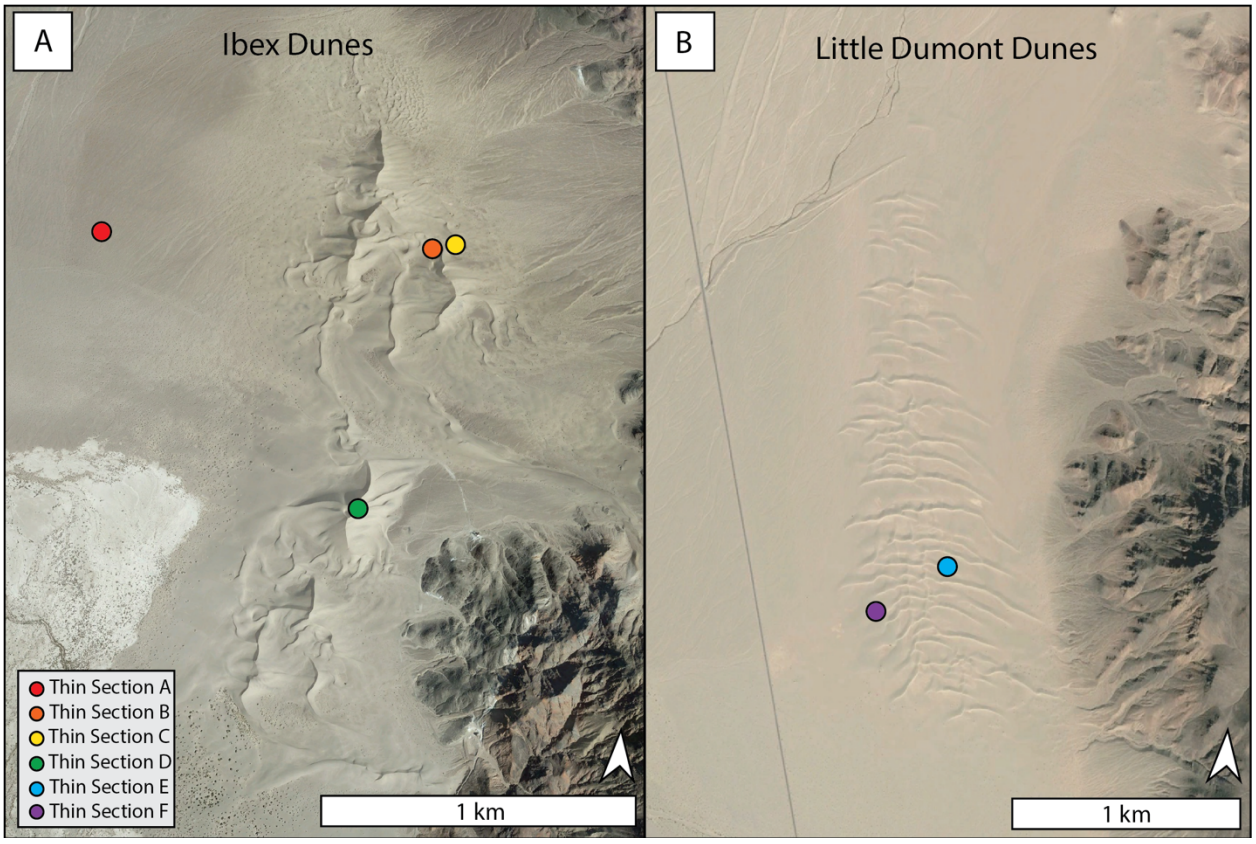

Figure 4.2. The Ibex dune field and Little Dumont dunes. (A) The Ibex dunes, showing sample collection locations for grains analyzed in thin section. The green circle indicates the location of thin section D, which was collected from the largest star dune at the study site. Other large star dunes and smaller transverse dunes are visible. The Saddle Peak Hills are seen in the bottom right. (B) The Little Dumont dunes and thin section collection locations. The Little Dumont dunes consist of a field of transverse dunes, much smaller than the large star dunes at the Ibex field. Background image acquired in 2014.

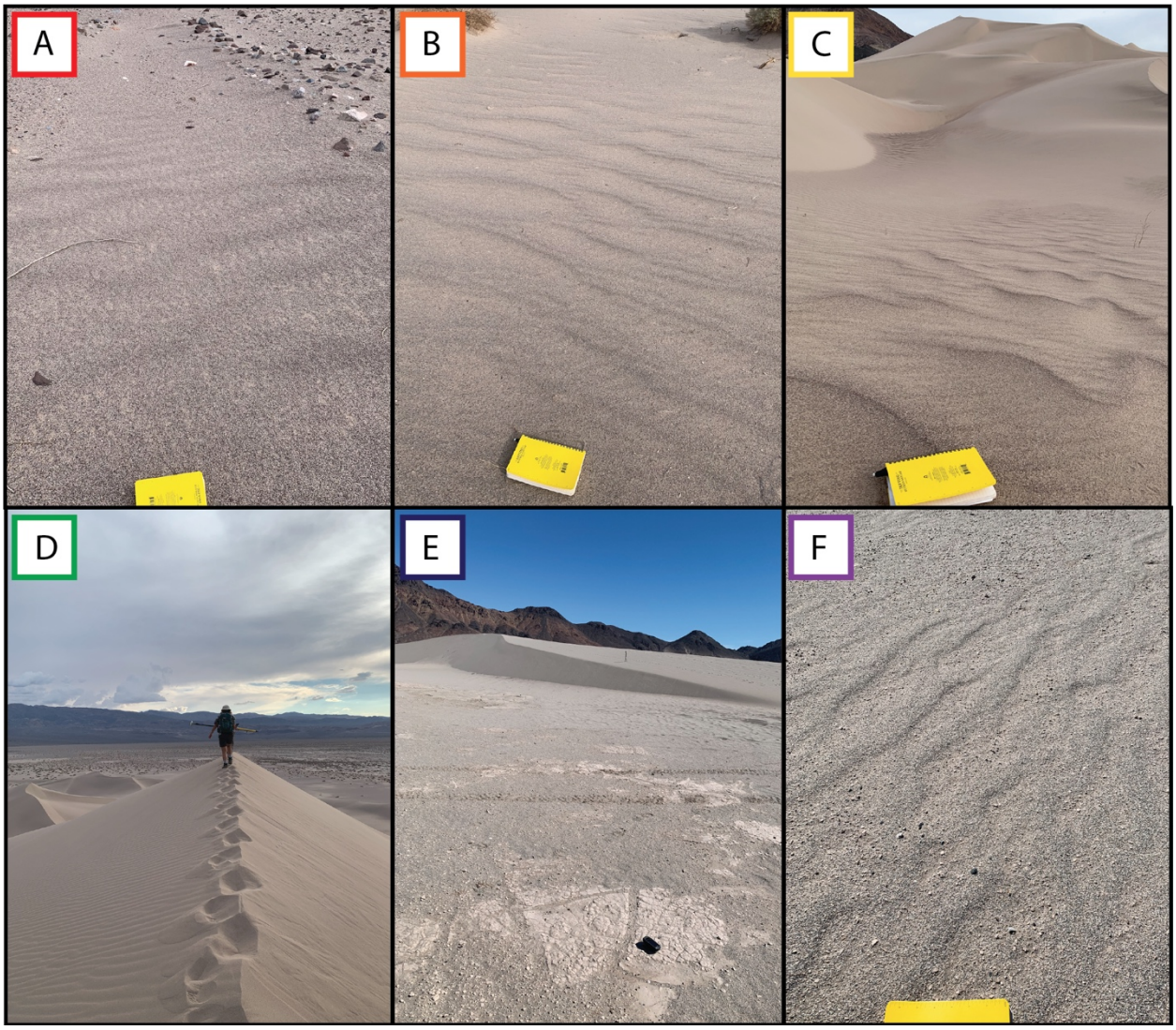

Figure 4.3. Thin section sample collection locations. Grain samples were taken from the locations shown in A-F and processed into thin sections for analysis. See Figs. 1 and 2 for locations. (A) Granule or coarse-grained ripples in the western margin of the Ibex dune field. Ventifacts visible in the background. This location corresponds to thin section A. (B) Compound ripples (with both primary and secondary crests) in an interdune space within the Ibex dune field. (C) Coarse grained compound ripples in an interdune space within the Ibex dune field. (D) Image of one of the crests of the largest star dune within the Ibex study area, where sand was collected to represent the composition of the dunes. Field assistant pictured for scale. (E) Mud cracks at the Little Dumont dune. In the background of the image is a small transverse dune. A thin section was created from the dune sands, and compared to the dunes at Ibex. Handheld GPS unit (~10 cm) pictured for scale. Tire tracks from recreational OHV usage were visible on portions of the dune. (F) Granule ripples at Little Dumont. These ripples were found at the margin of the Little Dumont dunes, in an area with minimal evidence of recent OHV activity (i.e., no obvious tire tracks).

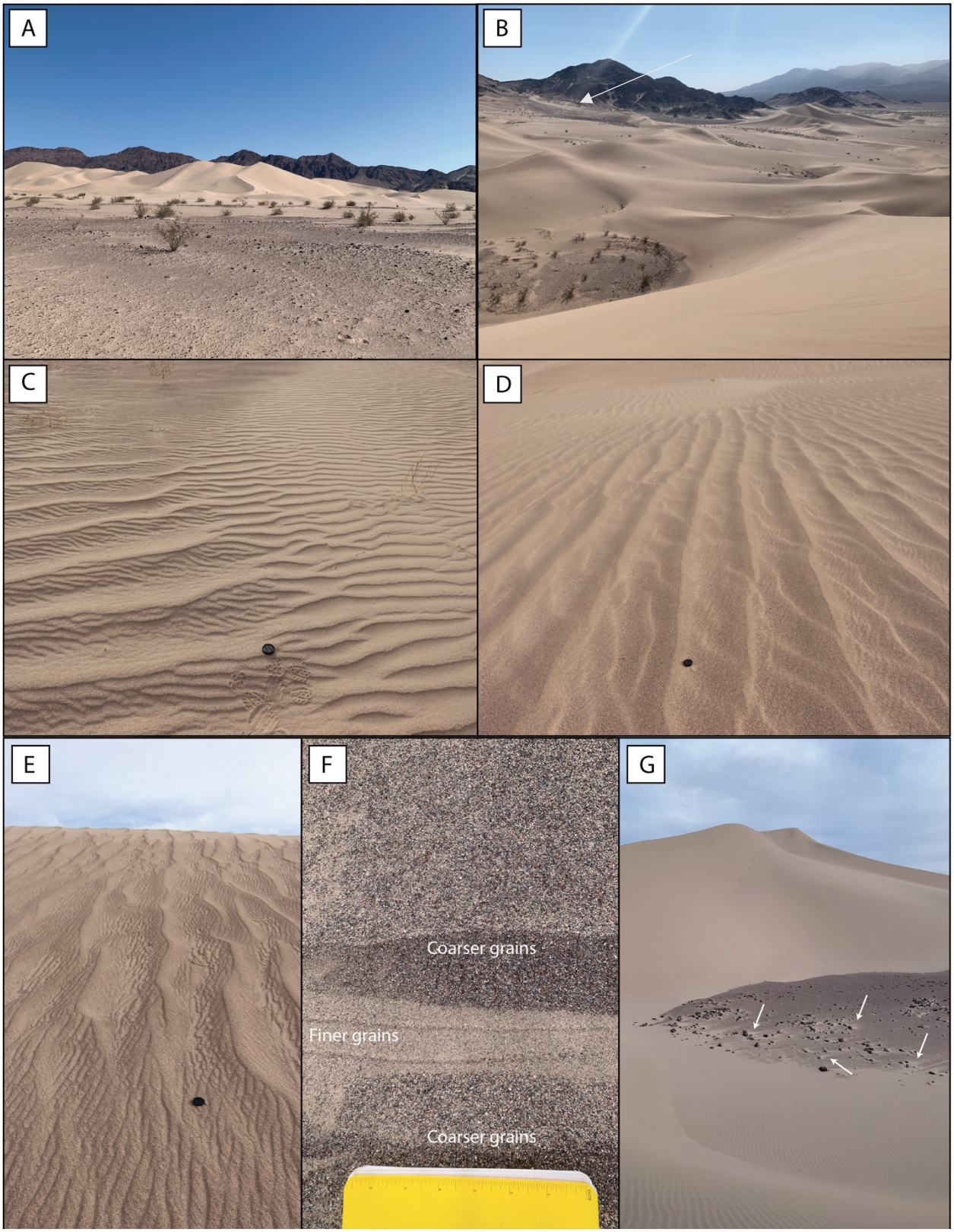

Figure 4.4. Bedforms and wake features in the Ibex Dune field. (A) The Ibex dunes, with the Saddle Peak Hills in the background. The large star dune in the center of the image is ~50 m high. Sparse vegetation is visible on the valley floor, around the dune margins. (B) View from the crest

of a dune, looking south across the Ibex study area. The dark material in the interdune spaces is the underlying alluvial fan. Where the fan material is exposed, sparse vegetation occurs. White arrow indicates the crest of a large longitudinal climbing dune, which is ascending the Saddle Peak Hills. (C) Multiple scales of ripples at the toe of a dune. On the left side of the image: compound ripples with larger primary crests are superposed by smaller impact ripples. On the right of the image: simple ripples with only one scale of crest. The separation between compound and simple ripples marks the toe of the dune. Lens cap (~5 cm) pictured for scale. (D) Compound ripples on a dune. These ripples have both primary and secondary crests, with ripples of two different scales superposed. Lens cap (~5 cm) provided for scale. (E) Compound ripples on the face of a longitudinal dune. These ripples have both primary and secondary crests, with ripples of two different scales superposed. The ripples were found on the climbing dune marked in (B). Lens cap (~5 cm) provided for scale. (F) The interior of a coarse grained ripple. The (darker) ripple surface armors an interior of finer (lighter) grains. This is an example of the ripples that were sampled and processed into thin sections. (E) Sand shadows in an interdune space. Examples of sand shadows (wake features) are indicated by white arrows. This image shows an interdune space where the alluvial fan material underlying the dunes is exposed. The larger cobbles in this material create an obstacle for the wind, resulting in wake features being deposited on the lee (downwind) side of the cobbles.

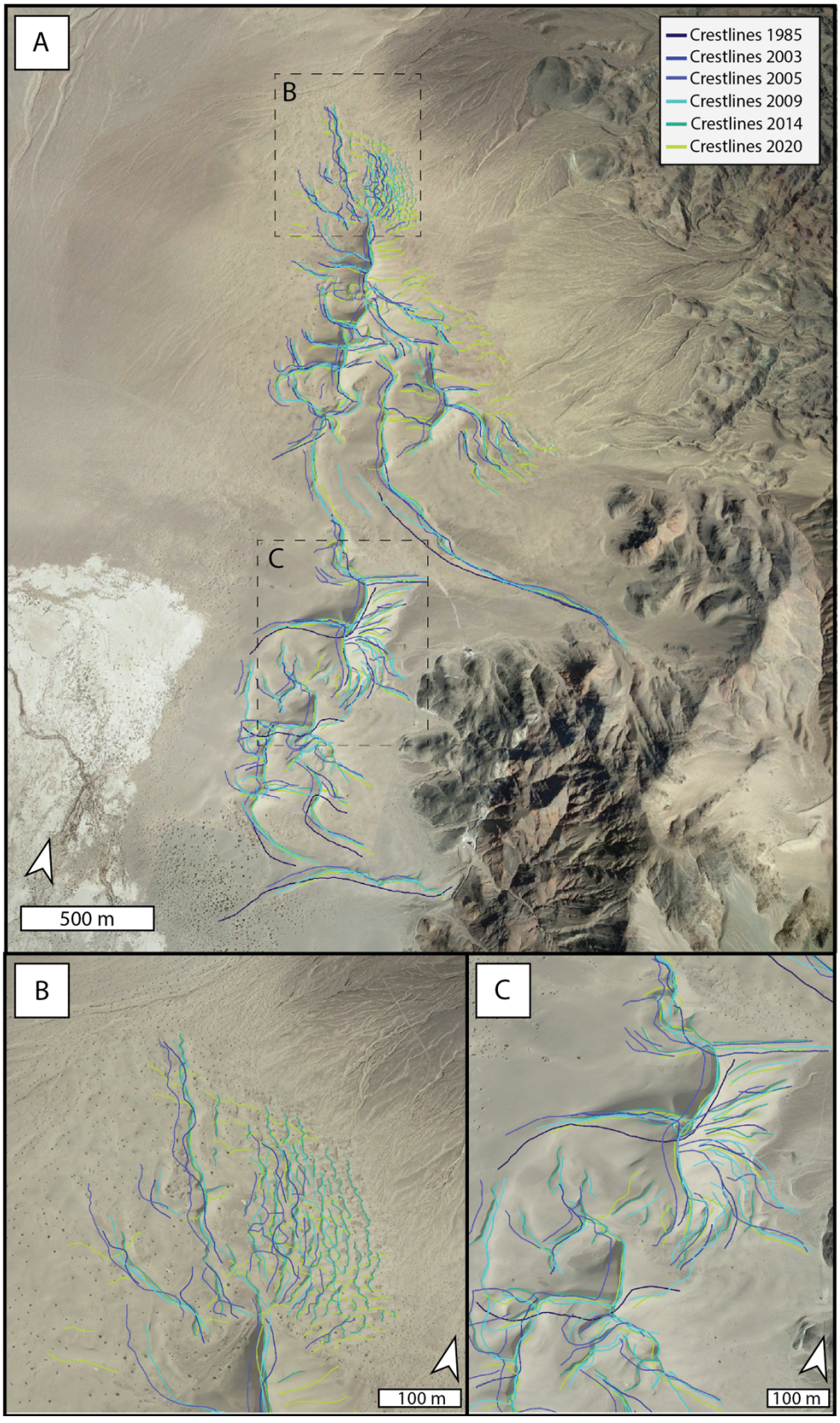
A
B
C
Crestlines 1985
Crestlines 2003
Crestlines 2005
Crestlines 2009
Crestlines 2014
Crestlines 2020
500 m
B
100 m
C
100 m

Figure 4.5. Crestline evolution through time from analysis of orbiter images. Colored lines (dark blue- light green) show crestlines mapped on historical images acquired between 1985 – 2020. Minimal net-migration occurred during this 37 year period, though back-and -forth migration of dune crests occurs frequently. The size and shape of the dunes does not vary significantly (especially for the larger star dunes). The overall dune field extent was consistent across all images. Background image acquired in 2014. (A) View of the Ibex dune field and mapped crestlines. (B) View of smaller transverse dunes in the north of the study area. Between 2014 (cyan) and 2020 (light green), the orientation of the primary crests of these dunes rotated 90º, from ~north-south to ~east-west. (C) View of the largest star dune in the study area. Smaller crests on the dune are visible in some images, and change position more often than the largest crests. Some sections of the crest have experiences very little (0-10 m) displacement over the observation period.

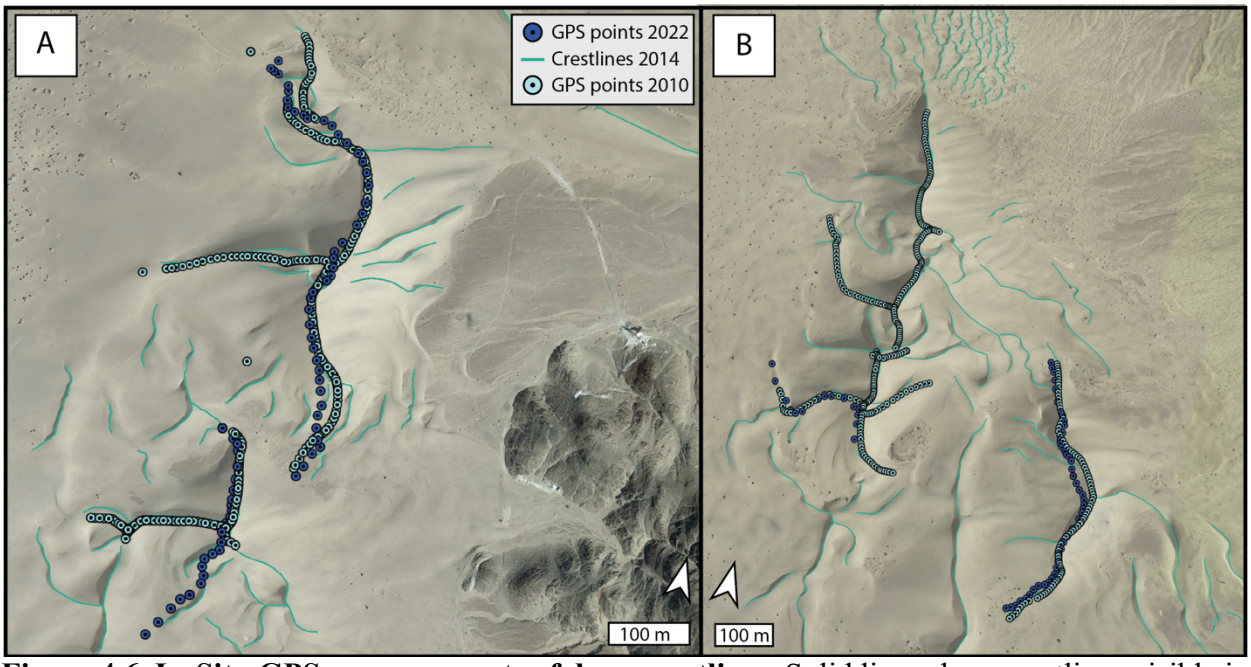

Figure 4.6. In-Situ GPS measurements of dune crestlines. Solid lines show crestlines visible in the orbital image acquired in 2014. Points show GPS measurements, made in both 2010 (light blur) and 2022 (dark blue). In several areas there was 0 net displacement between 2010 and 2022. Maximum measured displacements were ~30-50 m. Background image acquired in 2014. (A) Southern portion of the ibex study area, showing the largest star dune in the field. The ~north-south crestline of the dune has experienced between 0-30 m of net-migration in the past 12 years. (B) Dunes in the northern portion of the study area. The largest dunes shown here, especially those mapped in-situ, have also experienced very little net-migration over the observation period.

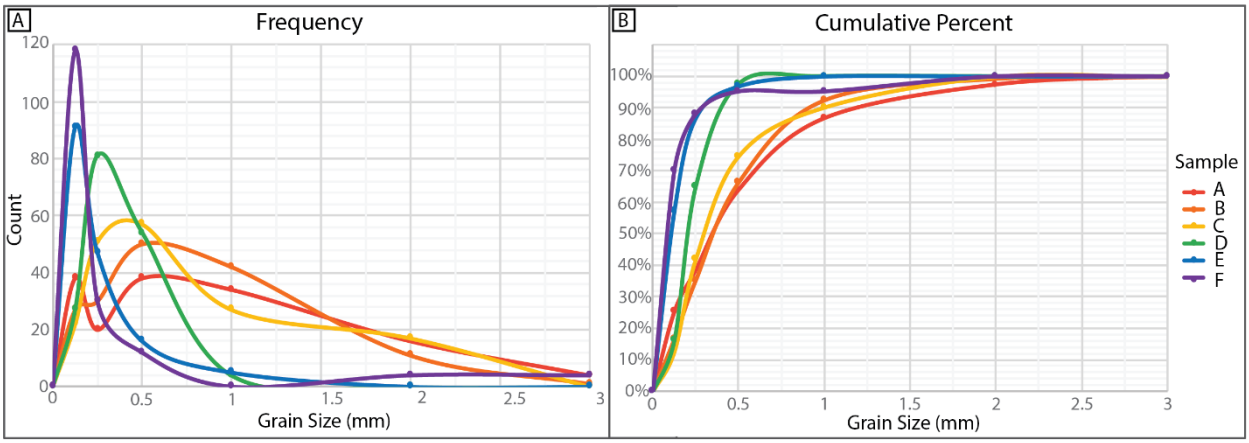

Figure 4.7. Grain size frequency distributions. See Figs. 4.1, 4.2, and 4.3 for additional information on sample locations. (A) Grain size frequency plot, produced based on our analysis of samples A-D from the Ibex study area, as well as E-F collected from Little Dumont, which were processed into thin sections. (B) Cumulative percent by grain size of the same samples. The analysis shows that >85% of each sample consisted of grains < 1 mm.

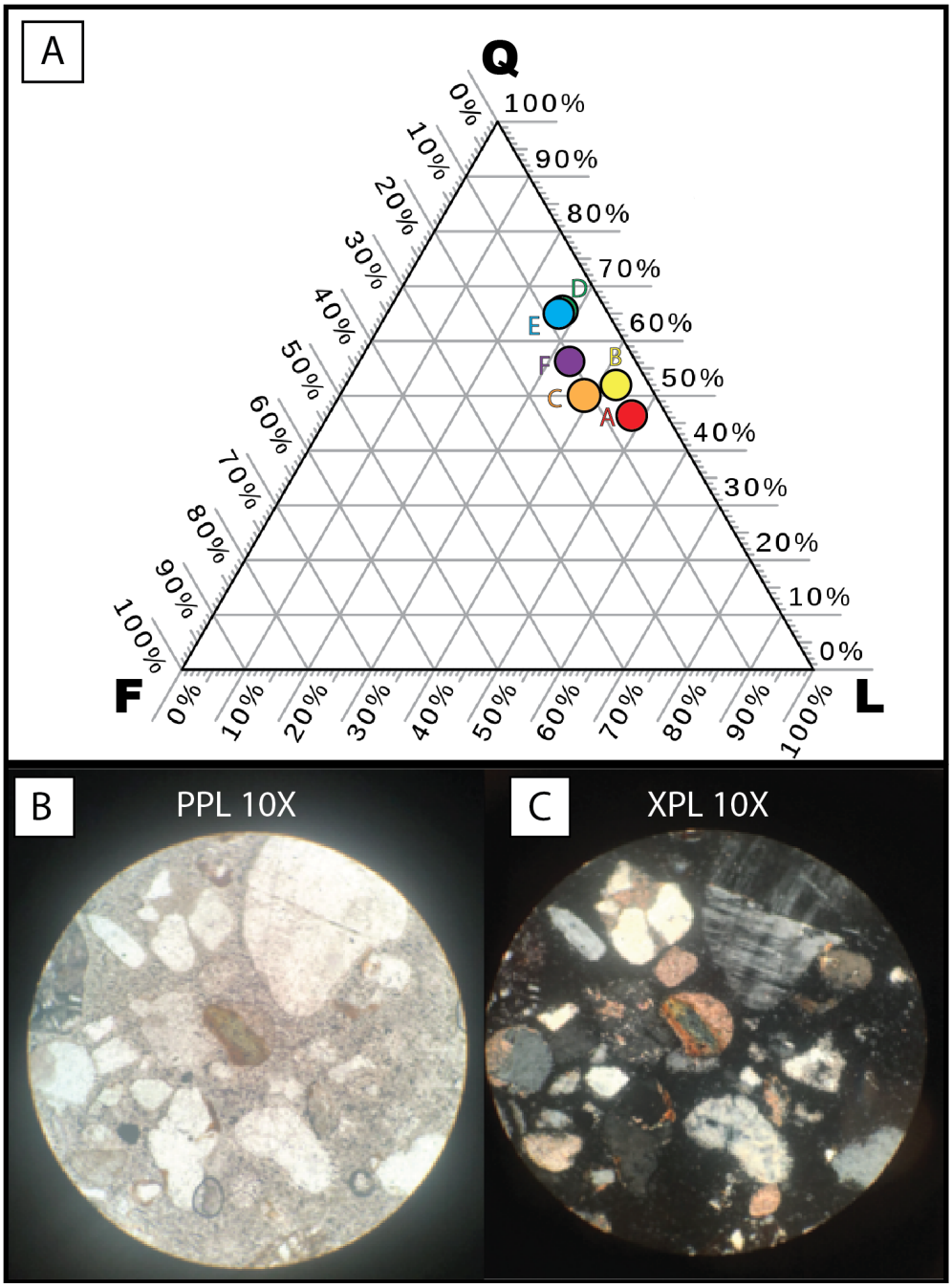

Figure 4.8. Composition of the thin sections. (A) Quartz-Feldspar-Lithics (QFL) ternary diagram showing the sample compositions. All six samples are compositionally similar to a sublitharenite sandstone. The two samples collected from dunes (D -- collected from Ibex, and E -- collected from Little Dumont) have nearly identical compositions. (B) Sample of thin section A, under plane polarized light and 10x magnification, showing the variety of mineralogies of the grains. (B) Sample of thin section A, under cross polarized light and 10x magnification, showing a variety of mineralogies of the grains.

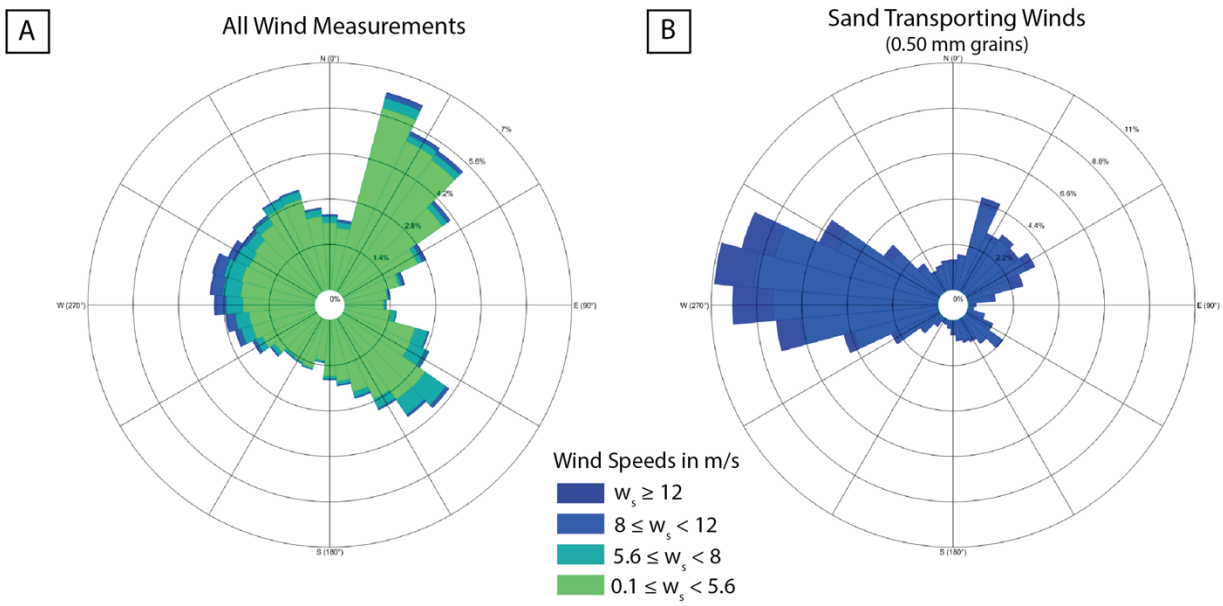

Figure 4.9. Wind speed measurements from March, 2021 to October, 2022. Wind rose diagrams showing wind origin, frequency and magnitude. (A) All wind measurements during the study period, for all wind speeds ≥0.1 m/s. The most frequent winds originate from the northeast, though winds from the west and southeast also contribute. (B) Wind speeds capable of transporting 0.50 mm grains. Using a threshold value for minimum wind speed required to initiate grain transport (8.43 m/s), only the winds ≥ this threshold value are shown. The winds capable of initiating transport of these grains are primarily from the west, which would result in net transport to the east.

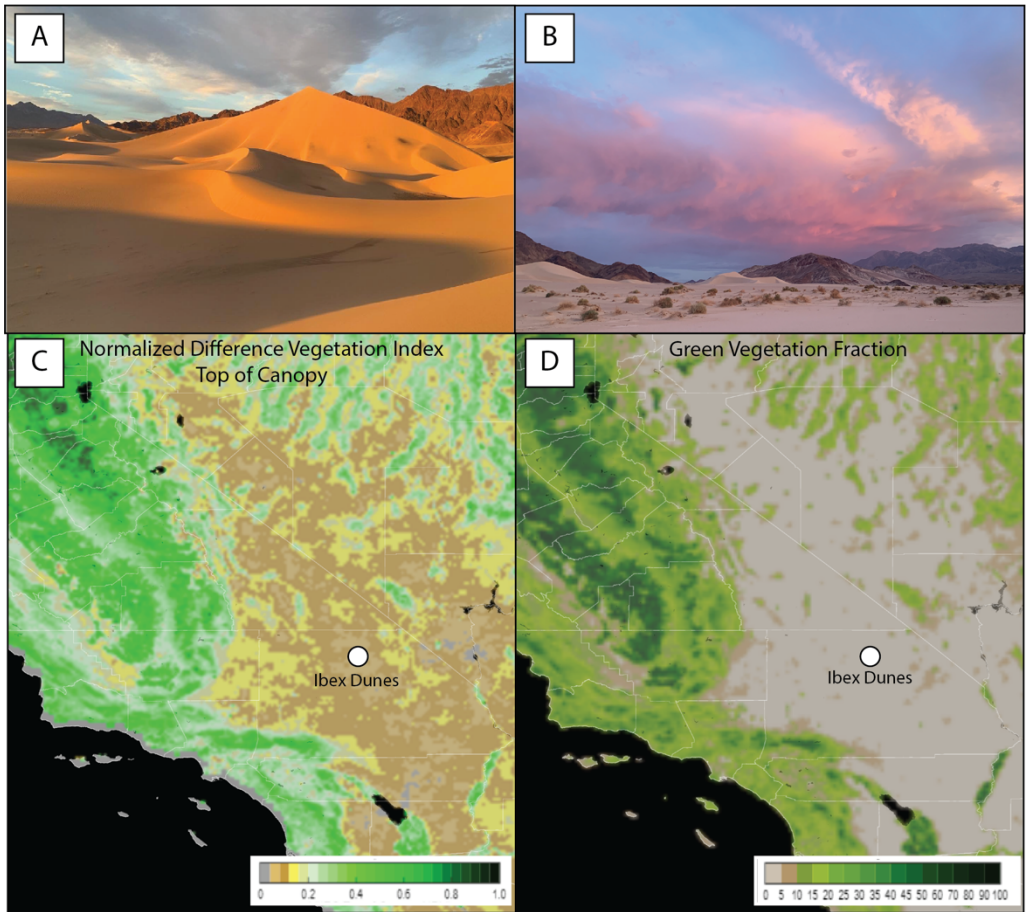

Figure 4.10. Vegetation coverage. In-situ and orbital view of vegetation at the Ibex dunes study area. (A) A large dune, with the Saddle Peak Hills visible in the background. No vegetation was seen on the dunes, nor in sand-covered interdune spaces. (B) Small dunes in the southern portion of the Ibex study area, with the Saddle Peak Hills in the background. At the margins of the dune field, where the underlying alluvial fan material was exposed, sparse vegetation occurs. The vegetation does not extend onto the dunes. (C) NDVI TOC map of southwestern California. The Ibex study area has a NDVI value of <0.04, meaning the vegetation in the region is extremely sparse. Map provided at 0.009-degree resolution by NOAA. (D) GVF map of southwestern California, again highlighting the overall extremely sparse vegetation at the study site and in the surrounding region. The calculated GVF for the area is 0-5%, and the map is provided at 4km/pixel resolution by NOAA.

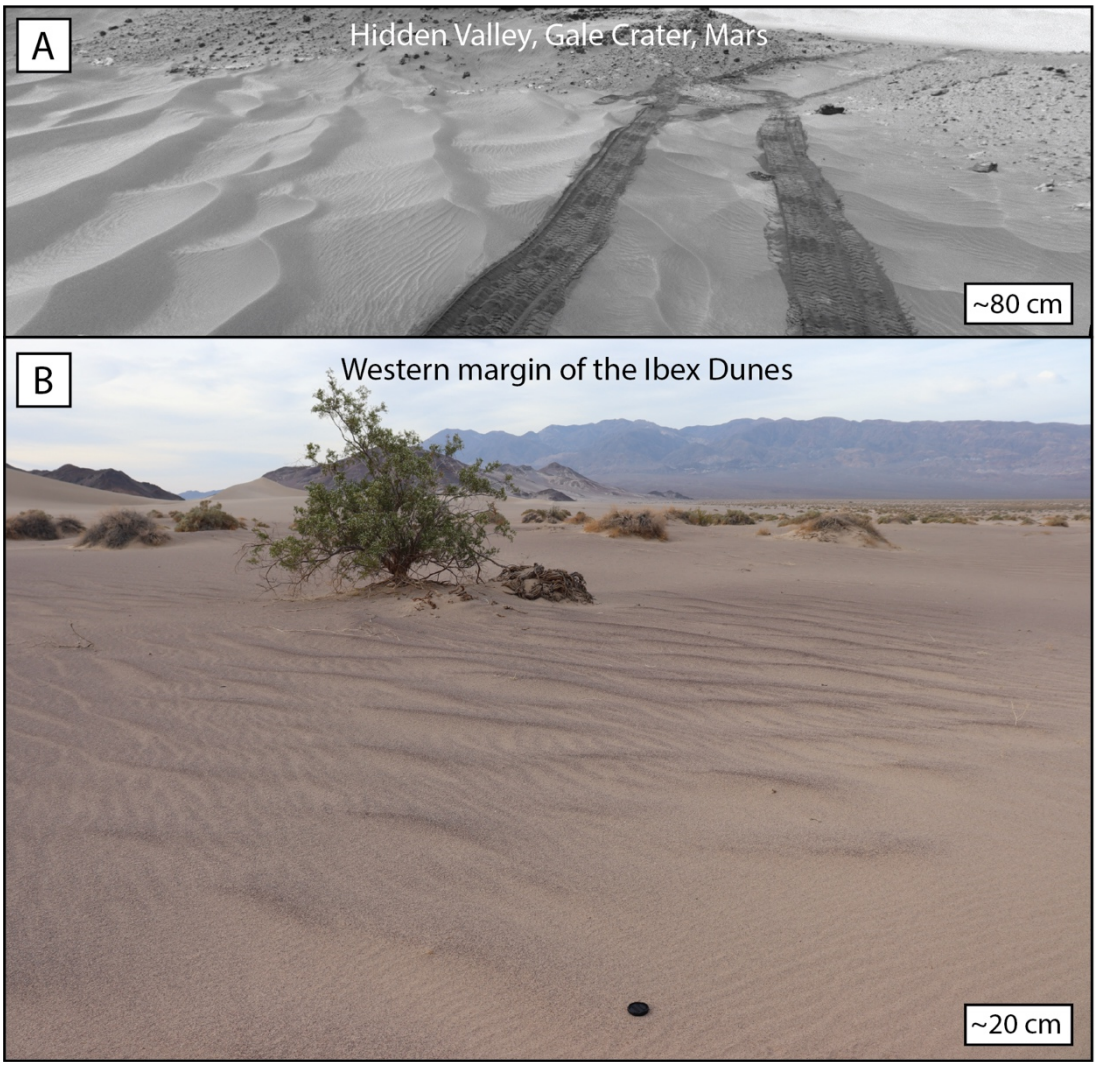

Figure 4.11. The Ibex dunes as a Mars analog: Comparison to the Hidden Valley Ripples in Gale crater, Mars. (A) Image of large compound ripples in Hidden Valley, Gale crater, acquired by the Curiosity rover. The larger (~10 cm high) ripples are superposed by smaller (~ a few cm) impact ripples. These ripples posed a driving hazard to the rover, and the attempted traverse was aborted (Bretzfelder and Day, 2021 and references therein). These ripples were found to be composed of fine grains and dust, armored by coarser grains. (B) Compound ripples at the Ibex study site. These ripples were armored by coarse (dark) grains, which are concentrated on the crests of both the primary and secondary ripples. The interiors of these ripples were composed of finer grains. Lens cap (~5 cm) pictured for scale.

Table 4.1. Total Dose Rate and OSL Ages. Sample information and results from OSL analysis of quartz grains collected from (1) the alluvial fan on which the Ibex dunes formed and (2) the toe of a large star dune in the study area.

Sample Information	Latitude (DD) N	Longitude (DD) W	Depth (m)	K (%)[a]	Th (ppm) [b]	U (ppm)[b]	Total Dose Rate ± 1σ (Gy/ka)	Equivalent Dose ± 1σ (Gy) [c]	OSL age ± 1σ (ka) [d]
Alluvial fan material collected to the north of the main Ibex dunes. (OSL-N)	35.72	116.38	0.40 ±0.005	3.1	8.5	2.36	4.43 ± 0.174	11.88 ± 2.06	2.68 ± 0.48
Collected near the toe of the large star dune in the Ibex field. (OSL-S)	35.69	116.37	0.43 ±0.005	3.4	6.5	1.84	4.45 ± 0.182	0.71 ± 0.12	0.16 ± 0.03

Grain size used 185–215 μm.
Radionuclide conversion factor after Guerin et al., 2011; α attenuation factor after Brennan et al., 1991; β attenuation factor after Guerin et al., 2012.
β etch depth attenuation after Bell, 1979, alpha efficiency after Olley et al., 1998
Cosmic dose rates after Prescott and Hutton, 1994.
Water content: 0.79 % for J1658 and 0.42% for J1659.

[a] K contents derived via ICP-OES with relative uncertainties of 5%.
[b] U and Th contents derived via ICP-MS with relative uncertainties of 5%.
[c] Minimum age model (MAM) after Galbraith et al., 1999 is used with 10% and three parameters.
[d] Ages are calculated in DRAC-calculator v. 1.2 (Durcan et al., 2015).

Table 4.2. Sand Grain Size Distributions. Information on the distribution of grain sizes for each thin section analyzed. Thin sections A-D were collected at the Ibex study area, and samples E-F were collected from nearby Little Dumont for comparison (see Fig. 4.3).

Thin Section	Location Description	D_{10} (mm)	D_{50} (mm)	D_{90} (mm)
A	Granule ripples to the west of the Ibex dunes. (Fig. 3A)	0.50	0.41	1.21
B	Compound ripples in an interdune space. (Fig. 3B)	0.10	0.50	1.00
C	Compound ripples on the lee face of a dune in the Ibex field. Primary ripples were armored by coarse grains. (Fig. 3C)	0.10	0.30	1.00
D	Crest of a large star dune in the Ibex field. (Fig. 3D)	0.10	0.20	0.40
E	Crest of a dune at Little Dumont. (Fig. 3E)	0.05	0.10	0.40
F	Granule ripples to the west of the Little Dumont dunes. (Fig. 3F)	0.05	0.10	0.30

4.9 Appendix (Supplemental Materials)

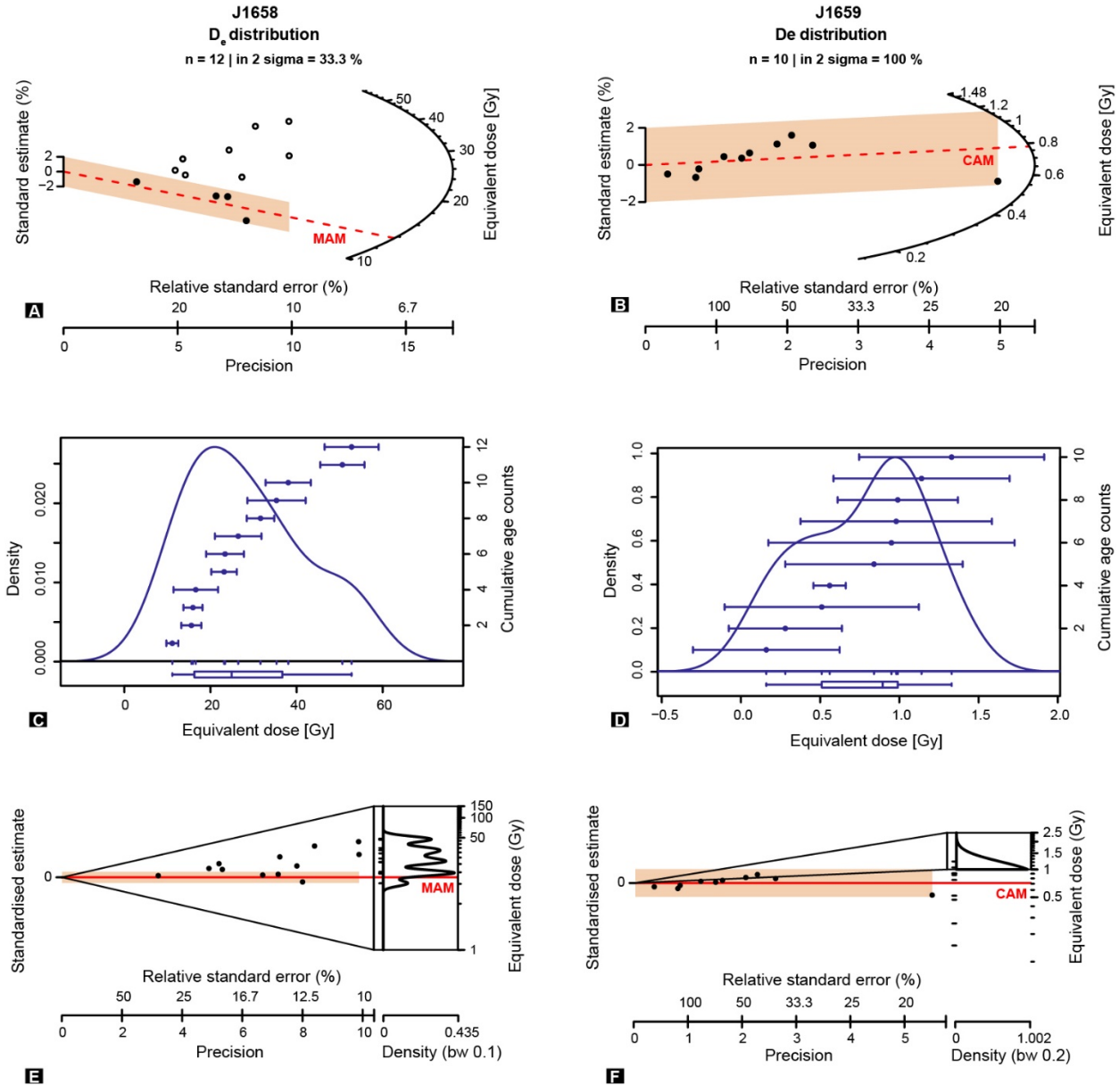

Figure 4.S1 OSL Analysis results Plots showing the scatter of small-aliquot D_e values. A) Radial plots showing the scatter of D_e values for the sample J1658 (OSL-N) with solid circles representing the values within 2σ error. B) Radial plots for the samples J1659 (OSL-S). C) and D) showing the kernel density distribution (KDE plots) of samples J1658 (OSL-N) and J1659 (OSL-S), respectively. E) and F) are abanico plots showing D_e values for the samples J1658 (OSL-N) and

J1659 (OSL-S), respectively. The bars and the dashed red lines in A), B), display the ± 2σ range and the MAM D_e, respectively. E), and F) display the ± 2σ range and the CAM D_e, respectively.

Figure 4.S2 OSL-S Sample location. This image was taken prior to collection of sample OSL-S. This image shows the depth from which the sample was collected, as well as the discernable layers in this portion of the dune. These layers indicate that this portion of the dune has remained stationary since the deposition of these layers.

4.10 References

Achilles, C. N., Downs, R. T., Ming, D. W., Rampe, E. B., Morris, R. V., Treiman, A. H., Morrison, S. M., Blake, D. F., Vaniman, D. T., Ewing, R. C., Chipera, S. J., Yen, A. S., Bristow, T. F., Ehlmann, B. L., Gellert, R., Hazen, R. M., Fendrich, K. V., Craig, P. I., Grotzinger, J. P., … Morookian, J. M. (2017). Mineralogy of an active eolian sediment from the Namib dune, Gale crater, Mars. *Journal of Geophysical Research: Planets*, *122*(11), 2344–2361. https://doi.org/10.1002/2017JE005262

Arnold, L.J. Roberts, R.G., 2009. Stochastic modelling of multi-grain equivalent dose (D_e) distributions: Implications for OSL dating of sediment mixtures. Quaternary Geochronology 4, 204–230.

Arvidson, R. E., Iagnemma, K. D., Maimone, M., Fraeman, A. A., Zhou, F., Heverly, M. C., Bellutta, P., Rubin, D., Stein, N. T., Grotzinger, J. P., & Vasavada, A. R. (2017). Mars Science Laboratory Curiosity Rover Megaripple Crossings up to Sol 710 in Gale Crater. *Journal of Field Robotics*, *34*(3), 495–518. https://doi.org/10.1002/rob.21647

Barrett, J. E., Virginia, R. A., Wall, D. H., Doran, P. T., Fountain, A. G., Welch, K. A., & Lyons, W. B. (2008). Persistent effects of a discrete warming event on a polar desert ecosystem. *Global Change Biology*, *14*(10), 2249–2261. https://doi.org/10.1111/j.1365-2486.2008.01641.x

Blackwelder, E. (1933). Lake Manly: An Extinct Lake of Death Valley. *Geographical Review*, *23*(3), 464. https://doi.org/10.2307/209632

Bøtter-Jensen, L., Andersen, C., Duller, G., Murray, A., 2003. Developments in radiation, stimulation and observation facilities in luminescence measurements. Radiation Measurements 37, 535–541.

Bøtter-Jensen, L., Bulur, E., Duller, G.A.T., Murray, A.S., 2000. Advances in luminescence instrument systems. Radiation Measurements 32, 523–528.

Bretzfelder, J. M. and M. Day (2021) "Alien Aeolian Bedforms: A Comparative Sedimentary Analysis of the Dingo Gap Bedform and Hidden Valley Ripple Traverses, Gale Crater, Mars." *Journal of Geophysical Research: Planets.* doi: 10.1029/2021JE006904

Bridges, N. T., Spagnuolo, M. G., de Silva, S. L., Zimbelman, J. R., & Neely, E. M. (2015). Formation of gravel-mantled megaripples on Earth and Mars: Insights from the Argentinean Puna and wind tunnel experiments. *Aeolian Research*, *17*, 49–60. https://doi.org/10.1016/j.aeolia.2015.01.007

Cary, S. C., McDonald, I. R., Barrett, J. E., & Cowan, D. A. (2010). On the rocks: The microbiology of Antarctic Dry Valley soils. *Nature Reviews Microbiology*, *8*(2), 129–138. https://doi.org/10.1038/nrmicro2281

Clarke, M. L., Richardson, C. A., & Rendell, H. M. (1995). Luminescence dating of mojave desert sands. *Quaternary Science Reviews*, *14*(7), 783–789. https://doi.org/10.1016/0277-3791(95)00051-8

Corinne Carter, Mingshi Chen, Zhangyan Jiang, & Yunyue Yu. (2020). *VI ALGORITHM THEORETICAL BASIS DOCUMENT VERSION HISTORY SUMMARY*.

Day, M., & Zimbelman, J. R. (2021). Ripples, megaripples, and TARs, Oh, My! Recommendations regarding Mars aeolian bedform terminology. *Icarus*, *369*, 114647. https://doi.org/10.1016/j.icarus.2021.114647

de Silva, S. L., Spagnuolo, M. G., Bridges, N. T., & Zimbelman, J. R. (2013). Gravel-mantled megaripples of the Argentinean Puna: A model for their origin and growth with implications for Mars. *GSA Bulletin*, *125*, 1912–1929. http://dx.doi.org/10.1130/B30916.1

Di Achille, G., & Hynek, B. M. (2010). Ancient ocean on Mars supported by global distribution of deltas and valleys. *Nature Geoscience*, *3*(7), Article 7. https://doi.org/10.1038/ngeo891

DICKINSON, W. R., BEARD, L. S., BRAKENRIDGE, G. R., ERJAVEC, J. L., FERGUSON, R. C., INMAN, K. F., KNEPP, R. A., LINDBERG, F. A., & RYBERG, P. T. (1983). Provenance of North American Phanerozoic sandstones in relation to tectonic setting. *GSA Bulletin*, *94*(2), 222–235. https://doi.org/10.1130/0016-7606(1983)94<222:PONAPS>2.0.CO;2

Durán, O., & Herrmann, H. J. (2006). Vegetation Against Dune Mobility. *Physical Review Letters*, *97*(18), 188001. https://doi.org/10.1103/PhysRevLett.97.188001

Durcan J.A., King G.E., Duller G.A.T., 2015. DRAC: Dose Rate and Age Calculator for trapped charge dating. Quaternary Geochronology 28: 54–61.

Edwards, S. R. (1993). Luminescence dating of sand from the Kelso Dunes, California. *Geological Society, London, Special Publications*, *72*(1), 59–68. https://doi.org/10.1144/GSL.SP.1993.072.01.07

Galbraith, R.F., Roberts, R.G., Laslett, G.M., Yoshida, H., Olley, J.M., 1999. Optical dating of single and multiple grains of quartz from Jinmium rock shelter, northern Australia: Part I, experimental design and statistical models. Archaeometry 41, 339–364.

Gottscho, A. D., Marks, S. B., & Jennings, W. B. (2014). Speciation, population structure, and demographic history of the Mojave Fringe-toed Lizard (Uma scoparia), a species of conservation concern. *Ecology and Evolution*, *4*(12), 2546–2562. https://doi.org/10.1002/ece3.1111

Hayward, R.K., Fenton, L.K., and Titus, T.N., 2014, Mars Global Digital Dune Database

(MGD(3)): Global dune distribution and wind pattern observations: ICARUS, v. 230, p. 38–46, doi:10.1016/j.icarus.2013.04.011.

Hooke, R. LeB. (1999). Lake Manly(?) Shorelines in the Eastern Mojave Desert, California. *Quaternary Research*, *52*(3), 328–336. https://doi.org/10.1006/qres.1999.2080

Huntley, D. J., Godfrey-Smith, D. I., & Thewalt, M. L. W. (1985). Optical dating of sediments. *Nature*, *313*(5998), 105–107. https://doi.org/10.1038/313105a0

Jiang, Z., Yunyue Yu, Ivan Csiszar, Mingshi Chen, Feng Shao, & Yuxiang He. (2021). *GVFP ALGORITHM THEORETICAL BASIS DOCUMENT VERSION 3.0 AUTHORS:*

John Weier & David Herring. (2000, August 30). *Measuring Vegetation (NDVI & EVI)* [Text.Article]. NASA Earth Observatory. https://earthobservatory.nasa.gov/features/MeasuringVegetation

Kim Stringfellow. (2016). *How the Timbisha Shoshone Got Their Land Back*. THE MOJAVE PROJECT. https://mojaveproject.org/dispatches-item/how-the-timbisha-got-their-land-back/

Laity, J. E., & Bridges, N. T. (2009). Ventifacts on Earth and Mars: Analytical, field, and laboratory studies supporting sand abrasion and windward feature development. *Geomorphology*, *105*(3), 202–217. https://doi.org/10.1016/j.geomorph.2008.09.014

Lapotre, M. G. A., Ehlmann, B. L., Minson, S. E., Arvidson, R. E., Ayoub, F., Fraeman, A. A., Ewing, R. C., & Bridges, N. T. (2017). Compositional variations in sands of the Bagnold Dunes, Gale Crater, Mars, from visible-shortwave infrared spectroscopy and comparison with ground truth from the Curiosity Rover. *Journal of Geophysical Research E: Planets*, *122*(12), 2489–2509. https://doi.org/10.1002/2016JE005133

Lapôtre, M. G. A., Ewing, R. C., & Lamb, M. P. (2021). An Evolving Understanding of Enigmatic Large Ripples on Mars. *Journal of Geophysical Research: Planets*, *126*(2), e2020JE006729. https://doi.org/10.1029/2020JE006729

Liu, J., Michalski, J. R., & Zhou, M.-F. (2021). Intense subaerial weathering of eolian sediments in Gale crater, Mars. *Science Advances*, *7*(32), eabh2687. https://doi.org/10.1126/sciadv.abh2687

Lü, Ping, Zhibao Dong, & Olivier Rozier. (n.d.). *The Combined Effect of Sediment Availability and Wind Regime on the Morphology of Aeolian Sand Dunes—Lü—2018—Journal of Geophysical Research: Earth Surface—Wiley Online Library*. Retrieved November 18, 2023, from https://agupubs.onlinelibrary.wiley.com/doi/full/10.1029/2017JF004361

MacDonald, A.A., 1966. *The Dumont Dune System of the Northern Mojave Desert California*, San Fernando Valley State College, Northridge, CA.

Madsen, A. T., & Murray, A. S. (2009). Optically stimulated luminescence dating of young sediments: A review. *Geomorphology*, *109*(1), 3–16. https://doi.org/10.1016/j.geomorph.2008.08.020

Mahan, S. A., Miller, D. M., Menges, C. M., & Yount, J. C. (2007). Late Quaternary stratigraphy and luminescence geochronology of the northeastern Mojave Desert. *Quaternary International*, *166*(1), 61–78. https://doi.org/10.1016/j.quaint.2006.12.010

Matsubara, Y., & Howard, A. D. (2009). A spatially explicit model of runoff, evaporation, and lake extent: Application to modern and late Pleistocene lakes in the Great Basin region, western United States. *Water Resources Research*, *45*(6). https://doi.org/10.1029/2007WR005953

Miura, T., Muratsuchi, J., & Vargas, M. (2018). Assessment of cross-sensor vegetation index compatibility between VIIRS and MODIS using near-coincident observations. *Journal of Applied Remote Sensing*, *12*(4), 045004. https://doi.org/10.1117/1.JRS.12.045004

Murphy, R. W., Trépanier, T. L., & Morafka, D. J. (2006). Conservation genetics, evolution and distinct population segments of the Mojave fringe-toed lizard, Uma scoparia. *Journal of Arid Environments*, *67*, 226–247. https://doi.org/10.1016/j.jaridenv.2006.09.023

Murray, A.S., Wintle, A.G., 2000. Luminescence dating of quartz using an improved single-aliquot regenerative-dose protocol. Radiation Measurements 32, 57–73.

Murray, A.S., Wintle, A.G., 2003. The single aliquot regenerative dose protocol: potential for improvements in reliability. Radiation Measurements 37, 377–381.

Narteau, C., Valdez, A., & Hargitai, H. (2014). Star Dune. In H. Hargitai & Á. Kereszturi, *Encyclopedia of Planetary Landforms* (pp. 1–5). Springer New York. https://doi.org/10.1007/978-1-4614-9213-9_447-1

National Park Service. (n.d.). *Sand Dunes—Death Valley National Park (U.S. National Park Service)*. Retrieved October 11, 2023, from https://www.nps.gov/deva/learn/nature/sand-dunes.htm

Nelson, M. S., Gray, H. J., Johnson, J. A., Rittenour, T. M., Feathers, J. K., & Mahan, S. A. (2015). User Guide for Luminescence Sampling in Archaeological and Geological Contexts. *Advances in Archaeological Practice*, *3*(2), 166–177. https://doi.org/10.7183/2326-3768.3.2.166

Nichols, G. (2009). *Sedimentology and stratigraphy* (2nd ed). Wiley-Blackwell.

Nielson, J., & Kocurek, G. (1987). Surface processes, deposits, and development of star dunes: Dumont dune field, California. *Geological Society of America Bulletin*, *99*(2), 177. https://doi.org/10.1130/0016-7606(1987)99<177:SPDADO>2.0.CO;2

NOAA. (2011). *Visible Infrared Imaging Radiometer Suite (VIIRS)*. National Environmental Satellite, Data, and Information Service. https://www.nesdis.noaa.gov/our-satellites/currently-flying/joint-polar-satellite-system/visible-infrared-imaging-radiometer-suite-viirs

NOAA. (2018). *NOAA VIs/GVF Website!* https://www.star.nesdis.noaa.gov/smcd/viirs_vi_web/index.php#

NPS. (n.d.). *Geology—Death Valley National Park (U.S. National Park Service)*. Retrieved October 11, 2023, from https://www.nps.gov/deva/learn/nature/geology.htm

Pavlik, B. M. (1989). Phytogeography of Sand Dunes in the Great Basin and Mojave Deserts. *Journal of Biogeography*, *16*(3), 227–238. https://doi.org/10.2307/2845259

Pye, K., & Tsoar, H. (2009). Aeolian Bed Forms. In K. Pye & H. Tsoar (Eds.), *Aeolian Sand and Sand Dunes* (pp. 175–253). Springer. https://doi.org/10.1007/978-3-540-85910-9_6

Rampe, E. B., Lapotre, M. G. A., Bristow, T. F., Arvidson, R. E., Morris, R. V., Achilles, C. N., Weitz, C., Blake, D. F., Ming, D. W., Morrison, S. M., Vaniman, D. T., Chipera, S. J., Downs, R. T., Grotzinger, J. P., Hazen, R. M., Peretyazhko, T. S., Sutter, B., Tu, V., Yen, A. S., … Treiman, A. H. (2018). Sand Mineralogy Within the Bagnold Dunes, Gale Crater, as Observed In Situ and From Orbit. *Geophysical Research Letters*, *45*(18), 9488–9497. https://doi.org/10.1029/2018GL079073

Rhodes, Edward J., (2011). Optically Stimulated Luminescence Dating of Sediments over the Past 200,000 Years. *Annu. Rev. Earth Planet. Sci.*, *39*, 461–488. https://doi.org/10.1146/annurev-earth-040610-133425

Schueth, J. D., & Laycock, D. (2022). *The Search for the World's Fastest Sand Dunes*.

Silvestro, S., Vaz, D.A., Ewing, R.C., Rossi, A.P., Fenton, L.K., Michaels, T.I., Flahaut, J., and Geissler, P.E., 2013, Pervasive aeolian activity along rover Curiosity's traverse in Gale

Crater, Mars: GEOLOGY, v. 41, p. 483–486, doi:10.1130/g34162.1.

Shao, Y., & Lu, H. (2000). A simple expression for wind erosion threshold friction velocity. *Journal of Geophysical Research: Atmospheres*, *105*(D17), 22437–22443. https://doi.org/10.1029/2000JD900304

Spalding, D. B. (1961). A Single Formula for the "Law of the Wall." *Journal of Applied Mechanics*, *28*(3), 455–458. https://doi.org/10.1115/1.3641728

Stringfellow, Kim. (2016). *How the Timbisha Shoshone Got Their Land Back*. THE MOJAVE PROJECT. https://mojaveproject.org/dispatches-item/how-the-timbisha-got-their-land-back/

US, N. P. S. (n.d.). *Hurricane Hilary in Death Valley National Park—Death Valley National Park (U.S. National Park Service)*. Retrieved October 11, 2023, from https://www.nps.gov/deva/learn/nature/hilary.htm

Vriend, N. M., Hunt, M. L., & Clayton, R. W. (2012). Sedimentary structure of large sand dunes: Examples from Dumont and Eureka dunes, California. *Geophysical Journal International*, *190*(2), 981–992. https://doi.org/10.1111/j.1365-246X.2012.05514.x

Ward, A.W., 1979, Yardangs on Mars - Evidence of recent wind erosion: Journal of Geophysical Research, v. 84, p. 8147–8166, doi:10.1029/JB084iB14p08147.

Weitz, C. M., Sullivan, R. J., Lapotre, M. G. A., Rowland, S. K., Grant, J. A., Baker, M., & Yingst, R. A. (2018). Sand Grain Sizes and Shapes in Eolian Bedforms at Gale Crater, Mars. *Geophysical Research Letters*, *45*(18), 9471–9479. https://doi.org/10.1029/2018GL078972

Wilson, I. G. (1972). Aeolian Bedforms—Their Development and Origins. *Sedimentology*, *19*(3–4), 173–210. https://doi.org/10.1111/j.1365-3091.1972.tb00020.x

Wintle, A. G. (1993). Luminescence dating of aeolian sands: An overview. *Geological Society, London, Special Publications*, *72*(1), 49–58. https://doi.org/10.1144/GSL.SP.1993.072.01.06

Yang, Z., Qian, G., Dong, Z., Tian, M., & Lu, J. (2021). Migration of barchan dunes and factors that influence migration in the Sanlongsha dune field of the northern Kumtagh Sand Sea, China. *Geomorphology*, *378*, 107615. https://doi.org/10.1016/j.geomorph.2021.107615

Yunyue Yu. (n.d.). *Center for Satellite Applications and Research—NOAA / NESDIS / STAR*. NOAA / NESDIS / STAR Website. Retrieved November 11, 2023, from https://www.star.nesdis.noaa.gov/star/index.php

Zimbelman, J. R. (2019). The transition between sand ripples and megaripples on Mars. *Icarus*, *333*, 127–129. https://doi.org/10.1016/j.icarus.2019.05.017

Zimbelman, J. R., & Williams, S. H. (2007). Eolian dunes and deposits in the western United States as analogs to wind-related features on Mars. In M. Chapman (Ed.), *The Geology of Mars: Evidence from Earth-Based Analogs* (pp. 232–264). Cambridge University Press. https://doi.org/10.1017/CBO9780511536014.010

CHAPTER 5: Sediment Motion Initiation: An Interplanetary Experimental Approach

5.1 Introduction

Aeolian sediment transport occurs across the solar system; wind-driven transport has been directly observed on Earth and Mars, and surface features interpreted to be aeolian bedforms have been imaged on Titan (e.g., Lorenz, 2014), Pluto (Telfer et al., 2018), Venus (e.g. Greely, 1989), Io (Macdondald et al., 2022) and Comet *67P*/Churyumov–Gerasimenko (Jia et al., 2017). The atmospheres of these planetary bodies are unique, and some (namely Io, Pluto, and Comet 67P) only possess ephemeral or transient atmospheres (Bourke et al., 2010; Craddock, 2011; Diniega et al., 2017, Telfer et al., 2018; Mcdonald et al., 2022). Modern Mars possesses a thin atmosphere, approximately <1% of Earth's (Table 5.1), and yet is dominated by aeolian activity. On the other end of the spectrum, aeolian dunes cover large swaths of the surface of Titan, which has an atmosphere ~4x thicker than Earth (Table 5.1). Both Mars and Titan are targets for current and upcoming surface exploration activities, motivating interest in sediment transport on these bodies.

Field and wind tunnel experiments form the basis of our understanding of particle motion initiation, but initial studies were limited to terrestrial boundary conditions and materials (Shields, 1936; Bagnold, 1937; Fletcher, 1976; Iverson and White, 1982; Iverson et al., 1987). However, the breadth of aeolian bedforms observed to date have formed under a variety of atmospheric conditions and are composed of materials with diverse properties (Table 5.1). Recent experiments by Burr et al. (2015a), and in-situ planetary observations by Baker et al. (2018), have shown that applying models developed under terrestrial boundary conditions to other planets, such as Titan and Mars, results in inaccurate predictions of particle motion initiation.

Grain motion (specifically saltation) is initiated when the surface shear velocity exceeds a fluid threshold (u_{*tf}), which is the critical shear velocity required to mobilize grains of diameter 'd' via fluid drag (Bagnold, 1941). In-situ data from the Mars Science Laboratory Curiosity rover (Curiosity) allowed Baker et al. (2018) to determine that grains on Mars are being transported below the threshold velocities predicted using analytical approximations for u_{*tf} (e.g. Shields, 1936; Bagnold, 1937; Fletcher, 1976; Iverson and White, 1982; Iverson et al., 1987; Shao and Lu, 2000). Wind tunnel experiments conducted in analog Mars and Titan conditions (Burr et al., 2015b; Swann et al., 2019), similarly resulted in u_{*tf} values that did not match model predictions. These analog experiments relied on a combination of altering fluid density, atmospheric pressure, and using analog sediments, such as crushed walnut shells (Burr et al., 2015b; Swann et al., 2019). Given the persisting discrepancy between experiments and planetary observations, we undertook a new experimental approach to understanding aeolian motion initiation.

This study used an open-plan wind tunnel (Fig. 5.1), operating at ambient atmospheric conditions, and six types of low-density plastic spheres as analog grains (Table 5.2), in order to develop an expression for u_{*tf} that predicts motion initiation under a range of conditions. Using pre-fabricated and custom-produced materials we studied analogs for particle behavior in a range of gravity and atmospheric environments. The resulting expression, created based on a fit to our experimental results, is consistent with observations from the Martian surface.

5.2 Methods

5.2.1 Controls on Sediment Motion and Analog Parameters

This study investigates in the initiation of saltation, which occurs at the threshold friction velocity (u_{*tf}). For a grain with diameter d, u_{*tf} is controlled by the relationship between drag (F_d), lift (F_L), gravity (F_g), the normal force (F_N, dependent on the geometry of the grain pocket), and interparticle cohesion (F_c). Motion can occur once the 'forward' and upward components of the driving forces (F_d and F_L) overcome the 'backward' and downward components of the resistive forces (F_g, F_N and F_c). This balance has been the basis of previous work to create expressions for u_{*tf} (e.g. Phillips, 1980). For grains with d > 200 μm, F_c becomes negligible compared to the gravitational force (Iversen et al., 1987, Shao and Lu, 2000). Grains with d > 200 μm have either been directly observed or modeled to be involved in aeolian transport on the planetary bodies listed in Table 5.1. For the purposes of the proposed study, we will be simulating the motion of particles in this gravity-dominated regime and ignoring any interparticle cohesion.

In order to study grain behavior under extraterrestrial boundary conditions while using a tunnel operating at ambient Earth atmospheric conditions, we must identify analog grains that experience the same balance of forces as the grains on the planetary body of interest. We relied on buoyancy similitude to achieve this; by using particles which are dynamically equivalent to non-terrestrial sediments. Specifically, we used the submerged weight:

$$\textbf{(1)}\ Submerged\ Weight\ (\omega) = g(\rho_{material} - \rho_{atm})$$

Where g is the gravitational acceleration, $\rho_{material}$ is the material density and, ρ_{atm} is the atmospheric density. This parameter was used by Swann et al. (2019) in their wind tunnel studies, and here we used ω to match particle properties (namely density) to analogous planetary environmental conditions. The upward buoyancy force is a component of F_L, and works opposite F_g (Fig. 5.2B), impacting the amount of wind required to initiate saltation. The downward force of gravity is due to particle mass, which is dictated by both material density and particle diameter. The dimensionless diameter:

$$\textbf{(2)}\ D_* = d(\rho_{atm}\omega/\mu)^{1/3}$$

considers the grain diameter (d), the particle buoyancy (ω), atmospheric density, and atmospheric viscosity (μ; Swann, 2019). The particle diameter has historically been used to model threshold shear velocities (u_{*tf} ; e.g., Shields, 1936; Bagnold, 1937; Fletcher, 1976; Iverson and White, 1982; Iverson et al., 1987; Shao and Lu, 2000), and the dimensionless diameter allows comparison of grains across a wide range of boundary conditions (Swann et al., 2019).

5.2.2 Analog Grains

By using the submerged weight to match analog grain buoyancies in terrestrial conditions to those on the planetary bodies of interest, we identified six suitable analog grain types, which were included in the experiments described below. Table tennis balls, ball pit balls, hydrophilic plastic beads (in their dry state), and three densities of 3D printed spheres were used; their specifications are listed in Table 5.2 (Fig. 5.3). Appropriate analog grains were identified for nitrogen ices on Pluto, organic compounds on Titan, basalt and SO_2 ice on Io, and basalt sands on Mars (Tables 5.1

and 5.2). Venusian saltation is poorly constrained due to the lack of surface information, and a suitable analog would require grains with densities similar to quartz or basalt. As this study was focused on using low density plastics rather than natural materials, Venusian conditions were not directly studied as part of this work.

5.2.3 Experimental Procedure and Equipment

The wind tunnel used to conduct these experiments is operated by the University of California Los Angeles. The open-flow tunnel operates at ambient temperature and pressure and measures 7 m x 2 m x 1 m (Fig. 5.1A). The fan is capable of generating wind speeds of up to 14 m/s, which was sufficient to mobilize five of the six types of grains studied. The PLA 2 grains (Table 5.2, Fig. 5.3B) required slightly higher windspeeds, and a separate device was used to generate faster wind flow for those experiments (a Ryobi cordless jet fan leaf blower placed 72 cm upwind of the test grains), though the other components of the experimental set up remained the same as in the other experiments. Flow in the wind tunnel moves towards the fan, and grains mobilized during experiments are caught in a sediment trap at the downwind end of the tunnel. Calibration tests of the tunnel indicated that the most consistent flow occurred approximately 2-3 m upwind from the fan, and experiments for this study were conducted in this portion of the tunnel.

This study investigated grain saltation, and in order for grains to saltate, rather than roll, the (immobile) bed on which the grains rest must have a similar roughness scale to the grains (Fig. 5.1B). If a grain is subject to a wind flow while on a relatively flat bed, the grain will begin rolling, as there is nothing impeding that motion. However, if the grain is resting in a ‘pocket’ between similarly sized grains, the geometry of the pocket may require the grain to saltate to escape the

'pocket.' For these experiments, beds of the appropriate roughness (test beds) were constructed using spheres of similar diameters to the analog grains being used (Figs. 5.1B, 5.4). Test beds for the table tennis and ball pit balls measured 2 m in length, while the bed used for the PLA spheres measured 30.5 cm, and the one used for the hydrophilic plastic beads measured 10 cm in length. The test bed lengths were determined based on the size of the analog grains, as well as their expected saltation lengths.

Experimental runs were recorded by two cameras, one mounted above the tunnel, with an overhead view of the test bed, and one on the side of the tunnel. Experiments began with an initial arrangement of grains on the test bed. Wind speeds were incrementally increased until motion was initiated, and then further increased until motion was 'continuous' across the bed, if possible. For the purposes of this experiment, continuous motion was defined as motion of ~30-50% of the grains present on the bed. Wind speeds were then decreased until motion ceased. Prior to the next run, the initial arrangement of grains was reset. Wind speeds were measured using three pitot tube anemometers, manufactured by PCE instruments (PCE-HVAC 2 model). The pitot tubes were mounted 5 (Z_1), 10 (Z_2), and 20 (Z_3) cm above the test surface (Fig. 5.4). The anemometer displays were mounted to be visible from outside of the tunnel, and the displayed measurements were recorded throughout the experiments. Wind speed was recorded once per second, and thresholds are reported as the average of three measurements: the value at the instant of initial saltation, the previous second, and the second immediately following. These values were then averaged across the five runs conducted for each of the six analog grain types. All analysis of video footage and sensor data was conducted by the same individual to mitigate variations in footage analysis.

5.3 Results

5.3.1 Motion initiation: The fluid threshold.

Saltation was achieved for all six analog grain types, enabling measurement of u_{*tf}, and results are listed in Table 5.3. The u_{*tf} value was calculated from the measured critical wind speed (U_{cr}) using the 'law of the wall' (Spalding, 1961):

$$\textbf{(3)}\ U_{cr} = (u_{*tf}/\kappa)(\ln(\tfrac{Z_n}{Z_0}))$$

Where κ is the von Kármán constant (0.4), Z_n is the measurement height above the test bed (either Z_1, Z_2 or Z_3), and Z_0 is the roughness length scale. Here, we approximate Z_0 as 75% of the diameter of the analog grain being investigated. The results are plotted in Figure 5.5, and a logarithmic fit to the experimental data yields the expression:

$$\textbf{(4)}\ \boldsymbol{u_{*tf} = -0.265 * \ln(\omega) + 3.4744}$$

$$\boldsymbol{(R^2 = 0.7678)}$$

Where ω is the submerged weight of the grain.

5.3.2 Sustaining and terminating particle motion: The general and impact thresholds.

As saltating grains impact the bed, they can transfer enough energy to cause the impacted particles to saltate, which can initiate motion across the entire bed (Kok, 2010). This cascading effect of saltating particles has been shown to be important to sediment transport on Mars, where available wind speeds may initially mobilize only a few particles. At higher shear velocities, particle motion

is continuous across the bed, which defines the general threshold (u_{*tg}). Particle motion terminates when the shear velocity falls below the impact threshold (u_{*ti}; shear velocity required to maintain saltation). The impact threshold (u_{*ti}) is less than u_{*tf}, which adds complexity to attempts to predict particle motion (Martin and Kok, 2018). On Earth, the impact threshold is about 80% of the fluid threshold (Bagnold, 1937), while on Mars it has been estimated to be closer to 10% (Kok, 2010), highlighting the variation in particle behavior under different conditions. In order to assess this relationship, we recorded the general threshold (u_{*tg}) when observed, and the impact threshold (u_{*ti}) values during the experiments. The expected relationship, based on observations from Earth and Mars, is that $u_{*tg} > u_{*tf} > u_{*ti}$. The table tennis balls followed this pattern (Fig. 5.6). However, for the other five grain types $u_{*tg} > u_{*ti} > u_{*tf}$, meaning that particle motion ceased at a higher velocity than the initiation velocity.

5.4 Discussion

5.4.1 Uncertainties and experimental limitations

Analog experiments are inherently limited, in that they can replicate certain features of the natural system, but are not the same in all aspects. A primary difference between the analog sediments used here (Table 5.2; Fig. 5.3) and the natural sediments (Table 5.1), are the sizes of the grains. Additionally, the surface properties of plastic are different from those of quartz, basalts, ice, and other organics, and thus any interparticle interactions are likely different, resulting in different requirements for saltation. However, previous work has shown that for sand grains (composed of quartz/basalt) with d > 200 μm, interparticle forces are negligible compared to other forces, and so we apply our results only to grains in this size regime.

This study specifically attempted to simulate low energy saltation in a turbulent fluid, a process known to occur on various planetary bodies. The Reynolds number is a dimensionless number which can be used to determine whether a flow is laminar or turbulent. When calculated for the conditions of our experiments, for windspeeds between 1-15 m/s (covering the range of measurements collected during experiments), the Reynolds number is >1000 (ranges from $1.3*10^5$ – $2*10^6$), indicating a fully turbulent flow. Assuming a fully turbulent flow in natural systems, our lab setting simulates this aspect of real flow.

The pitot tubes and anemometers used to measure the flow are manufactured with an accuracy of ±2.5% of the measured value, and report wind speeds with a resolution of 0.01 m/s. These measurements were recorded with a frequency of 1 Hz, by analyzing footage of the experiments in one second increments. Threshold values were identified based on degree of grain motion (first saltation, continuous saltation, saltation cessation; Fig. 5.6), but the determination of these thresholds is subjective, and thus introduces uncertainties in the reported values. Standard deviations in the average threshold values for each analog grain type were <10% of the average value in nearly all cases.

We found that the maximum wind speeds generated by the fan were in many cases limiting observations of the general and impact thresholds. In several cases, u_{*tg} was not reached, as the wind speeds were insufficient to mobilize >50% of the analog grains at once. As continuous motion was not achieved, the splash process, whereby saltating grains impacting the bed transfer energy to other grains, sustaining saltation below u_{*tf} (Fig. 5.6; Martin and Kok, 2018) was not active, and this resulted in u_{*ti} being higher than u_{*tf}, unlike in natural systems (aside from the

case of the table tennis balls; Fig. 5.6). In the case of the PLA 2 spheres, we had to deploy a separate device to provide increased wind speeds, beyond what the built-in tunnel fan is capable of, in order to initiate saltation. These observations highlight areas for improvement in future experiments in this realm.

The 'law of the wall' was used to calculate the u_{*tf} values (equation (3)). This equation includes a term Z_0 to account for the roughness length scale of the bed. In the scenario of a grain of diameter d resting on a bed of similar grains (i.e. Figs 5.1, 5.2, 5.4), the roughness scale of the bed is comparable to the grain diameter. Thus, for practical purposes, Z_0 is often approximated as being 66-75% of the grain diameter, and here we used the 0.75d. Each analog grain type then has a unique value for Z_0 (except for the three PLA grain types as all three had the same d). However, the value used is an approximation, as the appropriate value or expression for Z_0 is an area of open research. If, instead, we assume a constant value of 1 mm for Z_0, the trend in u_{*tf} among the analog grains changes, with the largest grains (table tennis and ball pit balls) having the lowest u_{*tf} values, and the smaller grains (PLA1-3 and plastic beads) having higher u_{*tf} values. This is more consistent with experimental observations, as the larger (less dense) grains were mobilized at lower measured wind speeds. Given that the assumption of a value for Z_0 is critical to the resulting u_{*tf} value and trend, we acknowledge that the approximation used may limit the resulting model's applicability to natural systems.

5.4.2 Existing expressions for the fluid threshold

Previous work to quantify the fluid threshold has generally focused on identifying the value for a given set of planetary boundary conditions, or using experimental data conducted under specific

terrestrial or analog conditions, while the objective of this work was to generalize the expression to more accurately predict the fluid thresholds on all non-terrestrial systems. Currently, most estimates of particle motion are made using the analytical approximation from Shao and Lu (2000):

$$\textbf{(5)}\ u_{*tf}(d) = \sqrt{A_N(\sigma_p g d + \frac{\gamma}{\rho d})}$$

Where A_N is 0.0123, γ is 3 x 10^{-4} kg/s^2, g is the acceleration due to gravity (9.8 m/s^2 on Earth), σ_p is the ratio of particle density to air density, d is the grain diameter, and ρ is the air density. These values can be adjusted based on the sediment composition and atmospheric properties of the planetary surface of interest (see planetary values in Table 5.1). This expression describes terrestrial grain motion well, but has been shown to be less accurate for planetary conditions (i.e., Burr et al., 2015a; Baker et al., 2018).

The Shao and Lu (2000) expression (equation (5)) is dependent on the grain diameter. The dimensionless diameter (D_*) from Swann et al. (2019) is able to capture the range of boundary conditions seen in our solar system grain sizes, compositions, and atmospheric densities; Table 5.1; equation (2); Fig. 5.7). The plot in Figure 5.7 shows our experimental results, compared with the Shao and Lu (2000) model predictions for Earth, Mars, and Titan, and results from other previous investigations into u_{*tf}. This plot is provided for comparison to previous literature, as u_{*tf} is commonly related to the grain diameter d (e.g., as in a Shields Diagram), here substituted for D_*. Using D_* rather than simply the diameter does begin to remedy the discrepancy between the model predictions and observations, as the values from other experiments and in-situ observations are a better fit to the model for $u_{*tf}(D_*)$ than $u_{*tf}(d)$. Our analog grains have D_* values beyond the range of natural sediments (Table 5.2), one factor which limits direct

comparison between the analog and natural sediments. However, the experimental results from the table tennis balls, ball pit balls, and plastic beads do align relatively well with the model predictions for the threshold values for grains with the respective D_* values in Earth conditions (Fig. 5.7). Given that the experiments were preformed in ambient Earth conditions, this is consistent with expectations. The PLA spheres did not align with model predictions, which is perhaps related to the observation that these grains were only mobilized by wind speeds at the upper limit of the equipment's capacity.

5.4.3 Validation of the new expression

The logarithmic fit to our data (equation (4); Fig. 5.5) is dependent on the submerged weight of the grain rather than the diameter. In order to determine whether the expression, and relationship between ω and u_{*tf}, is valid for planetary conditions, we must compare the output to observed values for u_{*tf}. Applying equation (4) to a grain of basalt on Mars (using ω for Mars from Table 5.1) yields a predicted u_{*tf} of 0.98 m/s^2. This is within the range of observed values reported by Baker et al. (2018) for basalt grains on Mars. This indicates that the new expression, formulated based on analog grain behaviors, does also capture the behaviors of natural sediments. Unfortunately, in-situ data is currently unavailable for other planetary bodies of interest, limiting our ability to validate our expression for bodies other than Mars. As additional data becomes available from upcoming surface exploration missions, the new expression can be assessed for accuracy.

5.4.4 Practical applications and implications for planetary missions

Understanding the conditions which lead to particle motion initiation is critical to human and robotic exploration mission safety and interpretation of aeolian features on other planetary bodies. The behavior of granular materials such as sand and dust pose a significant threat to crew health and equipment longevity in planetary exploration. For example, inhalation of Lunar dust, an issue during the Apollo missions, has been shown to have negative health effects (Cain, 2010; Lam et al., 2013), and airborne particles can impact ventilation systems. Some landed missions to Mars have experienced power decreases and eventual failure due to dust deposition on their solar panels (Lorenz and Reiss, 2015). Additionally, sand can abrade exposed equipment, causing damage (e.g. Datsiou and Overend, 2017). With upcoming missions to Titan and Venus, and active missions on Mars, understanding what wind conditions are likely to lead to sediment saltation is key.

5.5 Conclusions

The ever-growing number of high-resolution images of planetary surfaces throughout our solar system have shown that wind-driven transport is shaping the surfaces of at least seven planetary bodies (Table 5.1). Previous work to quantify the fluid threshold (u_{*tf}) has generally relied on experimental data collected under terrestrial boundary conditions (i.e., Shields, 1936; Bagnold, 1937; Fletcher, 1976; Iverson and White, 1982; Iverson et al., 1987), though we now know that transport occurs under a variety of conditions (Table 5.1). Analog experiments may not be perfect replicas of natural systems, but in many cases they can be used to simulate relevant aspects of the systems of interest. In the case of planetary aeolian transport, the relevant natural systems have a wide range of boundary conditions (Table 5.1). Using a wind tunnel operating at Earth ambient conditions (Fig. 5.1A), we were limited in which conditions we could alter in order to replicate the

conditions for grain saltation beyond Earth. We were unable to change the atmospheric density or composition, nor could we reduce the effects of Earth's gravity. However, we were able to use six types of low-density, spherical, plastic grains to simulate the net-buoyancy acting on grains on Mars, Io, Titan, and Pluto (Table 5.2; Figs. 5.2, 5.3, 5.5). Though we used grains much larger than those in natural aeolian systems, by using the submerged weight (after Swann et al., 2019) as a parameter to identify grains which would be suitable analogs for various planetary conditions, we have found an expression for u_{*tf} that is consistent with both our experimental results and observations from Mars (see Fig. 5.5). In-situ observations are presently limited to Mars, but as data from the surfaces of Venus and Titan are collected, this expression can be assessed for validity under additional boundary conditions. Future work may explore additional plastic (or other low-density material) grains to expand the range of simulated conditions and further refine the model.

5.6 Figures and Tables

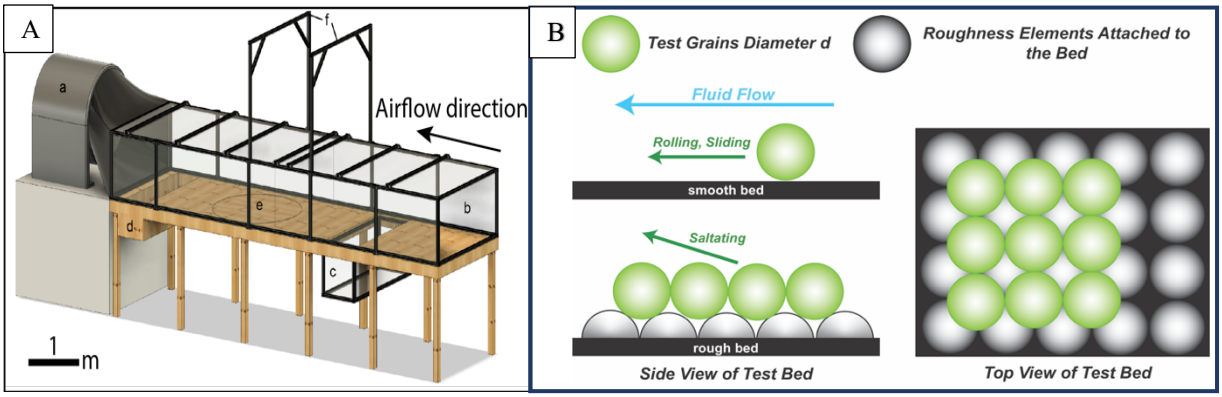

Figure 5.1. Experimental apparatus. (A) Schematic diagram of the wind tunnel used for this study. Individual components are labelled: (a) suction fan (downwind end of tunnel), (b) open end of tunnel (upwind), (d) sediment trap, (e) test area, (f) camera mounts. Optional device (c) was not used for this study. (B) Schematic of grains and test bed. Mobile analog grains with diameter d rest on a bed of immobile hemispheres (with diameter ~d). This roughness element enables saltation, rather than rolling or sliding across the bed.

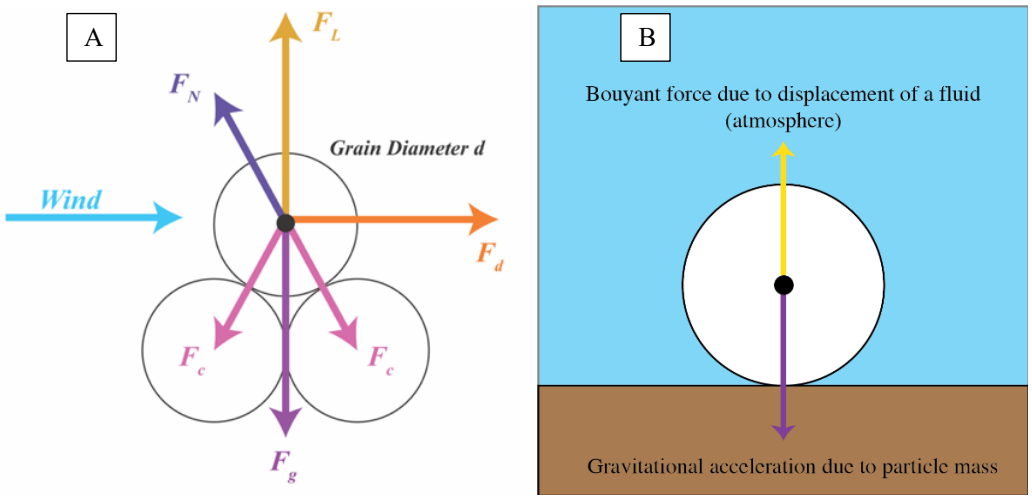

Figure 5.2. Forces acting on a grain. (A) Forces acting on a grain resting on a bed of similar grains. F_g: Gravitational force. F_L: Lift. F_d: Drag due to the motion of the fluid (wind). F_N: Normal force, which depends on the geometry of the grain pocket, and has components which act both upwards and against the forward motion of the particle (opposite to F_d). F_c: Interparticle cohesive forces, negligible for particles with d > 200 μm. (B) Buoyancy of a grain in a fluid, in this case an atmosphere. Upward force of buoyancy due to fluid displacement contributes to the lift, and acts opposite the gravitational pull.

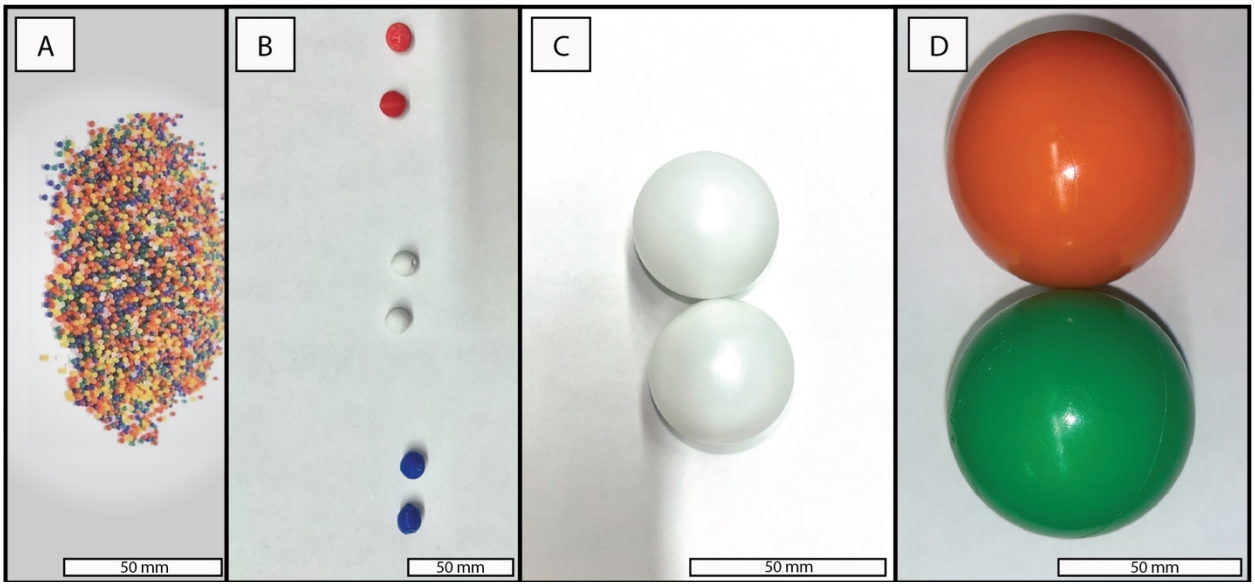

Figure 5.3. Analog Grains. Six analog grain types were used in the experiments. For details on grain properties, see Table 2. (A) Hydrophilic plastic beads. (B) 3D printed spheres, made of PLA. Three different densities were printed, represented by different colors (red, white, blue). (C) Table tennis balls. (D) Ball pit balls.

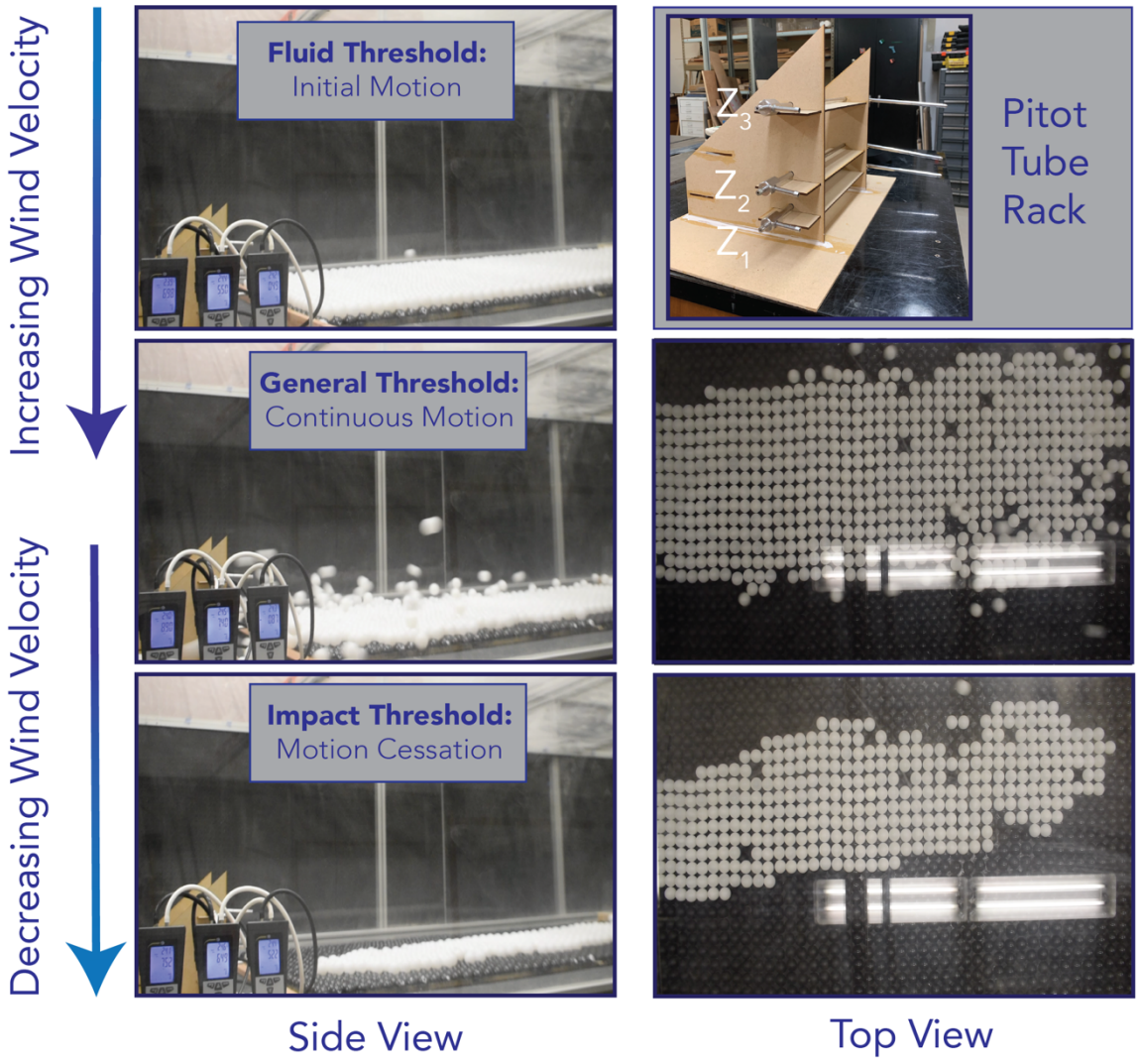

Figure 5.4. Experimental observations and measurement equipment. Saltation begins at the fluid threshold, which was identified by the first saltating grain. As wind speeds continue to increase, grain motion becomes continuous across the bed, at which point the general threshold is reached. Wind speeds were then decreased until motion terminated, which identifies the impact threshold. The right column shows the view from above, and the left column shows the view from the side during a trial using table tennis balls. The pitot tubes (and support rack) used to measure windspeeds throughout the experiments are shown on the top right.

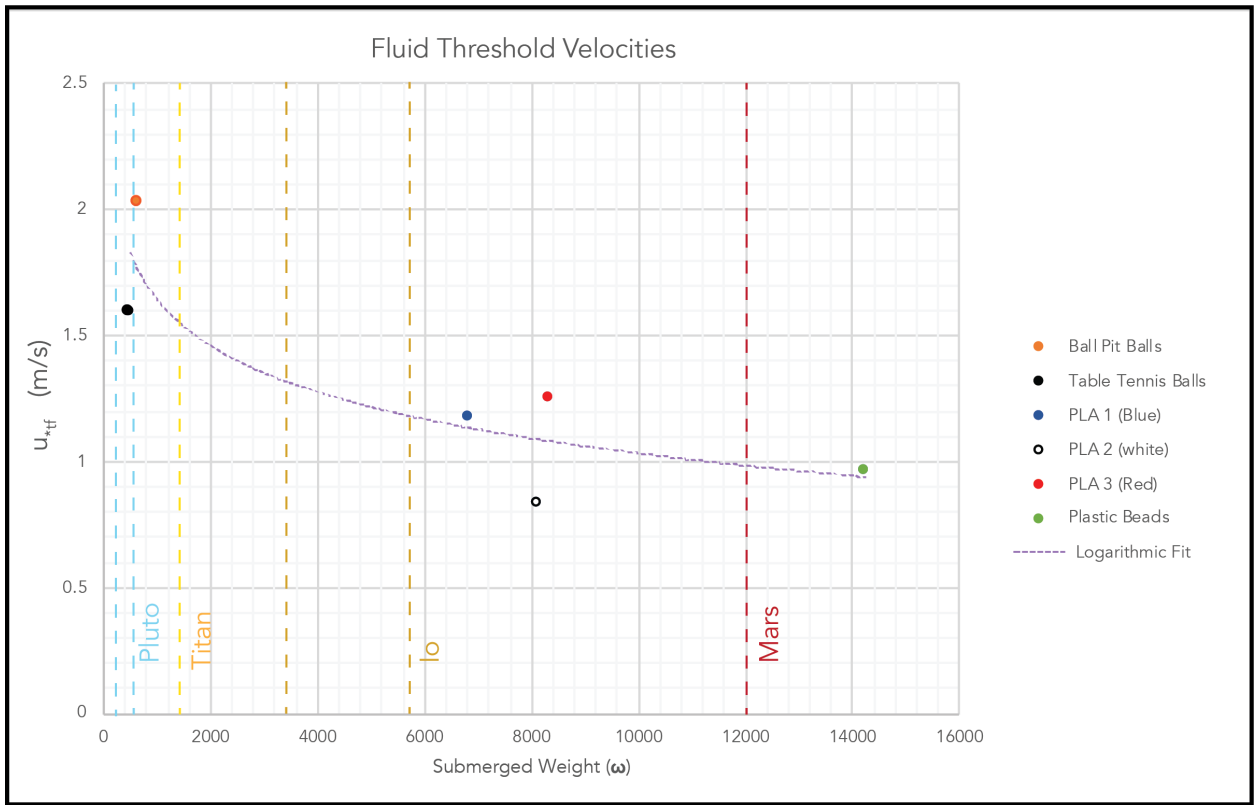

Figure 5.5. Fluid Threshold Velocities. Results of the experiments performed with six analog grain types (Tables 2 and 3, Fig. 3). The expression for the logarithmic fit (purple dashed line) is provided in equation (4). Submerged weight values for grains on Pluto (cyan), Titan (yellow), Io (tan), and Mars (red) are indicated by dashed lines (see Table 5.1 for additional details).

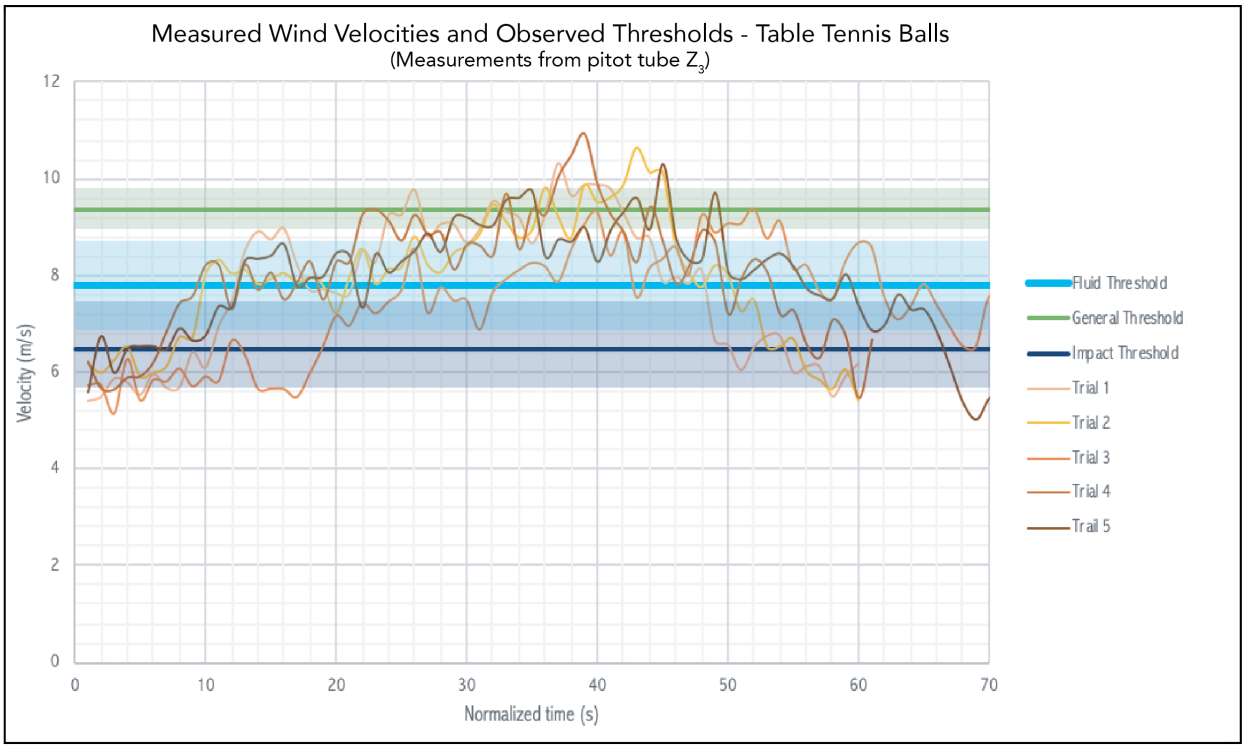

Figure 5.6. Wind speeds and thresholds for the Titan/Pluto analog grains. Wind speed measurements taken during the five trials performed using the table tennis balls are shown (light to dark brown lines), as well as the threshold values. Solid color lines indicate the average threshold values calculated from the measurements, and semi-transparent bars show ±standard deviation. The fluid threshold was above the impact threshold for these experiments, consistent with the behavior of natural sediments.

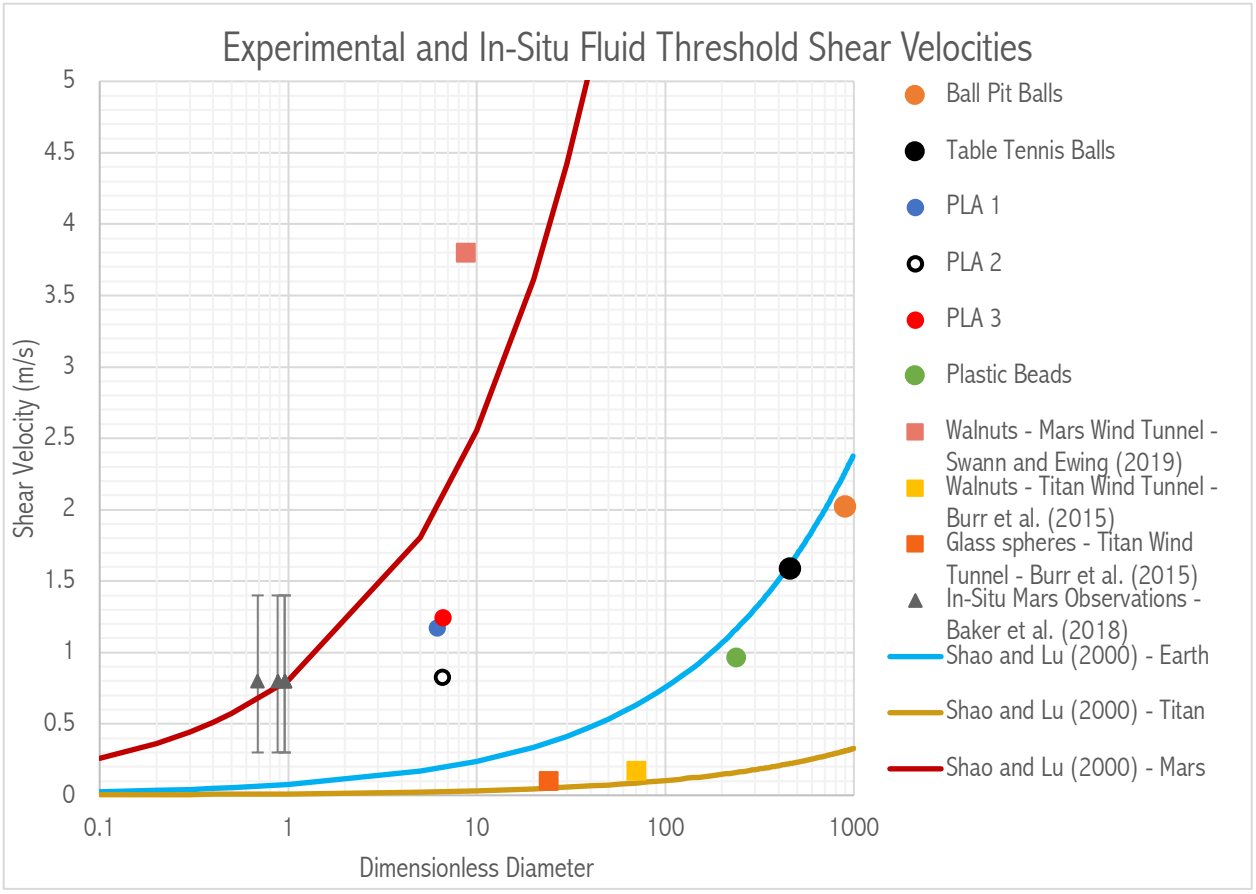

Figure 5.7. Experimental and in-situ results compared to model predictions. Results of this study are plotted as circles. Experimental results from other studies (Burr et al., 2015a, Burr et al., 2015b, Swann and Ewing, 2019), are plotted as squares. In-situ Mars observations and associated errors are plotted as triangles, based on results from Baker et al. (2018). Model outputs for the Shao and Lu (2000) expression are plotted as solid lines (equation (5)). The dimensionless diameter (Swann et al., 2019) has been substituted for the diameter term in equation (5). Appropriate variable values for Mars (red), Earth (blue), and Titan (tan), were input into equation (5), and resulting threshold predictions are shown.

Table 5.1. Properties of Planetary Bodies with Observed Aeolian Bedforms. $Submerged\ Weight\ (\omega) = g(\rho_{material} - \rho_{atm})$ and $Dimensionless\ Diameter\ (D_*) = d(\rho_{atm}\gamma/\mu)^{1/3}$ for μ = absolute atmospheric viscosity, after Swann et al. (2019). Grain diameters correspond to particle sizes either observed or predicted to be involved in aeolian transport. Lack of information regarding atmospheric conditions on Pluto and Io limits the calculation of D_*. Io calculations made using $7*10^{-9}$ kg/m^3 for atmospheric density. Material property information from Thomas, (1987), Greeley (1989), Lorenz et al. (1995), Basilevsky and Head (2003), Lorenz (2014), Burr et al. (2015a), Mendez Harper et al. (2017), Baker et al. (2018), Telfer et al. (2018), Weitz et al. (2018), Williams (2019), Filacchione et al. (2019), and Mcdonald et al. (2022). *Vapor densities of up to 10^{-5} kg/m^3 have been modelled for Comet 67P (Jia et al., 2017).

Planetary Body	Atmospheric Density (kg/m^3)	g (m/s^2)	Material	Material Density (kg/m^3)	Submerged Weight (ω)	Grain Diameter d (μm)	Dimensionless Diameter (D_*)
Earth	1.217	9.81	Basalt Quartz	3200 2650	26000 31000	62 – 2000	2.8 – 98
Mars	0.020	3.71	Basalt	3200	12000	50 – 3000	0.6 – 34
Pluto	0.00014	0.62	CH_4 Ice N_2 Ice	494 1030	310 640	200 - 300	--
Comet 67P	10^{-5}*	$2x10^{-4}$	H_2O Ice CO_2 Ice Silicates	1000 1600 ~2650	0.19 0.32 0.53	--	--
Io	4×10^{-9} – 7×10^{-9}	1.796	SO_2 Ice Basalt	1900 3200	3400 5600	50 - 250	--
Titan	5.28	1.32	Organics	~1000	1300	100 – 300 500 – 600	5.6 – 34
Venus	65	8.87	Basalt	3200	28000	< 4000	3.6

Table 5.2. Analog Grain Properties. Analog grains/materials and associated properties. Analog materials for Pluto, Titan, Io and Mars were used in this study; values for these planetary bodies can be found in Table 1. Dimensionless diameters (D_*) for natural sediments involved in aeolian transport in planetary systems range from 0.6 – 98.

Analog Material	Density (kg/m^3)	Average Diameter (mm)	Submerged Weight	D_*	Analog for…
Ball Pit Balls	67.48	59.52	649.38	901.72	Pluto (N_2)/Titan
Table Tennis Balls	52.75	37.02	505.02	458.02	Pluto (N_2)/Titan
3D printed PLA 1 (blue)	697.76	8	6826.13	6.17	Titan/Mars/Io
3D printed PLA 2 (white)	829.10	8	8113.3	6.54	Mars/Io
3D printed PLA 3 (red)	852.24	8	8340.13	6.6	Mars/Io
Hydrophilic Plastic Beads	1452.78	1.99	14225.36	238.42	Mars

Table 5.3. Fluid threshold values for analog grains. Fluid threshold values calculated from experimental results using equation (3).

Analog Material	u_{*tf} (m/s)
Ball Pit Balls	2.02
Table Tennis Balls	1.59
3D printed PLA 1 (blue)	1.17
3D printed PLA 2 (white)	0.83
3D printed PLA 3 (red)	1.25
Hydrophilic Plastic Beads	0.96

5.7 References

Bagnold, R. A. (1937). The Transport of Sand by Wind. *The Geographical Journal*, *89*(5), 409–438. https://doi.org/10.2307/1786411

Bagnold, R.A., 1941. The physics of blown sand and desert dunes. Methuen, New York.

Baker, M. M., Newman, C. E., Lapotre, M. G. A., Sullivan, R., Bridges, N. T., & Lewis, K. W. (2018). Coarse Sediment Transport in the Modern Martian Environment. *Journal of Geophysical Research: Planets*, *123*(6), 1380–1394. https://doi.org/10.1002/2017JE005513

Bourke, M. C., Lancaster, N., Fenton, L. K., Parteli, E. J. R., Zimbelman, J. R., & Radebaugh, J. (2010). Extraterrestrial dunes: An introduction to the special issue on planetary dune systems. *Geomorphology*, *121*(1–2), 1–14. https://doi.org/10.1016/j.geomorph.2010.04.007

Bretzfelder, J. M. and M. Day (2021) "Alien Aeolian Bedforms: A Comparative Sedimentary Analysis of the Dingo Gap Bedform and Hidden Valley Ripple Traverses, Gale Crater, Mars." *Journal of Geophysical Research: Planets.* doi: 10.1029/2021JE006904

Bridges, N. T., Ayoub, F., Avouac, J.-P., Leprince, S., Lucas, A., & Mattson, S. (2012). Earth-like sand fluxes on Mars. *Nature*, *485*(7398), 339–342. https://doi.org/10.1038/nature11022

Burr, D. M., Bridges, N. T., Marshall, J. R., Smith, J. K., White, B. R., & Emery, J. P. (2015b). Higher-than-predicted saltation threshold wind speeds on Titan. *Nature*, *517*(7532), 60–63. https://doi.org/10.1038/nature14088

Burr, D. M., Bridges, N. T., Smith, J. K., Marshall, J. R., White, B. R., & Williams, D. A. (2015a). The Titan Wind Tunnel: A new tool for investigating extraterrestrial aeolian environments. *Aeolian Research*, *18*, 205–214. https://doi.org/10.1016/j.aeolia.2015.07.008

Cain, J. R. (2010). Lunar dust: The Hazard and Astronaut Exposure Risks. *Earth, Moon, and Planets*, *107*(1), 107–125. https://doi.org/10.1007/s11038-010-9365-0

Craddock, R. A. (2012). Aeolian processes on the terrestrial planets: Recent observations and future focus. *Progress in Physical Geography: Earth and Environment*, *36*(1), 110–124. https://doi.org/10.1177/0309133311425399

Datsiou, K. C., & Overend, M. (2017). Artificial ageing of glass with sand abrasion. *Construction and Building Materials*, *142*, 536–551. https://doi.org/10.1016/j.conbuildmat.2017.03.094

Diniega, S., Kreslavsky, M., Radebaugh, J., Silvestro, S., Telfer, M., & Tirsch, D. (2017). Our evolving understanding of aeolian bedforms, based on observation of dunes on different worlds. *Aeolian Research*, *26*, 5–27. https://doi.org/10.1016/j.aeolia.2016.10.001

Filacchione, G., Groussin, O., Herny, C., Kappel, D., Mottola, S., Oklay, N., Pommerol, A., Wright, I., Yoldi, Z., Ciarniello, M., Moroz, L., & Raponi, A. (2019). Comet 67P/CG Nucleus Composition and Comparison to Other Comets. *Space Science Reviews*, *215*(1), 19. https://doi.org/10.1007/s11214-019-0580-3

Fletcher, B. (1976). The incipient motion of granular materials. *Journal of Physics D: Applied Physics*, *9*(17), 2471–2478. https://doi.org/10.1088/0022-3727/9/17/007

Greeley, R. (1989). *Aeolian Processes on Venus*. 21–22. http://adsabs.harvard.edu/full/1989LPICo.708...21G

Iversen, J. D., & White, B. R. (1982). Saltation threshold on Earth, Mars and Venus. *Sedimentology*, *29*(1), 111–119. https://doi.org/10.1111/j.1365-3091.1982.tb01713.x

Iversen, James D., Greeley, R., Marshall, J. R., & Pollack, J. B. (1987). Aeolian saltation threshold: The effect of density ratio. *Sedimentology*, *34*(4), 699–706. https://doi.org/10.1111/j.1365-3091.1987.tb00795.x

Jia, P., Andreotti, B., & Claudin, P. (2017). Giant ripples on comet 67P/Churyumov–Gerasimenko sculpted by sunset thermal wind. *Proceedings of the National Academy of Sciences*, *114*(10), 2509–2514. https://doi.org/10.1073/pnas.1612176114

Kok, J. F. (2010). An improved parameterization of wind-blown sand flux on Mars that includes the effect of hysteresis. *Geophysical Research Letters*, *37*(12). https://doi.org/10.1029/2010GL043646

Lam, C., Scully, R. R., Zhang, Y., Renne, R. A., Hunter, R. L., McCluskey, R. A., Chen, B. T., Castranova, V., Driscoll, K. E., Gardner, D. E., McClellan, R. O., Cooper, B. L., McKay, D. S., Marshall, L., & James, J. T. (2013). Toxicity of lunar dust assessed in inhalation-exposed rats. *Inhalation Toxicology*, *25*(12), 661–678. https://doi.org/10.3109/08958378.2013.833660

Lorenz, R. D., Lunine, J. I., Grier, J. A., & Fisher, M. A. (1995). Prediction of aeolian features on planets: Application to Titan paleoclimatology. *Journal of Geophysical Research: Planets*, *100*(E12), 26377–26386. https://doi.org/10.1029/95JE02708

Lorenz, Ralph D. (2014). Physics of saltation and sand transport on Titan: A brief review. *Icarus*, *230*, 162–167. https://doi.org/10.1016/j.icarus.2013.06.023

Lorenz, R. D., & Reiss, D. (2015). Solar Panel Clearing Events, Dust Devil Tracks, and in-situ Vortex Detections on Mars. *Icarus*, *248*, 162–164. https://doi.org/10.1016/j.icarus.2014.10.034

McDonald, G. D., Méndez Harper, J., Ojha, L., Corlies, P., Dufek, J., Ewing, R. C., & Kerber, L. (2022). Aeolian sediment transport on Io from lava–frost interactions. *Nature Communications*, *13*(1), Article 1. https://doi.org/10.1038/s41467-022-29682-x

Martin, R. L., & Kok, J. F. (2018). Distinct Thresholds for the Initiation and Cessation of Aeolian Saltation From Field Measurements. *Journal of Geophysical Research: Earth Surface*, *123*(7), 1546–1565. https://doi.org/10.1029/2017JF004416

Méndez Harper, J. S., McDonald, G. D., Dufek, J., Malaska, M. J., Burr, D. M., Hayes, A. G., McAdams, J., & Wray, J. J. (2017). Electrification of sand on Titan and its influence on sediment transport. *Nature Geoscience*, *10*(4), 260–265. https://doi.org/10.1038/ngeo2921

Phillips, M. (1980). A force balance model for particle entrainment into a fluid stream. *Journal of Physics D: Applied Physics*, *13*(2), 221–233. https://doi.org/10.1088/0022-3727/13/2/019

Shao, Y., & Lu, H. (2000). A simple expression for wind erosion threshold friction velocity. *Journal of Geophysical Research: Atmospheres*, *105*(D17), 22437–22443. https://doi.org/10.1029/2000JD900304

Shields, A. (1936). Application of similarity principles and turbulence research to bed-load movement. *CalTech Library*. https://repository.tudelft.nl/islandora/object/uuid%3Aa66ea380-ffa3-449b-b59f-38a35b2c6658

Silvestro, S., Chojnacki, M., Vaz, D. A., Cardinale, M., Yizhaq, H., & Esposito, F. (2020). Megaripple Migration on Mars. *Journal of Geophysical Research: Planets*, *125*(8), e2020JE006446. https://doi.org/10.1029/2020JE006446

Spalding, D. B. (1961). A Single Formula for the "Law of the Wall." *Journal of Applied Mechanics*, *28*(3), 455–458. https://doi.org/10.1115/1.3641728

Swann, C., Sherman, D. J., & Ewing, R. C. (2019). Experimentally Derived Thresholds for Windblown Sand on Mars. *Geophysical Research Letters*, *47*(3), e2019GL084484. https://doi.org/10.1029/2019GL084484

Telfer, M. W., Parteli, E. J. R., Radebaugh, J., Beyer, R. A., Bertrand, T., Forget, F., Nimmo, F., Grundy, W. M., Moore, J. M., Stern, S. A., Spencer, J., Lauer, T. R., Earle, A. M., Binzel, R. P., Weaver, H. A., Olkin, C. B., Young, L. A., Ennico, K., Runyon, K., & The New Horizons Geology, Geophysics and Imaging Science Theme Team (2018). Dunes on Pluto. *Science*, *360*(6392), 992–997. https://doi.org/10.1126/science.aao2975

Thomas, N. (1987). Condensation and sublimation on Io. *Monthly Notices of the Royal Astronomical Society*, *226*, 195–207. https://doi.org/10.1093/mnras/226.1.195

Weitz, C. M., Sullivan, R. J., Lapotre, M. G. A., Rowland, S. K., Grant, J. A., Baker, M., & Yingst, R. A. (2018). Sand Grain Sizes and Shapes in Eolian Bedforms at Gale Crater, Mars. *Geophysical Research Letters*, *45*(18), 9471–9479. https://doi.org/10.1029/2018GL078972

Williams, D. (2019). *Planetary Fact Sheet*. Retrieved April 18, 2021, from https://nssdc.gsfc.nasa.gov/planetary/factsheet/

CHAPTER 6: Summary and Conclusion

Though the research projects described above investigate phenomena on several different planetary bodies, all four studies are linked by the underlying theme of aeolian sediment transport. Wind shapes the surfaces of at least seven worlds in our solar system alone, several of which do not possess persistent atmospheres (Greely, 1989; Lorenz, 2014; Jia et al., 2017; Diniega et al., 2017; Telfer et al., 2018; Macdondald et al., 2022). This indicates that aeolian sediment transport is likely a pervasive process on planetary surfaces throughout our universe, and that wind can effectively transport sediments of a variety of compositions, under a wide range of boundary conditions (see Chapter 5).

Our exploration of Mars, a world dominated by aeolian activity for at least 3 billion years, provides in-situ information on surface features, enabling detailed investigations of how the formation and evolution of aeolian features relates to climate history (e.g., Banham et al., 2022, Watkins et al., 2022). The study described in Chapter 3 leveraged in-situ and orbital images of the enigmatic bedrock ridges in Gale crater to create a paleo-wind map of the crater. The resulting map indicates that the wind regime in the crater has remained consistent for the past ~3 billion years. The results also suggest that while the winds in Gale crater are responsible for the deposition and migration of dunes and ripples in some areas, in other areas the abrasive action of sand moving across the bedrock has eroded unique landforms into the surface of Aeolis Mons (Bretzfelder et al., 2024).

The perspective provided by the rovers is invaluable to our understanding of surface processes on Mars. While navigating the variable terrain, the rovers have encountered bedform types that are unique to Mars (and thus of scientific interest), but which also pose a driving hazard (e.g., Arvidson

et al., 2017). Chapter 2 of this work investigated the sedimentology of two bedform types encountered by Curiosity. Though similar in scale, the terra-mechanical properties of the bedforms were vastly different. The ~1.34 m bedform at Dingo Gap was traversed without incident, while an attempted crossing of the Hidden Valley ripples (~10s of cm in height) was aborted due to high wheel slippage. The results described in Chapter 2 indicate that the relative dust content of the two features has a strong impact on their suitability for a rover traverse. Additionally, the longevity of the wheel tracks left behind by the rover indicates that this area of Mars is not particularly active, at least not on the 2-3 Mars year timescale for which data was available. This result was surprising, as a global dust storm occurred during the observation period, and yet the aeolian activity associated with that event was insufficient to resurface the wheel tracks (Bretzfelder and Day, 2021).

In order to better understand features on Mars (and other planetary bodies), we must first identify and investigate analogous processes on Earth. There are several locations around the world that have been used as analogs for various different features or regions on the surface of Mars, but many are extremely difficult to access (e.g., Barret et al., 2008; Cary et al., 2010; de Silva et al., 2013; Bridges et al., 2015). One understudied, but potentially viable Martian analog site, is the Ibex dune field located in Death Valley National Park. The dunes are protected, and provide a natural laboratory for the study of aeolian processes. The research in Chapter 4 provides a field guide to the site, as existing literature on the dune field is scarce. Additionally, we highlighted the benefits and potential drawbacks to using these dunes as a Martian analog, in hopes of enabling future work in the area.

Given the range of conditions under which aeolian transport can occur, a comprehensive understanding of when grain motion is initiated is important for active and upcoming exploration efforts. Current models for the fluid threshold velocity (which is the shear velocity required to initiate saltation; e.g., Shao and Lu, 2000 and references therein), have been shown to be inaccurate for planetary conditions (Burr et al., 2015a; Burr et al., 2015b; Baker et al., 2018; Swann et al., 2019), so we sought to develop a new expression to model this threshold. Chapter 5 describes laboratory experiments using low-density plastic analog grains to investigate motion initiation under planetary boundary conditions. The results of the experiments were used to create a logarithmic fit, which relates the buoyancy of a given particle in an atmosphere to the fluid threshold velocity. When applied to Mars conditions, the new expression matches in-situ observations by Baker et al. (2018) of particle motion.

The work included here investigated processes that act over a range of timescales, from seconds to billions of years, and at spatial scales from individual grain behaviors to the migration and evolution of a dune field. The results address open questions, but also highlight areas for future investigations. As data from upcoming missions to Venus and Titan (two bodies where dunes have been observed) becomes available, more questions will certainly arise. However, the hope is that the results contained in this dissertation enable future investigations into wind-driven sediment transport throughout our solar system.

6.1 References

Arvidson, R. E., Iagnemma, K. D., Maimone, M., Fraeman, A. A., Zhou, F., Heverly, M. C., Bellutta, P., Rubin, D., Stein, N. T., Grotzinger, J. P., & Vasavada, A. R. (2017). Mars Science Laboratory Curiosity Rover Megaripple Crossings up to Sol 710 in Gale Crater. *Journal of Field Robotics*, *34*(3), 495–518. https://doi.org/10.1002/rob.21647

Baker, M. M., Newman, C. E., Lapotre, M. G. A., Sullivan, R., Bridges, N. T., & Lewis, K. W. (2018). Coarse Sediment Transport in the Modern Martian Environment. *Journal of Geophysical Research: Planets*, *123*(6), 1380–1394. https://doi.org/10.1002/2017JE005513

Banham, S. G., Gupta, S., Rubin, D. M., Bedford, C. C., Edgar, L. A., Bryk, A. B., Dietrich, W. E., Fedo, C. M., Williams, R. M., Caravaca, G., Barnes, R., Paar, G., Ortner, T., & Vasavada, A. R. (2022). Evidence for Fluctuating Wind in Shaping an Ancient Martian Dune Field: The Stimson Formation at the Greenheugh Pediment, Gale Crater. *Journal of Geophysical Research: Planets*, *127*(9), e2021JE007023. https://doi.org/10.1029/2021JE007023

Barrett, J. E., Virginia, R. A., Wall, D. H., Doran, P. T., Fountain, A. G., Welch, K. A., & Lyons, W. B. (2008). Persistent effects of a discrete warming event on a polar desert ecosystem. *Global Change Biology*, *14*(10), 2249–2261. https://doi.org/10.1111/j.1365-2486.2008.01641.x

Bretzfelder, J. M., & Day, M. (2021). Alien Aeolian Bedforms: A Comparative Sedimentary Analysis of the Dingo Gap Bedform and Hidden Valley Ripple Traverses, Gale Crater, Mars. *Journal of Geophysical Research: Planets*, *126*(8), e2021JE006904. https://doi.org/10.1029/2021JE006904

Bretzfelder, J. M., Stack, K. M., Fraeman, A. A., Day, M., Dietrich, W. E., & Bryk, A. B. (2024). Aeolian bedrock ridges in Gale crater, Mars. *Icarus*, *408*, 115855. https://doi.org/10.1016/j.icarus.2023.115855

Bridges, N. T., Spagnuolo, M. G., de Silva, S. L., Zimbelman, J. R., & Neely, E. M. (2015). Formation of gravel-mantled megaripples on Earth and Mars: Insights from the Argentinean Puna and wind tunnel experiments. *Aeolian Research*, *17*, 49–60. https://doi.org/10.1016/j.aeolia.2015.01.007

Burr, D. M., Bridges, N. T., Marshall, J. R., Smith, J. K., White, B. R., & Emery, J. P. (2015). Higher-than-predicted saltation threshold wind speeds on Titan. *Nature*, *517*(7532), Article 7532. https://doi.org/10.1038/nature14088

Burr, D. M., Bridges, N. T., Smith, J. K., Marshall, J. R., White, B. R., & Williams, D. A. (2015). The Titan Wind Tunnel: A new tool for investigating extraterrestrial aeolian environments. *Aeolian Research*, *18*, 205–214. https://doi.org/10.1016/j.aeolia.2015.07.008

Cary, S. C., McDonald, I. R., Barrett, J. E., & Cowan, D. A. (2010). On the rocks: The microbiology of Antarctic Dry Valley soils. *Nature Reviews Microbiology*, *8*(2), Article 2. https://doi.org/10.1038/nrmicro2281

de Silva, S. L., Spagnuolo, M. G., Bridges, N. T., & Zimbelman, J. R. (2013). Gravel-mantled megaripples of the Argentinean Puna: A model for their origin and growth with implications for Mars. *GSA Bulletin*, *125*, 1912–1929. http://dx.doi.org/10.1130/B30916.1

Diniega, S., Kreslavsky, M., Radebaugh, J., Silvestro, S., Telfer, M., & Tirsch, D. (2017). Our evolving understanding of aeolian bedforms, based on observation of dunes on different worlds. *Aeolian Research*, *26*, 5–27. https://doi.org/10.1016/j.aeolia.2016.10.001

Greeley, R. (1989). *Aeolian Processes on Venus*. 21–22. http://adsabs.harvard.edu/full/1989LPICo.708...21G

Jia, P., Andreotti, B., & Claudin, P. (2017). Giant ripples on comet 67P/Churyumov–Gerasimenko sculpted by sunset thermal wind. *Proceedings of the National Academy of Sciences*, *114*(10), 2509–2514. https://doi.org/10.1073/pnas.1612176114

Lorenz, R. D. (2014). Physics of saltation and sand transport on Titan: A brief review. *Icarus*, *230*, 162–167. https://doi.org/10.1016/j.icarus.2013.06.023

McDonald, G. D., Méndez Harper, J., Ojha, L., Corlies, P., Dufek, J., Ewing, R. C., & Kerber, L. (2022). Aeolian sediment transport on Io from lava–frost interactions. *Nature Communications*, *13*(1), Article 1. https://doi.org/10.1038/s41467-022-29682-x

Shao, Y., & Lu, H. (2000). A simple expression for wind erosion threshold friction velocity. *Journal of Geophysical Research: Atmospheres*, *105*(D17), 22437–22443. https://doi.org/10.1029/2000JD900304

Swann, C., Sherman, D. J., & Ewing, R. C. (2020). Experimentally Derived Thresholds for Windblown Sand on Mars. *Geophysical Research Letters*, *47*(3), e2019GL084484. https://doi.org/10.1029/2019GL084484

Telfer, M. W., Parteli, E. J. R., Radebaugh, J., Beyer, R. A., Bertrand, T., Forget, F., Nimmo, F., Grundy, W. M., Moore, J. M., Stern, S. A., Spencer, J., Lauer, T. R., Earle, A. M., Binzel, R. P., Weaver, H. A., Olkin, C. B., Young, L. A., Ennico, K., Runyon, K., & The New Horizons Geology, G. and I. S. T. T. (2018). Dunes on Pluto. *Science*, *360*(6392), 992–997. https://doi.org/10.1126/science.aao2975

Watkins, J. A., Grotzinger, J. P., Stein, N. T., Banham, S. G., Gupta, S., Rubin, D. M., Morgan, K. S., Edgett, K. S., Frydenvang, J., Siebach, K. L., Lamb, M. P., Sumner, D. Y., & Lewis, K. W. (2022). Burial and Exhumation of Sedimentary Rocks Revealed by the Base

Stimson Erosional Unconformity, Gale Crater, Mars. *Journal of Geophysical Research: Planets*, *127*(7), e2022JE007293. https://doi.org/10.1029/2022JE007293